

COMSAT
Technical Review

Volume 8 Number 1, Spring 1978

COMSAT TECHNICAL REVIEW

Volume 8 Number 1, Spring 1978

Advisory Board Joseph V. Charyk
William W. Hagerty
John V. Harrington
Sidney Metzger

Editorial Board Pier L. Bargellini, Chairman
Robert D. Briskman
S. J. Campanella
William L. Cook
Jorge C. Fuenzalida
R. W. Kreutel
Norman S. Lomas
Akos G. Revesz
George R. Welti

Editorial Staff Stephen D. Smoke
MANAGING EDITOR
Margaret B. Jacocks
TECHNICAL EDITOR
Edgar Bolen
PRODUCTION
Vicki A. Araujo
CIRCULATION

COMSAT TECHNICAL REVIEW is published twice a year by Communications Satellite Corporation (COMSAT). Subscriptions, which include the two issues published within a calendar year, are: one year, \$7 U.S.; two years, \$12; three years, \$15; single copies, \$5; article reprints, \$1. Make checks payable to COMSAT and address to Treasurer's Office, Communications Satellite Corporation, 950 L'Enfant Plaza, S.W., Washington, D.C. 20024, U.S.A.

© COMMUNICATIONS SATELLITE CORPORATION 1978

- 1 INTELSAT-IV IN-ORBIT LIQUID SLOSH TESTS AND PROBLEMS IN THE THEORETICAL ANALYSIS OF THE DATA **V. J. Slabinski**
- 41 PERFORMANCE OF HIGH-LEVEL DATA LINK CONTROL IN SATELLITE COMMUNICATIONS **A. K. Kaul**
- 89 INTERMODULATION IN MEMORYLESS NONLINEAR AMPLIFIERS ACCESSED BY FM AND/OR PSK SIGNALS **P. Y. K. Chang AND R. J. F. Fang**
- 141 A BOUND ON THE RELATIONSHIP BETWEEN INTERMODULATION NOISE AND CARRIER FREQUENCY ASSIGNMENT **Y. Hirata**
- 155 ANTENNA DEPOLARIZATION MEASUREMENTS USING SATELLITE SIGNALS **D. F. DiFonzo AND W. S. Trachtman**
- 187 THE COMSTAR BEACON RECEIVER **A. F. Standing**
- 205 CTR NOTES
QPSK BIT-ERROR RATE PERFORMANCE AS AFFECTED BY CASCADED LINEAR AND NONLINEAR ELEMENTS **C. Devieux, Jr.** 205
GEOSYNCHRONOUS SATELLITE LOG **W. L. Morgan** 219
- 247 1977 CTR AUTHOR INDEX
- 249 1977 INDEX OF PRESENTATIONS AND PUBLICATIONS BY COMSAT AUTHORS

INTELSAT IV in-orbit liquid slosh tests and problems in the theoretical analysis of the data*

V. J. SLABINSKI

(Manuscript received November 11, 1977)

Abstract

Each INTELSAT IV dual-spin spacecraft carries liquid hydrazine in four conispheric propellant tanks mounted on the spinning rotor section. The destabilizing effect of the liquid on attitude-nutation stability was determined from an extensive series of in-orbit tests. The liquid slosh driving frequency ratio (rotor nutation frequency/rotor spin rate) was varied over the range of 0.58 to 0.70 for the tests by rotating the spacecraft antenna platform at different rates in inertial space. A rotor-mounted accelerometer sensed the spacecraft nutation. The observed time constant for the nutation angle increase or decrease was corrected for the stabilizing contribution of the platform-mounted pendulum dampers to yield the net destabilizing dedamping contribution from the liquid slosh.

The in-orbit tests show two unexpected maxima in the dedamping contribution at driving frequency ratios that vary with the propellant loading. The rotor nutation frequency at the maxima is about one-third of the lowest mode liquid

*This paper is a revised version of one presented at the CNES-ESA Conference on "Attitude Control of Space Vehicles: Technological and Dynamical Problems Associated with the Presence of Liquid," Toulouse, France, October 10-12, 1977. It is based upon work performed at COMSAT under the sponsorship of the International Telecommunications Satellite Organization (INTELSAT). Views expressed in this paper are not necessarily those of INTELSAT.

slosh frequency given by ground test data for unspun tanks, and thus does not correspond to a simple resonance of the liquid. Ground tests with spinning systems have produced the same maxima, but the phenomenon is not yet understood.

Introduction

Definitions

A dual-spin spacecraft such as INTELSAT IV consists of a spinning rotor section and a normally despun antenna platform, with the two sections connected by a bearing assembly. The bearing axis is the intended spin axis for the spacecraft. This is an unstable axis because, by the common definition of dual-spin spacecraft, it is not the axis of maximum moment of inertia. The bearing axis may exhibit a small motion about the spacecraft's rotational angular momentum vector which is the result of two coning motions, a steady-state motion at a cone half-angle θ_W called the *wobble angle*, and a transient motion called *nutations* whose instantaneous cone half-angle θ_N is the *nutations angle*.

The INTELSAT IV spacecraft carry liquid hydrazine in four partially filled propellant tanks mounted on the rotor section. The liquid motion in response to nutation tends to increase the nutation angle at the rate $k_L\theta_N$, while the platform-mounted pendulum dampers tend to decrease the nutation angle at the rate $k_D\theta_N$. At small nutation angles, the nutation angle is observed to vary exponentially with time t :

$$\theta_N = \theta_{N,0} \exp \left[-\frac{t - t_0}{\tau} \right] \quad (1)$$

where τ is the time constant for nutation angle decay (τ positive) or growth (τ negative). Its inverse can be expressed as the difference of two positive numbers:

$$\frac{1}{\tau} = k_D - k_L \quad (2)$$

where k_D is the *damping contribution* from the platform dampers and k_L is the *dedamping contribution* from liquid slosh on the rotor. The latter contribution will be called "dedamping" for brevity. Spacecraft attitude stability requires $k_L < k_D$ so that τ is positive and any initial nutation damps out. A bound on k_L for all expected operating conditions is thus very important for successful spacecraft design and operation.

The liquid motion in the tanks is commonly referred to as "fuel slosh." This term is not strictly correct here, since hydrazine is a propellant rather than a fuel. Fuel is matter that produces power by combustion, that is, by combination with oxygen, while hydrazine produces its thrust on INTELSAT IV by catalytic decomposition. For this reason, the hydrazine motion will be called *liquid slosh*.

An important determining parameter for liquid slosh effects and hence k_L is the driving frequency ratio, ρ , defined as

$$\rho \equiv \frac{f_d}{\omega_{rz}} \quad (3)$$

where f_d is the liquid driving frequency due to nutation, and ω_{rz} is the rotor spin rate about the bearing axis, both expressed in units of rad/s. The importance of this ratio may be seen by considering that the centrifugal acceleration acting on the liquid in the tanks is $\omega_{rz}^2 R$, where R is some mean liquid distance from the spin axis. The restoring force on the liquid when displaced from equilibrium will be proportional to this acceleration so that the natural frequencies of the liquid are proportional to the square root of this quantity, $\omega_{rz} R^{1/2}$. Since the resonant frequencies are proportional to ω_{rz} , the ratio of driving frequency to liquid resonant frequency is proportional to ρ .

A dual-spin spacecraft offers a distinct advantage for the in-orbit determination of liquid slosh effects because ρ can be varied by merely rotating the platform. The liquid driving frequency during nutation is assumed to be the rotor nutation frequency, $\dot{\lambda}_r$, observed from rotor-fixed axes; hence, the variation of ρ with the platform spin rate ω_{pz} in inertial space is given by

$$\rho = \frac{|\dot{\lambda}_r|}{\omega_{rz}} = \left| \frac{I_{rz}}{I_t} \left[1 - \frac{I_{pz}\omega_{pz}}{H_z} \right]^{-1} - 1 \right| \quad (4)$$

where H_z = bearing axis component of the spacecraft's rotational angular momentum (constant to the first order for small nutation angles)

I_{pz}, I_{rz} = platform and rotor moments of inertia about the bearing axis

I_t = spacecraft moment of inertia about a transverse axis through the mass center.

Since a simple spinner can be considered as the rotor of a dual-spin space-

craft which lacks a platform, setting $I_{pz} = 0$ in equation (4) gives

$$\rho = \left| \frac{I_{rz}}{I_t} - 1 \right| \quad (\text{simple spinner}) \quad (5)$$

which shows that for a simple spinner ρ is fixed by its mass properties.

Test motivation

Prior to the first INTELSAT IV launch, Hughes Aircraft Co. performed ground tests to predict k_L for the expected spacecraft operating conditions (Reference 1, pp. 75-76). These tests indicated that any nutation would quickly decay, and that k_L was sensitive to ρ variations. However, they were performed for only a few different values of *fill fraction* (the percentage of the propellant tank volume occupied by liquid) and did not indicate two troublesome properties of k_L which were only discovered in 1974 as a result of orbital operation of the INTELSAT IV series of spacecraft. These discoveries raised questions concerning the attitude stability of the INTELSAT IV-A series of communications satellites then under development.

The first was that k_L is a strong function of the driving frequency ratio, ρ . This was discovered during the loss of antenna despun control by the INTELSAT IV F-7 spacecraft on March 21, 1974, when the antenna platform spun up to 25 rpm before recovery; k_L decreased twentyfold during a ρ value change of only 0.03. This discovery, that a small change in ρ can increase or decrease k_L by an order of magnitude, raised the possibility that INTELSAT IV-A, operating at different ρ values, might have k_L values significantly larger than those found previously in INTELSAT IV orbital operation.

This discovery also indicated a need for detailed knowledge of the k_L variation over the range of ρ values possible during an antenna platform spin-up. Such data would indicate whether loss of despun control could result in a rapid growth of the nutation angle to $\sim 90^\circ$, the "flat spin" condition from which spacecraft recovery might be difficult. Previous liquid slosh tests on the ground had been restricted to the ρ value corresponding to the despun platform condition.

The second discovery was that k_L appeared to become drastically larger with increasing fill fraction. The first five INTELSAT IV spacecraft launched had a 70-percent fill in transfer orbit after their initial spin-up. The sixth, INTELSAT IV F-8, was launched on November 21, 1974, with a 76-percent fill. The extra propellant was carried as ballast to compensate for an oversized solid propellant apogee motor. Nutation tests in transfer orbit

showed that this extra 6-percent fill doubled k_L . Since this fill fraction region had not been included in the ground tests, this raised a question concerning the magnitude of k_L for the INTELSAT IV-A spacecraft which were to use the same propellant tanks with an initial fill of 82 percent.

To resolve these questions, COMSAT conducted an extensive series of in-orbit nutation tests on the nearly identical spacecraft in the INTELSAT IV series in spring 1975. These tests took place in a 0-g environment and thus avoided the uncertainty inherent in ground testing regarding the correction, if any, which is required for the 1-g field.

Nutation test description

The basic test procedure consists of inducing spacecraft nutation and recording the continuously telemetered output of a nutation accelerometer mounted on the rotor. Figure 1 shows a typical nutation trace for a despun platform. In this case, nutation has been induced by firing an axial thruster for 0.5 s. The sensed acceleration from the nutation oscillates with the rotor nutation frequency, λ_r . This frequency may be determined directly from the time code on the strip chart by noting the time interval for a given number of nutation cycles. Scaling the amplitude at selected points along the nutation trace and fitting equation (1) to the measurements gives the time constant τ for the nutation decay or growth. The computed platform damper contribution k_D is then used in equation (2) to obtain the liquid slosh dedamping k_L .

The in-orbit tests experimentally determined k_L as a function of driving frequency ratio, ρ , and propellant tank fill fraction. The driving frequency ratio was varied by spinning the antenna platform at different rates in inertial space over a range of ± 20 rpm. Obviously, the spacecraft did not carry communications traffic during the tests. Spacecraft with greatly different fill fractions were available, since each satellite of the INTELSAT IV series had been in orbit for a different length of time and had depleted its maneuvering propellant by a different amount. Also, INTELSAT IV F-8 was tested before and after large inclination maneuvers to obtain data at fill fractions of about 66, 61, and 56 percent from the same spacecraft. Finally, to test the initial INTELSAT IV-A fill fraction, the last spacecraft to be launched in the series, INTELSAT IV F-1, was put into orbit loaded with an extra 22 kg of hydrazine propellant to give an initial fill fraction of 82 percent. Most of this extra propellant was expended in transfer orbit to help place this heavily loaded spacecraft into geostationary orbit.

The test data obtained and attempts to understand it are the subjects of this paper. The in-orbit test results prompted an extensive series of

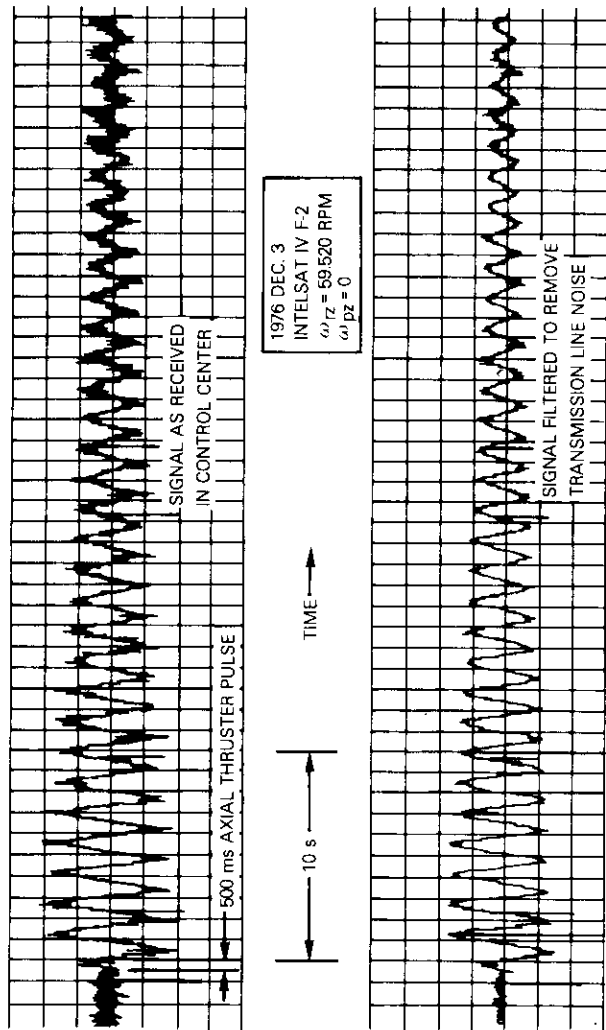


Figure 1. Nutation Accelerometer Output for a Despun Platform

liquid slosh ground tests by the spacecraft manufacturer, Hughes Aircraft Co. The large dedamping contributions found in both series of tests resulted in important modifications to the INTELSAT IV-A spacecraft design.

Basic nutation theory

The nutation theory presented herein allows for a cross product of inertia about the platform bearing axis. This cross product introduces additional acceleration frequencies in the rotor propellant tanks. Such additional frequencies due to spacecraft asymmetries may introduce unsuspected slosh effects.

Spacecraft model and platform coordinates

For the present analysis it may be assumed that all damper masses are caged and that the propellant is frozen in its equilibrium position so that each spacecraft section acts as a rigid body. It may also be assumed that the spacecraft is statically balanced so that the mass center of each section lies on the bearing axis. The spacecraft mass center then lies at a point *O* on the bearing axis which is taken as the origin of a right-handed Cartesian coordinate system $X_p Y_p Z_p$ fixed in the platform. The Z_p axis lies along the bearing axis, and the transverse axes $X_p Y_p$ are chosen so that there is no platform cross product of inertia about the $Y_p Z_p$ axes. The tensors giving the moments of inertia of the platform and rotor, respectively, are

$$(I_p) = \begin{bmatrix} I_{pt} & 0 & I_{pzz} \\ 0 & I_{pt} & 0 \\ I_{pzz} & 0 & I_{pz} \end{bmatrix}_p \tag{6}$$

$$(I_r) = \begin{bmatrix} I_{rt} & 0 & 0 \\ 0 & I_{rt} & 0 \\ 0 & 0 & I_{rz} \end{bmatrix}_p \tag{7}$$

where the *p* subscript outside tensor or vector brackets indicates platform-fixed axes. Equation (6) allows for a platform cross product of inertia I_{pzz} since this cross product produces additional acceleration frequencies in the rotor. Equation (7) assumes that the rotor is dynamically balanced so that the bearing axis is a principal axis. Both equations assume equal

moments of inertia I_{pt} and I_{rt} about any transverse axis through O so that the spacecraft moment of inertia about any transverse axis through O is given by

$$I_t = I_{pt} + I_{rt} \quad (8)$$

regardless of the relative orientation between platform and rotor. Another useful quantity is the spacecraft moment of inertia I_z about the bearing axis,

$$I_z = I_{pz} + I_{rz} \quad (9)$$

With respect to the platform-fixed axes, the angular velocities of the platform and rotor sections, respectively, in inertial space are given by

$$\vec{\omega}_p = \begin{bmatrix} \omega_{px} \\ \omega_{py} \\ \omega_{pz} \end{bmatrix}_p \quad (10)$$

$$\vec{\omega}_r = \begin{bmatrix} \omega_{rx} \\ \omega_{ry} \\ \omega_{rz} \end{bmatrix}_p \quad (11)$$

since the bearing constrains both sections to have the same X_p and Y_p components of angular velocity, ω_{px} and ω_{py} . The $+Z_p$ direction is chosen so that $\omega_{rz} > 0$. The angular momentum, \vec{H} , of the spacecraft about its mass center O is then

$$\vec{H} = \begin{bmatrix} H_x \\ H_y \\ H_z \end{bmatrix}_p = (I_p) \vec{\omega}_p + (I_r) \vec{\omega}_r \quad (12)$$

$$\vec{H} = \begin{bmatrix} I_t \omega_{px} + I_{pz} \omega_{pz} \\ I_t \omega_{py} \\ I_{px} \omega_{px} + I_{pz} \omega_{pz} + I_{rz} \omega_{rz} \end{bmatrix}_p \quad (13)$$

Because the platform-fixed axes rotate with an angular velocity $\vec{\omega}_p$ relative to inertial axes, the time derivative of any vector such as \vec{H} is given by

$$\frac{d\vec{H}}{dt} = \left[\frac{d\vec{H}}{dt} \right]_p + \vec{\omega}_p \times \vec{H} \quad (14)$$

where t is the time, and the brackets around the first term on the right side of the equation indicate a time derivative with respect to rotating axes. In the absence of external torques, $d\vec{H}/dt = 0$ and equation (14) gives

$$\left[\frac{d\vec{H}}{dt} \right]_p = -\vec{\omega}_p \times \vec{H} \quad (15)$$

as the differential equation of motion. In subsequent equations it will be assumed that the despin motor between the platform and rotor sections maintains a constant relative spin rate $\dot{\psi}$ between platform and rotor:

$$\dot{\psi} = \omega_{pz} - \omega_{rz} \quad (16)$$

so that

$$\dot{\omega}_{pz} = \dot{\omega}_{rz} \quad (17)$$

in equation (15), where a dot over a symbol indicates a time derivative.

Steady spin in platform coordinates

The spacecraft model described herein allows steady spin in platform coordinates as given by the following particular solution of equations (13) and (15):

$$\vec{\omega}_{p0} = \begin{bmatrix} \omega_{pz0} \\ 0 \\ \omega_{pz0} \end{bmatrix}_p \quad (18)$$

$$\omega_{rz} = \omega_{rz0} = \text{constant} \quad (19)$$

where
$$\omega_{pz0}(I_t \omega_{pz0} + I_{pz} \omega_{pz0}) - \omega_{pz0}(I_{px} \omega_{pz0} + I_{pz} \omega_{pz0} + I_{rz} \omega_{rz0}) = 0 \quad (20)$$

This equation has the solution

$$\frac{\omega_{px0}}{\omega_{rz0}} = \frac{-1 \pm \sqrt{1 + (b\omega_{pz0}/\omega_{rz0})^2}}{b} \quad (21)$$

where b is a dimensionless parameter defined as

$$b = \frac{2I_{pxz}\omega_{rz0}}{I_{rz}\omega_{rz0} + (I_{pz} - I_t)\omega_{pz0}} \quad (22)$$

This paper is concerned with spacecraft for which $|I_{pxz}/I_{rz}| \ll 1$ so that usually $|b| \ll 1$. Then, the ambiguous sign in equation (21) may be taken as positive to obtain a spin vector nearly parallel to the bearing axis. (The negative sign gives the "flat spin" solution.) In this case a binomial expansion of the square root in equation (21) gives

$$\omega_{px0} \simeq \frac{b\omega_{pz0}^2}{2\omega_{rz0}} \quad (23)$$

$$\omega_{pz0} = \frac{I_{pxz}\omega_{pz0}^2}{I_{rz}\omega_{rz0} + (I_{pz} - I_t)\omega_{pz0}} \quad (24)$$

Equation (24) shows that, if the platform is spinning ($\omega_{pz0} \neq 0$), a nonzero platform cross product of inertia gives $\omega_{px} \neq 0$ so that steady spin of the spacecraft occurs about a platform-fixed axis that is inclined to the bearing axis. The corresponding rotational angular momentum vector is also fixed in the X_pZ_p plane at an angle θ_W from the bearing axis as obtained from equations (12), (13), (18), and (19):

$$\tan \theta_W = \frac{\sqrt{H_x^2 + H_y^2}}{|H_{z0}|} \quad (25)$$

$$\tan \theta_W = \left| \frac{I_t\omega_{px0} + I_{pxz}\omega_{pz0}}{H_{z0}} \right| \quad (26)$$

where
$$H_{z0} = I_{pxz}\omega_{px0} + I_{pz}\omega_{pz0} + I_{rz}\omega_{rz0} \quad (27)$$

Since \vec{H} is fixed in inertial space, the bearing axis in this motion describes a cone of half-angle θ_W about \vec{H} in inertial space. This is the wobble motion.

Equation (26) may be expressed in a simple form when $|b| \ll 1$ so that equation (24) holds. Equation (24) gives

$$I_{pxz}\omega_{pz0} = \frac{\omega_{px0}}{\omega_{pz0}} \left[I_{rz}\omega_{rz0} + (I_{pz} - I_t)\omega_{pz0} \right] \quad (28)$$

which may be used to replace the second term in the numerator of equation (26) to yield

$$\tan \theta_W = \left| \frac{\omega_{px0}}{\omega_{pz0}} \left\{ \frac{I_{pz}\omega_{pz0} + I_{rz}\omega_{rz0}}{H_{z0}} \right\} \right| \quad (29)$$

Equation (27) shows that the expression within the braces is very nearly 1 for a small platform cross product; hence, equations (29) and (24) give

$$\tan \theta_W \simeq \left| \frac{\omega_{px0}}{\omega_{pz0}} \right| \quad (30)$$

$$\tan \theta_W = \left| \frac{I_{pxz}\omega_{pz0}}{I_{rz}\omega_{rz0} + (I_{pz} - I_t)\omega_{pz0}} \right| \quad (31)$$

as useful forms for numerical computation. Since H_y is zero here, equations (25) and (30) show that $\vec{\omega}_p$ and \vec{H} are parallel as required by equation (15) for steady spin.

Nutation in platform coordinates

For a dual spin spacecraft, $|I_{pxz}|/I_t$ and $|I_{pxz}|/I_z$ are quantities of the first order of smallness. To sufficient accuracy for this paper, the nutational motion about the steady spin motion is given by

$$\vec{\omega}_p = \begin{bmatrix} \omega_{px0} + \omega_t \cos \lambda_p \\ \omega_t \sin \lambda_p \\ \omega_{pz0} - k_z \omega_t \cos \lambda_p \end{bmatrix}_p \quad (32)$$

$$\omega_{rz} = \omega_{rz0} - k_z \omega_t \cos \lambda_p \quad (33)$$

with

$$k_z \equiv \frac{I_{pxz} \dot{\lambda}_p + \omega_{pz0}}{I_z \dot{\lambda}_p} \quad (34)$$

and

$$\lambda_p = \lambda_{p0} + \dot{\lambda}_p(t - t_0) \quad (35)$$

where $\dot{\lambda}_p$ is the platform nutation frequency given by

$$\dot{\lambda}_p = \frac{H_{z0}}{I_t} - \omega_{pz0} \quad (36)$$

λ_{p0} and ω_t are constants of integration, and λ_p essentially gives the azimuth of $\vec{\omega}_p$ about the steady spin solution for platform axes. This solution shows that in the presence of nutation both the platform and rotor spin rates exhibit a small oscillation at the platform nutation frequency when $I_{pxz} \neq 0$, even for the despun platform case ($\omega_{pz0} = 0$).

The accuracy of equations (32) and (33) may be verified by direct substitution into the differential equations of motion, equations (15) and (17). These equations give an exact solution for all ω_t values when $I_{pxz} = 0$; in this case $\omega_{pz0} = 0$ from equation (24) and ω_t becomes simply the magnitude of the transverse component of $\vec{\omega}_p$. When $I_{pxz} \neq 0$, the solution is correct for small ω_t values through terms of the first order in $I_t\omega_t/H_{z0}$ provided that $\dot{\lambda}_p$ is not small, more specifically, provided that the inequalities

$$I_t|\dot{\lambda}_p|^j \gg \frac{I_{pxz}^2}{I_z} |\omega_{pz0}|^j \quad (37)$$

hold for $j = 0, 1, 2, 3$. The different j values correspond to different neglected terms in the differential equations. Physically, the platform spin rate $\omega_{pz0} \simeq H_{z0}/I_t$, which gives $\dot{\lambda}_p \simeq 0$, is excluded because the nutational motion assumes a different character which is not of interest for this paper.

For small ω_t values, equations (32), (33), and (13) show that \vec{H} observed from platform axes precesses about its steady spin direction at a nearly constant angle, the nutation angle θ_N :

$$\tan \theta_N \simeq \frac{I_t\omega_t}{H_{z0}} \quad (38)$$

For small angles, θ_N is linearly proportional to ω_t .

Nutation in rotor coordinates

The nutation seen on the rotor is described by using right-handed rotor-fixed Cartesian axes X_r, Y_r, Z_r , with the origin at O and the $+Z_r$ axis coin-

cident with the $+Z_p$ and bearing axes. For these new axes,

$$\vec{\omega}_r = \begin{bmatrix} \omega_{rx} \\ \omega_{ry} \\ \omega_{rz} \end{bmatrix}_r \quad (39)$$

where an r subscript outside vector brackets indicates rotor-fixed axes, and

$$\omega_{rx} = \omega_{px} \cos \psi - \omega_{py} \sin \psi \quad (40)$$

$$\omega_{ry} = \omega_{px} \sin \psi + \omega_{py} \cos \psi \quad (41)$$

where ψ gives the angle about the bearing axis between the $+X_r$ and $+X_p$ directions. Equations (32), (33), (35), (36), and (17) then give

$$\vec{\omega}_r = \begin{bmatrix} \omega_{pz0} \cos \psi + \omega_t \cos \lambda_r \\ \omega_{pz0} \sin \psi + \omega_t \sin \lambda_r \\ \omega_{rz0} - k_z \omega_t \cos \lambda_r \end{bmatrix}_r \quad (42)$$

where $\lambda_r = \lambda_p + \psi = \lambda_{r0} + \dot{\lambda}_r(t - t_0) \quad (43)$

In equation (43), $\dot{\lambda}_r$ is the rotor nutation frequency given by

$$\dot{\lambda}_r = \dot{\lambda}_p + \dot{\psi} \quad (44)$$

$$\dot{\lambda}_r = \dot{\lambda}_I - \omega_{rz0} \quad (45)$$

where

$$\dot{\lambda}_I = \frac{H_{z0}}{I_t} \quad (46)$$

$\dot{\lambda}_I$ is the inertial nutation rate at small nutation angles, the rate at which the bearing axis precesses about \vec{H} in inertial space. Note that terms with three different frequencies are present in the rotor angular velocity.

Equation (45) shows that $\dot{\lambda}_r$ may be arbitrarily varied in the in-orbit

tests. Since $I_{pzz} \sim 0$, changing the platform spin rate varies ω_{rz0} but not $\dot{\lambda}_r$ because H_z stays constant. From equation (27), in the absence of thruster pulses,

$$H_{z0} = I_{pz}\omega_{pz0} + I_{rz}\omega_{rz0} = I_{rz}\omega_{rzd} = \text{constant} \quad (47)$$

where ω_{rzd} is the rotor spin rate with the platform despun. Equation (45) may be written as

$$\dot{\lambda}_r = \frac{I_{rz}}{I_t} \omega_{rzd} - \omega_{rz0} \quad (48)$$

Eliminating ω_{rz0} from equations (45) and (47) yields equation (4) for the variation of ρ as a function of ω_{pz0} . An alternate form giving ρ as a function of $\dot{\psi}$ is obtained by eliminating ω_{pz0} and ω_{rz0} from equations (16), (47), and (48):

$$\rho = \left| \frac{I_z}{I_t} \left[1 - \frac{I_{pz}\dot{\psi}}{I_{rz}\omega_{rzd}} \right]^{-1} - 1 \right| \quad (49)$$

Rotor accelerations and accelerometer

The acceleration \vec{a} about the spacecraft mass center O of a point P fixed in the rotor is obtained as follows. The X_r axis may be chosen so that the position vector for P is given by

$$\vec{r} = \begin{bmatrix} R_p \\ 0 \\ z_p \end{bmatrix}_r \quad (50)$$

This point has a velocity $\vec{\omega}_r \times \vec{r}$ about O ; hence, for rotating rotor axes,

$$\vec{a} = \left[\frac{d}{dt} (\vec{\omega}_r \times \vec{r}) \right]_r + \vec{\omega}_r \times (\vec{\omega}_r \times \vec{r}) \quad (51)$$

$$\vec{a} = \left[\frac{d\vec{\omega}_r}{dt} \right]_r \times \vec{r} + \vec{\omega}_r (\vec{\omega}_r \cdot \vec{r}) - \vec{r} \omega_r^2 \quad (52)$$

Keeping terms to first order in ω_{pz0} and ω_t in using equation (42) to eliminate $\vec{\omega}_r$ gives

$$\vec{a} = \begin{pmatrix} R_p [-\omega_{rz0}^2 + 2k_z \omega_t \omega_{rz0} \cos \lambda_p] \\ + z_p [\omega_{pz0} \omega_{pz0} \cos \psi + \omega_t (\dot{\lambda}_r + \omega_{rz0}) \cos \lambda_r] \\ R_p [k_z \omega_t \dot{\lambda}_p \sin \lambda_p] \\ + z_p [\omega_{pz0} \omega_{pz0} \sin \psi + \omega_t (\dot{\lambda}_r + \omega_{rz0}) \sin \lambda_r] \\ R_p [\omega_{pz0} (2\omega_{rz0} - \omega_{pz0}) \cos \psi] \\ + \omega_t (-\dot{\lambda}_r + \omega_{rz0}) \cos \lambda_r \end{pmatrix} \quad (53)$$

The large constant term $-R_p \omega_{rz0}^2$ in the X_r axis component gives the centripetal acceleration due to rotor spin.

Equation (53) makes it possible to interpret the output of an accelerometer located at P . There are two accelerometers mounted on the rotor at $R_p = 0.99$ m with their sensitive axis parallel to the bearing (Z_r) axis. Filtering their output to pass only frequencies between 0.03 and 35 Hz eliminates any contribution from the large X_r axis constant term that might be sensed due to accelerometer misalignment. The filtered output is transmitted by FM real-time telemetry to the ground where it is detected and displayed versus time on a strip chart recorder. The filter readily passes both Z_r axis terms for INTELSAT IV at its typical 50-rpm rotor spin rate: the wobble term with frequency $\dot{\psi} \sim -5$ rad/s and amplitude

$$A_W = R_p \omega_{pz0} (2\omega_{rz0} - \omega_{pz0}) \quad (54)$$

$$A_W \simeq \frac{R_p I_{pzz} (2\omega_{rz0} - \omega_{pz0}) \omega_{pz0}^2}{I_{rz} \omega_{rz0} + (I_{pz} - I_t) \omega_{pz0}} \quad (55)$$

from equations (53) and (24), and the nutation term with frequency $\dot{\lambda}_r \sim -4$ rad/s and amplitude proportional to ω_t , so that it is a measure of the nutation angle. For small platform spin rates, equation (55) gives the approximation

$$A_W \simeq 2R_p \frac{I_{pzz}}{I_{rz}} \omega_{pz0}^2 \quad (56)$$

which shows that the wobble term amplitude depends on the ratio I_{pzz}/I_{rz} .

Both the wobble and the nutation terms can appear in the nutation trace and thereby produce a beat phenomenon when the platform spins as shown in Figure 2 for INTELSAT IV-A, for which $I_{pzz}/I_{rz} = 0.06$. This

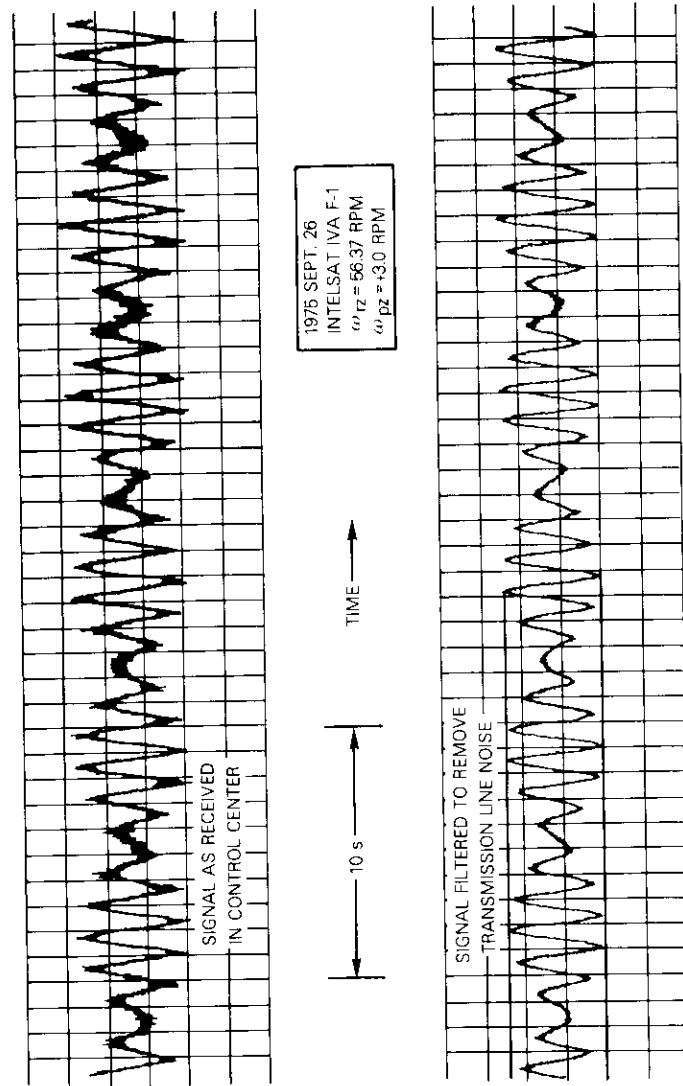


Figure 2. Nutation Accelerometer Output for a Spinning Platform with a Large Inertial Cross Product

moment of inertia ratio is large because of the INTELSAT IV-A antenna mast design. The resulting wobble term completely dominates the nutation trace at high platform spin rates and complicates the hand reduction of the nutation strip charts to yield nutation time constants. It is also possible that the liquid excitation by a large wobble term results in a significant contribution to the observed dedamping. INTELSAT IV does not have these problems because its antenna platform was dynamically balanced about the bearing axis to give a small I_{pzz} value. Its observed wobble motion gives $|I_{pzz}| \sim 0.13 \text{ kg}\cdot\text{m}^2$ so that $I_{pzz}/I_{rz} \sim 0.0006$ for this spacecraft. Thus, INTELSAT IV is ideally suited for spinning platform slosh tests. Its wobble term is detectable for $|\omega_{pz0}| > 8 \text{ rpm}$, but becomes troublesome only for $\omega_{pz0} \sim 18 \text{ rpm}$ near the $\dot{\lambda}_p \sim 0$ platform resonance.

Note that some terms in \vec{a} with frequency $\dot{\lambda}_p \sim 2 \text{ rad/s}$ are not detected by the rotor accelerometer because they do not appear for the Z_r axis. This observation indicates that all the rotor acceleration frequencies which might produce liquid slosh cannot be determined by merely performing a spectrum analysis of the telemetry record.

If P is a point in the propellant tank liquid, the Y_r and Z_r axis components of \vec{a} give the driving accelerations parallel to the free liquid surface which produce liquid slosh. The terms proportional to ω_i are responsible for the dedamping, since their effect on the liquid increases with the nutation angle. Such terms here have two different frequencies, $\dot{\lambda}_r$ and $\dot{\lambda}_p$, which are not harmonically related. The $\dot{\lambda}_p$ terms are *not* due to nonlinear effects, but arise from a theory linear in ω_i . The $\dot{\lambda}_r$ terms have the largest amplitude by a factor of 100; hence, this paper adopts the usual assumption that these terms give the only significant accelerations producing liquid slosh. The $\dot{\lambda}_p$ terms should not be completely dismissed, however. Although the $\dot{\lambda}_p$ term in the Y_r component has the small factor k_z , the liquid response at this frequency could be very large if $|\dot{\lambda}_p|$ equalled a natural frequency of the liquid. Note that this term persists even for a despun platform.

Theoreticians should develop the complete theory of such small acceleration terms due to vehicle inertia asymmetries and mass center misalignments because of the possibility of frequency coincidence with liquid resonances. It is possible that such a frequency coincidence with a well-understood liquid resonance might explain the anomalous resonances observed in orbit. Similar small acceleration terms should also occur for spinning test fixtures on the ground due to interactions with the earth's gravitational field. The amplitudes of such terms do not necessarily become zero because of a rapid vehicle spin rate.

Nutation test details

Nutation test procedure

The INTELSAT IV pendulum dampers are mounted in an open frame structure on the antenna platform. As a result, their temperature undergoes a large daily variation over a range of 100°C due to changes in shadowing and the direction of the incident sunlight as the earth-pointing antenna platform rotates at 1 rev/day in inertial space. This temperature variation causes a 40-percent change in the eddy-current damping force. To eliminate this variation from an extensive series of nutation tests extending over many hours, the platform was spun in sunlight in a "rotisserie mode" at 1 rpm for 6 hours before the tests to establish an equilibrium temperature.

For each test, the antenna despun control electronics were operated in the rate memory hold mode (Reference 2, pp. 295-299) and commanded to the proper relative spin rate $\dot{\psi}$ computed from equation (49) to give the desired ρ value. Spacecraft telemetry sent through an omnidirectional antenna indicated when the desired platform spin rate had been established. This spin rate can also be measured directly by recording the signal level of a carrier sent through a global beam antenna on the platform; the signal strength rises from zero once each platform spin period as the global beam illuminates the earth. With the spin rate established, accelerometer data were usually obtained over at least one nutation time constant. Only for tests with $\tau > 600$ s was this not always done.

For some unstable platform spin rates, the small nutation already present from starting transients would quickly increase to measurable levels. For other spin rates, measurable nutation was already present from a previous test. An axial thruster was fired to induce nutation only when necessary to avoid violating thermal constraints on thruster restarts at short time intervals. The tests were restricted to nutation angles less than 1°. To reduce the nutation angle following tests that gave unstable nutation, the platform was returned to the rotisserie mode or to some other platform spin rate that gave stable nutation rather than to the despun condition, in order to maintain the damper equilibrium temperature.

For the most accurate presentation of the data, the value of $\dot{\lambda}_r$ used to compute the ρ value actually occurring in each test should be measured on the nutation strip chart recording. For most of the tests, $\dot{\lambda}_r$ was computed from equation (48) simply because the rotor spin rate is readily obtained by telemetry from the rotor-mounted sun and earth sensors. Equation (48) gives a useful check on the spacecraft mass properties com-

puted from prelaunch measurements, but it strictly holds only for a rigid spacecraft. Liquid slosh in response to nutation may result in measurable differences from the values of equation (48). These differences could provide clues to the nature of the anomalous liquid resonances observed in the tests.

Reference 2 describes the INTELSAT IV spacecraft in great detail. Table 1

TABLE 1. MASS PROPERTIES FOR INTELSAT IV F-8

	Transfer Orbit	Synchronous Orbit	
		Start of Life	End of Life
Spacecraft Mass (kg)	1,404	753	608
Hydrazine Mass (kg)	144	142	0
Fill Fraction, f	0.758	0.747	0
Tank Center Location z_T Above Spacecraft Mass Center O (m)	+0.24	-0.24	-0.30
Moments of Inertia (kg m^2)			
$I_{\rho z}$	93	93	93
$I_{r z}$	321	255	201
I_t	1,131	702	663

lists the mass properties of a typical INTELSAT IV spacecraft based on ground measurements; adequate moment of inertia values for other synchronous orbit hydrazine loadings may be found by linear interpolation in the table. The following two subsections provide those details on the platform nutation dampers and propellant tanks necessary for a detailed understanding of the in-orbit tests.

Platform nutation dampers

Neer [1] adequately describes the two platform-mounted pendulum nutation dampers on INTELSAT IV and gives typical parameter values. The damping contribution from the i th damper is given by

$$k_{D,i} = \frac{m_i z_{D,i}^2}{I_i} \frac{\dot{\lambda}_i^3 (\xi_i \omega_{ni} \dot{\lambda}_p)}{(\omega_{ni}^2 - \omega_{pz}^2 - \dot{\lambda}_p^2)^2 + 4(\xi_i \omega_{ni} \dot{\lambda}_p)^2} \quad (57)$$

where m_i = mass of the i th damper pendulum

z_{D_i} = distance along the spacecraft bearing axis from the spacecraft mass center to the i th pendulum mass

ω_{n_i} = natural frequency of the i th pendulum

ζ_i = damping factor expressed as fraction of critical damping.

Haines and Leondes [3] derive this result using an energy sink model, which is an adequate approximation for this paper. The form of the equation presented here avoids singularities at $\lambda_p = 0$. Superposition is assumed to hold so that

$$k_D = k_{D,1} + k_{D,2} \quad (58)$$

Equations (57) and (58) were evaluated for each nutation test based on preflight ground measurements of the damper parameters. Then the liquid dedamping could be evaluated from the observed nutation time constant τ using equation (2) rewritten in the form

$$k_L = k_D - \frac{1}{\tau} \quad (59)$$

In some tests, the dedamping contribution is negligible compared to the damping contribution so that the right side of equation (59) involves the difference of two nearly equal numbers. The computed k_L values are very uncertain in such cases; therefore, such values have not been included in this paper.

The pendulum dampers swing in a plane parallel to the bearing axis but are not mounted directly on the bearing axis. At platform spin rates with absolute values above ~ 10 rpm, centrifugal forces peg the dampers against their stops, which prevents them from swinging. The most accurate dedamping values are determined with the dampers pegged because their damping contribution is then zero and $k_L = -1/\tau$ with no error due to uncertain damper parameters. The pegged dampers contribute an almost negligible $0.2 \text{ kg} \cdot \text{m}^2$ to I_{zz} .

Conispheric propellant tanks and fill fraction

Four conispheric tanks are mounted on the rotor at intervals of 90° about the bearing axis. Two such tanks are shown in cross section in Figure 3. The tank interior consists of a spherical section with an internal

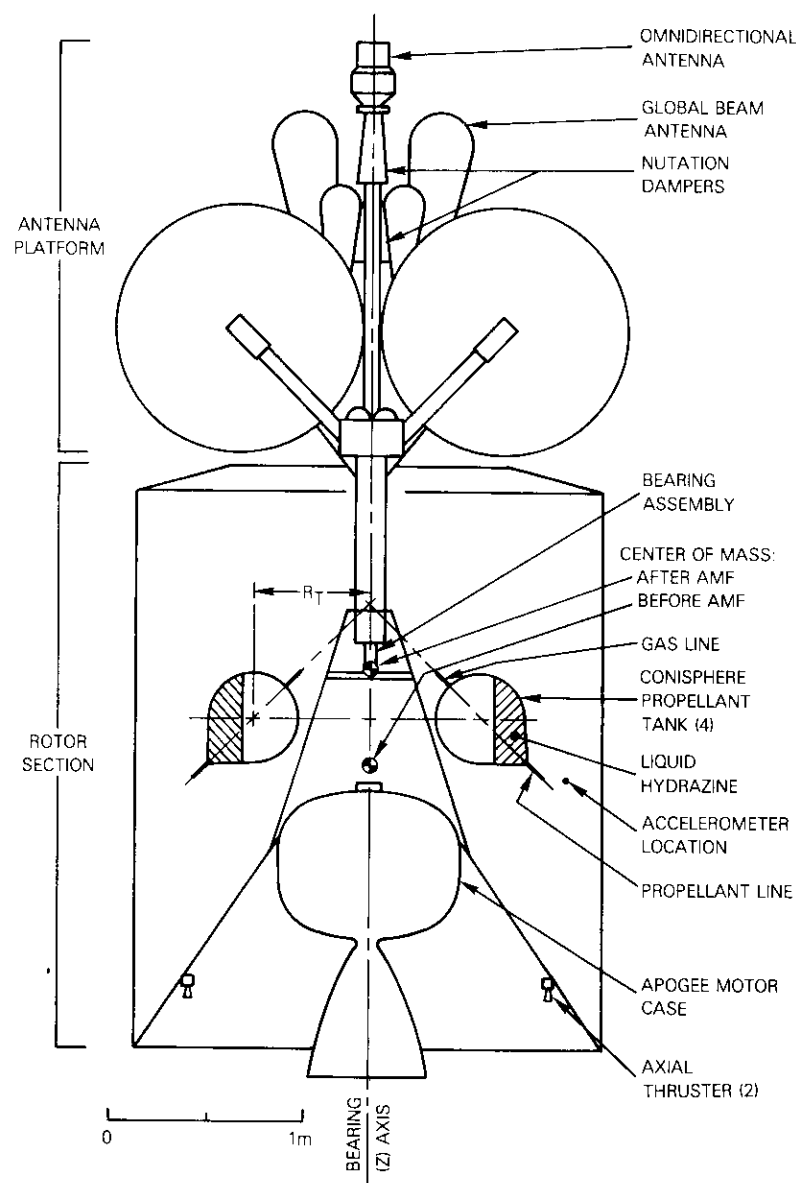


Figure 3. INTELSAT IV Spacecraft with Cutaway View of Rotor Section

radius of 0.221 *m* and a tangential conical section with a full cone angle of 85°. The cone axis passes through the bearing axis at an angle of 45°. This conispheric design allows propellant to drain completely from the tank through the apex of the cone under two conditions: on the ground when the spacecraft is vertical, and in orbit during thruster firings under the action of centrifugal forces and nitrogen gas pressurant in the tank. In theoretical discussions for fill fractions greater than 40 percent, the tanks are often assumed to be spherical since the conical section is then nearly full and the free liquid surface lies almost entirely within the spherical section. The cone volume outside a sphere inscribed in the tank is only 3.7 percent of the tank volume.

There are two independent propulsion subsystems; each pair of diametrically opposite tanks is connected to the same subsystem by two lines. A gas pressure equalization line connects at the point on the spherical wall directly opposite the cone apex, and a common propellant line connects at the cone apex so that the two tanks may drain evenly during use and maintain rotor balance. There is no oscillating transfer of liquid between tanks in response to nutation because of the high flow resistance in the connecting propellant line. This resistance is due to the length (3.25 m) and small inside diameter (5.3 mm) of the line. A high resistance is confirmed by the very long (18-min) time constant observed for the in-orbit liquid redistribution between tanks after an initial imbalance [4]. It will be assumed that the two tanks in a subsystem have identical fill fractions.

The center of each spherical section lies at a distance $R_T = 0.578$ m from the bearing axis, and at a bearing axis position $z_T = +0.24$ m above the spacecraft mass center *O* while in transfer orbit. The expulsion of 650 kg of solid propellant during apogee motor firing (AMF) shifts *O* toward the antenna platform so that $z_T = -0.24$ m after AMF. Since the tanks are nearly the same distance from *O* before and after AMF, it should be possible to combine dedamping values determined before and after. This is desirable because of the different ρ values obtainable before and after AMF; ρ due to nutation with the platform despun changes from 0.72 to 0.64.

The following considerations enter into the computation of the tank fill fraction. Hughes Aircraft Co. reports that each INTELSAT IV tank has an internal volume of 0.04689 m³ on the average with a standard deviation of 0.14 percent. Multiplying this volume by 1.008×10^3 kg/m³, the density of hydrazine at the tank operating temperature of 20°C, gives 47.26 kg for the hydrazine capacity of an unpressurized tank. The initial nitrogen gas pressure of 1.7 MN/m² increases the tank volume by 0.10 percent because of the thin wall construction. This volume increase is

reduced as the gas pressure decreases to 0.7 MN/m² with the depletion of propellant. The volume change should be included in the computation of the fill fraction for comparison of in-orbit tests with ground test data because the ground tests are often made with unpressurized tanks. The fill fraction, *f*, is computed by correcting the propellant mass, m_p (in kg), in the propulsion system for the propellant in the connecting lines and the spin-up thruster propellant reservoir (about 0.31 kg for each subsystem) to find the mass actually in the tanks; this figure is then divided by the total mass that the two tanks can hold at the existing pressure:

$$f = \frac{m_p - 0.31 \text{ kg}}{2(47.26 \text{ kg}) [1 + (0.0006 \text{ m}^2/\text{MN}) p]} \quad (60)$$

where the tank pressure, *p* (in MN/m²), is given by spacecraft telemetry. This formula has been used to compute all the in-orbit fill fractions quoted in this paper.

The propellant mass on board a spacecraft is somewhat uncertain because it is based on bookkeeping records of maneuvers and a predicted value of propellant flow when a thruster valve is opened. The accuracy of this propellant accounting was recently checked at COMSAT for some INTELSAT III satellites built by TRW, Inc. In May of 1977, the hydrazine was used to exhaustion in propelling these satellites into orbits high above synchronous altitude where they were abandoned. The end of spin speed changes and an accompanying more rapid drop in tank pressure indicated the point of exhaustion. Table 2 lists the hydrazine remaining in each system at this point according to COMSAT's accounting.

TABLE 2. INTELSAT III HYDRAZINE USE ACCOUNTING ERRORS

Parameter	INTELSAT III F-2 Propellant System		INTELSAT III F-6 Propellant System	
	1	2	1	2
Hydrazine at Launch (kg)	10.91	10.91	10.30	10.30
Hydrazine Left According to Accounting at Exhaustion (kg)	0.50	1.13	0.18	0.54
Accounting Underestimate of Propellant Use (%)	4.6	10.4	1.8	5.3
mean (%)			5.5	
standard deviation (%)			±3.1	

Table 2 shows that the accounting underestimated the propellant use by an average of 5.5 percent. If a similar error occurs for INTELSAT IV, the fill fractions listed in this paper for the most depleted tanks will be in error by 1 percent.

Nutation test results and interpretation

Data scaling

It is first necessary to consider whether any scaling should be applied to the observed dedamping values to make the data independent of arbitrary test parameters such as the rotor spin rate. For this discussion, a particular model for liquid slosh is assumed, not because this model accurately reflects reality, but only because it provides a simple illustration of scaling problems. Specifically, it is assumed that liquid slosh produces its destabilizing effect by the back and forth pendulum motion of the liquid mass in response to the nutation. Iorillo [5] models the liquid by an analogous mass-spring-dashpot damper mounted on the rotor at the tank center. This damper will be called the *Iorillo slosh model*. Iorillo shows that the dedamping from longitudinal oscillation (oscillation parallel to the bearing axis) is then given by

$$k_{Lz} = \frac{-R_T^2 (\dot{\lambda}_r + \omega_{rz})(\dot{\lambda}_r - \omega_{rz})^2 \dot{\lambda}_r c_d}{2I_t (\dot{\lambda}_r^2 - \omega_d^2)^2 + (\dot{\lambda}_r c_d / m_d)^2} \quad (61)$$

where c_d is the damping constant (the resistive force per unit velocity), m_d is the mass, and ω_d is the natural frequency of the damper. A similar expression holds for transverse oscillation, with R_T^2 replaced by z_T^2 . Because $\dot{\lambda}_r$ is generally negative for a dual spin spacecraft, the driving frequency ratio is given by

$$\rho = \frac{-\dot{\lambda}_r}{\omega_{rz}} \quad (62)$$

and

$$k_{Lz} = \frac{R_T^2 (1 - \rho)(1 + \rho)^2 \rho c_d}{2I_t (\rho^2 - \rho_{res}^2)^2 + \{\rho c_d / (m_d \omega_{rz})\}^2} \quad (63)$$

where

$$\rho_{res} = \frac{\omega_d}{\omega_{rz}} \quad (64)$$

gives the resonant frequency ratio. For the liquid case, since ω_d is propor-

tional to ω_{rz} as previously explained, ρ_{res} is independent of ω_{rz} .

The following special cases give the two extremes for spin rate scaling. For small damping constants, the expression within braces in the denominator is much smaller than ρ_{res}^2 . Then, for frequency ratios far below and far above resonance,

$$k_{Lz} \simeq \frac{R_T^2 (1 - \rho)(1 + \rho)^2 \rho c_d}{2I_t \rho_{res}^4} \quad (\rho \ll \rho_{res}) \quad (65)$$

$$k_{Lz} \simeq \frac{R_T^2 (1 - \rho)(1 + \rho)^2 \rho c_d}{2I_t \rho^4} \quad (\rho \gg \rho_{res}) \quad (66)$$

and the dedamping is independent of rotor spin rate. This is one scaling extreme. At the damper resonance,

$$k_{Lz} = \frac{R_T^2 (1 - \rho_{res})(1 + \rho_{res})^2 m_d^2 \omega_{rz}^2}{2I_t \rho_{res} c_d} \quad (\rho = \rho_{res}) \quad (67)$$

and the dedamping varies as the square of the rotor spin rate. This is the opposite scaling extreme.

These three cases indicate a scaling caveat: the dedamping value measured at a single rotor spin rate cannot be scaled to a different spin rate without some detailed knowledge of the dedamper mechanism such as the relation between the frequency ratio used in the test and resonance. Therefore, scaling will not be applied to the observed dedamping values with the exception of the following application. Equation (63) indicates that the dedamping value k_L measured for a spacecraft varies inversely with its transverse moment of inertia, I_t , so that the dedamping k'_L for a spacecraft with a different transverse inertia I'_t but identical tank geometry relative to the mass center is given by

$$k'_L = \frac{I_t}{I'_t} k_L \quad (68)$$

This scaling is used to combine transfer orbit data with data taken after AMF.

An important scaling application is the spin rate scaling of ground measurements using spinning test fixtures to orbiting satellites. These

ground tests usually involve very high spin rates to obtain a high Froude number, F_R (the ratio of centrifugal acceleration to gravitational acceleration), at the tank in order to minimize gravitational effects, while the in-orbit satellite has a much lower spin rate. However, the following difficulty arises when scaling isolated dedamping values from ground tests using full scale tanks. For isolated test points, the relation between the driving frequency ratio used and the liquid resonances is not known; hence, the scaling caveat just given warns that a simple scaling is not possible. In addition, an upper bound on the in-orbit dedamping may be obtained by using the scaling extreme from the Iorillo slosh model that gives the highest (most pessimistic) dedamping value. For scaling to lower spin rates, an upper bound is thus obtained by assuming that dedamping is independent of spin rate.

Cautions on the time constant group

The time constant group is discussed here since this quantity is sometimes misapplied in spin rate scaling. From a dimensional analysis, Neer and Salvatore, in Chapter 4 of Reference 6, propose the *dimensionless* time constant group τ_{cg} as a convenient parameter for correlating ground and in-orbit dedamping measurements. They give

$$\tau_{cg} = \frac{n\mu d_T^5 \omega_{rz} \tau_{DD}}{I_t} \quad (69)$$

$$\tau_{cg} = \text{function}(R_e, F_R, f, S, \rho, d_T/R_T, z_T/R_T) \quad (70)$$

where n = number of tanks

μ = mass density of the liquid

d_T = a characteristic tank dimension such as the sphere diameter for conispheric tanks

τ_{DD} = dedamping "time constant"

F_R = Froude number at the tank

\equiv centrifugal acceleration of tanks/gravitational acceleration (an infinite ratio in a 0-g field)

S = tank shape factor

R_T = distance of the tank (sphere) center from the bearing axis

z_T = tank height above spacecraft mass center

$$\tau_{DD} \equiv \frac{1}{k_L} \quad (71)$$

with the Reynolds number R_e defined as

$$R_e = \frac{\rho \omega_{rz} \mu d_T^2}{\eta} \quad (72)$$

where η is the liquid viscosity.

The functional relation in equation (70) is to be discovered empirically by experiment. This functional relation is useful only if the dimensionless parameters in the argument list can be varied individually. However, for the in-orbit dedamping measurements described herein, at least two of the parameters are always varied simultaneously; spinning the antenna platform at different inertial spin rates varies not only ρ but also R_e through the accompanying rotor spin rate change, as shown by equation (72). Therefore, the present paper does not use the time constant group.

For applications, equations (69) and (71) yield

$$k_L = \frac{n\mu d_T^5 \omega_{rz}}{I_t \tau_{cg}} \quad (73)$$

This equation must always be applied cautiously because τ_{cg} can be a function of the other parameters on the right side of the equation. For example, equation (73) gives no definite theoretical relation between k_L and ω_{rz} since equations (70) and (72) indicate that τ_{cg} is a possible function of ω_{rz} through the Reynolds number. From ground test data, Neer and Salvatore conclude in Chapter 7 of Reference 6 that τ_{cg} is independent of ω_{rz} at a resonance (k_L maximum); then k_L varies *linearly* with the rotor spin rate. Equation (67) from the Iorillo slosh model predicts a different result in this case, that k_L varies as *the square* of the rotor spin rate. If the Neer and Salvatore linear dependence could be verified by in-orbit tests, it could provide a valuable clue to the nature of the observed dedamping resonances.

Observed liquid resonances

Figures 4-8 show the observed dedamping values plotted versus the driving frequency ratio for various fill fractions. Figure 8, which com-

compares three different fill fractions, clearly shows that a change of a few percent in the fill fraction can result in a drastic change in the dedamping for a given ρ value. Note especially the increase in dedamping with increasing fill fraction at $\rho = 0.72$, the ratio for a despun platform while in transfer orbit. Each figure lists the dates for the nutation tests, the satellite used, and the satellite I_t value at the time of the tests for data scaling applications using equation (68). Figure 8 includes transfer orbit data scaled to the value $I_t' = 700 \text{ kg} \cdot \text{m}^2$ so that they may be readily compared with the rest of the data taken after AMF. The fill fractions for both propellant systems are always given since they may be very unequal.

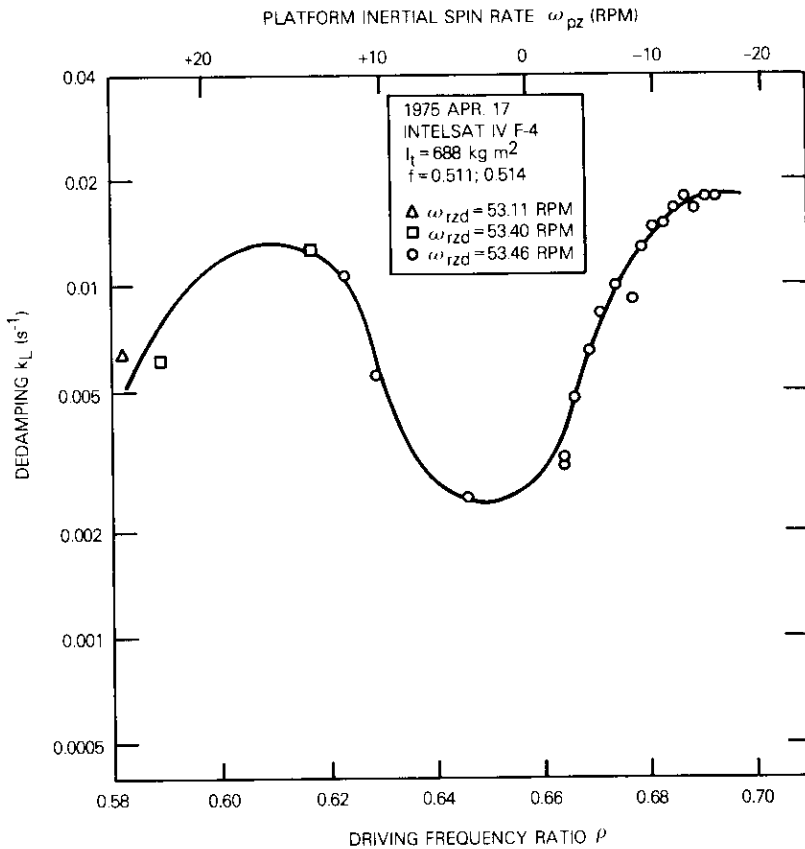


Figure 4. Tank Liquid Dedamping Contribution for a 51-Percent Fill Fraction

The data show distinct dedamping maxima which are interpreted as liquid resonances. These are called the *anomalous resonances* since their origin is not known. Two maxima are evident in some of the data: Figure 4 definitely shows two peaks, while Figure 5 shows one peak and part of a second. Figure 9 shows that the frequency ratio ρ_{res} at a maximum moves to higher values with increasing fill fraction, indicating that the anomalous resonances are actually due to the presence of liquid hydrazine on the rotor. Parallel straight lines have been drawn on the graph to indicate the trend of the data.

Thruster firings during some test series changed the spacecraft rota-

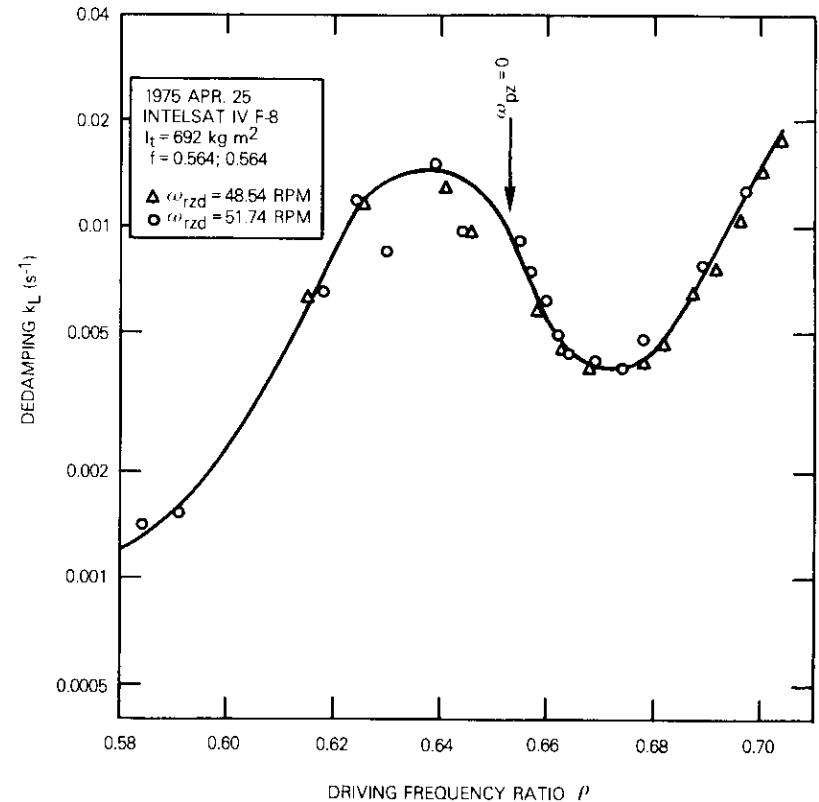


Figure 5. Tank Liquid Dedamping Contribution for a 56-Percent Fill Fraction

tional angular momentum so that different data sets for a given fill fraction may correspond to a significantly different rotor spin rate ω_{rzd} with the platform despun. Such data sets are distinguished by different plotting symbols. Figure 5 compares two such data sets taken before and after a rotor spin-up which changed ω_{rzd} from 48.54 to 51.74 rpm. The two data sets fall along the same curve although the data with the higher ω_{rzd} value appear to have slightly higher dedamping values. At the resonance peak, equation (67) from the Iorillo slosh model predicts a 12-percent difference between the data sets, while equation (73) from the time con-

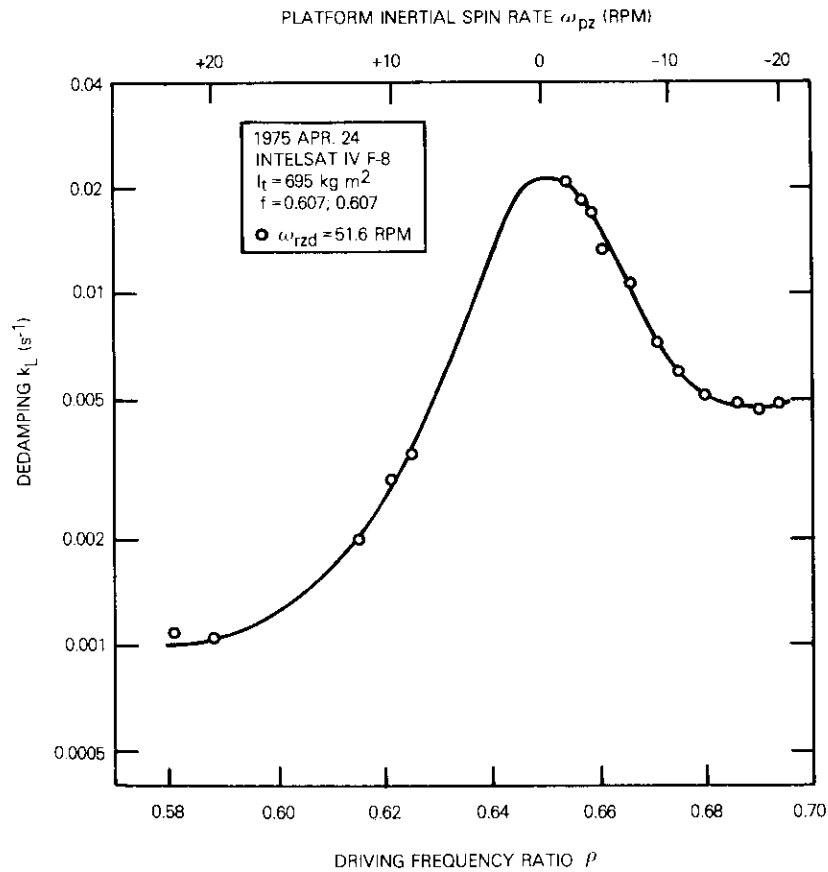


Figure 6. Tank Liquid Dedamping Contribution for a 61-Percent Fill Fraction

stant group predicts only a 6-percent difference. There is too much scatter in the data to decide between the two predictions.

Problems in the interpretation of the observed resonances

Before the in-orbit tests, *no* liquid resonance was expected within the range of frequency ratios tested. This opinion was based on ground measurements of the lowest mode natural frequency of the liquid in non-spinning spherical and conispheric tanks. Tests at COMSAT Laboratories

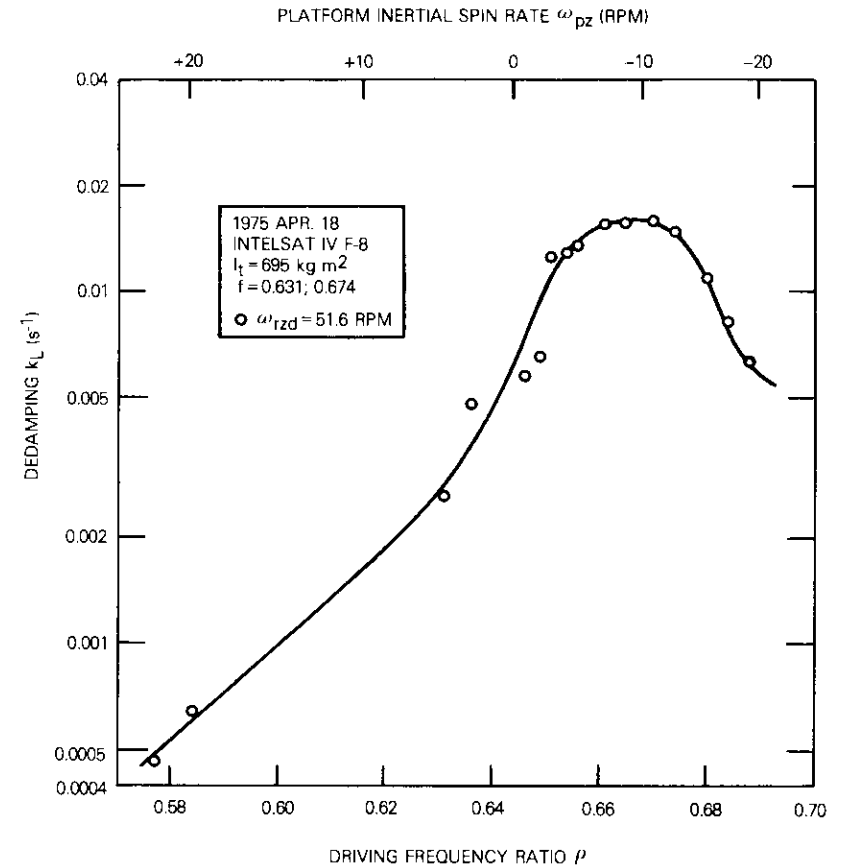


Figure 7. Tank Liquid Dedamping Contribution for a 63/67-Percent Fill Fraction

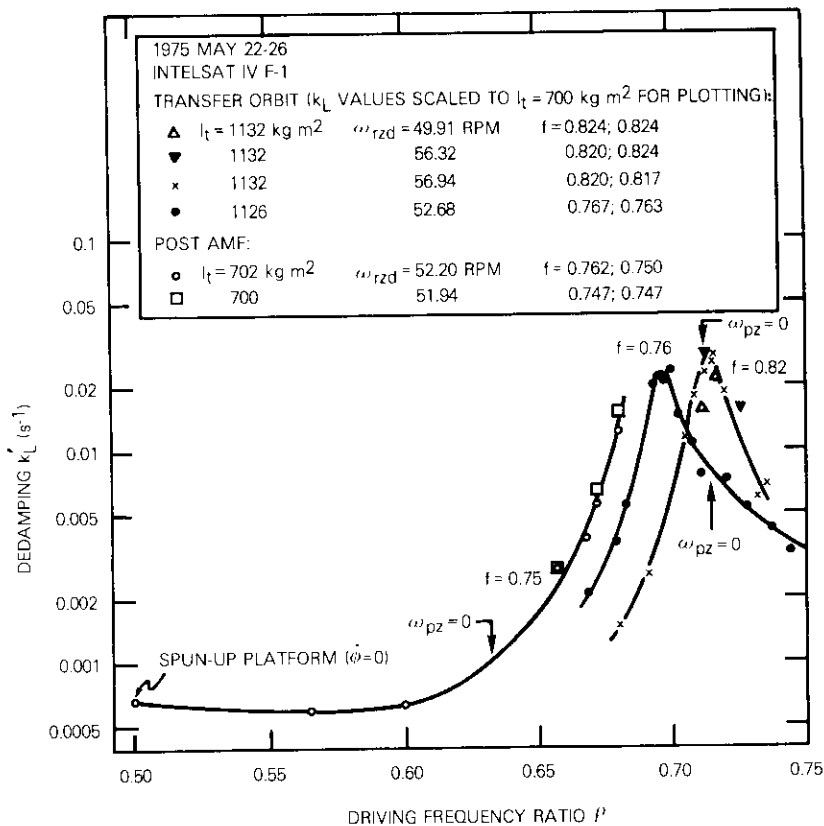


Figure 8. Tank Liquid Dedamping Contribution for Three Different Fill Fractions Obtained During Launch Operations

showed that the two tank geometries have the same natural frequency within 10 percent for a given fill fraction between 8 and 81 percent. These measurements indicated that the liquid resonance frequencies would always be much higher than the nutation frequency.

For small amplitudes, the lowest mode oscillation consists of liquid motion in the spherical tank section much like a rigid body undergoing a pendulum oscillation about an axis through the sphere center. This motion with a nearly planar free liquid surface is similar to the residual sloshing motion commonly observed in liquid containers such as water buckets and wine glasses. Because this is a pendulum-like motion, the

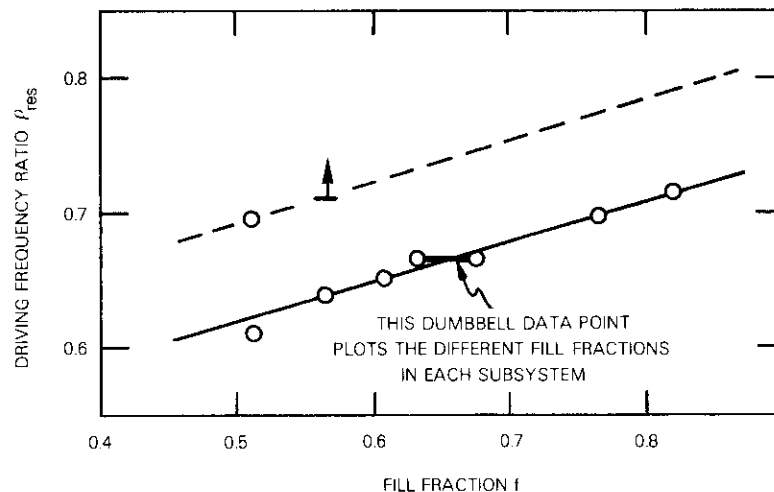


Figure 9. Driving Frequency Ratio at an Anomalous Resonance vs Fill Fraction for the Conispheric Tanks

ground measurements of natural frequency collected in Reference 7 can be scaled to in-orbit conditions by replacing the acceleration of gravity, g , in that figure with the appropriate centrifugal acceleration in the spacecraft tank. For longitudinal oscillations this acceleration is $\omega_{pz}^2 R_c$, where R_c is the distance from the bearing axis to the liquid mass center, while for transverse oscillations the effective acceleration is $\omega_{pz}^2 R_T$. The latter acceleration is smaller because, for transverse displacements from equilibrium, the mass center of the equivalent physical pendulum does not approach the bearing axis as rapidly as for longitudinal displacements. Indeed, for a pendulum pivot on the bearing axis ($R_T = 0$), transverse displacements keep the mass center at a constant distance from the bearing axis so there would be no centrifugal restoring force to produce oscillation. Table 3 compares the resulting predictions with the observed resonances for different fill fractions and shows that the predicted values are ~ 3 times the observed values.

The fact that the predicted frequency ratio for a transverse resonance is roughly three times the observed frequency ratio has led to speculation that a liquid resonance at a multiple of the nutation frequency was excited through nonlinear effects. This superharmonic resonance hypothesis to explain the dedamping peaks can be dismissed by the following two argu-

TABLE 3. OBSERVED IN-ORBIT LIQUID RESONANCES AND PREDICTED LOWEST MODE NATURAL FREQUENCIES*

Parameters	Fill Fraction, f				
	0.512	0.564	0.607	0.631; 0.674 (unequal systems)	0.819
Ratio of Liquid Depth, h , in Spherical Section to Tank Radius, r	0.991	1.062	1.123	1.157; 1.219	1.356
Natural Frequency Parameter, $\Delta_1(h/r) = \omega_n \sqrt{r/g}$ [7]	1.24	1.27	1.29	1.31; 1.34	1.42
Liquid Mass Center Distance from Bearing Axis for Spherical Section, R_c/r	3.00	2.96	2.92	2.91; 2.87	2.81
Predicted Natural Frequency Ratios: $\rho_{long} = \sqrt{R_c/r} \Delta_1$ for Longitudinal Oscillation	2.15	2.18	2.21	2.23; 2.26	2.38
$\rho_{trans} = \sqrt{R_T/r} \Delta_1$ for Transverse Oscillation	2.01	2.05	2.09	2.12; 2.16	2.30
Observed In-Orbit Ratio ρ_{res} for Anomalous Resonance	0.695; 0.610 (two resonances)	0.637	0.650	0.666	0.696
Predicted Value/Observed Value: ρ_{long}/ρ_{res}	3.1; 3.5	3.4	3.4	3.3; 3.4	3.4
ρ_{trans}/ρ_{res}	2.9; 3.3	3.2	3.2	3.2; 3.2	3.3

*The radius of the spherical tank section, $r = d_T/2 = 0.221$ m. The distance from the bearing axis to the tank sphere center, $R_T = 0.578$ m.

ments. First, an unpublished analysis by the author shows that, for an oscillating mass motion on the spacecraft in response to nutation, only the frequency component of the oscillation at the nutation frequency contributes to the dedamping. The tank liquid may undergo a large amplitude oscillation at its natural frequency due to a superharmonic resonance, but this oscillation is not at the nutation frequency and thus cannot produce a secular change in the nutation angle. Second, a careful analysis of several dozen nutation strip chart recordings shows that the observed nutation amplitude varies exponentially with time as given by equation (1).^{*} Therefore,

$$\dot{\theta} = \frac{\theta}{\tau} \quad (74)$$

where τ is a constant. The time rate of change of the nutation angle is thus proportional to the nutation angle; *i.e.*, the damping and dedamping mechanisms are operating in their linear range and nonlinear effects are not important.

To illustrate the difficulty of using a liquid pendulum-motion resonance to explain the in-orbit data, it can be attempted to model the dedamping by a simple pendulum of length l_p pivoted at a point fixed in the rotor with the pendulum point mass positioned within the liquid volume. Such pendulum models have the desired property that, as in the case of liquids, their natural frequency, ω_n , is proportional to the rotor spin rate. For longitudinal oscillations,

$$\frac{\omega_n}{\omega_{rs}} = \sqrt{\frac{R_c}{l_c}} \quad (75)$$

where R_c is now the distance of the pendulum mass from the bearing axis. For transverse oscillations,

^{*}Some small departures from an exponential fit to INTELSAT IV nutation data have been observed as follows. The amplitude for the first five cycles following a thruster pulse is often less than that predicted by an exponential fit, but this is attributed to an initial transient in the damper and liquid motions. The first few cycles are therefore excluded from the fit. The residuals from an exponential fit to the peaks of the following cycles sometimes show a systematic slow oscillation with period ~ 30 s, but the amplitude is of the same order as the measurement accuracy so that this is not conclusive evidence for departure from an exponential variation.

$$\frac{\omega_n}{\omega_{rz}} = \sqrt{\frac{R_c}{l_c} - 1} \quad (76)$$

For the ratio ω_n/ω_{rz} to be equal to the observed dedamping resonance ratio of ~ 0.66 , longitudinal oscillations require $l_c \simeq 2.3 R_c$; that is, the pendulum mass and pendulum pivot must be on opposite sides of the bearing axis. This is a physically unrealistic model. Transverse oscillations require $l_c \simeq 0.7 R_c$; that is, the pendulum pivot is outside the tank near the bearing axis instead of near the tank center. This is also an unsatisfactory model.

Conclusions and suggestions for further investigations

The in-orbit dedamping measurements and the considerations of the previous subsection lead to the following conclusions: (a) over the range of ρ values tested, there are two anomalous resonance peaks; (b) their cause is unknown. It is highly desirable to discover the excitation mechanism that causes the anomalous resonances so that mathematical models can be constructed that would allow ground test results to be easily scaled to in-orbit conditions. Useful information could be obtained from a spinning test fixture such as the angular motion fixture described by Martin in Reference 8 (pp. 9-12) or the spinning air bearing fixture at Hughes Aircraft Co. (Reference 6, Chapter 3; also Reference 1, p. 75, Figure 7) since these spinning fixtures also exhibit anomalous liquid resonances. However, these fixtures must be instrumented to provide quantitative measurements of the actual motion of the liquid. A closed circuit television camera is sometimes mounted on the rotating test vehicle to view the liquid contained in a transparent tank. Such cameras have not proven useful in quantitative work because nonlinear effects are likely to be introduced by the large nutational motion usually required to give measurable liquid motion. Such cameras can give useful qualitative results, however.

The author has proposed that *liquid height gauges* be used to obtain quantitative measurements of the amplitude and phase of the rise and fall of points on the free liquid surface. Even coarse (10-percent) measurements could define the surface motion from which the mode of liquid oscillation (longitudinal, transverse, or other) at resonance could be deduced. The gauge proposed here is based on the electrical conductance between an electrical probe and the tap water used in place of hydrazine

as the tank liquid in ground tests. As shown in Figure 10, two bare electrical probes ~ 2 mm in diameter are required: one probe, called the ground probe, extends several centimeters below the liquid surface, while the second probe, called the surface probe, extends only 2 or 3 mm below the surface. The surface probe should be mounted no closer than 2 mm to the tank wall to prevent water drops from forming between the probe and the tank wall and giving erratic conductivity variations.

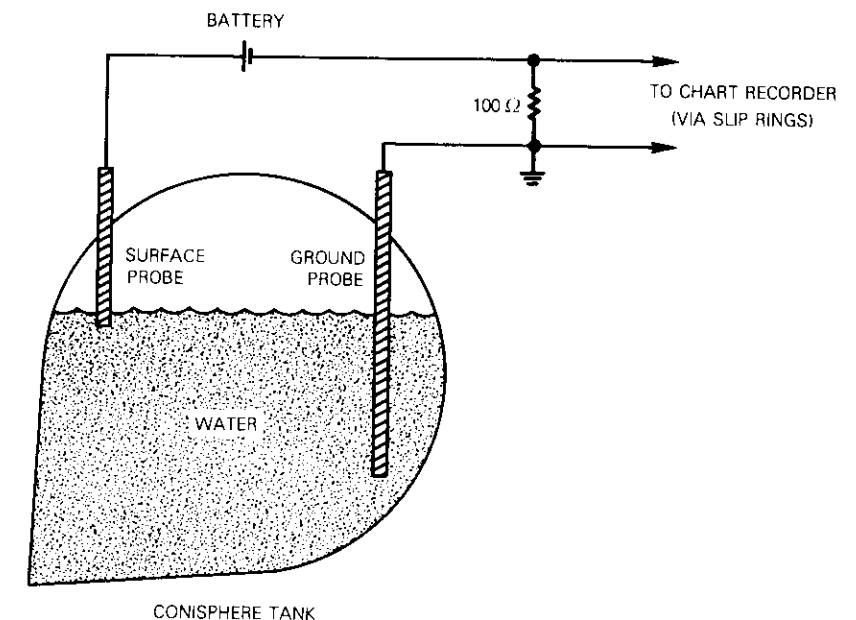


Figure 10. *Liquid Height Gauge Circuit for Liquid-Slosh Quantitative Measurements*

The electrical conductance of the water between the probes is of the order of $(10 \text{ k}\Omega)^{-1}$, and is largely independent of the distance between the probes. The liquid slosh measurements are based on the fact that this electrical conductance depends largely on the area of the surface probe in contact with the water. For a probe of uniform cross section, this area varies linearly with the depth of the surface probe in the water. Then, for the circuit shown in Figure 10, the electric current flowing between the probes varies linearly with liquid height as does the resulting voltage across the 100Ω signal resistor.

The voltage across the signal resistor thus reflects the changing height of the fluid at the surface probe due to liquid slosh. The surface motion should be restricted to ± 1 mm to ensure that the surface probe is always in the water, and to maintain a linear relation between voltage and surface height. Because of the small volume of each probe, several surface probes can be mounted at different places in the tank. These height gauges should be located so that different probes are sensitive to different modes of liquid slosh.

R. A. Curtis of COMSAT Laboratories has constructed and tested such a liquid height gauge. The apparatus gives satisfactory performance on the spinning test fixture described by Martin in Reference 8 (pp. 9-12). N. S. Lomas has used the fixture with a single height gauge and a television camera to look for resonances in a conispheric tank containing water at an 86-percent fill. A structural resonance limited the driving frequency ratio to values below 0.53, that is, to values far below the in-orbit resonance values. Liquid resonances associated with transverse and longitudinal oscillations were found for $\rho = 0.349$ and 0.407 respectively. These values are nearly one-half the resonance values of 0.72 and 0.80 predicted for $f = 0.86$ by the straight lines fit to in-orbit data in Figure 9. The liquid was oscillating at the driving frequency. No firm conclusions about these newly observed resonances can be made because the height gauge showed many large-amplitude harmonics of the driving frequency whose presence is unexplained.

Finally, experimental and theoretical consideration should be given to a possible *swirl oscillation* of the liquid, which is explained as follows. The body of the liquid, if treated as a rigid body sliding within a spherical tank, can oscillate with three degrees of freedom about three mutually orthogonal axes. Two of these axes are "parallel" to the equilibrium free liquid surface and correspond to the usual longitudinal and transverse oscillation of the liquid as a physical pendulum. The third axis is normal to the free liquid surface at the surface center and is the axis for swirl motion of the liquid. For a non-spinning tank on the ground, a displacement of the liquid about the swirl axis results in no restoring torque on the liquid; no swirl oscillation occurs in this case. On a spinning satellite, however, the equilibrium free liquid surface is a portion of a cylinder whose axis is the spin axis. A rigid-body displacement of the liquid about the swirl axis results in a restoring torque due to centrifugal forces which attempt to bring the cylindrical surface back into alignment with the *instantaneous* spin axis. The natural frequency of the resulting oscillation about the swirl axis may well correspond to an observed anomalous

resonance. This swirl oscillation would be driven by spacecraft nutation because the direction of the spin axis about the swirl axis oscillates with time.

Acknowledgments

The INTELSAT IV liquid slosh tests were a cooperative effort by many people at COMSAT. The initial analyses that led to the tests were performed by L. B. Ricks and A. A. Satterlee of COMSAT and J. O. Salvatore of Hughes Aircraft Co. L. R. Dest of COMSAT helped reduce most of the nutation strip chart recordings and suggested many improvements to the text of this paper.

References

- [1] J. T. Neer, "INTELSAT IV Nutation Dynamics," *Progress in Astronautics and Aeronautics*, Vol. 33, 1974, pp. 57-84; AIAA Paper No. 72-537.
- [2] Special INTELSAT IV Issue, *COMSAT Technical Review*, Vol. 2, No. 2, Fall 1972, pp. 271-576.
- [3] G. A. Haines and C. T. Leondes, "Eddy Current Nutation Dampers for Dual-Spin Satellites," *Journal of the Astronautical Sciences*, Vol. 21, 1973, pp. 1-25.
- [4] G. D. Gordon, G. R. Huson, and V. J. Slabinski, "Blocking Bubbles in the INTELSAT IV Fuel Lines," *COMSAT Technical Review*, Vol. 4, No. 2, Fall 1974, pp. 499-506.
- [5] A. J. Iorillo, "Nutation Damping Dynamics of Axisymmetric Rotor Stabilized Satellites," American Society of Mechanical Engineers Winter Meeting, Chicago, Illinois, November 1965, *ASME Miscellaneous Papers*, ESL Paper No. 238, pp. 11-19.
- [6] J. T. Neer and J. O. Salvatore, "Fuel Slosh Energy Dissipation on a Spinning Body," Report SCG 20047R, Hughes Aircraft Co., February 1972.
- [7] Sandor Silverman and H. Norman Abramson, "Lateral Sloshing in Moving Containers," *The Dynamic Behavior of Liquids in Moving Containers*, H. N. Abramson, ed., NASA SP-106, 1966, Ch. 2, p. 52, Figure 2.28.
- [8] E. R. Martin, "Experimental Investigations on the Fuel Slosh of Dual-Spin Spacecraft," *COMSAT Technical Review*, Vol. 1, No. 1, Fall 1971, pp. 1-20.



Victor J. Slabinski received a B.S. in Physics from Case Institute of Technology in 1961. He was a part-time instructor with the Physics Department at Case Western Reserve University until he received his Ph.D. in 1970. He then became a member of the technical staff in COMSAT's Astrodynamics Department, where he is concerned primarily with problems of satellite orbital and attitude mechanics and prediction.

Dr. Slabinski is a member of Tau Beta Pi, Sigma Xi, and the American Astronomical Society.

Index: data link, protocol, performance, prediction, HDLC, ISO, communications satellite

Performance of High-level Data Link Control in satellite communications

A. K. KAUL

(Manuscript received December 14, 1977)

Abstract

Analytic models are presented for predicting the performance of High-level Data Link Control (HDLC) Protocols, recently adopted as a standard by the International Standards Organization. These models, derived for satellite data communications, are also applicable to terrestrial data links and allow the evaluation of throughput efficiencies of computer communications links using HDLC. In addition, they have been used to estimate the maximum achievable throughput over a wide range of data transmission rates and bit error rates. The results and the tradeoffs presented will provide system designers with useful mathematical tools for selecting the optimal HDLC implementation for a particular application.

Introduction

Data link controls (DLCs) [1] are hardware and software protocols which regulate the flow of data and control information over a data communications link between computing devices or terminals. They also provide the necessary error recovery procedures, generally using an automatic repeat request (ARQ) technique [2], [3]. DLC protocols are essential in computer communications data links. Although a number of DLC

protocols are currently in use, the two most prevalent are IBM's BSC (binary synchronous communications) and SDLC [4], [5] (synchronous data link control). Attempts to establish standards for DLC protocols have culminated in the formulation of the ADCCP [6] (Advanced Data Communication Control Procedures) as a proposed American National Standards Institute (ANSI) standard and the HDLC [7]-[9] (High-level Data Link Control) recently adopted by the International Standards Organization (ISO) as an international standard.

This paper develops the mathematical tools for predicting the throughput of a data link using HDLC (unbalanced class) and a "reject" (also known as "go-back-N") error recovery procedure. The efficiency of reject retransmission strategies is [2]

$$\eta = \frac{1 - P_B}{1 + MP_B}$$

where P_B = block error probability
 M = number of full blocks transmittable in one round trip delay.

This expression was derived by assuming that a receiver can determine if a frame (or block) has a transmission error at the instant the frame arrives and that individual frames are acknowledged immediately. The paper will demonstrate that only the full duplex asynchronous response mode (FDX-ARM) of HDLC approaches this condition. However, even in this case, transmission of individual response messages for each error is delayed because frame errors or losses are recognized only after the next error-free out-of-sequence frame arrives. Thus, this expression, at best, approximates HDLC performance in the FDX-ARM.

HDLC protocol

HDLC provides a code-insensitive bit-oriented protocol. Transmission occurs in frames or blocks delimited by the flag sequence (01111110). Within each frame except the flag sequence, a zero is inserted at the transmitter after every five successive 1's. The zeros are removed at the receiver. The frame structure, which is shown in Figure 1, has an overhead of 48 bits per frame, while the length varies depending upon the length of the information field. In an HDLC frame format with an extended control field (in additional multiples of 8 bits), the overhead is 56 bits or more.

STANDARD I-FRAME FORMAT

FLAG	ADDRESS	CONTROL *	INFO	FCS †	FLAG
01111110	8 BITS	8 BITS	**	16 BITS	01111110

STANDARD S- FRAME FORMAT

FLAG	ADDRESS	CONTROL *	FCS †	FLAG
01111110	8 BITS	8 BITS	16 BITS	01111110

* EXTENDED HDLC FORMATS ALLOW INCREASE IN CONTROL FIELD IN MULTIPLES OF 8 BITS

** UNSPECIFIED NUMBERS OF BITS

† FRAME CHECK SEQUENCE

Figure 1. HDLC Frame Format

Transmitted frames can be purely supervisory or command frames (S-frames), or they can contain data (information frames).

In the unbalanced class of HDLC procedures for a point-to-point data link, one station is designated as primary and has the overall responsibility for link management. The other station, designated as secondary, responds to directives or commands from the primary whenever it receives an S-frame or information frame (I-frame) with the poll or final (P/F) bit "on" in the control field. The last frame of a response sequence by the secondary has the P/F bit on, indicating to the primary that no further response frames are outstanding. Only one poll command issued by the primary can be outstanding at a time. Secondary responses may involve responses to S-frames or acknowledgments for received I-frames.

An HDLC point-to-point procedure has three modes of operation. In the half duplex (HDX) mode, a unidirectional data link is operated in a 2-way alternate mode. The transmitting station sends out a sequence of I-frames with the P/F bit, which is part of the control field, set on in the

last frame. The link is then reversed for transmissions in the other direction (until the P/F bit is seen), which may consist of S -frames or I -frames. The numbering of sequenced I -frames is modulo M , and the maximum number of I -frames for which an acknowledgment can remain outstanding is defined by convention as the "maxout" parameter (N), which should not exceed $M - 1$.

The full duplex (FDX) mode is capable of simultaneous bidirectional data transmission. When operated in the normal response mode (NRM), the transmitter sets a P/F bit in the first frame following the receipt of an acknowledgment from the receiving station. In the asynchronous response mode, I -frames are acknowledged at the earliest opportunity without waiting for the detection of a P/F bit.

The error recovery procedure is as follows. Transmitted I -frames are numbered in sequence modulo M . In addition, each station maintains the "send state variable" (V_S), which is the sequence number of the next frame to be transmitted, and the "receive state variable" (V_R), which is the sequence number of the next I -frame expected by the station. Both V_S and V_R assume values between 0 and $M - 1$. All I -frames contain the "send sequence number" (n_S) identifying the frame, while all I - or S -frames contain the "receive sequence number" (n_R) of the next I -frame expected by the sender. Errors or data losses are detected at the receiver by comparing the n_S of the received I -frame with its local V_R . If n_S is greater than V_R , in-sequence frames have been lost. Lost frames are detected only when the next successful I -frame is received. If n_S and V_R match, the received frame is accepted and V_R is updated; otherwise, the received frame is ignored and V_R remains unchanged.

After a P/F bit is received, the receiver responds by issuing a "receive ready" (RR) with $n_R = V_R$, indicating that no frame losses have been identified and n_R is the next in-sequence I -frame expected, or by issuing a "reject" (REJ) response with $n_R = V_R$, indicating the need to retransmit from n_R . At each station V_S should not exceed the n_R of the last received S - or I -frame by more than the maxout (N) frames. In the case of FDX-ARM, RRS and REJS are issued without waiting for a P/F bit. "Time-out" periods are incorporated into the system so that the transmitter can reinitiate transmissions from the latest n_R value successfully received if no responses to a P/F bit are received within these periods. This avoids a total cessation of transmissions, which could occur if frames containing P/F bits or response frames are lost.

Finally, although in practice frame sequence numbers are numbered 0 through $M - 1$, an unbounded sequence number is used in this paper to identify individual frames and hence facilitate examination of individual

frames. The performance of HDLC under the selective reject error recovery procedure (using SREJ responses) is not discussed.

Mathematical models

The mathematical models of HDLC performance are based on the following assumptions and approximations to simplify the results:

a. Unidirectional data flow is assumed, with the primary station configured as the transmitter. The case of unidirectional data flow from the secondary is equivalent to the above in all cases except the FDX-NRM, in which performance is roughly equivalent to that for FDX-ARM with the primary station transmitting. Although bidirectional data flow is not included, performance estimates can be derived from the model by selecting appropriate values for the round trip delay.

b. P/F bits are never lost. For long frames, frame loss (or frame error) probability increases, and P/F bits can be lost. However, the system can always be designed to issue a P/F bit which is separate from the I -frame by enclosing it in a shorter S -frame.

c. Acknowledgment response frames are never lost due to transmission errors. This implies that the channel bit error rate is sufficiently low; hence, the short (48- or 56-bit) response frames generated by the secondary have an exceedingly low probability of transmission errors.

d. The occurrence of frame errors is assumed to be a stationary, random process.

e. In the HDX and FDX-NRM modes, frame errors are assumed to be detected upon arrival at the receiver. Comparison with simulation results shows that, when the single frame (for the poll frame) error probability is low, this assumption is justified. However, in the FDX-ARM mode, in which each individual frame is acknowledged at the earliest opportunity, the throughput becomes relatively more sensitive to this assumption. For this mode, a modified assumption that all frame errors are detected one frame later is used. This is valid as long as the probability of two or more consecutive frame errors is very low. For low frame error probabilities, since the probability of consecutive errors decreases with the power of the single frame error probability, this assumption can be employed as long as the single frame probability does not have very high values.

A comparison of the results derived from the models with those obtained from a software HDLC simulator (in which only assumption *d* is enforced)

indicates that these assumptions are valid over a moderate to high range of throughputs.

Before the models are presented, the following commonly used variables are defined:

N = maxout parameter (or required buffer size in frames)

b = frame length in bits including overhead

C = link capacity in bits per second

T_R = round trip delay in seconds

$d = CT_R/b =$ round trip delay in frames

$D = [d]^*$

S = probability of successful frame transmission, *i.e.*, with no errors or losses

m = maximum number of frames transmittable per cycle (definitions of a cycle differ for each mode).

The following subsections develop models for each of the three HDLC modes.

Half duplex

HDX operation is always in an NRM, since the ARM operation in HDX is equivalent to the NRM with modulo 2; *i.e.*, only one transmitted frame can remain outstanding at a time.

Figure 2 illustrates the operation of an HDX channel. The first error frame encountered in a frame sequence causes an REJ to be issued in response to the P/F bit. The next sequence starts with the retransmission of this erroneous frame followed by the frames in sequence (go-back-N error recovery), whether or not these frames were successfully transmitted earlier. A cycle consists of N (maxout) frames in sequence, followed by a delay of d frames while waiting for a response, after which the next cycle begins. All cycles are of equal duration, t , where

$$t = N + d \tag{1}$$

in units of frame transmission times. Further, the total number of frames B (new or retransmitted) transmitted per cycle is always N ; hence, the channel load L , or the average time the link is busy (*i.e.*, transmitting data), is always

$$L = \frac{N}{N + d} \tag{2}$$

* $[x] = x$ for integral x or next highest integral value of x for noninteger x .

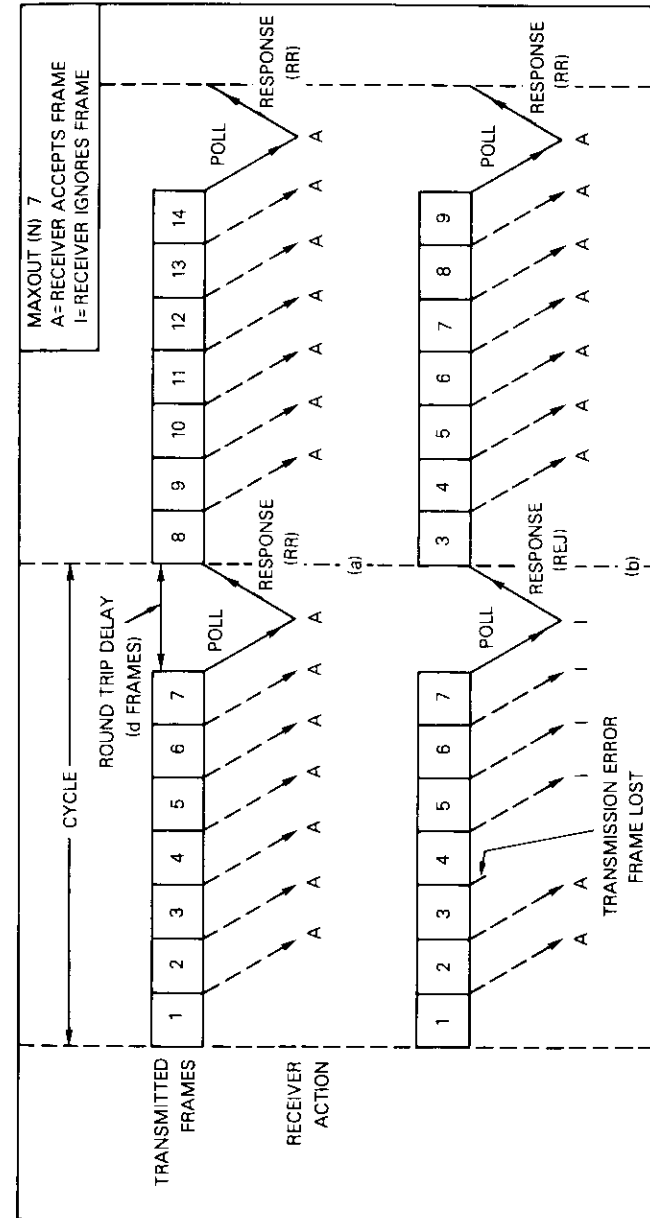


Figure 2. HDX Link Operation with Primary Transmitting
 a. without Transmission Errors b. with Transmission Error

If \bar{n} represents the average number of information frames transmitted successfully per cycle, then the throughput, η , is simply

$$\eta = \frac{\bar{n}}{t} = \frac{\bar{n}}{N + d} \quad (3)$$

If the occurrence of frame errors is assumed to be a stationary random process and R_k is defined as the probability that the first occurrence of a frame error in a cycle is after the $N - k$ th frame (i.e., k represents the number of retransmission frames in the next cycle), R_k can be written as

$$R_0 = S^N$$

$$R_k = S^{N-k}(1 - S) \quad , \quad k = 1, 2, \dots, N. \quad (4)$$

For a cycle with the first error after $N - k$ frames (with probability R_k), the number of successfully transmitted I -frames is $(N - k)$, since the rest must be retransmitted in the next cycle. For an R_0 cycle, the number of successfully transmitted frames is N . Hence,

$$\bar{n} = NR_0 + \sum_{k=1}^N (N - k) R_k \quad (5)$$

and equation (4) yields

$$\bar{n} = \frac{S(1 - S^N)}{1 - S} \quad (6)$$

Hence, the throughput [equation (3)] is

$$\eta = \frac{S(1 - S^N)}{(1 - S)(N + d)} \quad (7)$$

where $d = \frac{CT_R}{b}$.

Full duplex normal response mode

Figure 3 illustrates the operation of a data link in an *FDX-NRM*. A service cycle can be defined as the interval between the arrival of responses

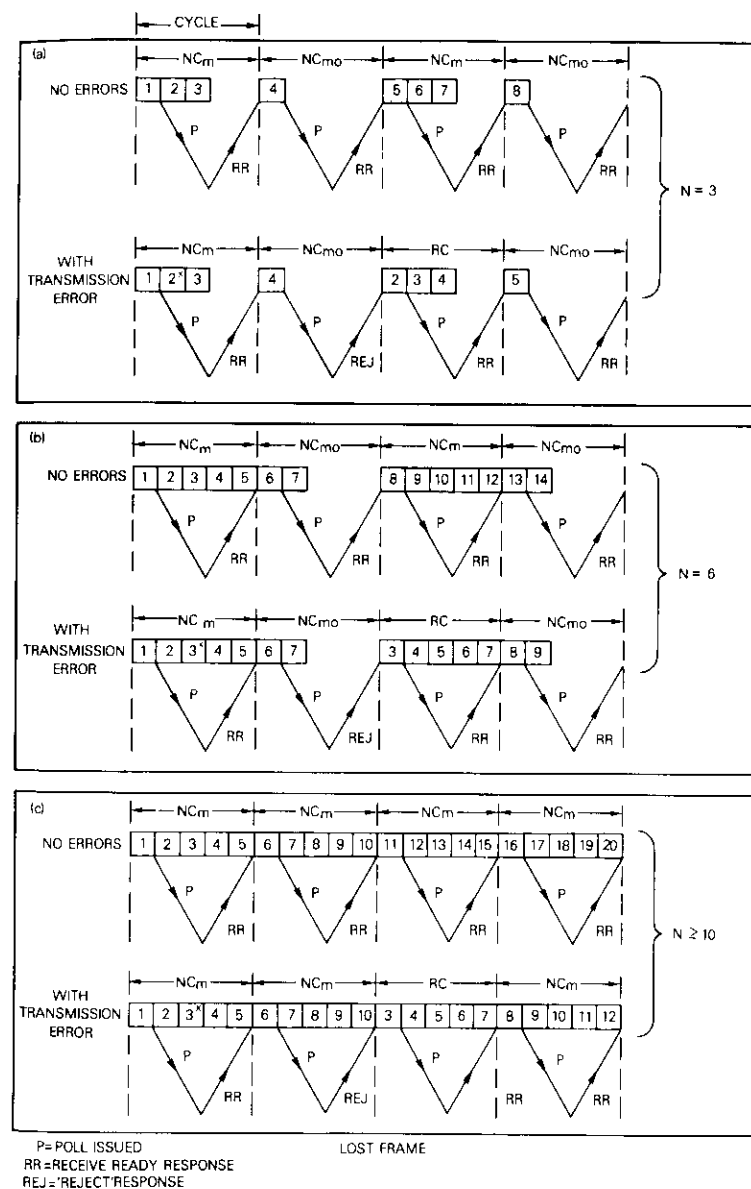


Figure 3. *FDX-NRM Scenarios (primary transmitting)*

to two successive P/F bits. The first frame of each cycle constitutes the polling frame. The maximum number of frames which can be transmitted per cycle is given by

$$m = \min[N, 1 + D] \quad (8)$$

Throughput is derived under two conditions depending on the amount of buffering available at the transmitter.

RESTRICTED BUFFER CASE

When the buffering at the transmit end is inadequate to ensure continuous transmission, *i.e.*,

$$2m - 1 > N \geq m \quad (9)$$

the following conditions (as shown in Figures 3a and 3b) can result:

- a. All cycles will contain either m or m_0 frames, where $m_0 = N - m + 1$.
- b. Two types of cycles occur: new cycles (NCs) in which all frames are new, and retransmit cycles (RCs) in which there are some retransmitted frames. Further, all RCs contain m frames while NCs can contain either m or m_0 frames.
- c. Two NCs of the same length cannot be transmitted consecutively.
- d. A retransmission may involve more than m frames (shown in Figure 4), causing some retransmitted frames to *overflow* into the next NC and thereby reducing the number of new frames transmitted in that NC. If the next cycle is also an RC, the cycle is simply repeated and has the same overflow. The possible cycle transitions are shown in Figure 5. For a random distribution of errors, the probability that the first error, which generates an REJ response for a group of m frames, occurs in the $(m - k + 1)$ th position, resulting in the retransmission of k frames from this group, is

$$r_k = S^{m-k}(1 - S) \quad , \quad k = 1, 2, \dots, m \quad (10)$$

while the probability of no errors, resulting in a "receive ready" (RR) response, is

$$r_0 = S^m \quad (11)$$

For the possible transitions shown in Figure 5 if the cycle transition

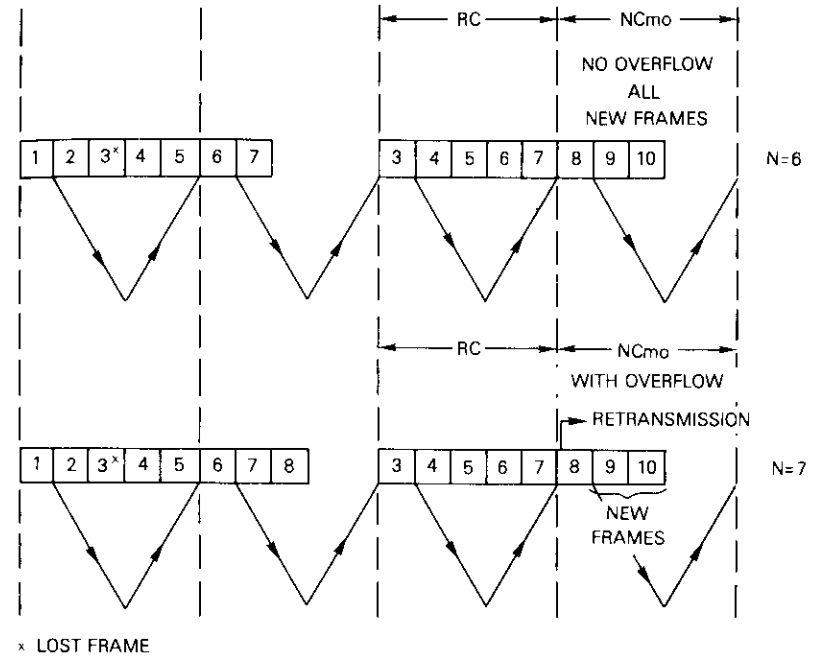


Figure 4. Retransmission Overflow into New Frame Cycles for FDX-NRM, Restricted Buffer Case

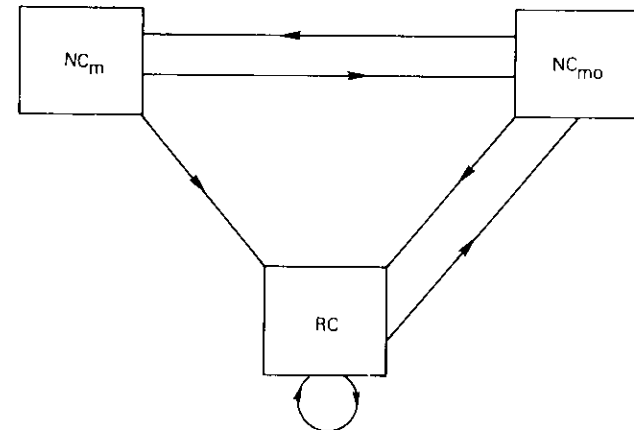


Figure 5. Possible Cycle Transitions in FDX-NRM, Restricted Buffer Case

probabilities for $X \rightarrow Y$ are represented by $[Y|X]$,

$$\begin{aligned} [R_m|R_m]^* &= 1 - S \\ [N_m|R_m]^* &= 0 \\ [N_{m_0}|R_m]^* &= S \end{aligned} \tag{12a}$$

$$\begin{aligned} [R_m|N_m] &= 1 - S^{m_0} \\ [N_m|N_m] &= 0 \\ [N_{m_0}|N_m] &= S^{m_0} \end{aligned} \tag{12b}$$

and

$$\begin{aligned} [R_m|N_{m_0}] &= 1 - S^m \\ [N_m|N_{m_0}] &= S^m \\ [N_{m_0}|N_{m_0}] &= 0 \end{aligned} \tag{12c}$$

where R_m = retransmission cycle (all of length m)
 N_m = new cycle of length m
 N_{m_0} = new cycle of length m_0 .

Note that the only new cycle which can follow an R_m cycle is N_{m_0} . This will be used later when considering overflows.

The equilibrium equations for the probabilities R_m , N_m , and N_{m_0} yield the equations

$$R_m = (1 - S) R_m + (1 - S^{m_0}) N_m + (1 - S^m) N_{m_0} \tag{13}$$

$$N_m = S^m N_{m_0} \tag{14}$$

$$N_{m_0} = S R_m + S^{m_0} N_m \tag{15}$$

Solving equations (14) and (15) with the normalization

$$N_{m_0} + N_m + R_m = 1 \tag{16}$$

yields equilibrium solutions

$$N_{m_0} = \frac{S}{Z} \tag{17}$$

* The outcome is determined only by what happens to the poll frame (first frame) of the R cycle, since preceding frames are ignored by the receiver.

$$N_m = \frac{S^{m+1}}{Z} \tag{18}$$

$$R_m = \frac{1 - S^{m+m_0}}{Z} = \frac{1 - S^{N+1}}{Z} \tag{19}$$

where $Z = 1 + S + S^{m+1} - S^{N+1}$. (20)

From equations (17)-(20) the average cycle length, \bar{t} , and the average number of frames, \bar{F} , transmitted per cycle can be computed as

$$\bar{t} = t_m(N_m + R_m) + t_{m_0}N_{m_0} \tag{21}$$

$$\bar{F} = m(N_m + R_m) + m_0N_{m_0} \tag{22}$$

where t_m and t_{m_0} are the lengths (in frames) of the cycles containing m and m_0 frames, respectively. Thus,

$$\bar{t} = \frac{1}{Z} \{ S t_{m_0} + (1 + S^{m+1} - S^{N+1}) t_m \} \tag{23}$$

$$\bar{F} = \frac{1}{Z} \{ m_0 S + m(1 + S^{m+1} - S^{N+1}) \} \tag{24}$$

and the channel load L is

$$L = \frac{\bar{F}}{\bar{t}} = \frac{m_0 S + m(1 + S^{m+1} - S^{N+1})}{S t_{m_0} + (1 + S^{m+1} - S^{N+1}) t_m} \tag{25}$$

The average number of new frames (\bar{n}) per cycle must be obtained to determine the throughput. Figure 3 indicates that the contribution from N_m cycles is m ; from R_m cycles the contribution is $m - k$ when $k \leq m$ and 0 when $k > m$, where k is the number of retransmissions implied in the R_m cycle. If $k > m$ some retransmissions can overflow from an R_m cycle to a succeeding N_{m_0} cycle.

If $R_m^{(k)}$ is defined as the probability of an R_m cycle associated with a chain of k retransmitted frames ($m_0 \leq k \leq N$), the probabilities conditioned on the preceding type of cycle (PC) are

$$\begin{aligned}
Pr\{R_m^{(k)} | PC = N_m\} &= 0 & k < m \\
&= (1 - S)S^{N-k} & m \leq k \leq N \\
Pr\{R_m^{(k)} | PC = N_{m_0}\} &= 0 & k < m_0 \\
&= (1 - S)S^{N-k} & m_0 \leq k \leq N \\
Pr\{R_m^{(k)} | PC = R_m^{(j)}\} &= \delta_{m,k}(1 - S) & j \leq m \\
&= \delta_{j,k}(1 - S) & m < j \leq N
\end{aligned}$$

where $\delta_{j,k}$ is the Kronecker delta function.

These results are obtained by noting that k is the sum of the outstanding frames in the cycle just completed (PC_1) and the retransmitted frames implied in the preceding cycle (PC_2) which generated the REJ response. When PC_1 is an $R_m^{(j)}$ cycle, an $R_m^{(m)}$ cycle is generated for $j \leq m$ and an $R_m^{(j)}$ cycle for $m < j \leq N$. Hence,

$$\begin{aligned}
R_m^{(k)} &= 0 & k < m_0 \\
&= (1 - S)S^{N-k}N_{m_0} & m_0 \leq k < m \\
&= (1 - S)S^{N-m}(N_{m_0} + N_m) + (1 - S) \sum_{j=m_0}^m R_m^{(j)} & k = m \\
&= (1 - S)S^{N-k}(N_{m_0} + N_m) + (1 - S)R_m^{(k)} & m < k \leq N
\end{aligned}$$

Summing $R_m^{(k)}$ from $k = m_0$ to $k = m$ and using equations (17)–(20) yields

$$\sum_{j=m_0}^m R_m^{(j)} = \frac{1}{Z} \left(S^{m_0-1} - S^m + S^{m+m_0-1} - S^{m+m_0} \right)$$

Hence,

$$\begin{aligned}
R_m^{(k)} &= 0 & k < m_0 \\
&= \frac{(1 - S)S^{N-k+1}}{Z} & m_0 \leq k < m \\
&= \frac{(1 - S)}{Z} \{ S^{m_0-1} + S^{m_0} - S^m + S^{m+m_0-1} \} & k = m \\
&= \frac{(1 - S)}{Z} (1 + S^m)S^{N-k} & m < k \leq N
\end{aligned} \tag{26}$$

Probabilities $R_m^{(k)}$ are considered instead of R_m because the number of new frames transmitted in an R_m cycle depends on k and is equal to $m - k$ for $1 \leq k < m$, and 0 for $m \leq k \leq N$. The contributions from N_{m_0} cycles, which must also be considered, are not always m_0 because of the possible overflow of retransmission frames from a preceding $R_m^{(k)}$ cycle. If an overflow of j frames is assumed, then the contribution of new frames from an N_{m_0} cycle is $m_0 - j$.

If $N_{m_0}^{(j)}$ is defined as the probability of an N_{m_0} cycle having an overflow ($0 \leq j < m_0$) from the preceding cycle,

$$\begin{aligned}
N_{m_0}^{(j)} &= [N_{m_0} | N_m] N_m + [N_{m_0} | R_m] \sum_{k=m_0}^m R_m^{(k)} & j = 0 \\
&= [N_{m_0} | R_m] R_m^{(m+j)} & 0 < j < m_0
\end{aligned}$$

and from equations (12), (18), and (26),

$$N_{m_0}^{(j)} = \begin{cases} \frac{1}{Z} [S^{m_0} - S^{m+1} + S^{m+m_0}] & j = 0 \\ \frac{(1 - S)(1 + S^m)}{Z} S^{m_0-j} & 0 < j < m_0 \end{cases}$$

The average number of new frames, \bar{n} , per cycle is expressed as

$$\bar{n} = mN_m + \sum_{k=m_0}^{m-1} (m - k)R_m^{(k)} + \sum_{j=0}^{m_0-1} (m_0 - j)N_{m_0}^{(j)}$$

which yields

$$\bar{n} = \frac{S(1 - S^{N+1})}{Z(1 - S)}$$

To establish the load and throughput, t_{m_0} and t_m in equation (23) must be determined. For $N < 1 + d$, $m = N$ and $m_0 = 1$; hence, $t_m = t_{m_0} = 1 + d$. For $N \geq 1 + d$ but $N < 1 + 2D$, $m = 1 + D$. Since $m \leq N < 2m - 1 (= 1 + 2D)$, then $m_0 < m$. Hence, $t_{m_0} = 1 + d$, while $t_m = m = 1 + D$. Therefore, the loads and throughputs are

$$L = \frac{(S + N)}{(1 + S)(1 + d)} , \quad N < 1 + d$$

$$= \frac{m_0 S + m(1 + S^{m+1} - S^{N+1})}{(1 + d)S + m(1 + S^{m+1} - S^{N+1})}, \quad 1 + d \leq N < 1 + 2D \quad (27)$$

and

$$\eta = \frac{\bar{n}}{\bar{i}} = \frac{S(1 - S^{N+1})}{(1 - S^2)(1 + d)} , \quad N < 1 + d$$

$$= \frac{S(1 - S^{N+1})}{(1 - S)[S(1 + d) + m(1 + S^{m+1} - S^{N+1})]} ,$$

$$1 + d \leq N < 1 + 2D \quad . \quad (28)$$

LARGE BUFFER CASE

When sufficiently large buffers are provided at the transmit end to ensure that $N \geq 2m - 1$ with $m = 1 + D$, all cycles are m frames long (Figure 3c), continuous transmission occurs, and the model simplifies to a large extent. The following results are obtained using the same procedure except that only N_m and R_m cycles exist and overflows now occur into the N_m cycles:

a. *Transition probabilities.* The transition probabilities are

$$\begin{aligned} [R_m | R_m] &= 1 - S \\ [N_m | R_m] &= S \\ [R_m | N_m] &= 1 - S^m \\ [N_m | N_m] &= S^m \end{aligned}$$

b. *Equilibrium cycle probabilities.* The equilibrium probabilities obtained from

$$N_m = SR_m + S^m N_m$$

and

$$N_m + R_m = 1$$

are

$$N_m = \frac{S}{1 + S - S^m} \quad (29)$$

$$R_m = \frac{1 - S^m}{1 + S - S^m} \quad (30)$$

c. *Cycle time and load.* Cycle time and load are constants, i.e.,

$$\bar{i} = m \quad (31a)$$

$$\bar{F} = m \quad (31b)$$

$$L = 1 \quad (31c)$$

d. *$R_m^{(k)}$ probabilities.* From

$$\begin{aligned} Pr\{R_m^{(k)} | PC = N_m\} &= 0 , & k < m \\ &= (1 - S)S^{2m-1-k} , & m \leq k \leq 2m - 1 \end{aligned}$$

$$\begin{aligned} Pr\{R_m^{(k)} | PC = R_m^{(j)}\} &= 0 , & j < m \\ &= \delta_{j,k}(1 - S) , & m \leq j \leq 2m - 1 \end{aligned}$$

the probabilities are

$$\begin{aligned} R_m^{(k)} &= 0 , & k < m \\ &= (1 - S)R_m^{(k)} + (1 - S)S^{2m-1-k}N_m , & m \leq k \leq 2m - 1 \end{aligned}$$

Hence,

$$\begin{aligned} R_m^{(k)} &= 0 , & k < m \\ &= \frac{(1 - S)S^{2m-1-k}}{1 + S - S^m} , & m \leq k \leq 2m - 1 \end{aligned} \quad (32)$$

No new frames can be sent in any R_m cycle.

e. *$N_m^{(j)}$ probabilities.* Obviously, all N_m cycles following an $R_m^{(k)}$ cycle (except $k = m$) will have an overflow $j = k - m$. Hence,

$$\begin{aligned} N_m^{(j)} &= [N_m | N_m]N_m + [N_m | R_m]R_m^{(m)} , & j = 0 \\ &= [N_m | R_m]R_m^{(m+j)} , & m > j \geq 1 \end{aligned}$$

which yields

$$N^{(j)} = \frac{S^m}{1 + S - S^m}, \quad j = 0$$

$$= \frac{(1 - S)S^{m-j}}{1 + S - S^m}, \quad m > j \geq 1 \quad (33)$$

f. Average number of new frames/cycle (\bar{n}). The average number of new frames per cycle is given by

$$\bar{n} = \sum_{j=0}^{m-1} (m - j)N_m^{(j)}$$

which yields

$$\bar{n} = \frac{S(1 - S^m)}{(1 - S)(1 + S - S^m)} \quad (34)$$

g. Throughput. Throughput is given by

$$\eta = \frac{\bar{n}}{T} = \frac{S(1 - S^m)}{m(1 - S)(1 + S - S^m)} \quad (35)$$

$$\text{where} \quad m = 1 + D \quad (36)$$

Full duplex asynchronous response mode

Since each individual frame is acknowledged by the receiver in the ARM, it is convenient to define a service cycle of variable length originating with either the first frame of a retransmission sequence, or the first frame transmitted after m consecutive frame transmissions without error, where

$$m = \min[N, 1 + D] \quad (37)$$

For this mode, two cases must be considered, depending on available buffering.

RESTRICTED BUFFER CASE

For $N < 1 + d$, the parameter m is identified as N . If the cycles (Figure 6a) are defined as either RC or NC depending on whether or not

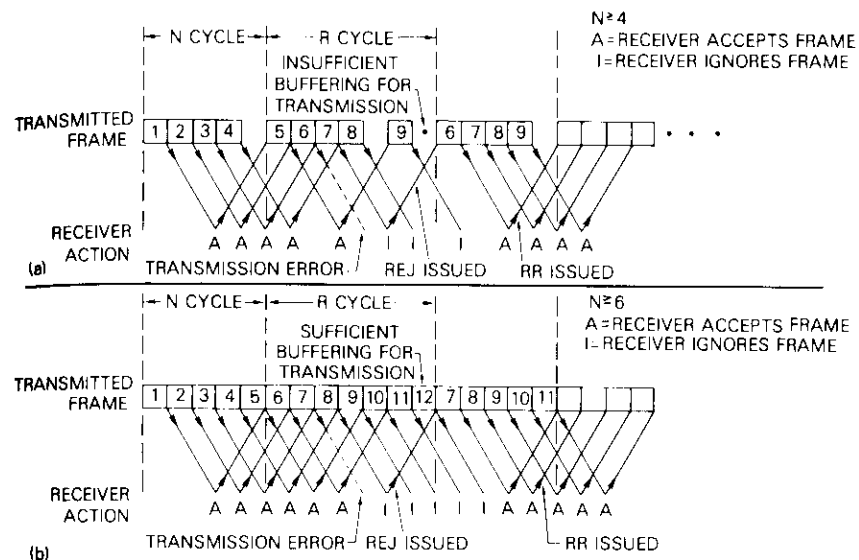


Figure 6 FDX-ARM Operation

a. with Restricted Buffers

b. with Large Buffers

at least one frame error occurs in the first m frames of the cycle, the probability (N_m), length (T), number of total frames (F), and number of successfully received frames (n) for an NC are

$$N_m = S^m \quad (38)$$

$$F_{N_m} = n_{N_m} = m \quad (39)$$

$$T_{N_m} = t \quad (40)$$

$$\text{where} \quad t = 1 + d \quad (41)$$

The probability of RC cycles in which the first frame error occurs at position k ($1 \leq k \leq m$) is

$$R_k = S^{k-1}(1 - S) \quad (42)$$

while

$$F_{R_k} = m + k - 1 \quad (43)$$

$$n_{R_k} = k - 1 \quad (44)$$

$$T_{R_k} = (t + k - 1) + 1 \quad (45)$$

where one has been added to the last equation because the error is detected. Hence, an acknowledgment is sent by the receiver one frame after the arrival of the erroneous frame, but the lack of buffering in the transmitter prevents any transmission and contribution to F_{R_k} .

The averages can now be computed as

$$\bar{F} = mS^m + \sum_{k=1}^m (m + k - 1)(1 - S)S^{k-1} \quad (46)$$

$$\bar{n} = mS^m + \sum_{k=1}^m (k - 1)(1 - S)S^{k-1} \quad (47)$$

$$\bar{T} = tS^m + \sum_{k=1}^m (t + k)(1 - S)S^{k-1} \quad (48)$$

or

$$\bar{F} = \frac{(1 - S^m)}{(1 - S)} \{m(1 - S) + S\} \quad (49)$$

$$\bar{n} = \frac{S(1 - S^m)}{(1 - S)} \quad (50)$$

$$\bar{T} = \frac{S(1 - S^m)}{(1 - S)} + t + 1 - (m + 1)S^m \quad (51)$$

The load and throughput are then

$$L = \frac{\bar{F}}{\bar{T}} = \frac{\{m(1 - S) + S\} \{1 - S^m\}}{S(1 - S^m) + (1 - S)[2 + d - (m + 1)S^m]} \quad (52)$$

and

$$\eta = \frac{S(1 - S^m)}{S(1 - S^m) + (1 - S)[2 + d - (m + 1)S^m]} \quad (53)$$

respectively.

LARGE BUFFER CASE

The condition $N \geq 1 + d$ implies that $m = t = 1 + D$ and, as shown in Figure 6b, although the R_k cycle length is still given by T_{R_k} of equation (45), there is sufficient buffering at the transmitter to continue frame transmissions. Hence, the expressions for T_{R_k} and F_{R_k} are replaced by $T_{R_k} = F_{R_k} = m + k$, and the averages are

$$\bar{T} = \bar{F} = \frac{(1 - S^m)}{(1 - S)} \{1 + m(1 - S)\} \quad (54)$$

while \bar{n} is still given by equation (50). The load and throughput are, respectively,

$$L = \frac{\bar{F}}{\bar{T}} = 1 \quad (55)$$

and

$$\eta = \frac{\bar{n}}{\bar{T}} = \frac{S}{1 + m(1 - S)} \quad (56)$$

Equation (56) differs slightly from the standard reject throughput [8],

$$\eta = \frac{S}{S + m(1 - S)}$$

because of the assumption that a frame error is detected at the arrival time of the next successful out-of-sequence frame rather than instantaneously.

Inclusion of frame overhead

Actual throughput differs from the "link throughput" derived in the models by a multiplicative factor $(1 - A/b)$, where A is the overhead per HDLC frame, *i.e.*, the total number of bits contained (Figure 1) in the flags (leader and trailer), the address, control, and FCS fields of an HDLC frame.

The following is the net throughput for the three HDLC modes obtained from the models after accounting for this overhead. For the HDX mode,

$$\eta = \frac{S(1 - S^N)(b - A)}{b(1 - S)(N + d)}$$

for all N . For the FDX-NRM,

$$\begin{aligned} \eta &= \frac{S(b - A)(1 - S^{N+1})}{b(1 - S^2)(1 + d)}, & N < 1 + d \\ &= \frac{S(b - A)(1 - S^{N+1})}{b(1 - S)[(1 + d)S + m(1 + S^{m+1} - S^{N+1})]}, & 1 + d \leq N < 1 + 2D \\ &= \frac{S(b - A)(1 - S^{1+D})}{b(1 + D)(1 - S)(1 + S - S^{1+D})}, & N \geq 1 + 2D \end{aligned}$$

where $m = 1 + D$. Finally, for the FDX-ARM,

$$\begin{aligned} \eta &= \frac{S(b - A)(1 - S^N)}{b\{S(1 - S^N) + (1 - S)[2 + d - (N + 1)S^N]\}}, & N < 1 + d \\ \eta &= \frac{S(b - A)}{b\{1 + (1 + D)(1 - S)\}}, & N \geq 1 + d. \end{aligned}$$

Model applications

The results obtained from the model can be used to predict the performance of a specific HDLC implementation over any data communications link. The link is characterized by its capacity, C (in bit/s), and by the round trip propagation delay, T_R , including an estimate of processing times associated with HDLC functions and channel turn-around times. The HDLC protocol is specified by its mode (*i.e.*, HDX, FDX-NRM, or FDX-ARM) and by the frame length, b , and modulo count, $N + 1$ or maxout N .

In addition, a model is necessary to determine the impact of channel noise on frame success probability, S . For channels characterized by the occurrence of random bit errors with a bit error rate (or bit error probability) β , the frame success probability, S , is given by

$$S = \mu^b \quad (57)$$

$$\text{where} \quad \mu = 1 - \beta \quad (58)$$

All subsequent discussion and results have been based on this error model. For channels with burst errors, the random error model still represents a worst case situation and can provide a conservative estimate of throughput.

Figure 7 shows the calculated link throughput as a function of frame length (including overhead) at several modulo counts for a terrestrial link (with an assumed 100-ms round trip delay) and a satellite link (with a 540-ms delay) for 9,600-bit/s, 56-Mbit/s and 1.544-Mbit/s data rates and bit error rates of 10^{-5} , 10^{-7} , and 0 (an ideal noise-free channel).

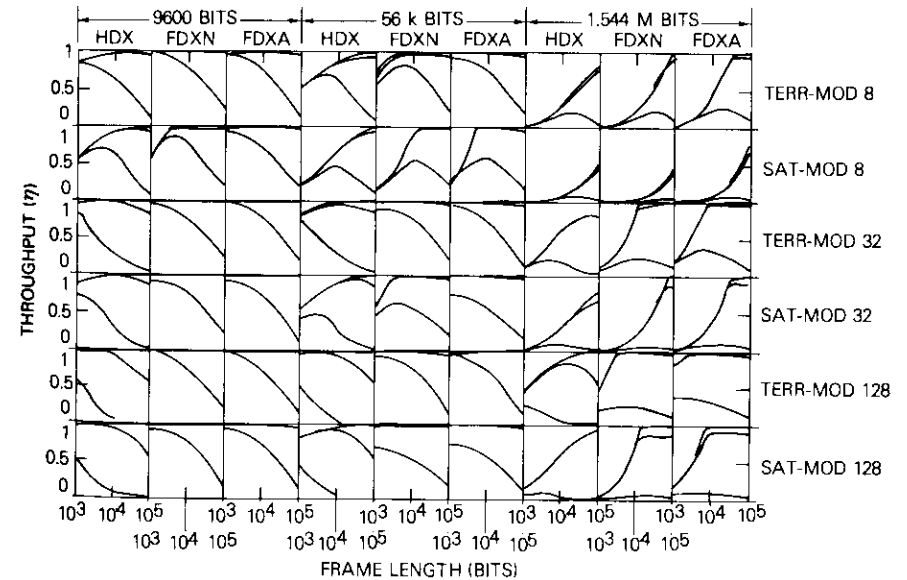


Figure 7. HDLC Performance at Representative Terrestrial (100-ms-delay) and Satellite Links

A detailed comparison with results from a software HDLC simulator (with time-outs adjusted to minimum possible values) shows good agreement. The simulation results approach the model predictions as the simulator is exercised for longer durations. Figures 8 and 9 compare simulation

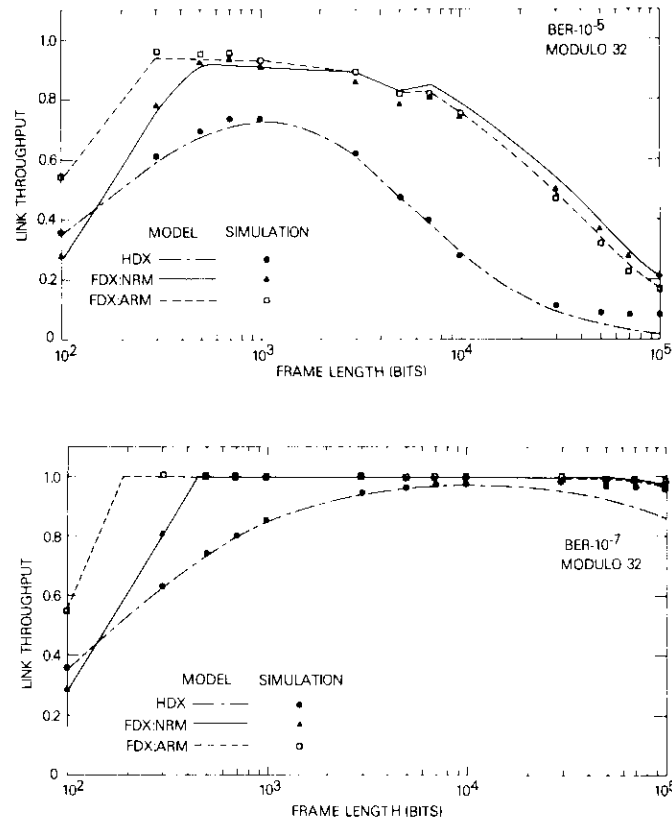


Figure 8. Model and Simulation Comparisons for a Terrestrial (100-ms) 56-kbit/s Data Link

runs of 5,000 frames. Some configurations exhibit significant differences, especially at large modulo values, for frame lengths with large frame error probabilities. Under these conditions, the number of time-outs in the simulator, which are not included in the model, increases substantially.

Maximum throughputs

Although the models are useful for predicting throughput for any protocol parameters, the closed form expressions derived can also determine optimal system designs. The system configuration which yields maximum throughput can be determined directly rather than by evaluating a finite

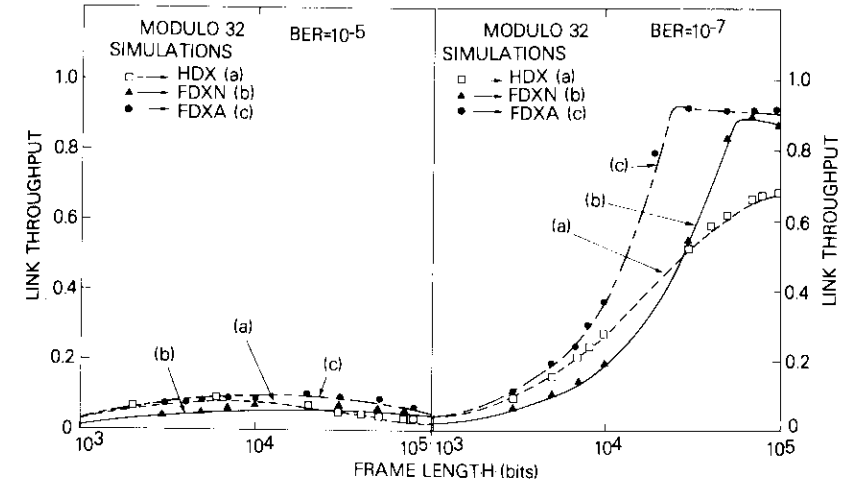


Figure 9. Model and Simulation Comparisons for a 1.544-Mbit/s Satellite Data Link

set of system options. The configuration for maximum throughput is considered separately for the three HDLC modes.

HALF DUPLEX

For the random error channel model [equation (57)], the throughput for the HDX mode can be written as

$$\eta = \frac{b\mu^b(1 - \mu^{Nb})}{(1 - \mu^b)(Nb + C_T)} \frac{(b - A)}{b} \tag{59}$$

or in terms of the buffer size, $B (= Nb)$, in bits

$$\eta = f(b)g(B)$$

where
$$f(b) = \frac{\mu^b(b - A)}{1 - \mu^b} \tag{60}$$

$$g(B) = \frac{(1 - \mu^B)}{(B + C_T)} \tag{61}$$

with the parameter C_T defined as the round trip propagation delay expressed in bits, and given by $C_T = CT_R$.

The optimal frame length, b_0 , for a given buffer size can be derived by using equation (59):

$$\left. \frac{\partial \eta}{\partial b} \right|_{b = b_0} = 0$$

or

$$1 - (b_0 + A) \ln \mu - \mu^{b_0} = 0 \tag{62}$$

which can be solved numerically for b_0 . Note that b_0 depends only on the channel bit error rate (through μ) for a given overhead A , and is independent of the other channel characteristics defined by C_T as well as the available buffering.

Similarly, for a given frame length, there is an optimal buffer size, B_0 , determined by the solution of the transcendental equation

$$\mu^{B_0} [1 - (B_0 + C_T) \ln \mu] = 1 \tag{63}$$

The optimal buffer size is independent of the frame length and depends only on the channel C_T and μ .

Substituting the optimal values for b_0 and B_0 into equation (59) yields the maximum achievable throughput,

$$\eta_0 = \frac{\mu^{b_0}(b_0 + A)(1 - \mu^{B_0})}{(1 - \mu^{b_0})(B_0 + C_T)} \tag{64}$$

Figure 10 shows the optimal frame length as a function of bit error rate, β , using equation (62) and assuming an overhead of 56 bits (extended HDLC frames). This yields a single universally applicable curve for a given overhead A , and is approximated by

$$b_0 = \sqrt{\frac{2A}{\beta}} \text{ bits} \tag{65}$$

Figure 11 shows the optimal buffer size, which is independent of frame lengths, as a function of round trip propagation delay, C_T , for several bit error rates. The results can be applied to both terrestrial and satellite data links by specifying the channel according to the variable C_T , which includes the various propagation delays. A set of universally applicable curves for

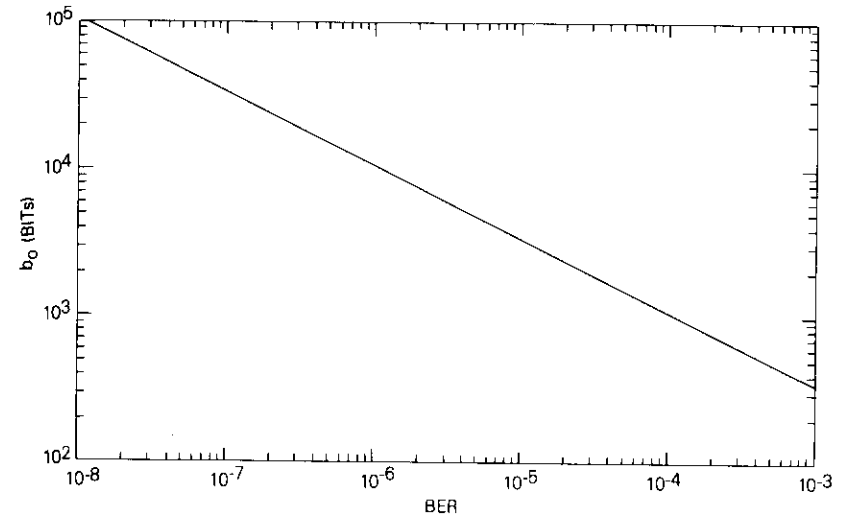


Figure 10. Optimal Frame Length (b_0) vs Bit Error Rate (BER) for HDLC HDX Mode (frame overhead, $A = 56$ bits)

maximum achievable throughput as a function of channel C_T for various bit error rates β and an assumed overhead of 56 bits is given in Figure 12. The maximum possible throughput decreases as β increases or as C_T increases. An increase in C_T implies an increase in either channel bit transmission rate, C , or in channel round trip delay, T_R . The impact of the longer satellite delay diminishes at a lower bit error rate.

Figure 12 shows the performance limits of HDX operation over a given channel, and Figures 10 and 11 describe the system configuration capable of achieving this peak throughput. The frame length is obtained from Figure 10 or equation (65), and the modulo count is approximately

$$M = \left\lceil \frac{B_0}{b_0} \right\rceil + 1 \tag{66}$$

Practical reasons preventing the implementation of b_0 or B_0 (e.g., limited buffering resources) may cause the achievable throughput to be lower than the peak value of Figure 12. These suboptimal tradeoffs are discussed in the next section.

The application of these results may be demonstrated by considering a 56-kbit/s link over a terrestrial communications facility (assuming

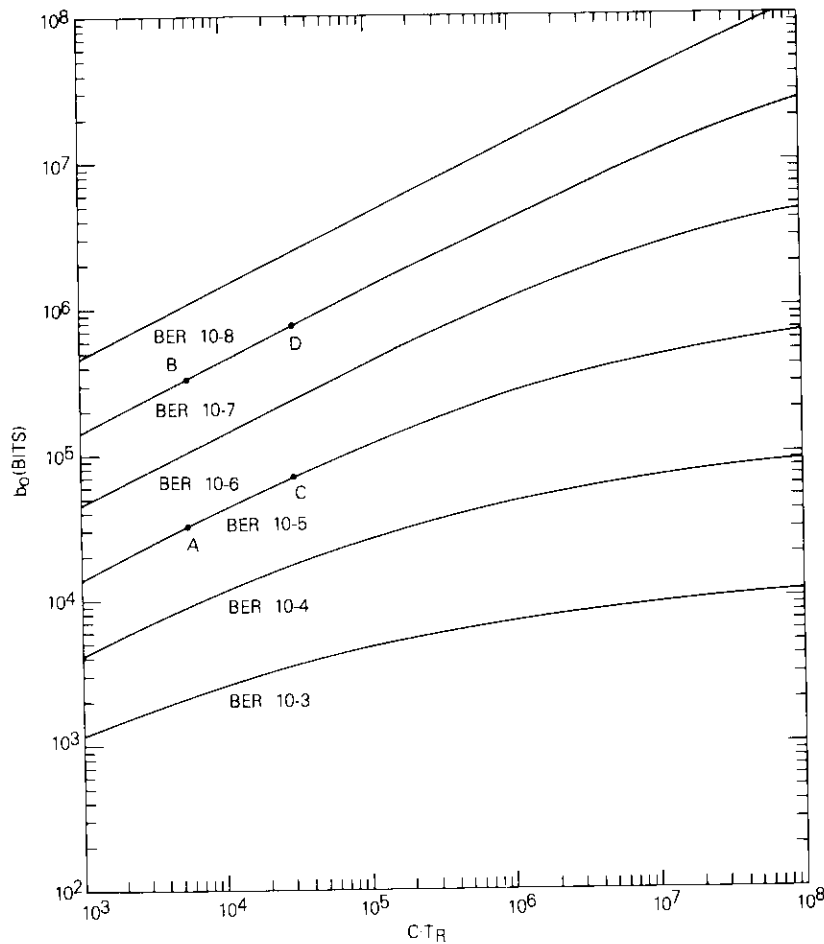


Figure 11. Optimal Buffer Size (B_0) vs C_T for HDLC HDX Mode ($A = 56$ bits)

$T_R \simeq 100$ ms) and a satellite channel (with $T_R \simeq 540$ ms). Bit error rates of 10^{-5} and 10^{-7} are selected. Table 1 gives the optimal frame length and modulo count for these system configurations and the resulting peak performance. These results are from Figure 12 (points A, B, C, and D) using $C_T = 5,600$ and $30,240$ for the terrestrial and satellite links, respectively.

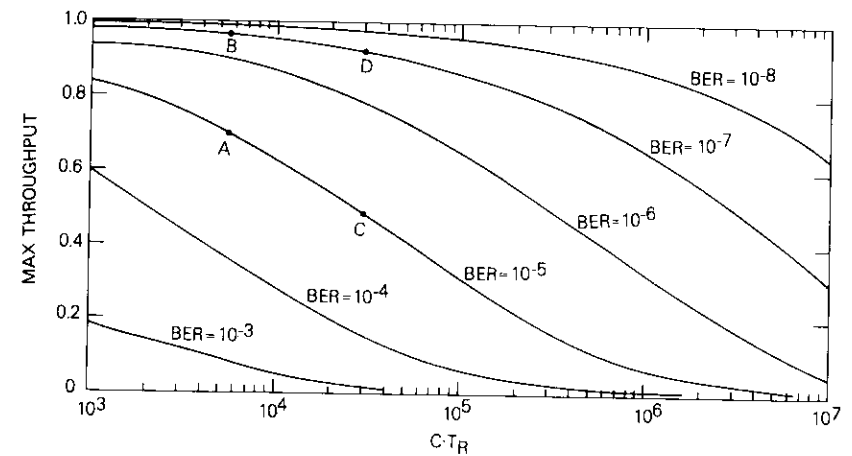


Figure 12. Maximum Achievable Throughput vs $C_T R$ for HDLC HDX Mode ($A = 56$ bits)

TABLE I. OPTIMAL THROUGHPUT CONFIGURATION

Link	Bit Error Rate	b (bits)	Optimal M^*	η^* (%)
Terrestrial (100 ms)	10^{-5}	3400	11	70
Satellite (540 ms)	10^{-7}	34000	11	96.5
	10^{-5}	3400	22	48
	10^{-7}	34000	24	92

* Approximate.

FULL DUPLEX NORMAL RESPONSE MODE

For any given frame length b , an evaluation of equations (28) and (35) shows that the maximum throughput for FDX-NRM occurs when

$$N \geq 1 + 2D(b) \quad (67)$$

and is given by

$$\eta = \frac{\mu^b \{1 - \mu^{b[1+D(b)]}\}}{[1 + D(b)](1 - \mu^b) \{1 + \mu^b - \mu^{b[1+D(b)]}\}} \left(\frac{b - A}{b} \right) \quad (68)$$

where

$$D(b) = \left\lceil \frac{C_T}{b} \right\rceil \quad (69)$$

This throughput is independent of buffer size (or modulo count) if equation (67) is satisfied. However, since $D(b)$ behaves as a step function, it is difficult to maximize equation (68) with respect to b . Assuming $D(b)$ is a smooth function of b yields the approximation

$$D(b) \simeq \frac{C_T}{b} \quad (70)$$

With this approximation, the optimal frame length b_0 is obtained by setting $\partial\eta/\partial b = 0$, which yields b_0 as the solution to the transcendental equation

$$\begin{aligned} &(b + C_T)(1 - \mu^{2b} - \mu^{b+C_T} + \mu^{2b+C_T}) \\ &\cdot \{\mu^b - \mu^{2b+C_T} + \ln \mu(b - A)(\mu^b - 2\mu^{2b+C_T})\} \\ &- \mu^b(b - A)(1 - \mu^{b+C_T})[1 - \mu^{2b} - \mu^{b+C_T} + \mu^{2b+C_T} \\ &+ \ln \mu(2\mu^{2b+C_T} - \mu^{b+C_T} - 2\mu^{2b})(b + C_T)] = 0 \quad (71) \end{aligned}$$

Figure 13 shows the optimal frame length as a function of channel C_T for various bit error rates as well as the minimum buffer size (modulo count)* specified by equation (67). Equations (67) and (71) indicate that, unlike the HDX case, the optimal frame length depends to some extent on channel C_T if sufficient buffering is provided. The buffering requirements also depend on the frame length.

The maximum achievable throughput under FDX-NRM operation [obtained by using b_0 in equation (68)] as a function of channel C_T and bit error rate is shown in Figure 14. A comparison of these results with those of Figure 12 for the HDX case reveals a difference in peak performance values. Also, in the FDX case, any modulo count larger than that defined by the minimum buffering requirement can be used; however, the HDX case always has an optimal modulo count, and larger (as well as smaller) values will yield lower throughputs.

* Buffer size = (modulo count - 1) times frame length.

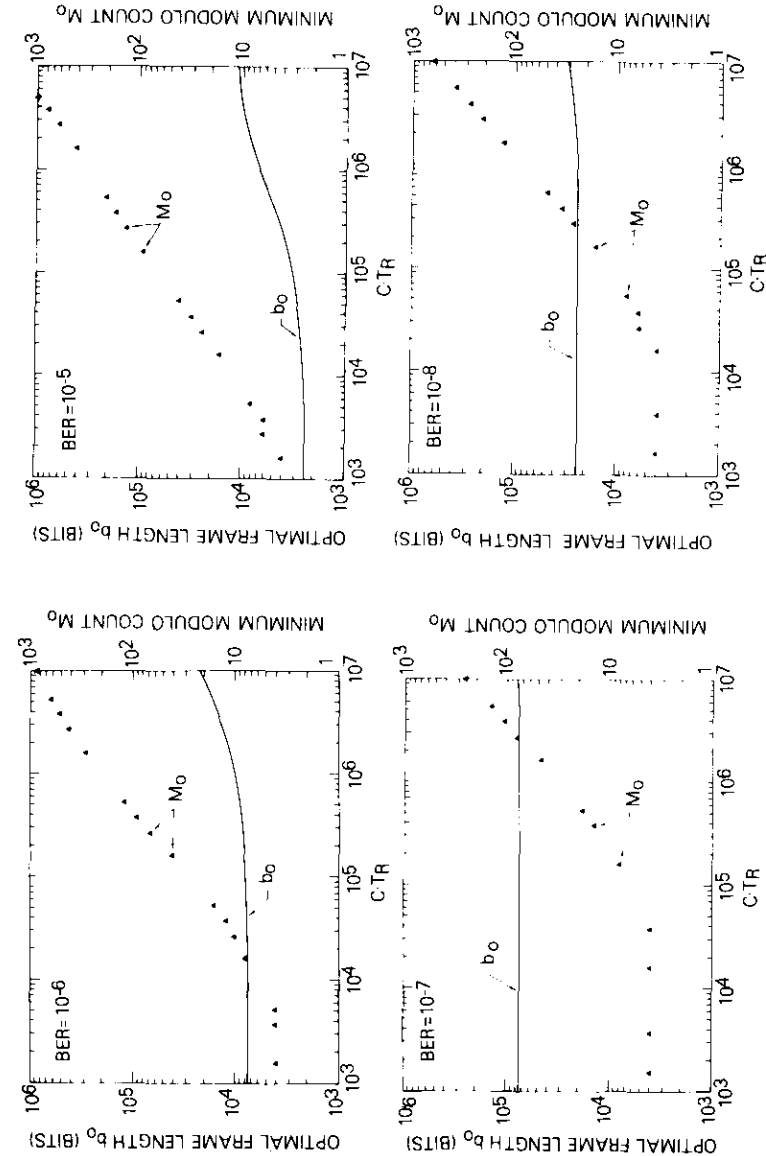


Figure 13. Optimal HDLC FDX-NRM System Configurations

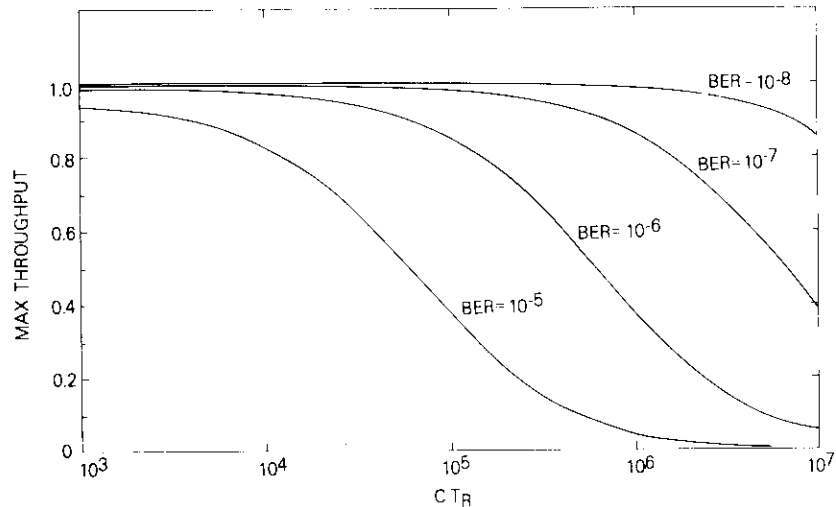


Figure 14. Maximum Achievable Throughput for HDLC FDX-NRM

FULL DUPLEX ASYNCHRONOUS RESPONSE MODE

If an approach similar to that used for the NRM case is employed, the maximum achievable efficiency for FDX-ARM with a given frame length b is obtained for buffer sizes satisfying

$$N \geq 1 + \left\lceil \frac{C_T}{b} \right\rceil \quad (72)$$

and the throughput is given by

$$\eta \simeq \frac{\mu^b}{1 + \left(1 + \frac{C_T}{b}\right)(1 - \mu^b)} \left(\frac{b - A}{b}\right) \quad (73)$$

The optimal frame length b_0 is obtained by setting

$$\frac{\partial \eta}{\partial b} = 0$$

which yields

$$-\mu^b(A + C_T) + (b - A)[(2b + C_T) \ln \mu - 2] + 2b + C_T = 0 \quad (74)$$

The optimal frame length and minimum buffer size (modulo count) are shown in Figure 15 as functions of channel C_T for various bit error rates. Figure 16 shows the maximum achievable throughputs under FDX-ARM operation.

Figure 17 shows the maximum achievable throughputs for the three HDLC modes at several bit error rates. In general, FDX-ARM allows the highest throughputs, followed by FDX-NRM and HDX, respectively. However, at lower bit transmission rates, the maximum achievable throughputs for both FDX modes do not differ significantly. There are also high-bit-error-rate regions where the HDX mode can slightly outperform the FDX-NRM mode, although the maximum throughputs are fairly low.

Suboptimal frame length and buffer tradeoffs

The evaluation of maximum achievable throughputs was based on the assumption that no constraints on frame length or buffer size existed; therefore, optimal values could be used. The design of a real system may impose constraints on frame length and restrictions on the available buffering. For this reason, the penalty imposed on the throughput by either suboptimal frame lengths or buffers should be explored.

HALF DUPLEX

For the HDX mode from equation (59) at constant $B (= Nb)$,

$$\frac{\eta(b)}{\eta_0(b_0)} = \frac{f(b)}{f(b_0)} = \frac{\mu^b(1 - \mu^b)(b - A)}{\mu^{b_0}(1 - \mu^{b_0})(b_0 - A)} \quad (75)$$

and at constant b ,

$$\frac{\eta(B)}{\eta_0(B_0)} = \frac{g(B)}{g(B_0)} = \frac{(1 - \mu^B)}{(1 - \mu^{B_0})} \left(\frac{B_0 + C_T}{B + C_T}\right) \quad (76)$$

Figure 18 shows the relative sacrifice in throughput for HDX operation caused by reducing frame length b from the optimal value b_0 (from Figure 10) while holding the buffer size B (in bits) constant at any value. If the buffer has the optimal value B_0 shown in Figure 11, then the curves can be interpreted as the relative loss in throughput from the maximum achievable values shown in Figure 12. Frame length can be reduced to some extent, depending on the bit error rate, without a significant sacrifice in throughput. The curves are applicable for all C_T values. However, the

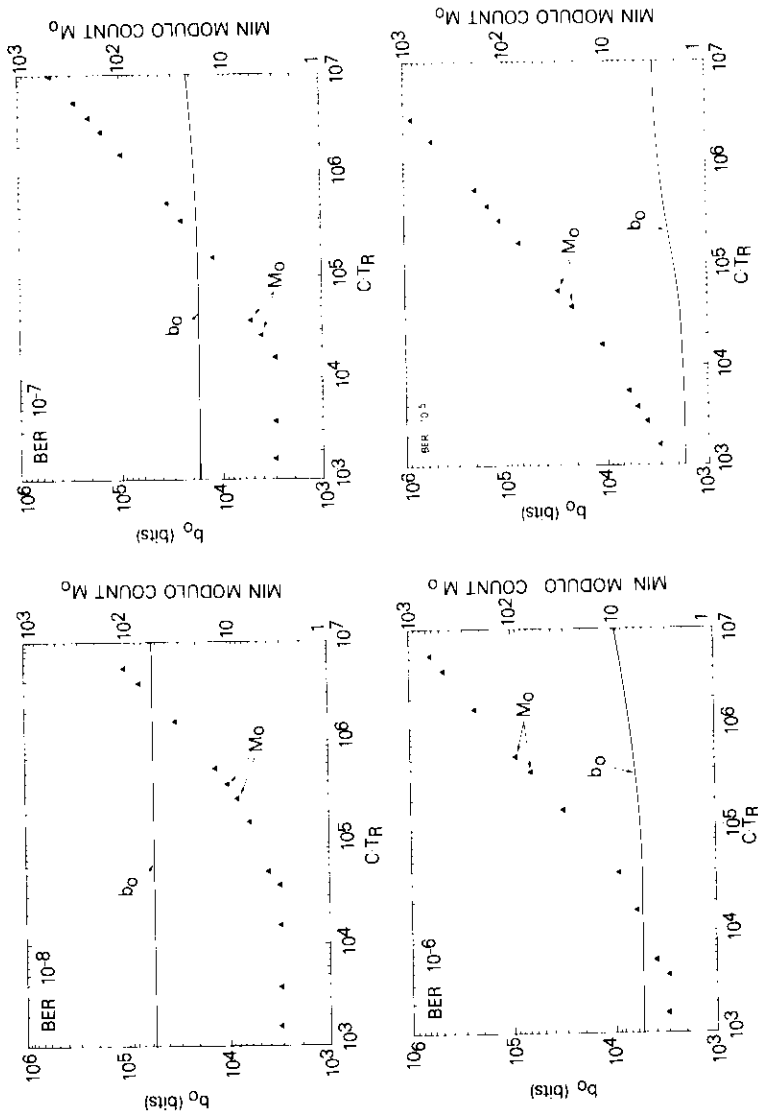


Figure 15. Optimal HDLC FDX-ARM System Configurations

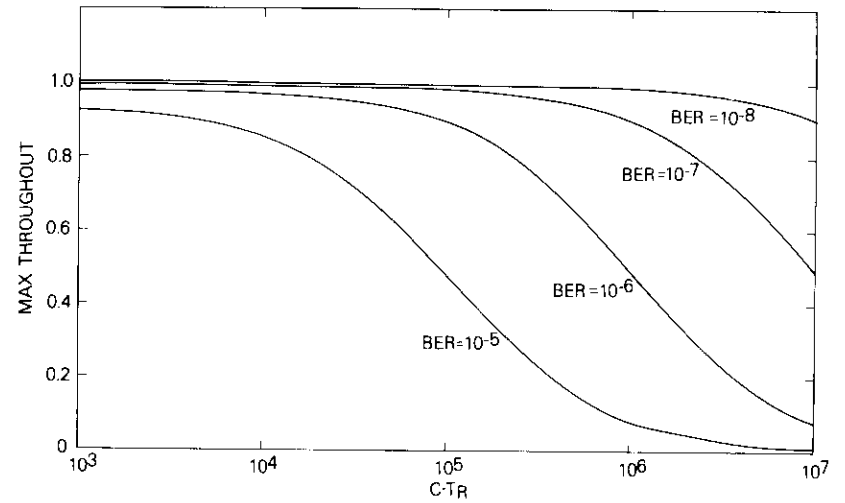


Figure 16. Maximum Achievable Throughput for FDX-ARM

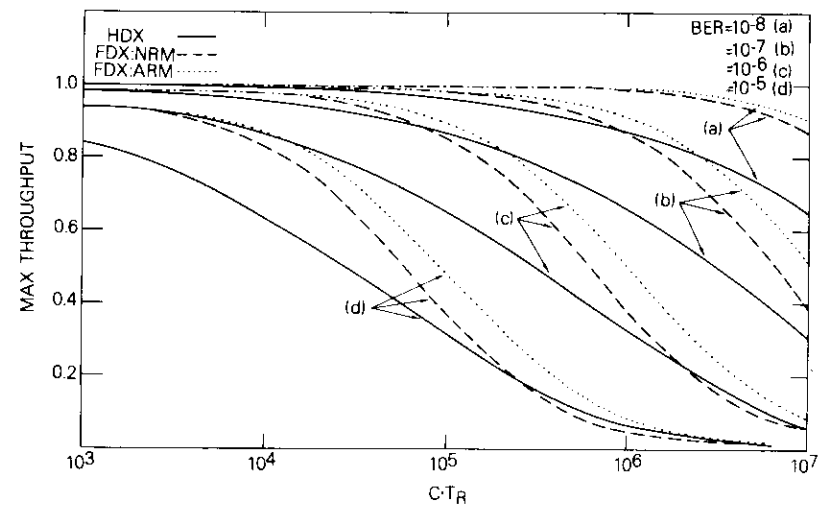


Figure 17. Relative Comparison of Maximum Achievable Throughputs

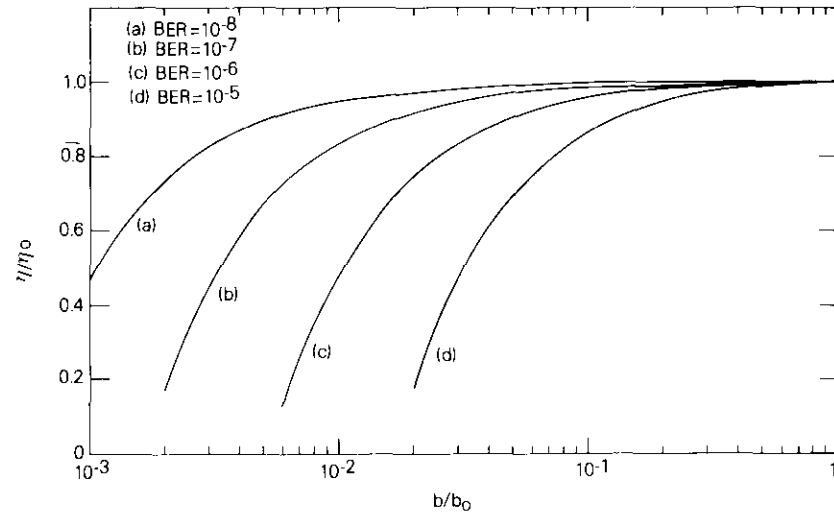


Figure 18. Frame Length-Throughput Tradeoffs for HDX Mode

buffer tradeoff at a constant frame length depends on C_T and the bit error rate, but not on the frame length. Figure 19 shows the buffer tradeoffs at any constant frame length. As before, if the optimal frame length b_0 is used, the curves represent the loss in throughput from the maximum achievable values. The C_T values correspond to data rates of 10-kbit/s, 50-kbit/s, 200-kbit/s, and 1.544-Mbit/s satellite channels ($T_R = 0.54$). The buffer size cannot be less than one frame length; hence, Figure 19 must be used with care since B/B_0 may be valid only above a certain point depending on C_T values and the bit error rate. These points are indicated on Figure 19 when optimal frame lengths are used.

FULL DUPLEX NORMAL RESPONSE MODE

For the FDH-NRM mode, the expressions for throughput cannot be put into the form of equation (59). Maximum throughput is given by equation (68) for any frame length if sufficiently large buffering is used [see equation (67)]. An optimal frame length b_0 can be found by solving equation (71). For other values of b , the throughput is lower. Figure 20 shows the throughput variation with frame length as a fraction of b_0 for a set of C_T values when sufficient buffering to satisfy equation (67) is available. As the bit error rate decreases, the tradeoff curves corresponding to different C_T values converge; the range over which b can be different from b_0 without a significant impact on throughput increases.

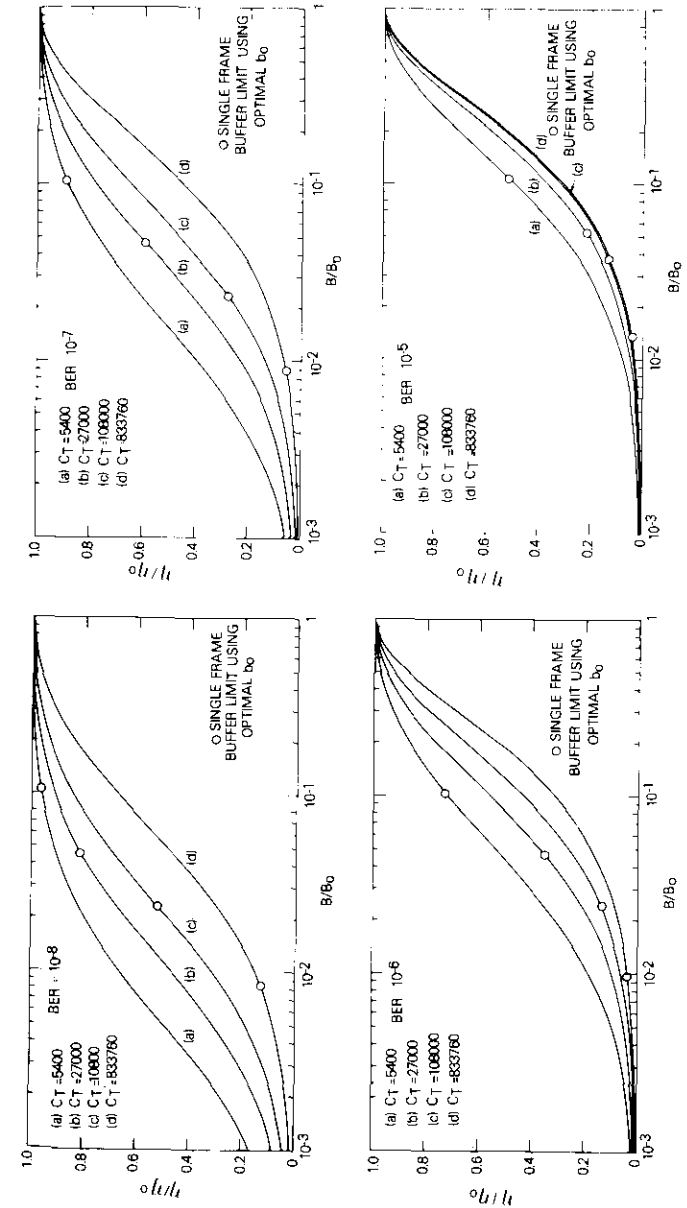


Figure 19. Buffer Size vs Throughput Tradeoff for HDX Mode

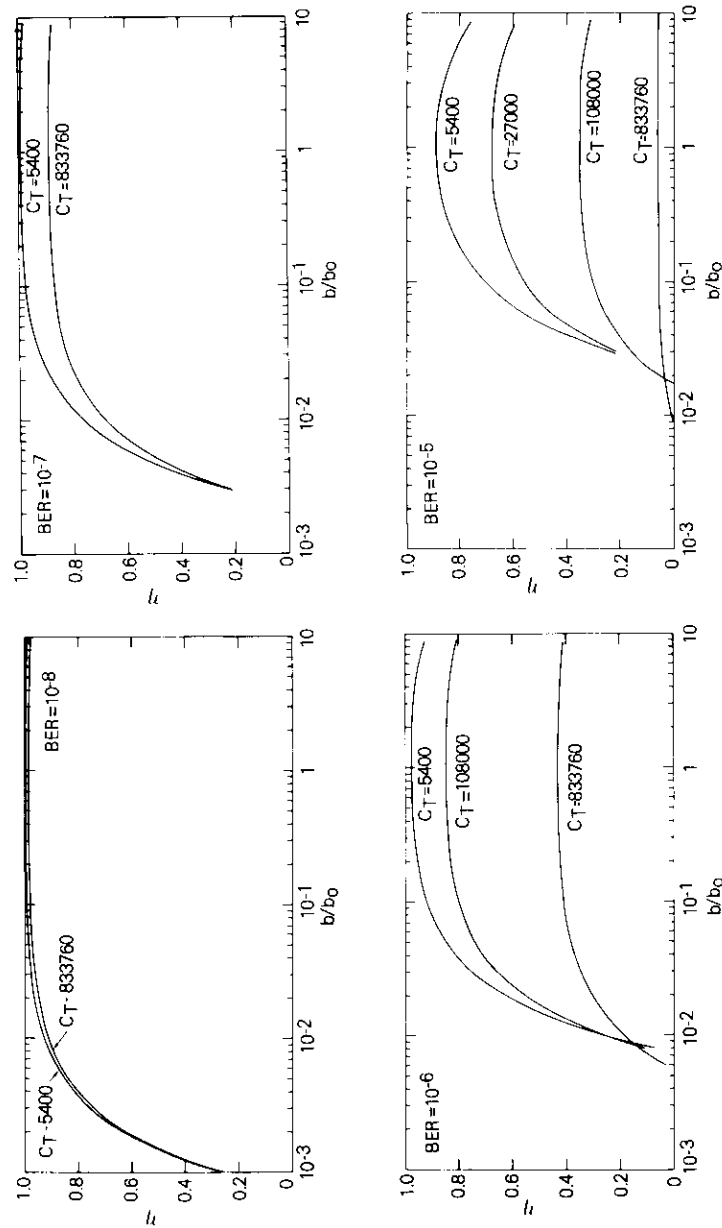


Figure 20. Frame Length vs Maximum Throughput Tradeoff for FDX-NRM

The impact of different buffer sizes on throughput for a given frame length b is revealed by investigating the impact of N , since $B = Nb$. For a given b , the throughput depends on both b and N , and the throughput expressions must be used over the appropriate regions of N . The tradeoffs for optimal b_0 are shown in Figure 21 for the same set of C_T values. The cut-off points for the curves correspond to the minimum possible value of N (i.e., unity). Unlike the preceding cases, Figure 21 does not represent a universal set of curves, and a different b ($\neq b_0$) requires a new set of curves.

FULL DUPLEX ASYNCHRONOUS RESPONSE MODE

For the FDX-ARM case the frame length and buffer tradeoffs are derived in the same manner as for the FDX-NRM case except that equations (72) and (73) and the corresponding throughput expressions are used. These results are shown in Figures 22 and 23. Figure 22 represents universal curves for the C_T values, while Figure 23 represents the tradeoffs only at the optimal frame length, b_0 .

PERFORMANCE AT SPECIFIED BUFFER SIZE

The performance of the three HDLC modes for a given buffer size B is examined. For the HDX cases, this simply involves using the frame length closest to b_0 ; FDX cases must be solved numerically because various N and b combinations are feasible for a given buffer size, and the combination yielding the highest throughput must be chosen. Figures 24-26, which are useful with restricted buffering resources, show the maximum throughputs for the three modes and a 9.6-kbit/s, 56-kbit/s and 1.544-Mbit/s satellite channel, respectively, at bit error rates of 10^{-5} , 10^{-6} , and 10^{-8} . These figures demonstrate that the HDX mode can actually outperform the FDX-NRM at higher transmission and bit error rates over a range of buffer sizes.

Conclusions

This paper has developed performance models for three separate modes of HDLC operation to predict performance capabilities and limits. Some of the tradeoffs involved in designing a data communications link are highlighted. The generalized results are presented for a wide range of data transmission rates and arbitrary propagation delays, and hence apply to both terrestrial and satellite data links.

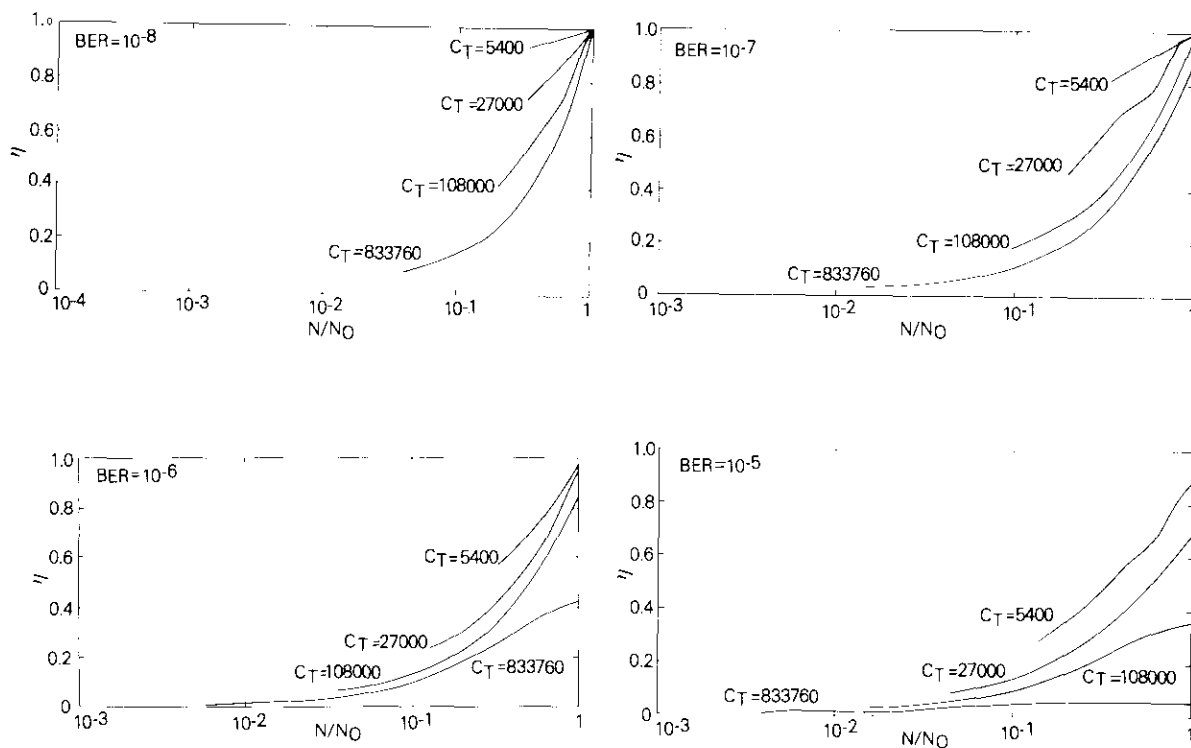


Figure 21. Buffer Size vs Maximum Throughput Tradeoff for FDX-NRM

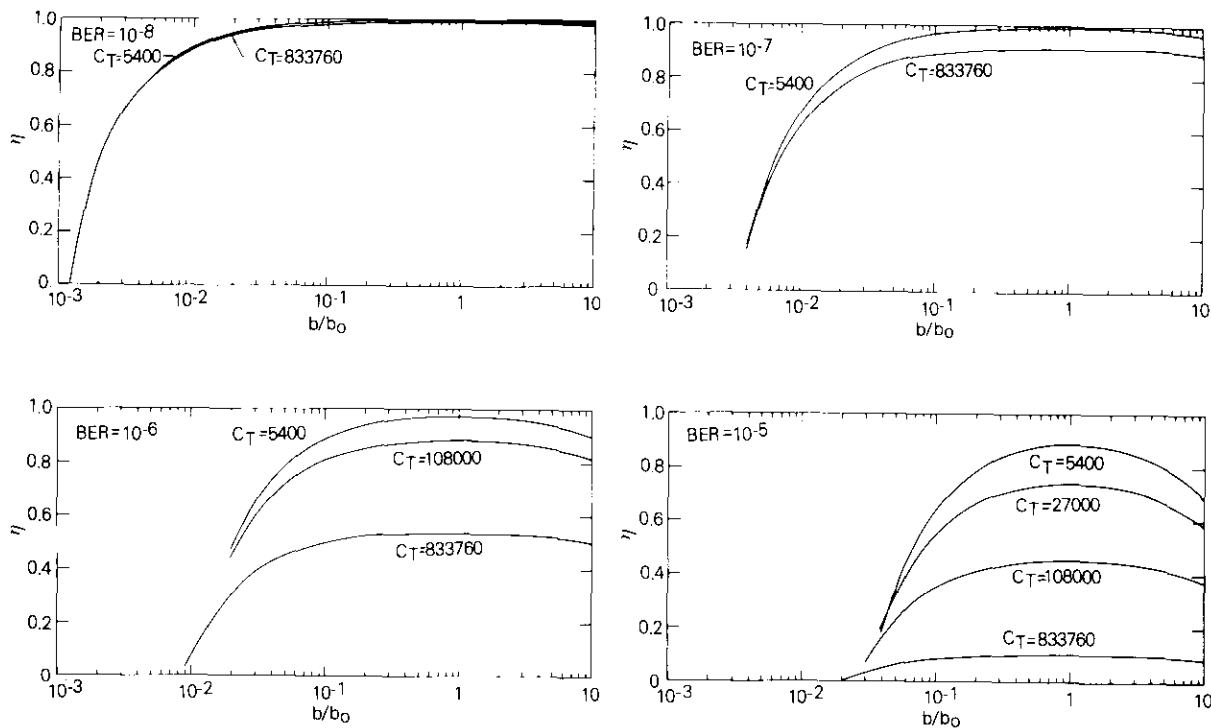


Figure 22. Frame Length vs Maximum Throughput Tradeoff for FDX-ARM

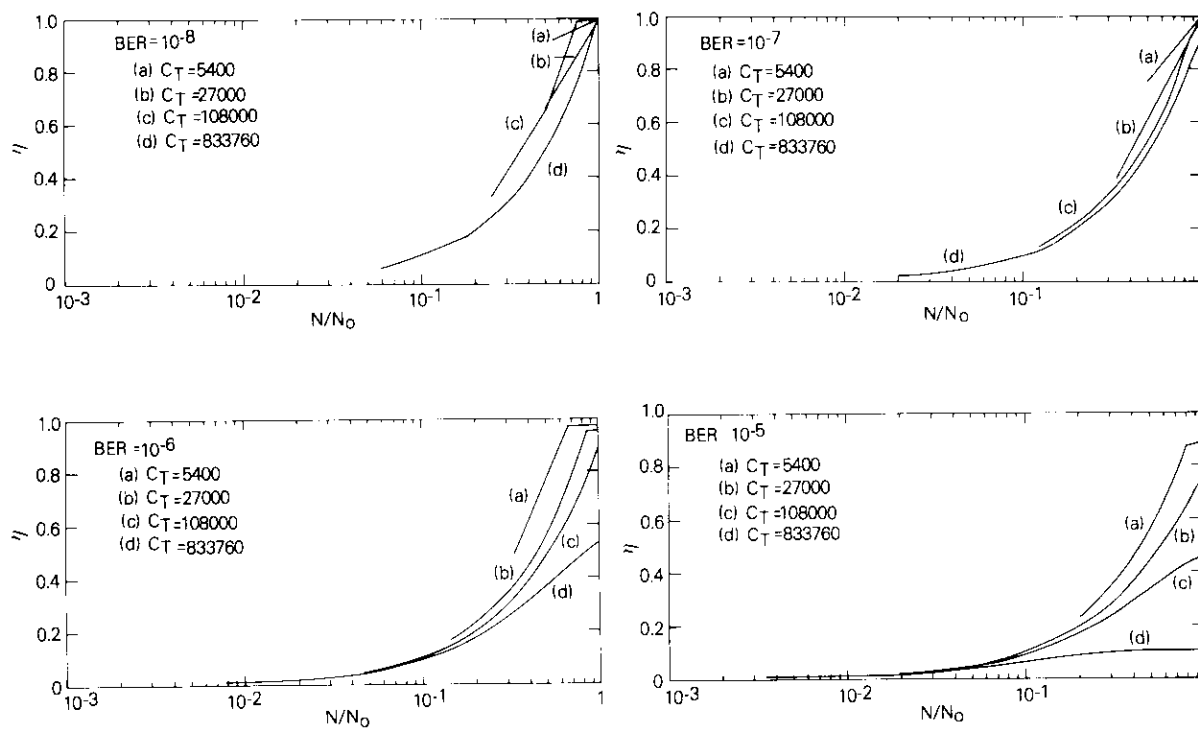


Figure 23. Buffer Size vs Maximum Throughput Tradeoff for FDX-ARM

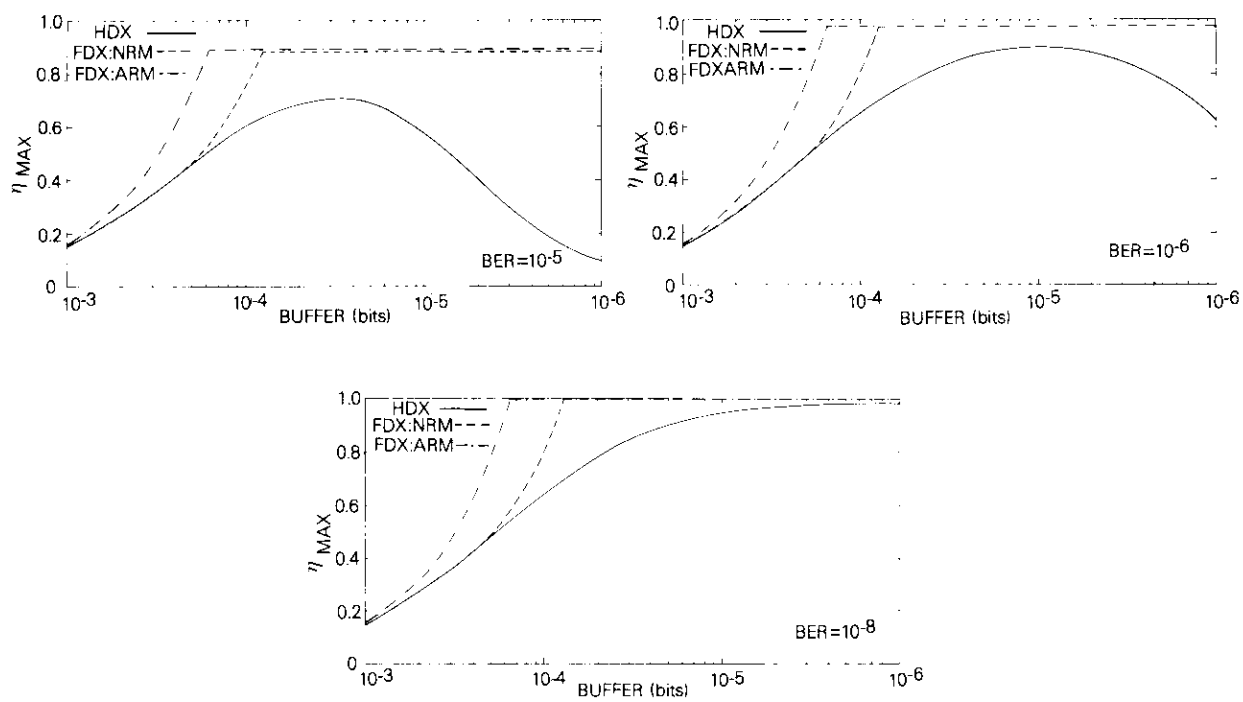


Figure 24. Maximum Throughput vs Buffer Size for a 9,600-bit/s Satellite Channel

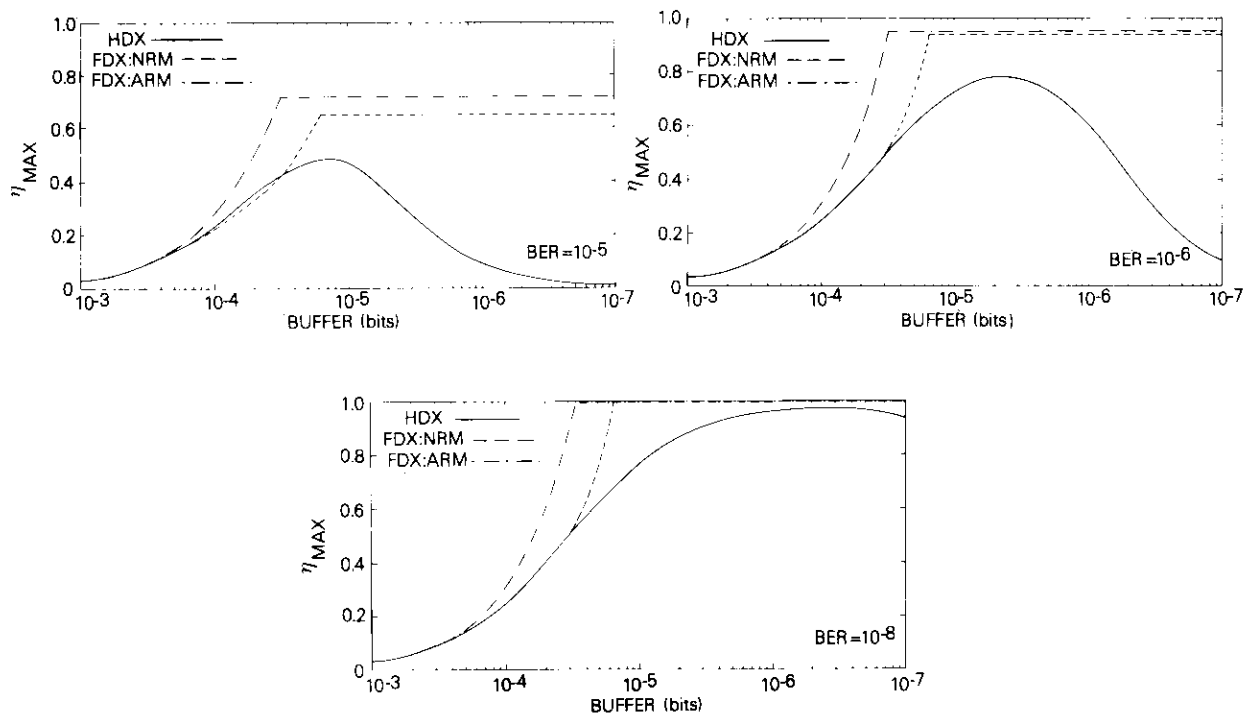


Figure 25. Maximum Throughput vs Buffer Size for a 56-kbit/s Satellite Channel

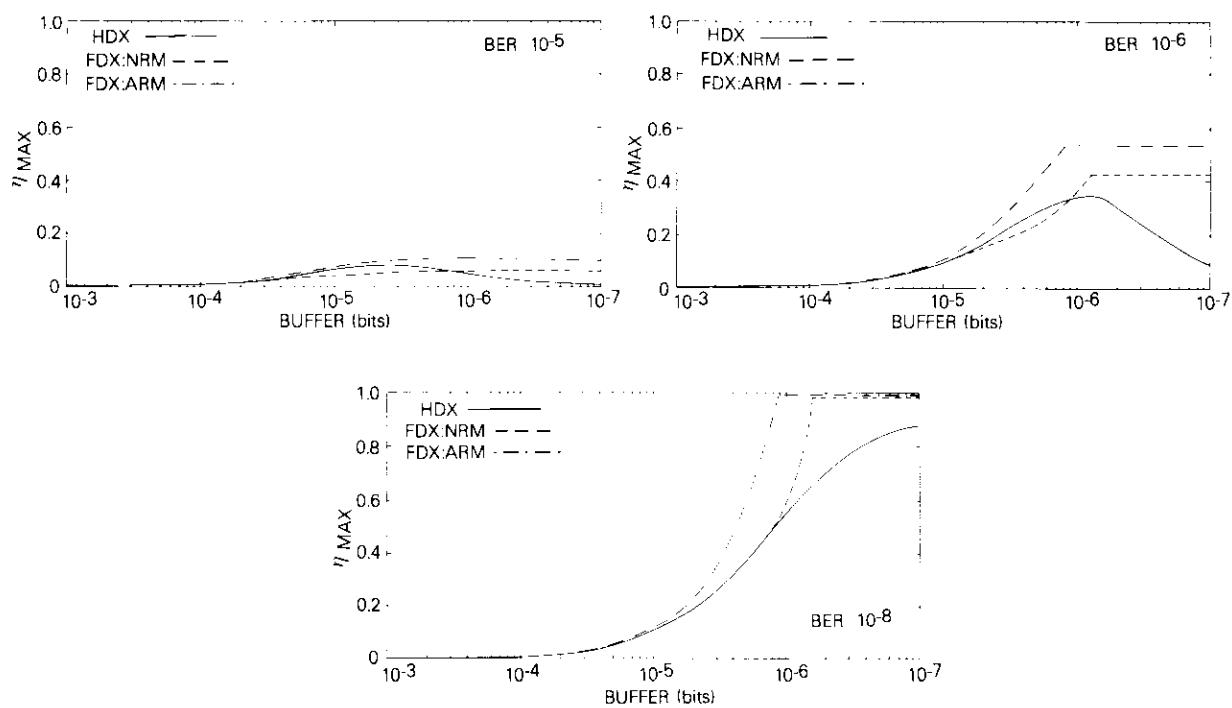


Figure 26. Maximum Throughput vs Buffer Size for a 1.544-Mbit/s Satellite Channel

For system design, Figures 12, 14, and 16 provide an estimate of maximum achievable throughputs over a given channel for the three HDLC modes. The bit error rates required for acceptably high throughput levels and the bit error rate improvement necessary for the forward error correction (FEC) coding schemes used in a hybrid system can be deduced. If there are no design constraints, Figures 10, 11, 13, and 15 indicate the approximate HDLC parameters (frame length and modulo count or maxout) which would yield the highest throughput. When either or both of these parameters are constrained, frame length and buffer size tradeoff curves similar to those in Figures 24 to 26 can be used to estimate design tradeoffs.

Acknowledgments

The author is indebted to Dr. William L. Cook and Mr. Robert C. Davis for their invaluable encouragement and support.

References

- [1] J. P. Gray, "Line Control Procedures," *Proc. IEEE*, Vol. 60, No. 11, Special Issue on Computer Communications, November 1972, pp. 1301-1312.
- [2] H. O. Burton, and D. D. Sullivan, "Errors and Error Control," *Proc. IEEE*, Vol. 60, No. 11, Special Issue on Computer Communications, November 1972, pp. 1293-1301.
- [3] A. Gatfield, "Error Control on Satellite Channels using ARQ Techniques," *COMSAT Technical Review*, Vol. 6, No. 1, Spring 1976, pp. 179-188.
- [4] R. A. Donnan, and J. R. Kersey, "Synchronous Data Link Control, A Perspective," *IBM Systems Journal*, Vol. 13, No. 2, 1974.
- [5] "IBM Synchronous Data Link Control General Information," IBM Corp. Publication No. GA27-3093, March 1974.
- [6] "Proposed American National Standard for Advanced Data Communication Control Procedures (ADCCP)," ANSI Document X3S34/589, Draft 6, October 1976.
- [7] "Data Communication—High Level Data Link Control Procedures—Frame Structure," ISO Document No. ISO3309-1976.
- [8] "Data Communication—High Level Data Link Control Procedures—Elements of Procedures (independent numbering)," ISO Document No. ISO/DIS 4335 (1976).
- [9] "Proposed Addendum to DIS 4335," ISO Document No. ISO/TC97/SC6, No. 1300.



Ashok K. Kaul received B.Sc. and M.Sc. degrees in physics from the University of Jammu in Kashmir, India, and a Ph.D. in physics from the University of Maryland. In 1973, he joined COMSAT Laboratories, where he is currently Assistant Manager of the Computer Systems Development Department of the Transmission Systems Laboratory, responsible for directing research and experiments in computer communications.

Index: intermodulation, phase-shift keying, frequency division multiple access, computer program, frequency modulation

Intermodulation in memoryless nonlinear amplifiers accessed by FM and/or PSK signals*

P. Y. K. CHANG AND R. J. F. FANG

(Manuscript received November 11, 1977)

Abstract

This paper analyzes the intermodulation between an arbitrary number of FM and PSK carriers which access a memoryless bandpass nonlinear amplifier in an FDMA mode. The FM carriers can be FDM/FM, TV/FM, and/or SCPC/FM, whereas the PSK carriers can be SCPC/PSK, PSK/TDMA, and/or PSK/FDMA. The RF and baseband power spectral densities of the intermodulation products, including the effect of multiple bands of thermal noise, have been analyzed for FDM/FM, PSK/FDMA, or TDMA carriers with mathematical expressions explicitly derived. For frequency plans involving SCPC/FM and/or PSK carriers, a special method is proposed to compute the power spectral density of the intermodulation. A user-oriented computer program, PRIME (Program of InterModulation Evaluation), has been written in terms of a command language and can be considered an extension of the CIA4 Intermodulation Analyzer, which is primarily limited to FDM/FM signals.

*This paper is based upon work performed at COMSAT Laboratories under the sponsorship of the International Telecommunications Satellite Organization (INTELSAT). Views expressed in this paper are not necessarily those of INTELSAT.

Introduction

Intermodulation is an important source of transmission system impairment in satellite communications because frequency-division multiple-access with FM signaling (FDMA/FM) has been an effective means of utilizing a satellite transponder. Various methods have been proposed to analyze, evaluate, and/or minimize intermodulation effects [1]–[15]. However, the primary interest has been the intermodulation computation for pure continuous wave (CW), FDM/FM, or PSK carriers operated in the FDMA mode. A mixture of these carriers has not yet been analyzed mathematically.

As other modulation/multiple-access systems such as single-channel-per-carrier FM (SCPC/FM), SCPC/PSK, FDMA/PSK, and/or time-division multiple-access PSK (TDMA/PSK) are gradually introduced into the predominantly FDMA/FM/FDM INTELSAT satellite system to carry international or leased traffic, a mixture of modulation/access techniques might exist in some nonlinear high-power amplifiers (HPAs) at the earth station or on board the satellite. For example, a standard A earth station may use a common nonlinear HPA to transmit FM/TV, FDMA/FM/FDM, and SCPC/PSK carriers to save earth station equipment and hence minimize costs. Other SCPC/FM carriers may be added later to the same HPA to communicate with other standard B earth stations via a transponder dedicated partially or totally to leased services. If sufficient power is still available at this HPA, time-division multiple-access (TDMA)/PSK may also be added to the INTELSAT TDMA network. The feasibility of such an arbitrary mixed mode of operation is clearly based upon the tolerance to intermodulate impairments of each individual carrier.

Another example is the potential use of a portion or multiple portions of an FDMA transponder for SCPC services via partial transponder leases. Cost-effective networks may be established between standard A and B earth stations, among standard B earth stations, and/or among standard A earth stations by using SCPC/PSK and/or SCPC/FM carriers within the SCPC portion(s) of the leased transponder. Thus, mixed FDMA/FM/FDM, SCPC/PSK, and SCPC/FM modes of operation may exist in satellite transponders dedicated partially or totally to the leased services.

The most powerful tool to date, the CIA4 Intermodulation Analyzer Program [12], seems inadequate for analyzing and evaluating intermodulation in the cited examples for several reasons: First, although the SCPC carriers may be sparse or unevenly spaced, the CIA4 Program must treat these carriers as a band of equivalent thermal noise if the total number of carriers exceeds 50. The validity of this approach may be questionable in

many applications. Second, every FM carrier is assumed to have a Gaussian-shaped power spectrum. This assumption seems adequate for most INTELSAT FM/FDM carriers because the modulation indices are close to or greater than unity; however, it is no longer valid for FM/TV or SCPC/FM carriers without voice activation or without energy dispersal in which case the power spectra generally contains highly peaked components (see Figure 6). These highly peaked power spectra may cause an impairment in the baseband of SCPC/FM carriers significantly different from that caused by Gaussian-shaped spectra, especially if the SCPC/FM carriers are equally spaced; the intermodulation products will become superimposed and will enhance the peakedness of the intermodulation power spectra. Third, the assumption that the power spectra of the PSK carriers are the convolution of rectangular window functions with Gaussian functions appears inadequate for applications with FDMA/PSK, TDMA/PSK, and/or sparse and unevenly spaced SCPC/PSK carriers because the actual intermodulation power spectra are significantly different from this assumption. Fourth, since the SCPC carriers may be allocated a bandwidth of 45 kHz and the FDM/FM carriers may be allocated bandwidths of any multiple of 1.25 MHz, an extremely large array size will be required in the CIA4 Program to characterize a 36-MHz or 72-MHz transponder with mixed SCPC and FDM/FM carriers with a resolution of the order of kilohertz. It is impractical to increase the number of carriers from 50 to 100, for example, and simultaneously allow kilohertz resolution. Fifth, in some situations the tail effects of large intermodulation products are not adequately included, especially when PSK carriers are involved. Finally, the CIA4 Program can handle only one band of thermal noise, not multiple bands.

The preceding discussion clearly explains the need for the intermodulation analysis for an arbitrary number of FM and PSK carriers with arbitrary power spectral shapes sharing a common nonlinear amplifier such as a traveling wave tube amplifier (TWTA).

This paper specifically addresses intermodulation analysis for systems with mixed operation of an arbitrary number of FDMA/FM/FDM, SCPC/PSK, SCPC/FM, FDMA/PSK and/or TDMA/PSK carriers in the presence of multiple bands of thermal noise.

The following section contains the general mathematical formulation of the problem and its solution. Subsequent sections describe the proposed practical "telescopic" approach for evaluating the RF intermodulation power spectral density for SCPC/FM and SCPC/PSK carriers and the baseband intermodulation power spectral density for SCPC/FM carriers, respectively. The RF and baseband third-order intermodulation power

spectral densities are investigated for FDM/FM, TV/FM, PSK/FDMA and/or PSK/TDMA carriers. The baseband noise power ratio (NPR) performance of SCPC/FM or FDMA/FM/FDM carriers can then be evaluated based on the computed intermodulation power spectral densities.

The analytical results obtained in these sections have been implemented on an IBM 360/65 in a computer program termed PRIME (Program for InterModulation Evaluation). This program is written in terms of a user-oriented computer language similar to that used in the CIA4 Program. Several numerical examples illustrate the use of PRIME software. The first three examples concerned a hypothetical frequency plan of a mixed mode operation of SCPC/FM, SCPC/PSK, FDM/FM or TV/FM. Example 1 calculates the RF and baseband intermodulation power spectra falling onto a particular SCPC/FM carrier and the baseband impairments caused by this intermodulation noise. Example 2 evaluates the RF intermodulation power spectrum falling onto a particular SCPC/PSK carrier. When the up-link and down-link C/N_o are known, the BER performance degradation in the desired SCPC/PSK carrier caused by the intermodulation products can be found. Example 3 computes the RF and baseband intermodulation power spectra for a particular FDM/FM carrier and the NPR impairments. Example 4 illustrates the use of PRIME in evaluating the power spectrum of a mixed FDMA/FM and PSK system. The final section of this paper, which concludes the intermodulation analyses and proposes areas for further study, is followed by the appendices which provide detailed mathematical derivations.

Mathematical model

In the development of this mathematical model, basic concepts and notations similar or identical to those in Reference 11 will be used to simplify the extension work from the CIA4 Program to PRIME. When the input to a memoryless bandpass nonlinear amplifier (e.g., a helix TWTA) is an arbitrary mixture of FDM/FM, SCPC/FM, SCPC/PSK, FDMA or TDMA/PSK, thermal noise, and/or unmodulated continuous wave (CW) carriers as shown in Figure 1, input signals can be represented by

$$\begin{aligned} e_i(t) &= \text{Re} \left\{ \sum_{i=1}^{m+n} A_i(t) \exp [j\omega_0 t + j\omega_i t + j\phi_i(t)] \right\} \\ &= \text{Re} \left\{ \sum_{i=1}^{m+n} A_i(t) \exp [j\theta_i(t)] \right\} \end{aligned} \quad (1)$$

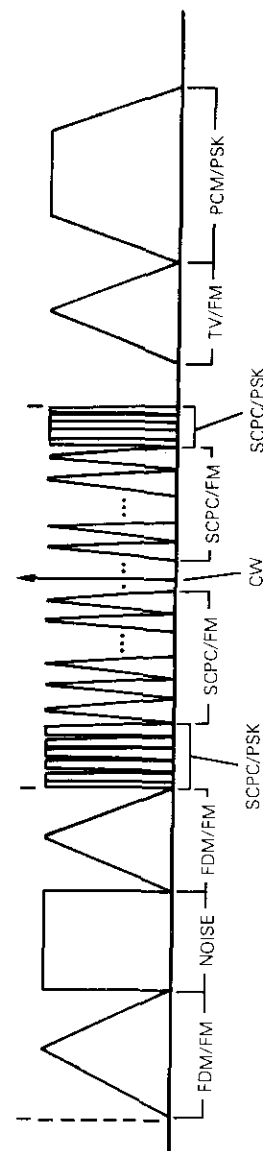


Figure 1. A Hypothetical Carrier Plan for a Mixed FM and PSK System

where m and n are the total number of input carriers and the total number of bands of thermal noise, respectively. The center frequencies of these $m + n$ input signals are located at $\omega_0 + \omega_l$ rad/s, where ω_0 is the center frequency of the bandpass nonlinear amplifier. The time functions, $A_l(t)$ and $\phi_l(t)$, are the amplitude and phase of the l th signal, respectively. Note that, for the n bands of thermal noise, $A_l(t)$ and $\phi_l(t)$, $l = m + 1, m + 2, \dots, m + n$, are statistically independent random processes having first-order probability density functions of Rayleigh and uniform distributions, respectively. For convenience, equation (1) uses the notation

$$\theta_l(t) = \omega_l t + \phi_l(t) \quad .$$

The memoryless bandpass nonlinear amplifier can be characterized by the complex envelope model $g(\rho) \exp\{jf(\rho)\}$ [11]. Namely, if the envelope of the input signal to the memoryless bandpass amplifier is $\rho(t)$, then the output (complex) envelope is $g\{\rho(t)\} \exp\{jf[\rho(t)]\}$, where $g(\cdot)$ and $f(\cdot)$, respectively, are the amplitude and phase nonlinearities as functions of the input envelope. Reference 11 shows that the following Bessel series approximation to the nonlinear characteristics $g(\rho) \exp\{jf(\rho)\}$ is quite suitable for numerical computation:

$$g(\rho) \exp\{jf(\rho)\} \approx \sum_{p=1}^L b_p J_1(p\alpha\rho) \quad (2)$$

where J_1 is the first-order Bessel function of the first kind. The parameters α and L and the complex coefficients b_p are chosen so that the right-hand side of equation (2) yields the best fit to the measured $g(\rho)$ and $f(\rho)$.

With the complex envelope approximation of equation (2), the output of the nonlinear amplifier can be obtained by paralleling the derivation given in Reference 11 and can be explicitly written as

$$e_o(t) = \text{Re} \left[\sum_{k_1, k_2, \dots, k_{m+n} = -\infty}^{\infty} M(k_1, k_2, \dots, k_{m+n}; t) \right. \\ \cdot \exp \left\{ j \left[\omega_0 t + \sum_{l=1}^m k_l \theta_l(t) \right] \right\} \exp \left\{ j \left(\omega_0 t + \sum_{l=m+1}^{m+n} k_l \omega_l t \right) \right. \\ \left. \left. + j \sum_{l=m+1}^{m+n} k_l \tan^{-1} \left[\frac{\eta_{ls}(t)}{\eta_{lc}(t)} \right] \right\} \right] \quad (3)$$

where the circle in the summation sign denotes that the summation is

taken over all possible integers k_l so that $\sum_{l=1}^{m+n} k_l = 1$. The function $M(k_1, k_2, \dots, k_{m+n}; t)$ in equation (3) is defined as

$$M(k_1, k_2, \dots, k_{m+n}; t) \equiv \sum_{p=1}^L b_p \prod_{l=1}^m J_{k_l}[\alpha p A_l(t)] \\ \cdot \prod_{l=m+1}^{m+n} J_{k_l} \left[\alpha p \sqrt{\eta_{lc}^2(t) + \eta_{ls}^2(t)} \right] \quad (4)$$

where $\eta_{lc}(t)$ and $\eta_{ls}(t)$ are the in-phase and quadrature components of the input thermal noise centered at $\omega_0 + \omega_l$. The phase angle of the $(l - m)$ th input thermal noise, $\tan^{-1}[\eta_{ls}(t)/\eta_{lc}(t)]$, is denoted as $\psi_l(t)$.

If the m input carriers include m_1 SCPC/FM, m_2 SCPC/PSK, m_3 FDM/FM, m_4 FDMA or TDMA/PSK, m_5 TV/FM, and m_6 unmodulated CW carriers,* equation (4) can be rearranged to yield

$$M(k_1, k_2, \dots, k_{m+n}; t) = \sum_{p=1}^L B_p(t) \prod_{q=1}^6 P_q(p, t) \quad (5)$$

$$\text{where } B_p(t) \equiv b_p \prod_{l=m+1}^{m+n} J_{k_l} \left[\alpha p \sqrt{\eta_{lc}^2(t) + \eta_{ls}^2(t)} \right] \quad (6)$$

$$P_q(p, t) \equiv \prod_{l=N_{q-1}+1}^{N_q} J_{k_l}[\alpha p A_l(t)] \quad (7)$$

and

$$N_q \equiv m_q + N_{q-1}, \quad q = 1, 2, \dots, 6 \quad (8)$$

with $N_0 = 0$.

Equations (3) and (5) through (8) can be used to find the RF power spectral density of $e_o(t)$ and the RF and baseband intermodulation power spectra, as shown in the following three subsections.

RF power spectral density $S_o(f)$ at the output of the nonlinear amplifier

The autocorrelation of the signal $e_o(t)$ at the output of the nonlinear amplifier is required to evaluate the RF intermodulation power spectrum.

*In the current analysis, only angle-modulated carriers will be treated.

Let $e_o(t + \tau) = \text{Re}\{a\}$, $e_o(t) = \text{Re}\{b\}$, and $\text{Re}\{a\} \text{Re}\{b\} = 1/2 \text{Re}\{ab^* + ab\}$. Then, the autocorrelation function of $e_o(t)$ can be found, based on equations (3) and (2):

$$\begin{aligned} \langle E[e_o(t + \tau) e_o(t)] \rangle &= \frac{1}{2} \text{Re} \sum_{k_1, k_2, \dots, k_{m+n} = -\infty}^{\infty} \exp \left(j\omega_o \tau + j \sum_{l=1}^{m+n} k_l \omega_l \tau \right) \\ &\cdot \left\langle E \left\{ M(k_1, k_2, \dots, k_{m+n}; t + \tau) M^*(k_1, k_2, \dots, k_{m+n}; t) \right. \right. \\ &\cdot \exp \left[j \sum_{l=1}^m k_l \psi_l(t, \tau) \right] \exp \left[j \sum_{l=m+1}^{m+n} k_l \left\{ \tan^{-1} \left[\frac{\eta_{l_s}(t + \tau)}{\eta_{l_c}(t + \tau)} \right] \right. \right. \\ &\left. \left. \left. - \tan^{-1} \left[\frac{\eta_{l_s}(t)}{\eta_{l_c}(t)} \right] \right\} \right] \right\rangle \end{aligned} \quad (9)$$

where $\langle \cdot \rangle$ and $E[\cdot]$ denote time and ensemble averages, respectively, and

$$\psi_l(t, \tau) \equiv \phi_l(t + \tau) - \phi_l(t) \quad (10)$$

To obtain equations (9) and (10), the high-frequency components around $2\omega_o$ have been ignored, since $2\omega_o$ is outside the band of the bandpass nonlinear amplifier.

In general, the expectation term of equation (9) is difficult to evaluate because $M(k_1, k_2, \dots, k_{m+n}; t)$ is a complicated function of t . However, for SCPC/FM carriers without voice activation, FDMA/FM/FDM carriers, SCPS/PSK carriers, FDMA/PSK or TDMA/PSK carriers, and unmodulated CW carriers, the envelope at the input of the nonlinear amplifier can be assumed to be constant for the intermodulation evaluation.* Namely, $A_l(t) = A_l$ for $l = 1, 2, \dots, m$.

*The TDMA/PSK bursts are assumed to be constantly "on" to permit a conservative estimate of the intermodulation products. The impairments caused by the on-and-off nature of the TDMA bursts are not within the scope of this paper; they are treated in References 16 and 17.

Even with this assumption, $M(k_1, k_2, \dots, k_{m+n}; t)$ remains a function of t because $B_p(t)$ in equation (6) depends upon the envelopes of the n input thermal noise. However, since $\eta_l(t)$ are independent band-limited Gaussian random processes of rectangular power spectral densities centered at $\omega_o + \omega_l$ for all $l = 1, 2, \dots, n$,

$$E[\eta_l(t + \tau) \eta_i^*(t)] = \lambda_{l-m}^2 \rho_{l-m}(\tau) \delta_{li} \quad \text{for all } l, i \quad (11)$$

$$E[\eta_l(t + \tau) \eta_i(t)] = 0 = E[\eta_l(t)] \quad \text{for all } l, i \quad (12)$$

$$\begin{aligned} E[\eta_{l_c}(t + \tau) \eta_{l_c}(t)] &= E[\eta_{l_s}(t + \tau) \eta_{l_s}(t)] \\ &= \frac{1}{2} \lambda_{l-m}^2 \rho_{l-m}(\tau) \quad \text{for all } l \end{aligned} \quad (13)$$

where δ_{li} is the Kronecker delta function, and λ_{l-m}^2 and $\rho_{l-m}(\tau)$ are the RF power and normalized autocorrelation function of the Gaussian random process $\eta_l(t)$, respectively. It should be noted that the shape of $\rho_{l-m}(\tau)$ around the center frequency $\omega_o + \omega_l$ is $(\sin x)/x$ because its power spectral density is rectangular.

Since the amplitude and phase of $\eta_l(t)$ are independent random variables with Rayleigh and uniform probability density functions, respectively, and $A_l(t) = A_l$ for $l = 1, 2, \dots, m$, the autocorrelation function $R_o(\tau)$ of $e_o(t)$ can be derived in Appendix A as

$$\begin{aligned} R_o(\tau) &\equiv \langle E[e_o(t + \tau) e_o(t)] \rangle \\ &= \frac{1}{2} \text{Re} \sum_{k_1, k_2, \dots, k_{m+n} = -\infty}^{\infty} H(k_1, k_2, \dots, k_{m+n}; \tau) \\ &\cdot \prod_{i=1}^5 Q_i(\tau) \exp \left(j\omega_o \tau + j \sum_{l=1}^{m+n} k_l \omega_l \tau \right) \end{aligned} \quad (14)$$

where $H(k_1, k_2, \dots, k_{m+n}; \tau)$

$$\begin{aligned} &\equiv \sum_{p=1}^L \sum_{q=1}^L b_p b_q^* \left[\prod_{l=1}^m J_{k_l}(\alpha p A_l) \right] \left[\prod_{l=1}^m J_{k_l}(\alpha q A_l) \right] \\ &\cdot \exp \left[-\frac{1}{2} \alpha^2 (p^2 + q^2) \sum_{i=1}^n \lambda_i^2 \right] \\ &\cdot \left\{ \prod_{l=m+1}^{m+n} I_{k_l} [\alpha^2 p q \lambda_{l-m}^2 \rho_{l-m}(\tau)] \right\} \end{aligned} \quad (15)$$

and

$$Q_i(\tau) \equiv \left\langle \prod_{l=N_{i-1}+1}^{N_i} E\{\exp[jk_l \psi_l(t, \tau)]\} \right\rangle. \quad (16)$$

In equation (15), I_{k_i} is the k_i th-order modified Bessel function of the first kind. When $n = 1$ and $m = m' - 1$, equation (15) can be reduced to equation (19) of Reference 11, as expected. Therefore, Fourier transformation of equation (14) can be used to obtain the desired power spectral density, $S_0(f)$, of the nonlinear amplifier output.

RF third-order intermodulation power spectral density

Since $H(k_1, k_2, \dots, k_{m+n}; \tau)$ is a function of $\rho_i(\tau)$ only through the modified Bessel function I_ν , it can be made a more explicit function of $\rho_i(\tau)$ by using the power series expansion

$$I_\nu(Z) = \sum_{s=0}^{\infty} \frac{1}{s!(|\nu| + s)!} \left(\frac{Z}{2}\right)^{|\nu|+2s}. \quad (17)$$

That is,

$$\begin{aligned} & H(k_1, k_2, \dots, k_{m+n}; \tau) \\ & \equiv \sum_{p=1}^L \sum_{q=1}^L b_p b_q^* \left[\prod_{l=1}^m J_{k_l}(\alpha p A_l) \right] \left[\prod_{l=1}^n J_{k_l}(\alpha q A_l) \right] \\ & \cdot \exp \left[-\frac{1}{2} \alpha^2 (p^2 + q^2) \sum_{i=1}^n \lambda_i^2 \right] \\ & \cdot \sum_{S_{m+1}, \dots, S_{m+n}=0}^{\infty} \prod_{l=m+1}^{m+n} \{ [S_l!(|k_l| + S_l)!]^{-1} 2^{-|k_l|-2S_l} \\ & \cdot (\alpha^2 p q)^{|k_l| + 2S_l} (\lambda_{l-m}^2)^{[|k_l| + 2S_l]} [\rho_{l-m}(\tau)]^{|k_l| + 2S_l} \}. \end{aligned} \quad (18)$$

Hence, the order of intermodulation is simply $\sum_{l=1}^{m+n} |k_l| + 2 \sum_{l=m+1}^{m+n} S_l$. To find the third-order RF intermodulation power spectrum, only those terms in equations (14) and (18) which satisfy the condition that $\sum_{l=1}^{m+n} |k_l| + 2 \sum_{l=m+1}^{m+n} |S_l| = 3$ must be singled out for Fourier transformation. Since this approach is tedious and time-consuming, especially for a large number of SCPC carriers, the simplified "telescopic" method described in the following section should be used.

The following observations can simplify the intermodulation evaluation. For the FDM/FM carriers used in the INTELSAT network, the modula-

tion indices are close to or greater than unity and the baseband modulating signal can be regarded as a Gaussian process. The power spectral density of the modulated process can be approximated by a Gaussian function. Hence,

$$\begin{aligned} Q_3(\tau) &= \prod_{l=N_2+1}^{N_3} \exp \{ -k_l^2 [R_{\phi_l}(0) - R_{\phi_l}(\tau)] \} \\ &= \exp \left\{ -\sum_{l=N_2+1}^{N_3} k_l^2 [R_{\phi_l}(0) - R_{\phi_l}(\tau)] \right\} \\ &\approx \exp \left[-\sum_{l=N_2+1}^{N_3} k_l^2 2\pi^2 \sigma_l^2 \tau^2 \right] \end{aligned} \quad (19)$$

where σ_l^2 is the multicarrier rms frequency deviation of the l th FDM/FM carrier.

For SCPC/FM carriers without voice activation, the corresponding $Q_i(\tau)$ is more complicated because the power spectral density is not Gaussian shaped, but is rather highly peaked. However, given the measured power spectral density of the SCPC/FM signal, the characteristic function $E[\exp\{jk_l \psi_l(t, \tau)\}]$ can be computed by Fourier transformation; hence,

$$\begin{aligned} Q_i(\tau) &= \prod_{l=1}^{N_i} \exp \{ -k_l^2 [R_{\phi_l}(0) - R_{\phi_l}(\tau)] \} \\ &= \prod_{l=1}^{N_i} \int S_{1_l}(f) e^{j2\pi f k_l \tau} df \end{aligned} \quad (20)$$

where $S_{1_l}(f)$ is the power spectral density of the l th SCPC/FM carrier.

For SCPC/PSK, FDMA or TDMA/PSK, or TV/FM carriers, it can be assumed that the corresponding $Q_2(\tau)$, $Q_4(\tau)$ and $Q_6(\tau)$ can be obtained by Fourier transformation of the measured power spectral density:

$$Q_2(\tau) = \prod_{l=N_1+1}^{N_2} \int S_{2_l}(f) e^{j2\pi f k_l \tau} df \quad (21)$$

$$Q_4(\tau) = \prod_{l=N_3+1}^{N_4} \int S_{4_l}(f) e^{j2\pi f k_l \tau} df \quad (22)$$

$$Q_6(\tau) = \prod_{l=N_4+1}^{N_5} \int S_{6_l}(f) e^{j2\pi f k_l \tau} df \quad (23)$$

The power spectral density of the third-order intermodulation can be found as follows:

$$\begin{aligned}
 S_3^0(f) &\equiv F[R_3^0(\tau)] \\
 &= \frac{1}{2} \operatorname{Re} \sum_{k_1, k_2, \dots, k_{m+n} = -\infty}^{\infty \dagger} \sum_{p=1}^L \sum_{q=1}^L b_p b_q^* \left[\prod_{l=1}^m J_{k_l}(\alpha p A_l) \right] \\
 &\cdot \left[\prod_{l=1}^m J_{k_l}(\alpha q A_l) \right] \exp \left[-\frac{1}{2} \alpha^2 (p^2 + q^2) \sum_{i=1}^n \lambda_i^2 \right] \\
 &\cdot \sum_{l_1, l_2, \dots, l_n = 0}^{\infty} \left[\prod_{i=1}^n \frac{(\lambda_{m+i}^2 \alpha^2 p q / 2)^{2l_i + |k_{m+i}|}}{l_i! (l_i + |k_{m+i}|)!} \right] \\
 &\cdot F \left\{ \prod_{i=1}^n [\rho_i(\tau)]^{2l_i + |k_{m+i}|} \right\} \\
 &\otimes F[Q_1(\tau)] \otimes F[Q_2(\tau)] \otimes F[Q_3(\tau)] \otimes F[Q_4(\tau)] \otimes F[Q_5(\tau)] \\
 &\otimes F \left\{ \exp \left[j\omega_0 \tau + j \sum_{i=1}^{m+n} k_i \omega_i \tau \right] \right\} \quad (24)
 \end{aligned}$$

where $F[\cdot]$ and \otimes denote the Fourier transformation and convolution, respectively. The dagger (\dagger) on the summation sign denotes that the summation is taken over the additional constraint that

$$\sum_{i=1}^{m+n} |k_i| + 2 \sum_{i=1}^n |l_i| = 3 \quad .$$

The Fourier transforms $F[Q_1(\tau)]$, $F[Q_2(\tau)]$, $F[Q_4(\tau)]$, and $F[Q_5(\tau)]$ can be found by using convolutions in the frequency domain of the corresponding measured power spectrum. The Fourier transform $F[Q_3(\tau)]$ can be found by using a Gaussian power spectral density with a total mean square deviation equal to the sum of the individual mean square deviations of the FDM/FM carriers.

Special care must be taken in the evaluation of the partially coherent 2A-B type intermodulation products where A is a QPSK signal. If $S(f)$ is the measured power spectrum of the QPSK signal $x(t) = \cos[\omega_c t + \phi(t)]$, where $\phi(t)$ is the 4-phase modulating process, then the power spectrum of the signal representing 2A is the power spectrum of $y(t) = \cos[2\omega_c t + 2\phi(t)]$. Thus, $y(t)$ is effectively a 2-phase PSK signal centered around $2\omega_c$, with a shape identical to that of the QPSK signal $x(t)$.

Similarly, if $S'(f)$ is the measured power spectrum of the SCPC/FM/TV signal represented by $x'(t) = \cos[\omega_c t + \phi'(t)]$, where $\phi'(t)$ is the baseband

modulating process, then the power spectrum of signal representing 2A is the power spectrum of $y'(t) = \cos[2\omega_c t + 2\phi'(t)]$. Thus the measured power spectrum of $y'(t)$ is needed for SCPC/FM or FM/TV. However, for FDMA/FM/FDM signals, the power spectrum of 2A can be easily obtained from that of A by simply increasing the variance of the Gaussian-shaped power spectrum representing A by a factor of 4.

Baseband third-order intermodulation power spectral density for FM carriers

The output signal, $e_o(t)$, in equation (3) contains the desired carriers, the intermodulation products, and other cross-modulation terms. Without loss of generality, the carrier at $\omega_0 + \omega_1$ can be assumed to be the desired signal; the output of the nonlinear amplifier around the desired signal and including the desired signal can be written as [11]

$$\begin{aligned}
 e_{o1}(t) &= \operatorname{Re} \{ \exp [j(\omega_0 + \omega_1) t + j\phi_1(t)] M_o \} \\
 &+ \operatorname{Re} \{ \exp [j(\omega_0 + \omega_1) t + j\phi_1(t)] [M(1, 0, \dots, 0; t) - M_o] \} \\
 &+ \operatorname{Re} \left\{ \exp (j\omega_0 t) \sum_{k_1, k_2, \dots, k_{m+n} = -\infty}^{\infty \prime} \exp \left[j \sum_{l=1}^{m+n} k_l \omega_l t \right] \right. \\
 &\cdot \exp \left[j \sum_{l=1}^m k_l \phi_l(t) \right] M(k_1, k_2, \dots, k_{m+n}; t) \\
 &\left. \cdot \exp \left[j \sum_{l=m+1}^{m+n} k_l \phi_l(t) \right] \right\} \quad (25)
 \end{aligned}$$

where the prime denotes that the term corresponding to $k_1 = 1, k_l = 0$ for all $l \neq 1$, and

$$\begin{aligned}
 M(1, 0, \dots, 0; t) &\equiv \sum_{p=1}^L b_p J_1(\alpha p A_1) \left[\prod_{l=2}^m J_0(\alpha p A_l) \right] \\
 &\cdot \left[\prod_{l=m+1}^{m+n} J_0 \{ \alpha p \gamma_l(t) \} \right] \quad (26)
 \end{aligned}$$

$$\begin{aligned}
 M_o &\equiv \langle E[M(1, 0, \dots, 0; t)] \rangle \\
 &= \sum_{p=1}^L b_p J_1(\alpha p A_1) \left[\prod_{l=2}^m J_0(\alpha p A_l) \right] \left[\prod_{l=m+1}^{m+n} \langle E\{J_0[\alpha p \gamma_l(t)]\} \rangle \right] \\
 &= \sum_{p=1}^L b_p \exp \left(-\frac{1}{2} \alpha^2 p^2 \sum_{i=1}^n \lambda_i^2 \right) J_1(\alpha p A_1) \prod_{l=2}^m J_0(\alpha p A_l) \quad (27)
 \end{aligned}$$

$$M(k_1, k_2, \dots, k_{m+n}; t) \equiv \sum_{p=1}^L b_p \left[\prod_{i=1}^m J_{k_i}(\alpha p A_i) \right] \cdot \left[\prod_{i=m+1}^{m+n} J_{k_i}(\alpha p \gamma_i(t)) \right] \quad (28)$$

$$\gamma_i(t) \equiv [\eta_{ic}^2(t) + \eta_{io}^2(t)]^{1/2}, l = m + 1, m + 2, \dots, m + n \quad (29a)$$

$$\phi_l(t) \equiv \tan^{-1} \left[\frac{\eta_{is}(t)}{\eta_{ic}(t)} \right], l = m + 1, m + 2, \dots, m + n \quad (29b)$$

Following the same representation used in Reference 11, equation (24) can be written as

$$e_{o1}(t) \equiv \text{Re}\{\exp[j(\omega_0 + \omega_1)t + j\phi_1(t)] \cdot M_o[1 + R(t) + I(t)]\} \quad (30)$$

where $R(t) + jI(t)$ represents the total distortion for the pure signal component at the nonlinear amplifier output. Since the distortion for all practical systems is usually much smaller than the desired signal, *i.e.*, $|R(t) + jI(t)| \ll 1$, the baseband phase distortion in the desired carrier can be written as

$$D(t) \equiv \tan^{-1} \frac{I(t)}{1 + R(t)} \approx I(t) \quad (31)$$

where $I(t) \equiv \text{Im } M_o^{-1}[M(1, 0, \dots, 0; t) - M_o]$

$$+ \text{Im} \left\{ M_o^{-1} \sum_{k_1, k_2, \dots, k_{m+n} = -\infty}^{\infty} \exp \left[-j\omega_1 t + j \sum_{i=1}^{m+n} k_i \omega_i t \right] \cdot \exp \left[j(k_1 - 1) \phi_1(t) + j \sum_{i=2}^{m+n} k_i \phi_i(t) \right] \cdot M(k_1, k_2, \dots, k_{m+n}; t) \right\} \quad (32)$$

The power spectral density, $S_d(f)$, of the baseband frequency distortion can be found by obtaining the autocorrelation function, $R_I(\tau)$, of $I(t)$, since

$$S_d(f) = f^2 S_D(f) \quad (33)$$

and

$$S_D(f) \equiv F\{\langle E[D(t + \tau) D(t)] \rangle\} \approx F\{\langle E[I(t + \tau) I(t)] \rangle\} \equiv F\{R_I(\tau)\} \quad (34)$$

In Appendix B, the autocorrelation function, $R_I(\tau)$, has been derived, namely,

$$R_I(\tau) = \sum_{l_1, l_2, \dots, l_n = 0}^{\infty} [\text{Im}\{N(1, 0, \dots, 0; l_1, l_2, \dots, l_n)\}]^2 \cdot \prod_{i=1}^n [\rho_i(\tau)]^{2l_i} + \frac{1}{2} \text{Re} \sum_{k_1, k_2, \dots, k_{m+n} = -\infty}^{\infty} \{ |N(k_1, k_2, \dots, k_{m+n}; l_1, l_2, \dots, l_n)|^2 \cdot \Delta(k_1, k_2, \dots, k_{m+n}; \tau) + |N(2 - k_1, k_2, \dots, k_{m+n}; l_1, l_2, \dots, l_n)|^2 \cdot \Delta^*(k_1, k_2, \dots, k_{m+n}; \tau) + (-1)^{k_1} N(k_1, k_2, \dots, k_{m+n}; l_1, l_2, \dots, l_n) \cdot N(2 - k_1, k_2, \dots, k_{m+n}; l_1, l_2, \dots, l_n) \cdot \Delta(k_1, k_2, \dots, k_{m+n}; \tau) + (-1)^{k_1} N(2 - k_1, k_2, \dots, k_{m+n}; l_1, l_2, \dots, l_n) \cdot N(k_1, k_2, \dots, k_{m+n}; l_1, l_2, \dots, l_n) \cdot \Delta^*(k_1, k_2, \dots, k_{m+n}; \tau) \} \quad (35)$$

where

$$N(k_1, k_2, \dots, k_{m+n}; l_1, l_2, \dots, l_n) \equiv M_o^{-1} \sum_{i=1}^L b_p \left[\prod_{i=1}^m J_{k_i}(\alpha p A_i) \right] \exp \left[-\frac{1}{2} \alpha^2 p^2 \sum_{i=1}^n \lambda_i^2 \right] \cdot \left[\prod_{i=1}^n \frac{(\alpha_i^2 \lambda_i^2 p^2 / 2)^{2l_i + |k_{m+i}|}}{l_i! (l_i + |k_{m+i}|)!} \right]^{1/2} \quad (36)$$

$$\Delta(k_1, k_2, \dots, k_{m+n}; \tau)$$

$$\begin{aligned} &\equiv \left\langle E \left\{ \exp \left[j(k_1 - 1) \psi_1(t, \tau) + j \sum_{i=2}^m k_i \psi_i(t, \tau) \right] \right\} \right\rangle \\ &\cdot \exp \left[j(k_1 - 1) \omega_1 \tau + j \sum_{i=2}^{m+n} k_i \omega_i \tau \right] \prod_{i=1}^n [\rho_i(\tau)]^{2l_i + k_{m+i}} \end{aligned} \quad (37)$$

$$\Delta(k_1, k_2, \dots, k_{m+n}; \tau)$$

$$\begin{aligned} &= \left[\prod_{i=1}^5 Q_i(\tau) \right] \exp \left[j(k_1 - 1) \omega_1 \tau + j \sum_{i=2}^{m+n} k_i \omega_i \tau \right] \\ &\cdot \prod_{i=1}^n [\rho_i(\tau)]^{2l_i + k_{m+i}} \end{aligned} \quad (38)$$

The $Q_i(\tau)$ in equation (38) have been defined in equation (16) according to carrier types. When $n = 1$ and $m = m' - 1$, equations (35) through (38) can be reduced to equations (34) through (36) in Reference 11, as expected. Therefore, the baseband power spectral density, $S_{\Delta\nu}(f)$, of the ν th-order intermodulation can be found by using equations (33) through (38) and by singling out the terms in equation (35) that satisfy

$$\sum_{i=1}^{m+n} |k_i| + 2 \sum_{i=1}^n |l_i| = \nu \quad (39)$$

However, this is again tedious and time-consuming. For a large number of SCPC carriers, approximations similar to those explained in the section entitled "Baseband Third-Order Intermodulation for SCPC/FM Carriers" may be used. For a moderate number of carriers, equations (35) through (38) can be implemented by extending the capability of the CIA4 program.

RF third-order intermodulation power spectral density for SCPC carriers

A hypothetical frequency plan for mixed SCPC/FM, SCPC/PSK, and FDM/FM operation in a 36-MHz transponder is shown in Figures 2 and 3. The spiked nature of the SCPC/FM power spectra may produce highly peaked intermodulation products if the SCPC/FM carriers are equally spaced. These spiked intermodulation products may create a baseband distortion which is significantly different from that produced by a uniform

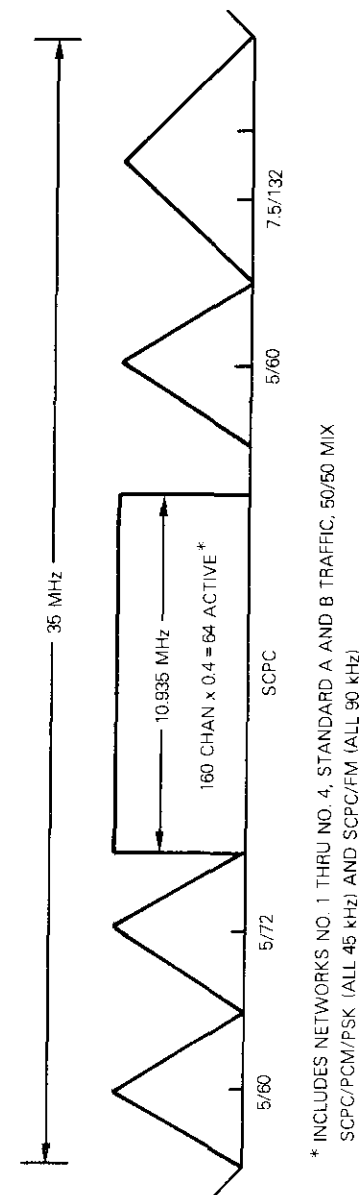
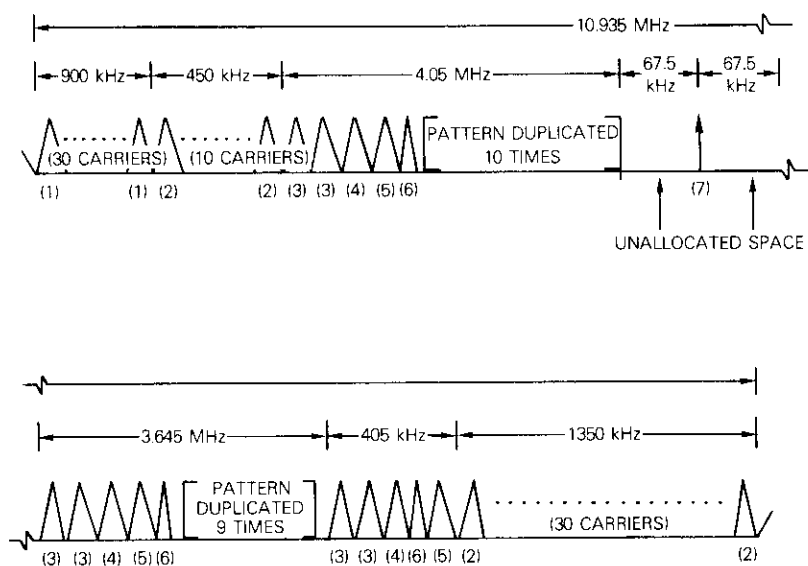


Figure 2. Transponder Carrier Configuration



* NOTE THAT THE FREQUENCY PLAN SHOWS THE AVAILABLE CHANNEL BANDWIDTH SLOTS. NOT ALL OF THE SLOTS ARE OCCUPIED SIMULTANEOUSLY. AN ACTIVITY FACTOR OF 40% FOR 160 CHANNELS WAS ASSUMED.

- (1) 45 kHz SCPC/PCM/PSK - STANDARD A TO B
- (2) 45 kHz SCPC/PCM/PSK - STANDARD B TO B
- (3) 90 kHz SCPC/FM - STANDARD B TO B
- (4) 90 kHz SCPC/FM - STANDARD A TO B
- (5) 90 kHz SCPC/FM - STANDARD B TO A
- (6) 45 kHz SCPC/PCM/PSK - STANDARD B TO A
- (7) UNMODULATED PILOT FREQUENCY

Figure 3. Frequency Plan for Networks with 50-Percent SCPC/PCM/PSK and 50-Percent SCPC/FM

band of thermal noise. A "telescopic" approach, based on the results presented in the preceding section, is proposed to evaluate the RF third-order intermodulation power spectral density for the SCPC/FM or SCPC/PSK carriers in the hypothetical frequency plan shown in Figures 2 and 3. This method consists of two steps:

a. *Gross Intermodulation Computation.* One or more band(s) of SCPC carriers, FM and/or PSK, shown in Figure 2 are first replaced by

one or more bands of equivalent thermal noise with the same amount of RF power by assuming a certain voice activity factor for the SCPC carriers. The third-order intermodulation power spectral density in terms of dB/MHz, excluding the intermodulation products generated solely by the noise band(s) or equivalently solely by the SCPC carriers, can be evaluated with the CIA4 Program or the PRIME software. That is, this step computes only the third-order intermodulation between FDM/FM, PSK/FDMA, PSK/TDMA, and/or the SCPC carriers, with the latter regarded as a band(s) of equivalent thermal noise. If there are no SCPC carriers, this step can be omitted.

b. *Macroscopic Intermodulation Computation.* Since the intermodulation products in the *gross* step are only for relatively large carriers (at least 1.25 MHz as opposed to 90 or 45 kHz) or the band(s) of SCPC carriers regarded as equivalent thermal noise, the power spectral density is relatively flat or constant in the entire RF bandwidth of any particular SCPC carrier. Therefore, the third-order intermodulation power spectral density in the *gross* step can be considered flat in the particular SCPC carrier and can be regarded as an equivalent thermal noise with the same power spectral density. This *macroscopic* step (b) closely examines the RF third-order intermodulation generated between the SCPC carriers themselves.

Since there are m_1 SCPC/FM and m_2 SCPC/PSK carriers, the third-order intermodulation between the SCPC carriers themselves can be evaluated from equations (14), (16), and (18) by setting $k_l = 0$ for all $l > N_2 \equiv m_1 + m_2$ and singling out terms satisfying $\sum_{i=1}^{N_2} |k_i| = 3$. That is,

$$R_3^0(\tau) \equiv \frac{1}{2} \operatorname{Re} \sum_{k_1, k_2, \dots, k_{m+n} = -\infty}^{\infty} Q_1(\tau) Q_2(\tau) \cdot H(k_1, k_2, \dots, k_{N_2}, 0, 0, \dots, 0; \tau) \exp \left[j\omega_0\tau + j \sum_{i=1}^{N_2} k_i \omega_i \tau \right] \quad (40)$$

where the triple primes denote that the summation is taken under the condition $\sum_{i=1}^{N_2} |k_i| = 3$ and $k_l = 0$, for all $l > N_2$, and $H(k_1, k_2, \dots, k_{N_2}, 0, 0, \dots, 0; \tau)$

$$\equiv \left| \sum_{p=1}^L b_p \left[\prod_{i=1}^N J_{k_i}(\alpha p A_i) \right] \left[\prod_{i=N_2+1}^m J_0(\alpha p A_i) \right] \exp \left[-\frac{1}{2} \alpha^2 p^2 \sum_{i=1}^n \lambda_i^2 \right] \right|^2 \equiv |N(k_1, k_2, \dots, k_{N_2}, 0, 0, \dots, 0; 0, 0, \dots, 0)|^2 \quad (41)$$

Therefore, the power spectral density of the third-order intermodulation between the SCPC carriers themselves can be found by using the Fourier transform of $R_3^0(\tau)$,

$$S_3^0(f) \equiv F\{R_3^0(\tau)\} \quad (42)$$

However, since many of these third-order intermodulation products will fall outside the band(s) of SCPC carriers and even more will fall outside the channel bandwidth of a particular (e.g., worst-case) SCPC carrier, it is not necessary to generate all the third-order intermodulation products from equations (40) through (42). Only the intermodulation products falling into the band(s) of SCPC carriers or onto a particular SCPC carrier need to be generated. The PRIME software can be used to generate only those third-order intermodulation products which will have contributions within the frequency bounds specified by the user. These generated intermodulation products will be sorted according to type (i.e., $A + B - C$ or $2A - B$) and their contributors (i.e., the particular combination of SCPC/FM and SCPC/PSK carriers), since the power level and spectral shape of these intermodulation products are generally not the same. The sorted intermodulation products will be combined within the frequency range set by the user to produce the resultant intermodulation power spectral density. This third-order intermodulation power spectral density will then be added to that generated under the *gross* step. The final added power spectral density will be the desired third-order intermodulation power spectral density within the frequency range specified by the user.

Baseband third-order intermodulation for SCPC/FM carriers

As noted in the Subsection entitled "Baseband third-order intermodulation power spectral density for FM carriers," the baseband third-order intermodulation evaluation of equations (33) through (38) for SCPC/FM carriers can be extremely tedious and time consuming. In this "telescopic" approach, the baseband third-order intermodulation power spectrum due to carriers other than purely SCPC carriers can be easily computed from the *gross* step. The additional third-order intermodulation power spectrum purely due to SCPC carriers falling on a particular SCPC/FM carrier* can

*Without loss of generality, the carrier centered at $\omega_0 + \omega_1$ is assumed to be the one of interest.

be evaluated in the *macroscopic* step from equations (33) through (38).

Since only the third-order intermodulation between SCPC carriers themselves is of interest, the first summation in equation (35) does not contain third-order intermodulation and the second summation in equation (35) should be taken under the additional constraint that $\sum_{l=1}^{N_2} |k_l| = 3$ and $k_l = 0$, for all $l > N_2$. Namely,

$$\begin{aligned} R_{SCPC}(\tau) \equiv & \frac{1}{2} \operatorname{Re} \sum_{k_1, k_2, \dots, k_{N_2} = + - \infty}^{\infty} \{ \\ & |N(k_1, k_2, \dots, k_{N_2}, 0, \dots, 0; 0, 0, \dots, 0)|^2 \\ & \cdot \Delta(k_1, k_2, \dots, k_{N_2}, 0, 0, \dots, 0; \tau) \\ & + |N(2 - k_1, k_2, \dots, k_{N_2}, 0, \dots, 0; 0, 0, \dots, 0)|^2 \\ & \cdot \Delta^*(k_1, k_2, \dots, k_{N_2}, 0, 0, \dots, 0; \tau) \\ & + (-1)^{k_1} N(k_1, k_2, \dots, k_{N_2}, 0, 0, \dots, 0; 0, 0, \dots, 0) \\ & \cdot N(2 - k_1, k_2, \dots, k_{N_2}, 0, 0, \dots, 0; 0, 0, \dots, 0) \\ & \cdot \Delta(k_1, k_2, \dots, k_{N_2}, 0, 0, \dots, 0; \tau) \\ & + (-1)^{k_1} N(2 - k_1, k_2, \dots, k_{N_2}, 0, 0, \dots, 0; 0, 0, \dots, 0) \\ & \cdot N(k_1, k_2, \dots, k_{N_2}, 0, 0, \dots, 0; 0, 0, \dots, 0) \\ & \cdot \Delta^*(k_1, k_2, \dots, k_{N_2}, 0, 0, \dots, 0; \tau) \} \quad (43) \end{aligned}$$

where the summation is taken under the additional constraint that $\sum_{l=1}^{N_2} |k_l| = 3$, $k_l = 0$ for all $l > N_2$, and

$$\begin{aligned} & N(k_1, k_2, \dots, k_{N_2}, 0, \dots, 0; 0, 0, \dots, 0) \\ & \equiv M_0^{-1} \sum_{p=1}^L b_p \left[\prod_{l=1}^{N_2} J_{k_l}(\alpha p A_l) \right] \left[\prod_{l=N_2+1}^m J_0(\alpha p A_l) \right] \\ & \cdot \exp \left[-\frac{1}{2} \alpha^2 p^2 \sum_{i=1}^n \lambda_i^2 \right] \quad (44) \end{aligned}$$

$$\begin{aligned} & \Delta(k_1, k_2, \dots, k_{N_2}, 0, 0, \dots, 0; \tau) \\ & \equiv Q_1(\tau) Q_2(\tau) \exp \left[j(k_1 - 1) \omega_1 \tau + j \sum_{l=1}^{N_2} k_l \omega_l \tau \right] \quad (45) \end{aligned}$$

Thus, Fourier transformation of equation (43) will produce the desired

third-order intermodulation between the SCPC carriers in the particular SCPC/FM carrier with center frequency at $\omega_0 + \omega_1$. That is,

$$S_{SCPC}(f) = f^2 F[R_{SCPC}(t)] \quad (46)$$

Since only the baseband of the particular SCPC/FM carrier centered at frequency $\omega_0 + \omega_1$ is being considered, only those third-order intermodulation products falling into the baseband of this particular carrier must be evaluated. The computed third-order intermodulation power spectral density is then combined with the baseband equivalent of the RF third-order intermodulation generated by the *gross* step to produce the overall baseband power spectral density.

RF and baseband intermodulation power spectral density for carriers other than SCPC

As indicated previously, there are m_3 FDM/FM, m_4 FDMA or TDMA/PSK, m_5 TV/FM, and m_6 unmodulated CW carriers. The RF third-order intermodulation power spectral density can be obtained by first using the *gross* step to include all third-order intermodulation products except those created purely by SCPC carriers, and then by using the *macroscopic* step to include the intermodulation products generated between carriers themselves falling into the desired non-SCPC carrier within the frequency range specified by the user. The sum of the power spectral densities generated by these two steps will give the desired overall third-order intermodulation power spectral density.

These two steps can be bypassed for those carriers that are unaffected by the intermodulation generated between the SCPC carriers themselves. The band(s) of SCPC carriers should be replaced with the band(s) of noise, and then the third-order intermodulation falling into the desired carrier should be directly evaluated, including the intermodulation products generated purely by the SCPC carriers.

The baseband third-order intermodulation power spectral density for FDM/FM and TV/FM carriers can be found by using the same method that was used for SCPC/FM. However, in many applications in which the desired carrier is only slightly affected by the SCPC carriers, *gross* and *macroscopic* steps can be bypassed. The baseband third-order intermodulation should be evaluated directly from the carrier configuration by regarding the band(s) of SCPC carriers as equivalent band(s) of noise, including the third-order intermodulation products due to the SCPC carriers themselves.

Baseband S/N and NPR for FM carriers

In the computations of the baseband signal-to-noise (S/N) ratio of the SCPC/FM carriers, let the test tone be represented by

$$x(t) \equiv \Delta f \cos \omega_m t \quad (47)$$

and the FM modulated carrier by this test tone be represented by

$$y(t) \equiv A \cos (\omega_0 t + \beta \sin \omega_m t) \quad (48)$$

where A is the amplitude of the FM carrier and $\beta = \Delta f/\omega_m$ is the modulation index. Also, let the 2-sided power spectral density, $S_\phi(f)$, of the baseband distortion due to intermodulation be $f^2 S_\phi(f)$. Then the demodulated S/N is

$$S/N = \frac{A^2(\Delta f)^2/2}{\int_{-b}^b f^2 S_\phi(f) df} \quad (49)$$

where $2b$ is the baseband bandwidth. To derive equation (49), it is assumed that the carrier-to-intermodulation power ratio is high enough for the demodulator to be operated above the threshold and that the intermodulation noise can be regarded as Gaussian noise for analysis.

If psophometric weighting $P(f)$ and de-emphasis network $W(f)$ are used, then

$$S/N_w = \frac{A^2(\Delta f)^2/2}{\int_{-b}^b f^2 S_\phi(f) P(f) W(f) df} \quad (50)$$

for SCPC/FM. The weighting function $W(f)$ can be obtained from the C.C.I.R. reference book.

For FDM/FM carriers, the baseband intermodulation power spectral density is relatively flat, and may be assumed to be constant in the 4-kHz channel of interest for many applications. Hence, according to Reference 18,

$$S/N_{jam} = \left[\frac{C}{N} \right] \frac{B}{b} \left[\frac{f_r}{f_m} \right]^2 PW \quad (51)$$

$$B = 2[3.16 g f_r + f_m] \quad (52)$$

where S/N_{fdm} = weighted S/N at the 0-dBm0 test-tone level

$[C/N]$ = carrier-to-noise ratio over the Carson's Rule bandwidth, B

b = channel bandwidth = 3.1 kHz

f_r = rms test-tone deviation (kHz)

f_m = top baseband frequency $\simeq 4.2 \times n$ (kHz)

n = number of baseband channels

P = psophometric weighting factor = 2.5 dB

W = pre-emphasis gain = 4 dB

$g = 10^{-(L/20)}$

$L = -15 + 10 \log n, \quad n \geq 240$ channels

$= -1 + 4 \log n, \quad n < 240$ channels .

However, for FDM/FM carriers which are affected by the third-order intermodulation between SCPC carriers themselves, the baseband intermodulation power spectral density may be highly peaked due to the intermodulation products generated purely by SCPC/FM carriers. Consequently, certain baseband channels may experience significantly more degradation than others. Equations (51) and (52) can no longer be applied. Instead, the following relationship should be employed:

$$S/N_w = \frac{\beta_{rms}^2 f_h^2 P(f_t) W(f_t)}{(f_h - f_l) f_l^2 S_\phi(f_l)}$$

where β_{rms} = rms modulation index of the desired signal

f_h = highest baseband channel frequency

f_l = lowest baseband channel frequency

f_t = midfrequency of baseband channel under consideration

$P(f)$ = frequency response of pre-emphasis network

$W(f)$ = psophometric weighting function.

The baseband S/N can be converted to NPR in terms of picowatts referring to a 0-dBm0 test tone.

PRIME software and illustrative examples

PRIME software, which is designed to compute the third-order RF and baseband intermodulation between an arbitrary mix of SCPC/FM, SCPC/PSK, FDM/FM, TV/FM, FDMA or TDMA/PSK, and CW carriers and one or more bands of thermal noise (see Figure 1), has the following capabilities:

a. The memoryless nonlinear amplifier can have arbitrary amplitude and phase characteristics that do not have discontinuous derivatives.

b. As many as 110 carriers can be handled as inputs to the nonlinear amplifier.

c. The power spectral densities of the RF and baseband third-order intermodulation can be generated for a wide range of carrier combinations. However, for TV/FM and FDMA or TDMA/PSK carriers, the measured power spectral densities must be given as input data. The baseband power spectral density of the third-order intermodulation is computed only for SCPC/FM and FDM/FM carriers, but the RF third-order intermodulation power spectral density is computed for all carriers.

d. One or more bands of thermal noise can be incorporated.

e. The third-order intermodulation products can be generated, sorted, and categorized according to intermodulation frequencies, types, and levels.

f. C/N in dB is calculated for all carrier types, whereas S/N in dB and noise power in picowatts due to intermodulation are computed for SCPC/FM and FDM/FM carriers.

g. The RF and baseband intermodulation power spectral densities can be listed and/or written on a data set to be plotted by SPEAKEZ.

h. The effect of FM or PSK receiver filters on the RF intermodulation power spectral density has been included.

i. The identification number, carrier frequency, carrier levels at the input and output of the nonlinear amplifier and carrier phases can be listed.

j. The maximum number of intermodulation products that can be sorted is about 3,000.

k. The third-order intermodulation power spectral densities in a specific frequency range specified by the user or in a specific carrier can be calculated and listed or plotted by SPEAKEZ.

With these capabilities the current version of PRIME can be regarded as an extension of the CIA4 Program.

Four numerical examples are provided to illustrate the use of the

PRIME software. The first three examples deal with the hypothetical carrier configuration shown in Figure 4. The fourth example deals with the power spectral density of intermodulation in a mixed FM/FDM and FDMA/PSK transponder. Each example will focus on the SCPC/FM, SCPC/PSK, FDM/FM, and PSK/FDMA carriers, respectively.

Example 1. RF and baseband third-order intermodulation in SCPC/FM carriers

In the hypothetical frequency plan in Figure 4, a total of 160 SCPC channels plus an unmodulated pilot tone are assigned to a 10,935-MHz frequency band. Of these 160 SCPC channels, 80 are for SCPC/FM and the other 80 are for SCPC/PSK carriers. They are arranged as shown in Figure 3. The SCPC/FM and SCPC/PSK carriers are allocated 90- and 45-kHz slots, respectively. Because of their higher power level (-28.3 -dB input level with respect to single-carrier saturation of the satellite TWTA), the SCPC/PSK carriers transmitted into a standard B earth station from either a standard A or a standard B earth station are placed at the edges of the 10.935-MHz band. The remaining 80 SCPC/FM and 20 SCPC/PSK carriers are assigned with four SCPC/FM carriers followed by one SCPC/PSK carrier. The input levels of SCPC/FM carriers are -36.1 dB relative to single-carrier saturation of the satellite TWTA regardless of whether they are transmitted into a standard A or standard B earth station. The input level of an SCPC/PSK carrier transmitted into a standard A earth station is -35.1 dB relative to the single-carrier saturation level of the TWTA. These input levels are computed based upon the assumption that 40 percent of the SCPC/PSK carriers and 40 percent of the SCPC/FM carriers are active at any given time and, when compared with the other FDM/FM carriers, will yield a -10 -dB total input backoff. The carrier parameters are shown in Table 1.

With a 40-percent voice activity factor, a worst-case carrier configuration of the third-order intermodulation products between SCPC carriers may resemble Figure 5. There are 30 SCPC/FM carriers and 34 SCPC/PSK carriers plus one pilot tone with input levels given in Table 1.

Figure 6 shows the measured power spectral densities without energy dispersion techniques in the SCPC/FM carriers; Figure 7 shows the power spectral density of the SCPC/PSK carriers. These data can be input to the PRIME software to evaluate the RF and baseband third-order intermodulation falling onto any of the SCPC/FM carriers. The power spectral densities for the FDM/FM carriers are automatically determined because Gaussian-shaped power spectral densities have been assumed in the PRIME software.

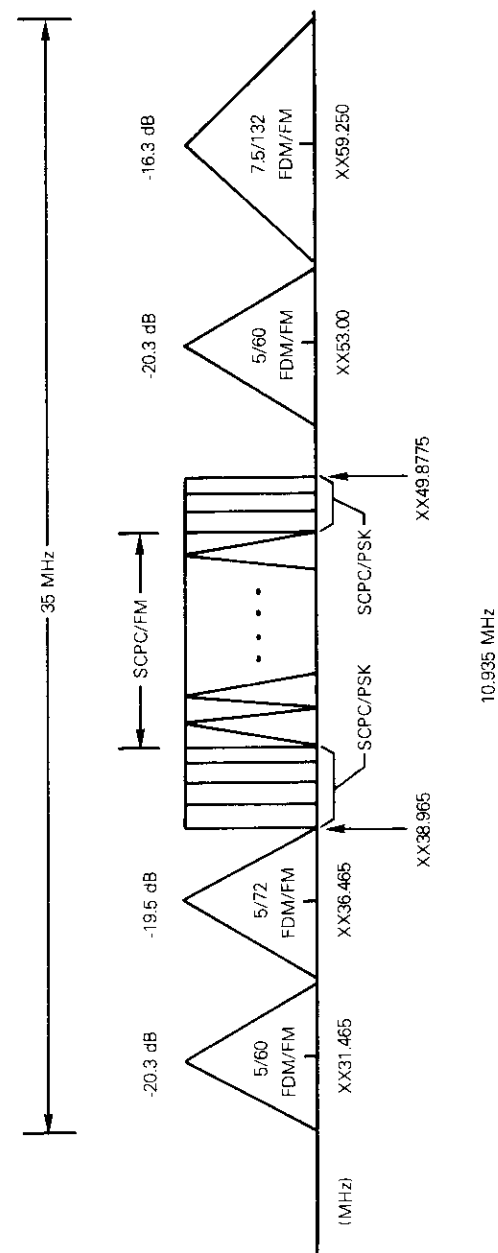


Figure 4. Frequency Plan for Examples 1, 2, and 3

TABLE 1. EARTH STATION E.I.R.P. AND TRANSPONDER INPUT BACKOFFS FOR CARRIERS IN FIGURE 3

Carrier	Earth Station e.i.r.p. (dBW)	Carrier Input Backoff ^a (dB)
5/60 (MHz/ch)	77.8	-20.3
5/72 (MHz/ch)	78.6	-19.5
7.5/132 (MHz/ch)	81.8	-16.3
SCPC/FM (all cases)	62.0	-36.1 ^b
SCPC/PSK (A to B and B to B)	69.8	-28.3 ^b
SCPC/PSK (B to A)	63.0	-35.1 ^b

^a The total e.i.r.p. is 88.1 dBW. Input backoff is based upon a -10-dB total input backoff (with respect to single-carrier saturation of the satellite TWT).

^b Includes a 40-percent activity factor.

For the RF and baseband intermodulation power spectral densities at XX41.755 MHz, the computed RF and baseband intermodulation power spectral densities can be illustrated by using SPEAKEZ on a CRT terminal as shown in Figures 8 and 9, respectively. Clearly, as expected, these power spectral densities are rather peaked. The resulting baseband S/N and NPR have also been computed. When there is FM receive predetection filtering, the S/N and NPR are 57.9 dB and 1640 pW0p, respectively.

Example 2. RF third-order intermodulation in SCPC/PSK carriers

This example uses the same carrier configuration and transmission parameters as example 1 to evaluate the third-order RF intermodulation power spectral densities in the SCPC/PSK carriers whereby the link degradation and/or the bit-error rate can be evaluated. Again the emphasis is on the XX39.6075-MHz to XX39.8075-MHz frequency range around the desired carrier at XX39.7075 MHz. The computed RF third-order power spectral density is shown in Figure 10. For this example, the carrier-to-intermodulation noise ratio at the SCPC/PSK demodulator is 30.7 dB.

Example 3. RF and baseband intermodulation in FDM/FM carriers

Based on the carrier configuration and transmission parameters used in Example 1, this example evaluates the RF and baseband third-order intermodulation falling into a desired FDM/FM carrier. For FDM/FM car-

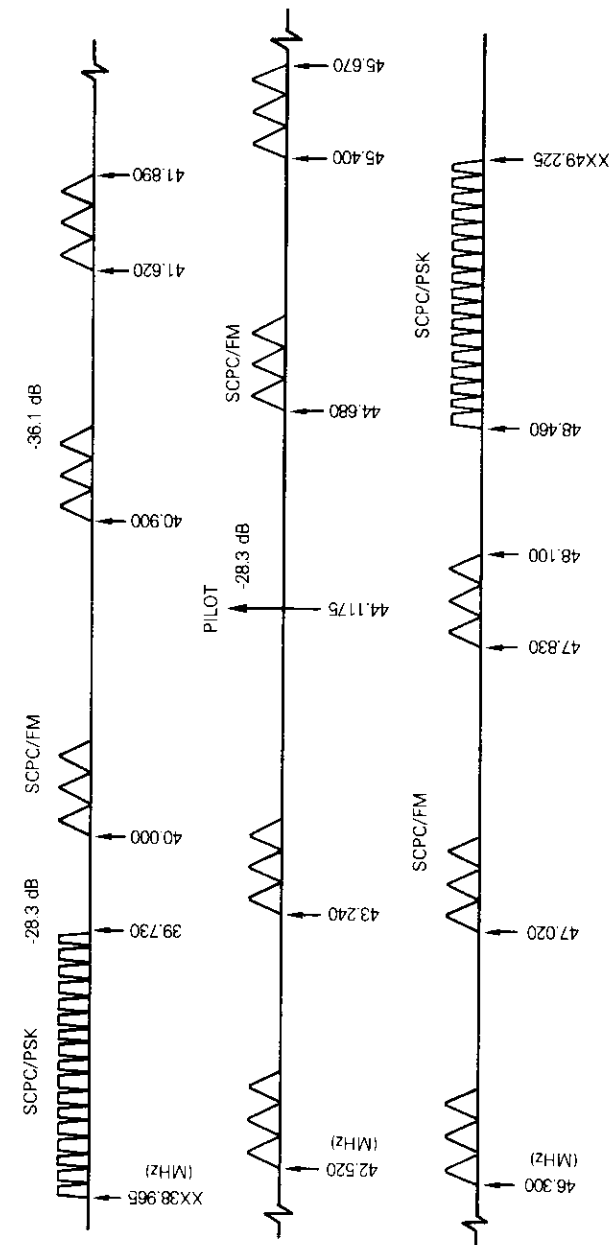


Figure 5. Frequency Plan for SCPC Carriers for Example 1

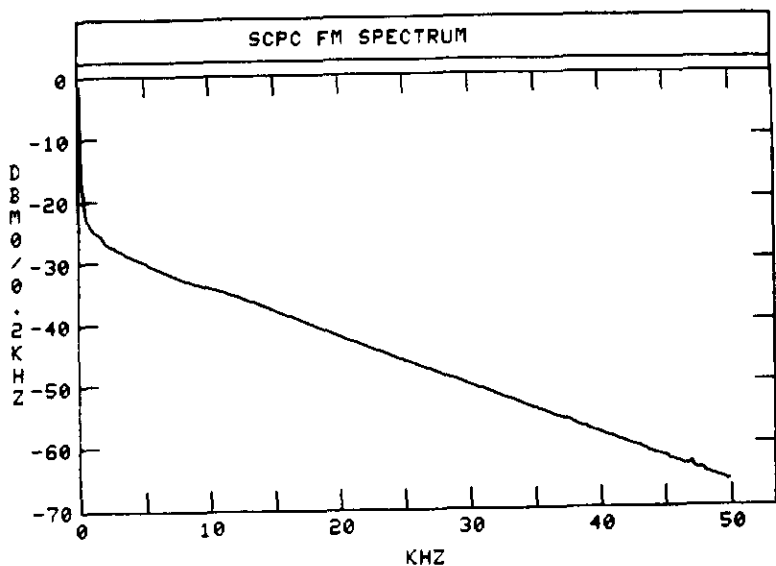


Figure 6. Power Spectral Density of SCPC/FM Carriers

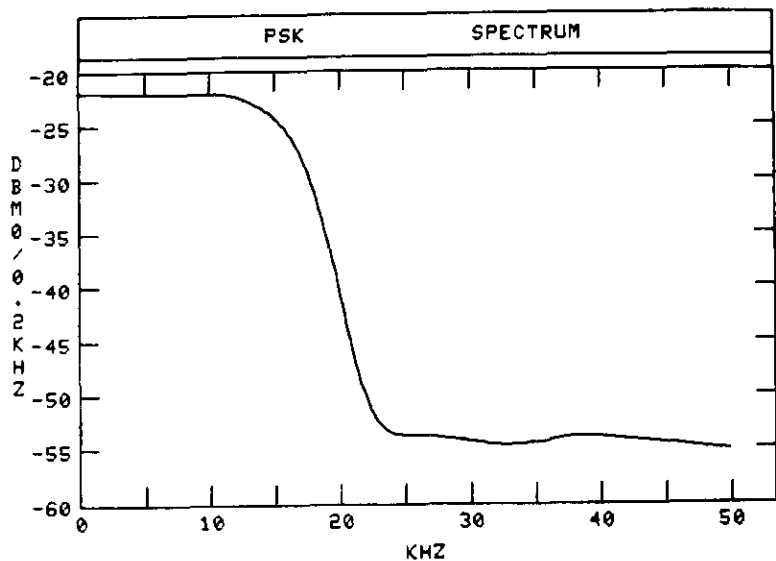
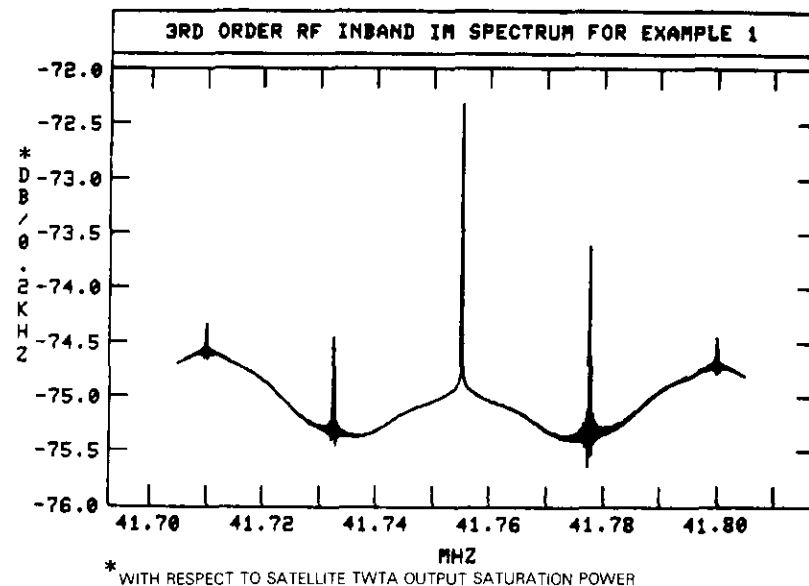
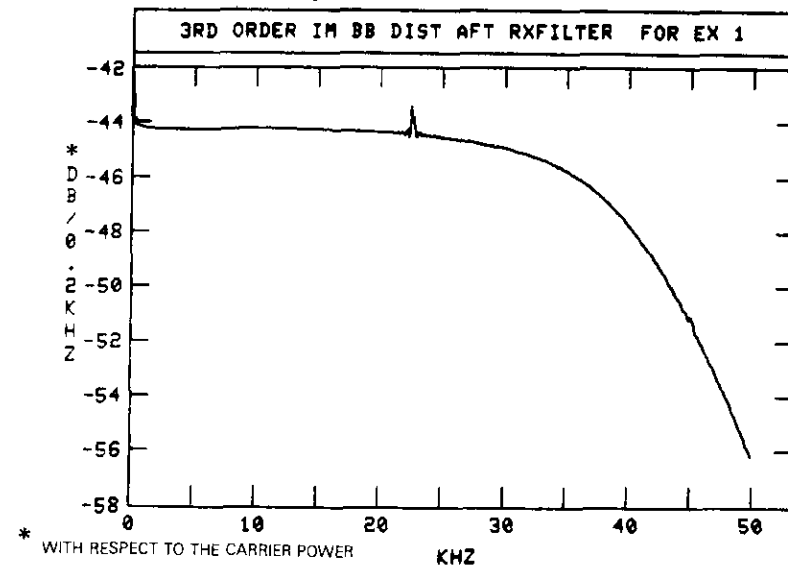


Figure 7. Measured SCPC/PSK Power Spectral Density



* WITH RESPECT TO SATELLITE TWTA OUTPUT SATURATION POWER

Figure 8. RF Power Spectral Density of the Intermodulation Noise at the Input of the Receiver of the SCPC Carrier at XX41.755 MHz



* WITH RESPECT TO THE CARRIER POWER

Figure 9. Baseband Power Spectral Density of the Intermodulation Noise in SCPC carrier at XX41.755 MHz

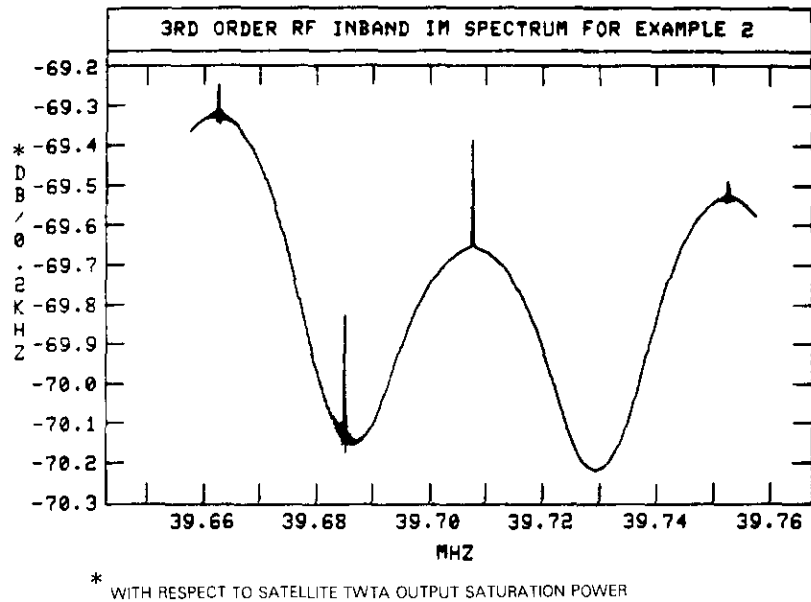


Figure 10. RF Third-Order Intermodulation Power Spectral Density at the SCPC/PSK Centered at XX39.7075 MHZ

riers which are unaffected by the third-order intermodulation solely between the SCPC carriers, the simplest approach is to replace the individual SCPC carriers with a band of thermal noise of the same amount of power, assuming a 40-percent activity factor. With this approach both the RF and baseband power spectral densities of the third-order intermodulation products can be evaluated by PRIME. For carriers which are affected by the third-order intermodulation between the SCPC carriers themselves, the same approach can be utilized to compute the rough RF power spectral density of the intermodulation. However, to compute the baseband or the RF power spectral density in a specific range of frequencies, the SCPC carriers must be individually input as in examples 1 and 2, since the intermodulation power spectral density might be spiked due to the intermodulation between the SCPC carriers themselves.

For the FDM/FM carrier centered around 36.465 MHz, the RF and baseband intermodulation power spectral densities are shown in Figures 11 and 12, respectively, by considering the SCPC carriers individually. Note that in Figure 11 the center frequency of the desired carrier is 36.465 MHz; two spiked intermodulation spectra at 36.445 and 36.4675 MHz,

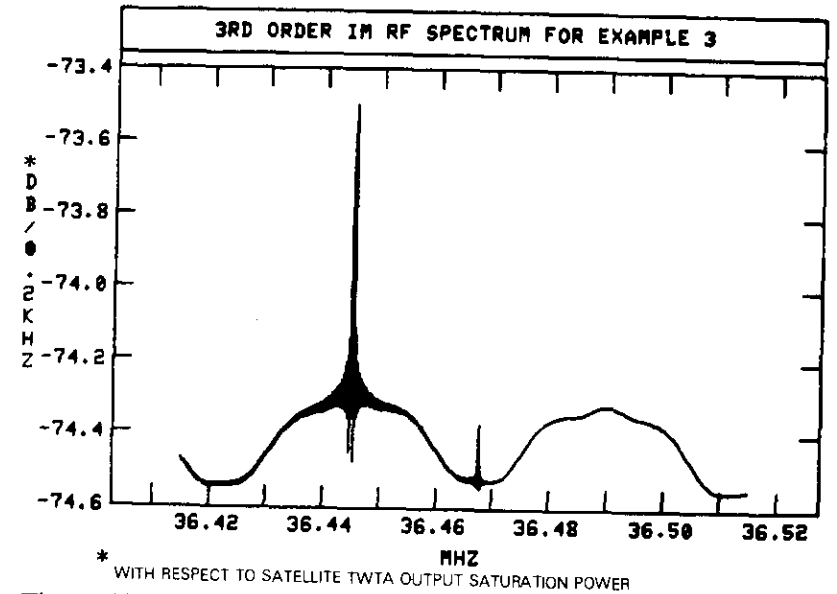


Figure 11. Intermodulation Power Spectral Densities for the FDM/FM Carrier Centered at 36.465 MHZ with the Consideration of Individual SCPC carriers

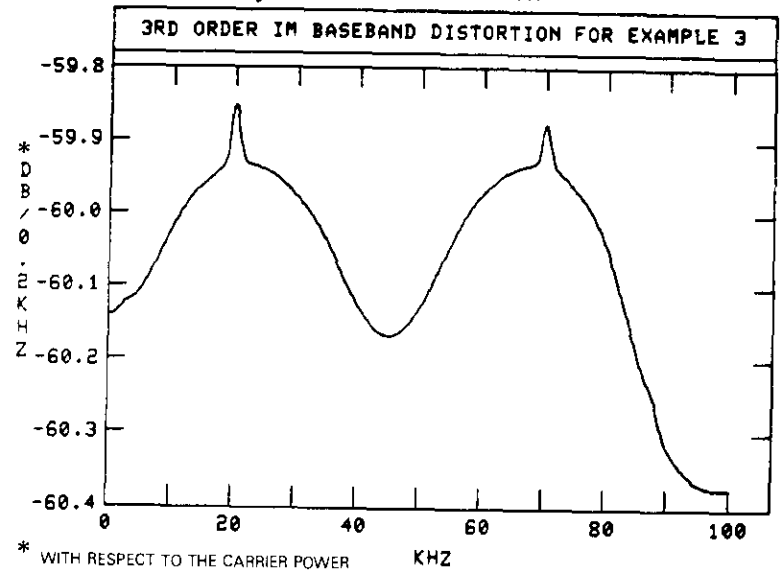


Figure 12. Baseband Intermodulation Power Spectral Density when SCPC Carriers are Individually Considered

respectively, are in the frequency range of interest, which is near the 36.465-MHz carrier frequency. The spike at 36.445 MHz is contributed by fifty-four $A + B - C$ type third-order intermodulation products and two $2A - B$ type third-order intermodulation products between SCPC/FM carriers. The spike at 36.4675 is contributed by one $A + B - C$ type intermodulation product involving two SCPC/FM carriers and the unmodulated pilot tone. These spikes are separated from the 36.465-MHz center frequency of the FDM/FM carrier by 20 and 2.5 kHz, respectively. These different frequencies appear as bumps in the demodulated baseband of the FM carrier as shown in Figure 12. Note that the bump at 2.5 kHz is barely noticeable. The bump at 70 kHz is contributed by another intermodulation spike at 36.535 MHz (not shown in Figure 11). Clearly, the baseband channel close to the bumps will suffer greater degradation than the others. The baseband degradation in some 4-kHz channels could be significantly higher when the SCPC carriers are individually considered in the intermodulation analysis than when they are regarded as a band of thermal noise.

Example 4. RF intermodulation power spectral density for mixed FDMA/FM/FDM and FDMA/PSK systems

The carrier configuration for this example is shown in Figure 13, in which one PSK and two FM carriers share the same 35-MHz satellite transponder. The third-order RF intermodulation power spectral density is shown in the whole transponder. The input levels of these three carriers are selected so that the carrier densities are identical. The individual carrier levels are -11.43 , -14.44 , and -17.45 dB (with respect to the TWTA saturation) centered at 6102.5, 6117.5, and 6125.0 MHz, respectively.

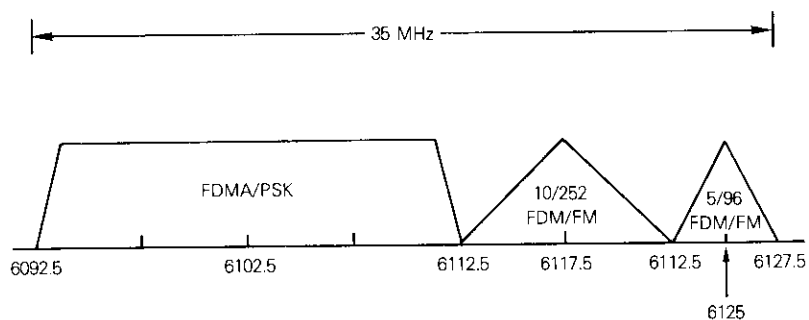
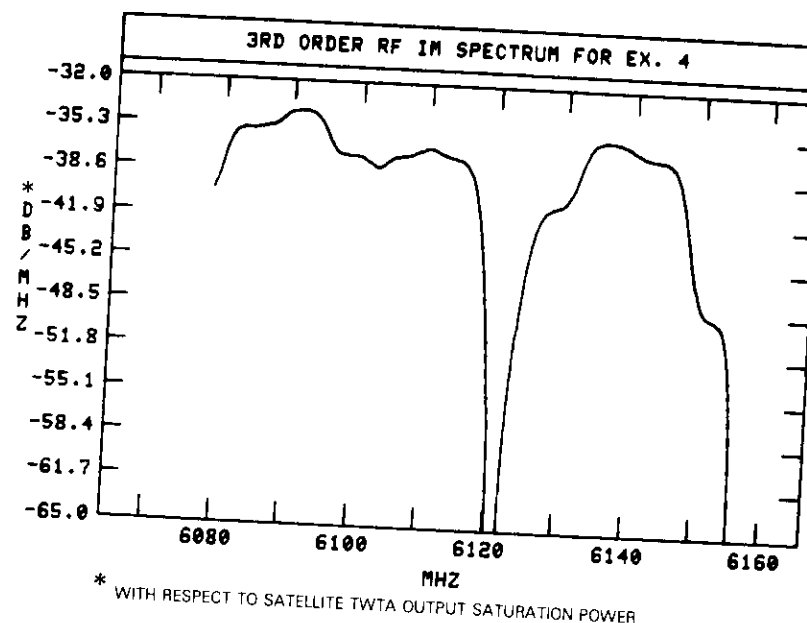


Figure 13. Frequency Plan for Example 4

The computed RF third-order intermodulation power spectral density is shown in Figure 14. The RF third-order intermodulation is fairly uniform within the transponder (from 6092.5 to 6127.5 MHz), as expected. With this power spectral density, the total link $C/(N_o + IM)$ can be computed if both up-link and down-link C/N_o 's are known. Hence, the BER performance of the PSK carrier can be obtained.



* WITH RESPECT TO SATELLITE TWTA OUTPUT SATURATION POWER

Figure 14. RF Power Spectral Density of the Third-Order Intermodulation for Example 4

Conclusions and discussion

This paper has derived the analytical expressions for both the RF and FM baseband power spectral density of the third-order intermodulation between an arbitrary number of SCPC/FM, SCPC/PSK, FM/FDM, FM/TV, FDMA or TDMA/PSK, CW carriers and one or more bands of thermal noise in a zero-memory bandpass nonlinear amplifier. A telescopic method has been proposed to compute the power spectral density of the intermodulation for carrier configurations including SCPC/FM carriers. A user-oriented computer program, PRIME, has been developed in terms of a command

language similar to that used in the CIA4 Program to evaluate the RF and baseband intermodulation power spectral densities. Numerical examples illustrate the use of PRIME, including the baseband performance of the FM carriers. It has been observed that, when SCPC/FM carriers are involved, the RF and baseband intermodulation power spectral densities can be highly peaked and care must be taken in using the assumption that they can be regarded as a band of equivalent thermal noise. In some cases, the discrepancies can be significant.

Fifth-order intermodulation has not been implemented in PRIME, although the mathematical analysis given herein is general enough to cover this case. The baseband performance of FM/TV carriers is not included, since the subjective effect caused by various types of intermodulation noise must be carefully evaluated. Moreover, the on/off effects of the SCPC carriers and the envelope fluctuations of the PSK signals are omitted from the analysis and are not included in PRIME.

References

- [1] M. Gyi, "Some Topics on Limiters and FM Demodulators," Technical Report No. 7050-3, Stanford Electronics Laboratories, Stanford University, July 1965.
- [2] J. W. Schwartz, J. M. Aein, and J. Kaiser, "Modulation Techniques for Multiple Access to a Hard-Limiting Satellite Repeater," *Proc. IEEE*, Vol. 54, No. 5, May 1966, pp. 763-777.
- [3] P. D. Shaft, "Limiting of Several Signals and Its Effect on Communications System Performance," *IEEE Transactions on Communications Technology*, COM-13, No. 4, December 1965, pp. 504-512.
- [4] J. J. Jones, "Hard-Limiting of Two Signals in Random Noise," *IEEE Transactions on Information Theory*, IT-9, January 1963, pp. 34-42.
- [5] A. L. Berman and C. E. Mahle, "Nonlinear Phase Shift in Traveling Wave Tube as Applied to Multiple-Access Communications Satellites," *IEEE Transactions on Communications Technology*, COM-18, No. 1, February 1970, pp. 37-48.
- [6] R. F. Pawula, T. S. Fong, and M. R. O'Sullivan, "Intermodulation Distortion in Frequency Multiplexed Satellite Repeaters," *Proc. IEEE*, Vol. 59, No. 2, February 1971, pp. 213-218.
- [7] R. J. Westcott, "Investigation of Multiple FM/FDM Carriers Through a Satellite TWT Operating Near Saturation," *Proc. IEE*, Vol. 114, No. 6, June 1967, pp. 726-750.
- [8] A. R. Kaye, D. A. George, and M. J. Eric, "Analysis and Compensation of Bandpass Nonlinearities for Communication," *IEEE Transactions on Communication*, COM-20, No. 5, October 1972, pp. 965-972.
- [9] N. M. Blachman, "Detectors, Bandpass Nonlinearities, and Their Optimization; Inversion of the Chebyshev Transform," *IEEE Transactions on Information Theory*, IT-17, July 1971, pp. 398-404.
- [10] O. Shimbo, "Effects of Intermodulation, AM-PM Conversion, and Additive Noise in Multicarrier TWT Systems," *Proc. IEEE*, Vol. 59, No. 2, February 1971, pp. 230-238.
- [11] J. C. Fuenzalida, O. Shimbo, and W. L. Cook, "Time-Domain Analysis of Intermodulation Effects Caused by Nonlinear Amplifiers," *COMSAT Technical Review*, Vol. 3, No. 1, Spring 1973, pp. 89-143.
- [12] J. C. Fuenzalida, W. L. Cook, and O. Shimbo, "The Intermodulation Analyzer (CIA4) User's Manual," COMSAT Technical Memorandum CL-48-72, September 1972.
- [13] W. C. Babcock, "Intermodulation Interference in Radio Systems," *Bell System Technical Journal*, January 1953, pp. 63-73.
- [14] R. J. F. Fang and W. A. Sandrin, "Carrier Frequency Assignment for Nonlinear Repeaters," *COMSAT Technical Review*, Vol. 7, No. 1, Spring 1977, pp. 227-245.
- [15] R. B. McClure, "Analysis of Intermodulation Distortion in an FDMA Satellite Communications System with a Bandwidth Constraint," *Conference Record*, International Conference on Communications, 1970, pp. 8-29.
- [16] R. J. F. Fang, "Modulation Transfer From TDMA On-Off Bursting to FM Carriers In Memoryless Nonlinear Devices, Part I-Power Spectra," *IEEE Transactions on Communications*, to be published.
- [17] R. J. F. Fang, "Modulation Transfer From TDMA On-Off Bursting To FM Carriers In Memoryless Nonlinear Devices, Part II-Baseband Performance," *IEEE Transactions on Communications*, April 1978, pp. 439-449.
- [18] J. L. Dicks, P. H. Schultze, and C. H. Schmit, "The INTELSAT IV Communications System," edited by P. L. Bargellini, *COMSAT Technical Review*, Vol. 2, No. 2, Fall 1972.

Appendix A. Derivation of $R^0(\tau)$

From equation (9) and the assumption that $A_l(t) = A_l$ for $l = 1, 2, \dots, m$, the autocorrelation $R^0(\tau)$ of the $e_o(t)$ can be derived as follows:

$$\begin{aligned}
 R^0(\tau) &\equiv \langle E[e_o(t + \tau) e_o(t)] \rangle \\
 &= \frac{1}{2} \operatorname{Re} \sum_{k_1, k_2, \dots, k_{m+n} = -\infty}^{\infty} \exp \left[j\omega_0 t + j \sum_{l=1}^{m+n} k_l \omega_l \tau \right] \\
 &\quad \cdot \sum_{p=1}^L \sum_{q=1}^L b_p b_q^* \left[\prod_{l=1}^m J_{k_l}(\alpha p A_l) \right] \left[\prod_{l=1}^m J_{k_l}(\alpha q A_l) \right] \\
 &\quad \cdot \left\langle E \left\{ \exp \left[j \sum_{l=1}^m k_l \psi_l(t, \tau) \right] \right\} E \left\{ \prod_{l=m+1}^{m+n} J_{k_l}[\alpha p r_l(t + \tau)] \right\} \right. \\
 &\quad \left. \cdot J_{k_l}[\alpha q r_l(t)] \exp[jk_l \phi_l(t + \tau) - jk_l \phi_l(t)] \right\rangle \quad \text{(A-1)}
 \end{aligned}$$

where the property of statistical independence between the m input carriers and n bands of noise has been applied, and

$$r_l(t) \equiv [\eta_{lc}^2(t) + \eta_{ls}^2(t)]^{1/2} \quad \text{(A-2)}$$

$$\phi_l(t) \equiv \tan^{-1} \left[\frac{\eta_{ls}(t)}{\eta_{lc}(t)} \right] \quad \text{(A-3)}$$

are the amplitude and phase, respectively, of the band-limited Gaussian random process $\eta_l(t)$ with properties shown in equations (11) through (13). Since $\eta_{lc}(t)$ and $\eta_{ls}(t)$ are statistically independent, the expression in equation (A-1) can be written as

$$\begin{aligned}
 R^0(\tau) &= \frac{1}{2} \operatorname{Re} \sum_{k_1, k_2, \dots, k_{m+n} = -\infty}^{\infty} \exp \left[j\omega_0 \tau + j \sum_{l=1}^{m+n} k_l \omega_l \tau \right] \\
 &\quad \cdot \prod_{p=1}^L \sum_{q=1}^L b_p b_q^* \left[\prod_{l=1}^m J_{k_l}(\alpha p A_l) \right] \left[\prod_{l=1}^m J_{k_l}(\alpha q A_l) \right] \prod_{l=1}^5 Q_l(\tau) \\
 &\quad \cdot \left\langle \sum_{l=m+1}^{m+n} \left[E \{ J_{k_l}[\alpha p r_l(t + \tau)] J_{k_l}[\alpha q r_l(t)] \} \right] \right\rangle
 \end{aligned}$$

$$\cdot \exp[jk_l \phi_l(t + \tau) - jk_l \phi_l(t)] \rangle \quad \text{(A-4)}$$

where
$$Q_i(\tau) \equiv \prod_{l=N_{i-1}+1}^{N_i} E[\exp[jk_l \psi_l(t, \tau)]] \quad \text{(A-5)}$$

with N_i defined in equation (8). It should be noted that $\psi_l(t, \tau) \equiv \psi_l(t + \tau) - \psi_l(t) = 0$ for all l 's corresponding to the cws since each cw has a fixed phase angle. Consequently, $Q_0(\tau) = 1$ and is not shown in equation (19). It should also be noted that each $Q_i(\tau)$ in equation (20) is a product of the characteristic function of the incremental process of the baseband angle modulation. The problem now is to evaluate the expectation term in equation (A-4) with respect to noise processes $\{r_l(t + \tau), \phi_l(t + \tau), r_l(t), \phi_l(t)\}$ or $\{\eta_{lc}(t + \tau), \eta_{ls}(t + \tau), \eta_{lc}(t), \eta_{ls}(t)\}$.

Assume that \underline{n} is a zero-mean Gaussian row vector defined as

$$\underline{n} = (\underline{n}_1, \underline{n}_2) \quad , \quad \underline{n}_1 = (n_{11}, n_{12}) \quad , \quad \underline{n}_2 = (n_{21}, n_{22}) \quad \text{(A-6)}$$

with mean vector

$$E[\underline{n}] = 0 \quad \text{(A-7)}$$

and covariance matrix

$$K \equiv E[\underline{n}'\underline{n}] = \begin{bmatrix} \sigma^2 & 0 & \sigma^2 \rho & 0 \\ 0 & \sigma^2 & 0 & \sigma^2 \rho \\ \hline \sigma^2 \rho & 0 & \sigma^2 & 0 \\ 0 & \sigma^2 \rho & 0 & \sigma^2 \end{bmatrix} \quad \text{(A-8)}$$

Also, denote

$$\lambda \equiv (\det K)^{1/2} = \sigma^4(1 - \rho^2) \quad \text{(A-9)}$$

$$M \equiv \lambda K^{-1} = \sigma^2 \left[\begin{array}{c|c} I & \rho I \\ \hline -\rho I & I \end{array} \right] \quad \text{(A-10)}$$

where I is the 2×2 identity matrix. Then, the probability density function of \underline{n} can be written as

$$\begin{aligned}
 f(\underline{n}) &= \frac{1}{4\pi^2 \lambda} \exp \left[-\frac{1}{2\lambda} \underline{n} M \underline{n}' \right] \\
 &= \frac{1}{4\pi^2 \lambda} \exp \left[-\frac{\sigma^2}{2\lambda} (|\underline{n}_1|^2 + |\underline{n}_2|^2) \right] \exp \left[\frac{\sigma^2 \rho}{\lambda} \underline{n}_1 \underline{n}_2' \right] \quad \text{(A-11)}
 \end{aligned}$$

If

$$R_1 \equiv |n_1| = \sqrt{n_{11}^2 + n_{12}^2} \quad , \quad R_2 \equiv |n_2| \equiv \sqrt{n_{21}^2 + n_{22}^2} \quad (\text{A-12})$$

$$\xi_1 \equiv \tan^{-1} \left(\frac{n_{12}}{n_{11}} \right) \quad , \quad \xi_2 \equiv \tan^{-1} \left(\frac{n_{22}}{n_{21}} \right) \quad . \quad (\text{A-13})$$

Then, equation (A-11) can be rewritten in terms of polar coordinates:

$$f(R_1, R_2, \xi_1, \xi_2) = \frac{R_1 R_2}{4\pi^2 \lambda} \exp \left[-\frac{\sigma^2}{2\lambda} (R_1^2 + R_2^2) \right] \cdot \exp \left[\frac{\sigma^2 \rho}{\lambda} R_1 R_2 \cos (\xi_1 - \xi_2) \right] \quad . \quad (\text{A-14})$$

Therefore, the expectation factor in equation (A-4) can be obtained by evaluating

$$T \equiv E \{ J_k(aR_1) J_k(bR_2) \exp[jk(\xi_1 - \xi_2)] \} \quad (\text{A-15})$$

$$T = \int_0^\infty \int_0^\infty \int_0^{2\pi} \int_0^{2\pi} dR_1 dR_2 d\xi_1 d\xi_2 J_k(aR_1) J_k(bR_2) \cdot \exp[jk(\xi_1 - \xi_2)] f(R_1, R_2, \xi_1, \xi_2) \\ = \int_0^\infty \int_0^\infty dR_1 dR_2 \frac{R_1 R_2}{\lambda} \exp \left[-\frac{\sigma^2}{2\lambda} (R_1 + R_2) \right] J_k(aR_1) J_k(bR_2) \cdot \int_0^{2\pi} d\xi_2 \frac{1}{2\pi} \int_0^{2\pi} d\xi_1 \frac{1}{2\pi} \exp \left[\frac{\sigma^2 \rho}{\lambda} R_1 R_2 \cos (\xi_1 - \xi_2) \right] \cdot \exp[jk(\xi_1 - \xi_2)] \quad . \quad (\text{A-16})$$

Changing variables $\xi_1' = \xi_1 - \xi_2$ and $\xi_2' = \xi_2$ and using the identity (Reference A1, p. 20)

$$I_k(z) = \frac{1}{2\pi} \int_0^{2\pi} e^{z \cos \theta} e^{jk\theta} d\theta \quad (\text{A-17})$$

in equation (A-16) yields

$$T = \int_0^\infty \int_0^\infty \frac{R_1 R_2}{\lambda} \exp \left[-\frac{\sigma^2}{2\lambda} (R_1^2 + R_2^2) \right] J_k(aR_1) J_k(bR_2) \cdot I_k \left(\frac{\sigma^2 \rho}{\lambda} R_1 R_2 \right) dR_1 dR_2 \quad . \quad (\text{A-18})$$

According to Reference A2, p. 718, and Reference A1, p. 395,

$$\int_0^\infty e^{-wx^2} I_n(ux) J_n(vx) x dx = \frac{1}{2w} \exp \left[\frac{u^2 - v^2}{4w} \right] J_n \left(\frac{uv}{2w} \right) \quad (\text{A-19})$$

$$\int_0^\infty e^{-wx^2} J_n(ux) J_n(vx) x dx = \frac{1}{2w} \exp \left[-\frac{u^2 + v^2}{4w} \right] I_n \left(\frac{uv}{2w} \right) \quad . \quad (\text{A-20})$$

Therefore, integrals in equation (A-18) can be successively evaluated to yield

$$T = \exp \left[-\frac{\sigma^2}{2} (a^2 + b^2) \right] I_k(\sigma^2 \rho ab) \quad . \quad (\text{A-21})$$

The definition of λ in equation (A-9) has been utilized to obtain equation (A-21).

The application of equations (A-21) and (A-15) to equation (A-4) yields

$$R^0(\tau) = \frac{1}{2} \operatorname{Re} \sum_{k_1, k_2, \dots, k_{m+n} = -\infty}^{\infty} \exp \left[j\omega_0 \tau + j \sum_{i=1}^{m+n} k_i \omega_i \tau \right] \cdot H(k_1, k_2, \dots, k_{m+n}; \tau) \prod_{i=1}^5 Q_i(\tau) \quad (\text{A-22})$$

where

$$H(k_1, k_2, \dots, k_{m+n}; \tau) \equiv \sum_{p=1}^L \sum_{q=1}^L b_p b_q^* \left[\prod_{i=1}^m J_{k_i}(\alpha p A_i) \right] \cdot \left[\prod_{i=1}^m J_{k_i}(\alpha q A_i) \right] \cdot \prod_{i=m+1}^{m+n} \left\{ I_{k_i}[\alpha^2 p q \lambda_{i-m}^2 \rho_{i-m}(\tau)] \right. \\ \left. \cdot \exp \left[-\frac{1}{2} \alpha^2 (p^2 + q^2) \lambda_{i-m}^2 \right] \right\} \quad (\text{A-23})$$

and λ_i and $\rho_i(\tau)$ are defined in equations (11) and (13).

References

[A1] G. N. Watson, *A Treatise on the Theory of Bessel Functions*, 2nd ed., Cambridge, U.K.: University Press, 1966.
 [A2] I. S. Gradshteyn and I. M. Ryzhik, *Tables of Integrals, Series, and Products*, 45th ed., New York: Academic Press, 1965.

Appendix B. Derivation of $R_I(\tau)$

As in equation (A-40) in Reference BI, the baseband distortion in equation (32) can be rewritten to simplify the evaluation of the autocorrelation function $R_I(\tau)$:

$$\begin{aligned}
 I(t) = & \text{Im}\{M_o^{-1} [M(1, 0, \dots, 0; t) - M_o]\} \\
 & + \text{Im} \left[M_o^{-1} \sum_{k_1, k_2, \dots, k_{m+n} = -\infty}^{\infty} \left\{ \exp \left[-j\omega_1 t + j \sum_{l=1}^{m+n} k_l \omega_l t \right] \right. \right. \\
 & \cdot \exp \left[j(k_1 - 1) \phi_1(t) + j \sum_{l=2}^{m+n} k_l \phi_l(t) \right] M(k_1, k_2, \dots, k_{m+n}; t) \\
 & + \exp \left[j\omega_1 t - j \sum_{l=1}^{m+n} k_l \omega_l t \right] \\
 & \cdot \exp \left[j(1 - k_1) \phi_1(t) - j \sum_{l=2}^{m+n} k_l \phi_l(t) \right] \\
 & \left. \left. \cdot M(2 - k_1, -k_2, \dots, -k_{m+n}; t) \right\} \right] \quad (B-1)
 \end{aligned}$$

where the double primes indicate that the summation is taken over all pairs of $(k_1, k_2, \dots, k_{m+n})$ and $(2 - k_1, -k_2, \dots, -k_{m+n})$ with the exception of $k_1 = 1$ and $k_l = 0$ for $l = 2, 3, \dots, m + n$, and the circle in the summation indicates the additional constraint that $\sum_{l=1}^{m+n} k_l = 1$.

When the identity $\text{Im}(a) \text{Im}(b) = 1/2 \text{Re}(ab^* - ab)$ is used between any two arbitrary complex numbers a and b , the autocorrelation function $R_I(\tau)$ can be found as follows:

$$R_I(\tau) \equiv \langle E[I(t + \tau) I(t)] \rangle \equiv \sum_{i=1}^9 \langle T_i \rangle \quad (B-2)$$

where

$$\begin{aligned}
 T_1 \equiv & \frac{1}{2} \text{Re} \left[|M_o|^{-2} E \{ [M(1, 0, \dots, 0; t + \tau) - M_o] \right. \\
 & \cdot [M^*(1, 0, \dots, 0; t) - M_o^*] - [M(1, 0, \dots, 0; t + \tau) - M_o] \\
 & \left. \cdot [M(1, 0, \dots, 0; t) - M_o] \right] \quad (B-3)
 \end{aligned}$$

$$T_2 \equiv \frac{1}{2} \text{Re} \left[|M_o|^{-2} \sum_{k_1, k_2, \dots, k_{m+n} = -\infty}^{\infty} \sum_{p_1, p_2, \dots, p_{m+n} = -\infty}^{\infty} E \left\{ M_o^{-1} [M(1, 0, \dots, 0; t + \tau) - M_o] \right. \right.$$

(continued on next page)

$$\begin{aligned}
 & \cdot E \left\{ \exp \left[j(k_1 - 1) \theta_1(t + \tau) + j \sum_{l=2}^{m+n} k_l \theta_l(t + \tau) \right] \right. \\
 & \cdot \exp \left[-j(p_1 - 1) \theta_1(t) - j \sum_{l=2}^{m+n} p_l \theta_l(t) \right] \\
 & \cdot M(k_1, k_2, \dots, k_{m+n}; t + \tau) M^*(k_1, k_2, \dots, k_{m+n}; t) \\
 & - \exp \left[j(k_1 - 1) \theta_1(t + \tau) + j \sum_{l=2}^{m+n} k_l \theta_l(t + \tau) \right] \\
 & \cdot \exp \left[j(p_1 - 1) \theta_1(t) + j \sum_{l=2}^{m+n} p_l \theta_l(t) \right] \\
 & \left. \left. \cdot M(k_1, k_2, \dots, k_{m+n}; t + \tau) M(k_1, k_2, \dots, k_{m+n}; t) \right\} \right] \quad (B-4)
 \end{aligned}$$

$$\begin{aligned}
 T_3 \equiv & \frac{1}{2} \text{Re} \left[|M_o|^{-2} \sum_{k_1, k_2, \dots, k_{m+n} = -\infty}^{\infty} \sum_{p_1, p_2, \dots, p_{m+n} = -\infty}^{\infty} E \left\{ \exp \left[j(1 - k_1) \theta_1(t + \tau) - j \sum_{l=2}^{m+n} k_l \theta_l(t + \tau) \right] \right. \right. \\
 & \cdot \exp \left[-j(1 - p_1) \theta_1(t) + j \sum_{l=2}^{m+n} p_l \theta_l(t) \right] \\
 & \cdot M(2 - k_1, -k_2, \dots, -k_{m+n}; t + \tau) \\
 & \cdot M^*(2 - p_1, -p_2, \dots, -p_{m+n}; t) \\
 & - \exp \left[j(1 - k_1) \theta_1(t + \tau) - j \sum_{l=2}^{m+n} k_l \theta_l(t + \tau) \right] \\
 & \cdot \exp \left[j(1 - p_1) \theta_1(t) - j \sum_{l=2}^{m+n} p_l \theta_l(t) \right] \\
 & \cdot M(2 - k_1, -k_2, \dots, -k_{m+n}; t + \tau) \\
 & \left. \left. \cdot M(2 - p_1, -p_2, \dots, -p_{m+n}; t) \right\} \right] \quad (B-5)
 \end{aligned}$$

$$T_4 \equiv \frac{1}{2} \text{Re} \left[|M_o|^{-2} \sum_{k_1, k_2, \dots, k_{m+n} = -\infty}^{\infty} E \left\{ M_o^{-1} [M(1, 0, \dots, 0; t + \tau) - M_o] \right. \right.$$

(continued on next page)

$$\begin{aligned} & \cdot M^*(k_1, k_2, \dots, k_{m+n}; t) \exp \left[-j(k_1 - 1) \theta_1(t) - j \sum_{i=2}^{m+n} k_i \theta_i(t) \right] \\ & - M_o^{-1} [M(1, 0, \dots, 0; t + \tau) - M_o] M(k_1, k_2, \dots, k_{m+n}; t) \\ & \cdot \exp \left[j(k_1 - 1) \theta_1(t) + j \sum_{i=2}^{m+n} k_i \theta_i(t) \right] \} \end{aligned} \quad (\text{B-6})$$

$$\begin{aligned} T_5 & \equiv \frac{1}{2} \operatorname{Re} \left[|M_o|^{-2} \sum_{k_1, k_2, \dots, k_{m+n} = -\infty}^{\infty} E \left\{ M_o^{-1} [M(1, 0, \dots, 0; t + \tau) - M_o] \right. \right. \\ & \cdot M^*(2 - k_1, -k_2, \dots, -k_{m+n}; t) \\ & \cdot \exp \left[-j(1 - k_1) \theta_1(t) + j \sum_{i=2}^{m+n} k_i \theta_i(t) \right] \\ & - M_o^{-1} [M(1, 0, \dots, 0; t + \tau) - M_o] M(2 - k_1, -k_2, \dots, -k_{m+n}; t) \\ & \left. \left. \cdot \exp \left[j(1 - k_1) \theta_1(t) - j \sum_{i=2}^{m+n} k_i \theta_i(t) \right] \right\} \right] \end{aligned} \quad (\text{B-7})$$

$$\begin{aligned} T_6 & \equiv \frac{1}{2} \operatorname{Re} \left[|M_o|^{-2} \sum_{k_1, k_2, \dots, k_{m+n} = -\infty}^{\infty} E \left\{ M_o^{*-1} [M^*(1, 0, \dots, 0; t) - M_o^*] \right. \right. \\ & \cdot M(k_1, k_2, \dots, k_{m+n}; t + \tau) \\ & \cdot \exp \left[j(k_1 - 1) \theta_1(t + \tau) + j \sum_{i=2}^{m+n} k_i \theta_i(t + \tau) \right] \\ & - M_o^{-1} [M(1, 0, \dots, 0; t) - M_o] M(k_1, k_2, \dots, k_{m+n}; t + \tau) \\ & \left. \left. \cdot \exp \left[j(k_1 - 1) \theta_1(t + \tau) + j \sum_{i=2}^{m+n} k_i \theta_i(t + \tau) \right] \right\} \right] \end{aligned} \quad (\text{B-8})$$

$$\begin{aligned} T_7 & \equiv \frac{1}{2} \operatorname{Re} \left[|M_o|^{-2} \sum_{k_1, k_2, \dots, k_{m+n} = -\infty}^{\infty} E \left\{ M_o^{*-1} [M^*(1, 0, \dots, 0; t) - M_o^*] \right. \right. \\ & \cdot M(2 - k_1, -k_2, \dots, -k_{m+n}; t + \tau) \end{aligned}$$

(continued on next page)

$$\begin{aligned} & \cdot \exp \left[j(1 - k_1) \theta_1(t + \tau) - j \sum_{i=2}^{m+n} k_i \theta_i(t + \tau) \right] \\ & - M_o^{-1} [M(1, 0, \dots, 0; t) - M_o] M(2 - k_1, -k_2, \dots, -k_{m+n}; t + \tau) \\ & \cdot \exp \left[j(1 - k_1) \theta_1(t + \tau) - j \sum_{i=2}^{m+n} k_i \theta_i(t + \tau) \right] \} \end{aligned} \quad (\text{B-9})$$

$$\begin{aligned} T_8 & \equiv \frac{1}{2} \operatorname{Re} \left[|M_o|^{-2} \sum_{k_1, k_2, \dots, k_{m+n} = -\infty}^{\infty} \sum_{p_1, p_2, \dots, p_{m+n} = -\infty}^{\infty} E \left\{ \right. \right. \\ & \cdot \exp \left[j(k_1 - 1) \theta_1(t + \tau) + j \sum_{i=2}^{m+n} k_i \theta_i(t + \tau) \right] \\ & \cdot \exp \left[-j(1 - p_1) \theta_1(t) + j \sum_{i=2}^{m+n} p_i \theta_i(t) \right] \\ & \cdot M(k_1, k_2, \dots, k_{m+n}; t + \tau) M^*(2 - p_1, -p_2, \dots, -p_{m+n}; t) \\ & - \exp \left[j(k_1 - 1) \theta_1(t + \tau) + j \sum_{i=2}^{m+n} k_i \theta_i(t + \tau) \right] \\ & \cdot \exp \left[j(1 - p_1) \theta_1(t) - j \sum_{i=2}^{m+n} p_i \theta_i(t) \right] \\ & \left. \left. \cdot M(k_1, k_2, \dots, k_{m+n}; t + \tau) M(2 - p_1, -p_2, \dots, -p_{m+n}; t) \right\} \right] \end{aligned} \quad (\text{B-10})$$

$$\begin{aligned} T_9 & \equiv \frac{1}{2} \operatorname{Re} \left[|M_o|^{-2} \sum_{k_1, k_2, \dots, k_{m+n} = -\infty}^{\infty} \sum_{p_1, p_2, \dots, p_{m+n} = -\infty}^{\infty} E \left\{ \right. \right. \\ & \cdot \exp \left[-j(k_1 - 1) \theta_1(t) - j \sum_{i=2}^{m+n} k_i \theta_i(t) \right] \\ & \cdot \exp \left[j(1 - p_1) \theta_1(t + \tau) - j \sum_{i=2}^{m+n} p_i \theta_i(t + \tau) \right] \\ & \left. \left. \cdot M^*(k_1, k_2, \dots, k_{m+n}; t) M(2 - p_1, -p_2, \dots, -p_{m+n}; t + \tau) \right\} \right] \end{aligned}$$

(continued on next page)

$$\begin{aligned}
& - \exp \left[j(k_1 - 1) \theta_1(t) + j \sum_{i=2}^{m+n} k_i \theta_i(t) \right] \\
& \cdot \exp \left[j(1 - p_1) \theta_1(t + \tau) - j \sum_{i=2}^{m+n} p_i \theta_i(t + \tau) \right] \\
& \cdot M(k_1, k_2, \dots, k_{m+n}; t) M(2 - p_1, -p_2, \dots, -p_{m+n}; t + \tau) \left. \vphantom{\exp} \right\} .
\end{aligned} \tag{B-11}$$

It should be noted that $\theta_l(t) \equiv \omega_l t + \phi_l(t)$ for all l . The time averages of T_4 , T_5 , T_6 , and T_7 are all zero since the time averages of the individual expectation terms are zero in equations (B-6) through (B-9). The time averages of T_2 , T_3 , T_8 , and T_9 are all zero except when $k_l = p_l$ for $l = 1, 2, \dots, m+n$.

Substituting the definitions of M_o and $M(1, 0, \dots, 0; t)$ given in equations (26) and (27) into equation (B-3) and applying equations (A-15) and (A-21) yield

$$\begin{aligned}
\langle T_1 \rangle &= \frac{1}{2} \operatorname{Re} \left\{ |M_o|^{-2} \langle E[M(1, 0, \dots, 0; t + \tau) M^*(1, 0, \dots, 0; t)] \rangle - 1 \right. \\
& \quad \left. - |M_o|^{-2} \langle E[M(1, 0, \dots, 0; t + \tau) M(1, 0, \dots, 0; t)] \rangle + M_o M_o^* \right\} \\
&= \frac{1}{2} \operatorname{Re} \left[|M_o|^{-2} \sum_{p=1}^L \sum_{q=1}^L b_p b_q^* J_1(\alpha p A_1) J_1(\alpha q A_1) \right. \\
& \quad \cdot \left[\prod_{i=2}^m J_0(\alpha p A_i) \right] \left[\prod_{i=2}^m J_0(\alpha q A_i) \right] \\
& \quad \cdot \prod_{i=1}^n \left\{ \exp \left[-\frac{1}{2} \alpha^2 (p^2 + q^2) \lambda_i^2 \right] I_0[\alpha^2 p q \lambda_i^2 \rho_i(\tau)] \right\} - 1 \\
& \quad - |M_o|^{-2} \sum_{p=1}^L \sum_{q=1}^L b_p b_q J_1(\alpha p A_1) J_1(\alpha q A_1) \\
& \quad \cdot \left[\prod_{i=2}^m J_0(\alpha p A_i) \right] \left[\prod_{i=2}^m J_0(\alpha q A_i) \right] \\
& \quad \cdot \prod_{i=1}^n \left\{ \exp \left[-\frac{1}{2} \alpha^2 (p^2 + q^2) \lambda_i^2 \right] I_0[\alpha^2 p q \lambda_i^2 \rho_i(\tau)] \right\} + \frac{M_o}{M_o^*} \Bigg] \\
&= -|M_o|^{-2} \sum_{p=1}^L \sum_{q=1}^L \operatorname{Im}(b_p) \operatorname{Im}(b_q^*) J_1(\alpha p A_1) J_1(\alpha q A_1)
\end{aligned}$$

(continued on next page)

$$\begin{aligned}
& \cdot \left[\prod_{i=2}^m J_0(\alpha p A_i) \right] \left[\prod_{i=2}^m J_0(\alpha q A_i) \right] \\
& \cdot \exp \left[-\frac{1}{2} \alpha^2 (p^2 + q^2) \sum_{i=1}^n \lambda_i^2 \right] \prod_{i=1}^n \left\{ I_0[\alpha p q \alpha^2 \lambda_i^2 \rho_i(\tau)] - 1 \right\} \\
&= \sum_{l_1, l_2, \dots, l_n=0}^{\infty} \left\{ \operatorname{Im}[N(1, 0, \dots, 0; l_1, l_2, \dots, l_n)] \right\}^2 \\
& \cdot \prod_{i=1}^n [\rho_i(\tau)]^{2l_i}
\end{aligned} \tag{B-12}$$

where the prime denotes the exclusion of the term corresponding to $l_1 = l_2 = \dots = l_n = 0$, and

$$\begin{aligned}
& N(k_1, k_2, \dots, k_{m+n}; l_1, l_2, \dots, l_n) \\
& \equiv M_o^{-1} \sum_{p=1}^L b_p \left[\prod_{i=1}^M J_{k_i}(\alpha p A_i) \right] \exp \left[-\frac{1}{2} \alpha^2 p^2 \sum_{i=1}^n \lambda_i^2 \right] \\
& \cdot \left[\prod_{i=1}^n \frac{(\alpha^2 \lambda_i^2 p^2 / 2)^{2l_i + |k_{m+i}|}}{l_i! (l_i + |k_{m+i}|)!} \right]^{1/2} .
\end{aligned} \tag{B-13}$$

The time average $\langle T_2 \rangle$ is zero except when $k_l = p_l$, in which case

$$\begin{aligned}
\langle T_2 \rangle & \equiv \frac{1}{2} \operatorname{Re} \left[|M_o|^{-2} \sum_{k_1, k_2, \dots, k_{m+n} = -\infty}^{\infty} \right. \\
& \quad \cdot \exp \left[j(k_1 - 1) \omega_1 \tau + j \sum_{i=2}^{m+n} k_i \omega_i \tau \right] \\
& \quad \cdot \left\langle E \left\{ \exp \left[j(k_1 - 1) \psi_1(t, \tau) + j \sum_{i=2}^m k_i \psi_i(t, \tau) \right] \right\} \right. \\
& \quad \cdot E \left\{ M(k_1, k_2, \dots, k_{m+n}; t + \tau) M^*(k_1, k_2, \dots, k_{m+n}; t) \right. \\
& \quad \cdot \left. \left. \exp \left[j \sum_{l=m+1}^{m+n} k_l \psi_l(t, \tau) \right] \right\} \right. \Bigg] \\
&= \frac{1}{2} \operatorname{Re} \left\{ |M_o|^{-2} \sum_{k_1, k_2, \dots, k_{m+n} = -\infty}^{\infty} \right.
\end{aligned}$$

(continued on next page)

$$\begin{aligned}
 & \cdot \exp \left[j(k_1 - 1) \omega_1 \tau + j \sum_{i=2}^{m+n} k_i \omega_i \tau \right] \\
 & \cdot \left\langle E \left\{ \exp \left[j(k_1 - 1) \psi_1(t, \tau) + j \sum_{i=2}^m k_i \psi_i(t, \tau) \right] \right\} \right\rangle \\
 & \cdot \sum_{p=1}^L \sum_{q=1}^L b_p b_q^* \left[\prod_{i=1}^m J_{k_i}(\alpha p A_i) \right] \left[\prod_{i=1}^m J_{k_i}(\alpha q A_i) \right] \\
 & \cdot \exp \left[-\frac{1}{2} \alpha^2 (p^2 + q^2) \sum_{i=1}^n \lambda_i^2 \right] \prod_{j=1}^n I_{k_{m+j}} [pq \alpha^2 \lambda_j^2 \rho_j(\tau)] \Big\} \\
 = & \frac{1}{2} \operatorname{Re} \sum_{k_1, k_2, \dots, k_{m+n} = -\infty}^{\infty} \sum_{l_1, l_2, \dots, l_n = 0}^{\infty} \\
 & \cdot |N(k_1, k_2, \dots, k_{m+n}; l_1, l_2, \dots, l_n)|^2 \\
 & \cdot \Delta(k_1, k_2, \dots, k_{m+n}; \tau)
 \end{aligned} \tag{B-14}$$

where $\Delta(k_1, k_2, \dots, k_{m+n}; \tau)$

$$\begin{aligned}
 & \equiv \left\langle E \left\{ \exp \left[j(k_1 - 1) \psi_1(t, \tau) + j \sum_{i=2}^m k_i \psi_i(t, \tau) \right] \right\} \right\rangle \\
 & \cdot \exp \left[j(k_1 - 1) \omega_1 \tau + j \sum_{i=2}^{m+n} k_i \omega_i \tau \right] \\
 & \cdot \prod_{i=1}^n [\rho_i(\tau)]^{2l_i + |k_{m+i}|} .
 \end{aligned} \tag{B-15}$$

Since $J_{-n}(X) = (-1)^n J_n(X)$, the following can be similarly obtained:

$$\begin{aligned}
 T_3 = & \frac{1}{2} \operatorname{Re} \left\{ |M_0|^{-2} \sum_{k_1, k_2, \dots, k_{m+n} = -\infty}^{\infty} \right. \\
 & \cdot \exp \left[-j(k_1 - 1) \omega_1 \tau - j \sum_{i=2}^{m+n} k_i \omega_i \tau \right] \\
 & \cdot \left\langle E \left\{ \exp \left[-j(k_1 - 1) \psi_1(t, \tau) - j \sum_{i=2}^m k_i \psi_i(t, \tau) \right] \right\} \right\rangle \\
 & \cdot \sum_{p=1}^L \sum_{q=1}^L b_p b_q^* J_{2-k_1}(\alpha p A_1) J_{2-k_1}(\alpha q A_1) \\
 & \cdot \left[\prod_{i=2}^m (-1)^{k_i} J_{k_i}(\alpha p A_i) \right] \left[\prod_{i=2}^m (-1)^{k_i} J_{k_i}(\alpha q A_i) \right]
 \end{aligned}$$

(continued on next page)

$$\begin{aligned}
 & \cdot \exp \left[-\frac{1}{2} \alpha^2 (p^2 + q^2) \sum_{i=1}^n \lambda_i^2 \right] \\
 & \cdot (-1)^{2k} \prod_{i=1}^n I_{k_{m+i}} [pq \alpha^2 \lambda_i^2 \rho_i(\tau)] \Big\}
 \end{aligned} \tag{B-16}$$

where $k = \sum_{i=1}^n k_{m+i}$. (B-17)

Hence,

$$\begin{aligned}
 T_3 = & \frac{1}{2} \operatorname{Re} \sum_{k_1, k_2, \dots, k_{m+n} = -\infty}^{\infty} \sum_{l_1, l_2, \dots, l_n = 0}^{\infty} \\
 & \cdot |N(2 - k_1, k_2, \dots, k_{m+n}; l_1, l_2, \dots, l_n)|^2 \\
 & \cdot \Delta^*(k_1, k_2, \dots, k_{m+n}; \tau) .
 \end{aligned} \tag{B-18}$$

$$\begin{aligned}
 \langle T_8 \rangle = & -\frac{1}{2} \operatorname{Re} \left\{ |M_0|^{-2} \sum_{k_1, k_2, \dots, k_{m+n} = -\infty}^{\infty} \right. \\
 & \cdot \exp \left[j(k_1 - 1) \omega_1 \tau + j \sum_{i=2}^{m+n} k_i \omega_i \tau \right] \\
 & \cdot \left\langle E \left\{ \exp \left[j(k_1 - 1) \psi_1(t, \tau) + j \sum_{i=2}^m k_i \psi_i(t, \tau) \right] \right\} \right\rangle \\
 & \cdot (-1)^{k'} \sum_{p=1}^L \sum_{q=1}^L b_p b_q J_{k_1}(\alpha p A_1) J_{2-k_1}(\alpha q A_1) \\
 & \cdot \left[\prod_{i=2}^m J_{k_i}(\alpha p A_i) \right] \left[\prod_{i=2}^m J_{k_i}(\alpha q A_i) \right] \\
 & \cdot (-1)^k \exp \left[-\frac{1}{2} \alpha^2 (p^2 + q^2) \sum_{i=1}^n \lambda_i^2 \right] \\
 & \cdot \prod_{i=1}^n I_{k_{m+i}} [pq \alpha^2 \lambda_i^2 \rho_i(\tau)] \Big\}
 \end{aligned} \tag{B-19}$$

$$\begin{aligned}
 \langle T_8 \rangle = & \frac{1}{2} \operatorname{Re} \sum_{k_1, k_2, \dots, k_{m+n} = -\infty}^{\infty} (-1)^{k_1} \sum_{l_1, l_2, \dots, l_n = 0}^{\infty} \\
 & \cdot N(k_1, k_2, \dots, k_{m+n}; l_1, l_2, \dots, l_n) \\
 & \cdot N(2 - k_1, k_2, \dots, k_{m+n}; l_1, l_2, \dots, l_n) \\
 & \cdot \Delta(k_1, k_2, \dots, k_{m+n}; \tau) .
 \end{aligned} \tag{B-20}$$

In equation (B-19),

$$k' \equiv \sum_{i=2}^m k_i$$

and

$$k' + k + 1 = \sum_{i=2}^{m+n} k_i + 1 = 1 - k_1 + 1 = 2 - k_1 \quad (\text{B-21})$$

$$\begin{aligned} \langle T_8 \rangle &= -\frac{1}{2} (-1)^{k+k'} \operatorname{Re} \left\{ |M_0|^{-2} \sum_{k_1, k_2, \dots, k_{m+n} = -\infty}^{\infty} \right. \\ &\cdot \exp \left[-j(k_1 - 1) \omega_1 \tau - j \sum_{i=2}^{m+n} k_i \omega_i \tau \right] \\ &\cdot \left\langle E \right\rangle \exp \left[-j(k_1 - 1) \psi_1(t, \tau) - j \sum_{i=2}^m k_i \psi_i(t, \tau) \right] \left. \right\rangle \\ &\cdot \sum_{p=1}^L \sum_{q=1}^L b_p b_q J_{2-k_1}(\alpha p A_1) J_{k_1}(\alpha q A_1) \\ &\cdot \left[\prod_{i=2}^m J_{k_i}(\alpha p A_i) \right] \left[\prod_{i=2}^m J_{k_i}(\alpha q A_i) \right] \\ &\cdot \exp \left[-\frac{1}{2} \alpha^2 (\rho^2 + q^2) \sum_{i=1}^n \lambda_i^2 \right] \prod_{i=1}^n I_{k_{m+i}}[\rho q \alpha^2 \lambda_i^2 \rho_i(\tau)] \left. \right\} \\ &= \frac{1}{2} \operatorname{Re} \sum_{k_1, k_2, \dots, k_{m+n} = -\infty}^{\infty} (-1)^{k_1} \sum_{l_1, l_2, \dots, l_n = 0}^{\infty} \\ &\cdot N(2 - k_1, k_2, \dots, k_{m+n}; l_1, l_2, \dots, l_n) \\ &\cdot N(k_1, k_2, \dots, k_{m+n}; l_1, l_2, \dots, l_n) \\ &\cdot \Delta^*(k_1, k_2, \dots, k_{m+n}; \tau) \quad (\text{B-22}) \end{aligned}$$

Substitute equations (B-12), (B-14), (B-17), (B-20), and (B-22) into equation (B-2) and note that $\langle T_4 \rangle = \langle T_5 \rangle = \langle T_6 \rangle = \langle T_7 \rangle = 0$. The autocorrelation function $R_I(\tau)$ can then be found.

Reference

[B1] J. C. Fuenzalida, O. Shimbo, and W. L. Cook, "Time-Domain Analysis of Intermodulation Effects Caused by Nonlinear Amplifiers," *COMSAT Technical Review*, Vol. 3, No. 1, Spring 1973, pp. 89-143.



Peter Y. Chang is a technical staff member of the Communications Systems Analysis Department of the Transmission System Laboratory at COMSAT Laboratories. Currently he is involved with satellite communications and transmission systems studies, including intermodulation and transponder nonlinear effect studies for INTELSAT. He received a B.S.E.E. in electrical engineering from Cheng Kung University in Taiwan in 1967 and M.S.E.E., M.Ph., and Ph.D. degrees from Columbia University in 1969, 1973, and 1975.

Before joining COMSAT in 1976, he worked for Computer Sciences Corporation in satellite communications and transmission systems operation. He is a member of Eta Kappa Nu, Sigma Xi and IEEE.

Russell J. F. Fang is Manager of the Communications Systems Analysis Department of the Transmission Systems Laboratory at COMSAT Laboratories. He is responsible for research and studies of advanced communications systems concepts and techniques for international and domestic satellite communications. Born in Chungking, China, he received a B.S. in electrical engineering from National Taiwan University in 1962, and an M.S. and a Ph.D. in electrical engineering from Stanford University in 1964 and 1968. Before joining COMSAT in 1968, he was employed by Stanford Electronics Laboratories (1965-1968), Stanford Research Institute (1964-1965), and the Chinese Air Force Electronics and Ordnance Division, Taiwan (1962-1963).



A bound on the relationship between intermodulation noise and carrier frequency assignment

Y. HIRATA

(Manuscript received July 15, 1977)

Abstract

This paper describes the relationship between third-order intermodulation products and assigned bandwidth. A lower bound of the third-order intermodulation products falling into signal channels is derived using the concept of difference triangular sets. In addition, solutions of the intermodulation/minimum frequency assignment sequence are given for practical applications. A comparison of such optimum solutions with the lower bound derived in this paper indicates that the latter is useful for evaluating the relationship between the utilization efficiency of the assigned bandwidth and the intermodulation impairment level.

Introduction

In communications satellites, several carriers use a common power amplifier whose nonlinearities (AM/AM or AM/PM conversion effects) result in intermodulation noise. If some bandwidth margin is available, the intermodulation products falling into the frequency slots of the signal channel can be reduced by properly distributing the channels within this bandwidth. Channel assignment sequences such as those originally pro-

posed by Babcock [1] are examples of this approach which are completely free of third-order intermodulation products at the assigned carrier frequencies. Fang and Sandrin have generalized the strategy to generate an intermodulation-free channel allocation by using difference sets [2]. In addition, solutions for up to 30 signal channels have been obtained by Hirata and Yasuda [3].

Intermodulation-free channel assignments are not necessarily efficient in terms of bandwidth utilization, especially if a large number of signal channels must be accommodated. For example, 20 signal channels would require 10 times more total bandwidth than the minimum equal-spacing assignment. This paper addresses the problem of more efficient bandwidth channel assignment by allowing some intermodulation products to fall into the signal channel while minimizing the number falling into the worst signal channel. The lower bound of third-order intermodulation products falling into the worst channel is derived theoretically, and the relationship between the assigned frequency bandwidth and the improvement factor of intermodulation products is determined. Examples of optimum frequency assignment sequences are presented and their performance is compared with the lower bounds.

General expression

It is assumed that multiple signals with identical amplitude and bandwidth are amplified by a common nonlinear device, and that the highest channel frequency is less than twice the lowest channel frequency. Therefore, the set of signal channel frequencies is expressed as integers

$$\{a_i\} = \{a_1, a_2, \dots, a_s, \dots, a_k\} \tag{1}$$

- where a_1 = frequency of the lowest signal channel
(= 1)
- a_s = frequency of the sth signal channel
($a_s > a_{s-1}$)
- a_k = frequency of the highest signal channel
(equal to the normalized assigned bandwidth)
- k = number of signal channels.

In general, the third-order intermodulation product, generated by three signals with frequencies of $a_i, a_j,$ and $a_l,$ falls into the frequency a_s satisfying the relationship

$$a_s = a_i + a_j - a_l \tag{2}$$

Therefore, the total number of third-order intermodulation products falling into frequency a_s is*

$$N(a_s, k, s) = \sum_{i=1}^{s-1} \sum_{j=1}^{k-1} \sum_{l=j+1}^k \delta(d_{is} - d_{jl}) + \sum_{i=s+1}^k \sum_{j=1}^{k-1} \sum_{l=j+1}^k \delta(d_{si} - d_{jl}) - (k - 1) \tag{3}$$

where $d_{ij} = a_j - a_i, \quad j > i$

and
$$\delta(x) = \begin{cases} 1, & x = 0 \\ 0, & x \neq 0 \end{cases}$$

Figure 1 shows the general expression and some examples of the difference triangular set $\{d_{ij}\}$ consisting of the distance between the center frequencies of the two arbitrary signal channels. The number of third-order intermodulation products falling into a signal channel can be determined from this figure or from equation (3). For example, for signal channel a_3 ($= 4$) as shown in Figure 1b, the elements of the triangular set related to a_3 ($d_{13}, d_{23}, d_{34}, d_{35}, d_{36}$) take the integers 3, 1, 3, 4, and 7, and these integers are repeated in the difference triangular set 3, 2, 3, 3, and 2 times, respectively. Therefore, the total number of intermodulation products, $N(11, 6, 3)$, becomes $3 + 2 + 3 + 3 + 2 - 5 = 8$. Similarly, for the equal-spacing allocation (Figure 1c), $N(6, 6, 3)$ becomes $4 + 5 + 5 + 4 + 3 - 5 = 16$. On the other hand, in the case of Figure 1d, every element assumes different integers, representing the intermodulation-free channel allocation.

*In equation (3), two kinds of third-order intermodulation products, the $A + B - C$ and the $2A - B$ products, are combined within a single formula by assuming that the power of the $A + B - C$ intermodulation is twice that of the $2A - B$ product. Although this assumption is not rigorous, little error results because most of the intermodulation noise power is contained in $A + B - C$ type products [4]. For example, for equal space allocation, the error is less than 10 percent for more than 5 carriers and less than 5 percent for more than 10 carriers.

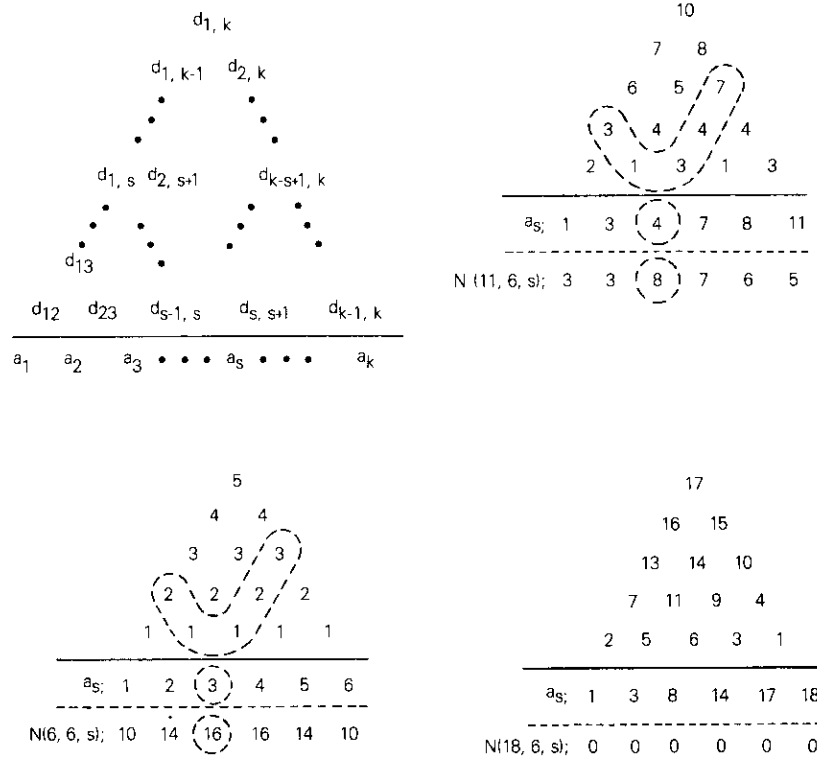


Figure 1. Difference Triangular Set of Carrier Frequency Assignment

Intermodulation products in equal-spacing assignment

If it is assumed that k signals are allocated equal spacing, the number of third-order intermodulation products falling into the s th signal channel, $I_0(k, s)$, can be derived from equation (3) as follows:

$$I_0(k, s) = \frac{(k-1)(k-2)}{2} + (s-1)(k-s) \quad (4)$$

This equation demonstrates that the number of third-order intermodulation products is higher at the middle channel, and that the ratio of its maximum to its minimum is 3 to 2 if the number of signals is large.

Lower bounds of intermodulation products

The lower bound for the number of intermodulation products falling into the signal channel can be derived as a function of the number of signal channels and the assigned bandwidth using the difference triangular set. Generally, the following procedures determine the channel assignment sequence which minimizes the intermodulation products falling into the worst signal channel:

- a. the signal channels are assigned so that the total of the intermodulation products falling into these signal channels is minimized,
- b. the signal channels are assigned so that the intermodulation products are uniformly distributed.

The total number of intermodulation products falling into signal channels, $T(a_k, k)$, is

$$T(a_k, k) = \sum_{s=1}^k N(a_k, k, s) = 2\{A^2(a_k - 1) + A^2(a_k - 2) + \dots + A^2(2) + A^2(1)\} - k(k - 1) \quad (5)$$

where $A(L)$ indicates the number of times L appears. In Figure 1c, since $A(5) = 1$, $A(4) = 2$, $A(3) = 3$, $A(2) = 4$, and $A(1) = 5$, $T(a_k, k)$ becomes

$$T(6, 6) = 2(1^2 + 2^2 + 3^2 + 4^2 + 5^2) - 6(6 - 1) = 80.$$

In equation (5), the sum of $A(L)$, $L = 1, 2, \dots, a_k - 1$, is

$$A(a_k - 1) + A(a_k - 2) + \dots + A(2) + A(1) = \frac{k(k-1)}{2} \quad (6)$$

Equation (6) denotes that the sum of the number of appearances is equal to the total number of elements contained in the difference triangular set. Equations (5) and (6) demonstrate that $T(a_k, k)$ is proportional to the sum of the squares of the $A(L)$ terms, $L = 1, 2, \dots, a_k - 1$, while the sum of the $A(L)$'s is a constant. Therefore, $T(a_k, k)$ can be minimized by distributing $A(L)$ as uniformly as possible.

The difference triangular set $\{d_{ij}\}$ is characterized as follows: the value of the maximum element d_{1k} is equal to $a_k - 1$, and each element must satisfy the relationship

$$d_{ij} - d_{i'j'} \geq (j - i) - (j' - i'), \quad i \leq i' < j' \leq j$$

The following relationships are obtained by considering these characteristics:

$$d_{1,k} = a_k - 1 \tag{7a}$$

$$d_{1,k-1}, d_{2,k} \leq a_k - 2 \tag{7b}$$

$$d_{1,k-2}, d_{2,k-1}, d_{3,k} \leq a_k - 3 \tag{7c}$$

$$d_{ij} \leq a_k + (j - i) - k \tag{7d}$$

These relationships and the inequality $d_{ij} > d_{i'j'}$, where $i \leq i' < j' \leq j, j - i > j' - i'$, yield

$$A(a_k - 1) = 1 \tag{8a}$$

$$A(a_k - 2) \leq 2 \tag{8b}$$

$$A(a_k - 3) \leq 3 \tag{8c}$$

$$A(a_k - l) \leq l, \quad l = 1, 2, \dots, a_k - 1 \tag{8d}$$

Consequently, the lower bound of $T(a_k, k)$ can be derived by assuming the difference triangular set in which the integers $a_k - l$, where $l = 1, 2, \dots, M$, appear l times, and the other integers, $1, 2, \dots, a_k - M - 1$, appear m times (see Appendix A), where m is the average number of appearances for integers less than $a_k - M$, and M is the integer satisfying the conditions

$$m - 1 < M \leq m \tag{9}$$

If such a difference triangular set is realized, the following relationship among M, m, a_k , and k can be obtained:

$$\begin{aligned} \frac{k(k-1)}{2} &= \frac{M(M+1)}{2} + m(a_k - M - 1) \\ &= (\text{total number of elements}) \end{aligned} \tag{10}$$

If it is assumed that $M = m$,

$$m \simeq \left(a_k - \frac{1}{2}\right) - \sqrt{\left(a_k - \frac{1}{2}\right)^2 - k(k-1)} \tag{11}$$

and the lower bound of the total intermodulation products, $T_l(a_k, k)$, becomes

$$\begin{aligned} T_l(a_k, k) &= 2\{1^2 + 2^2 + \dots + M^2 + m^2(a_k - M - 1)\} \\ &\quad - k(k-1) \\ &= \frac{M(M+1)(2M+1)}{3} + m\{k(k-1) - M(M+1)\} \\ &\quad - k(k-1) \end{aligned} \tag{12}$$

When this total is constant, the intermodulation products falling into the worst signal channel can be minimized by assuming a flat distribution. Therefore, the lower bound of the intermodulation products of the worst channel, $I(a_k, k)$ is

$$\begin{aligned} I(a_k, k) &= \frac{T_l(a_k, k)}{k} \\ &= (m-1)(k-1) + \frac{M(M+1)(2M-3m+1)}{3k} \end{aligned} \tag{13}$$

Although the lower bound of the intermodulation products can be estimated by using equations (13), (11), and (9), the following criteria determine the expected intermodulation performance improvement as a function of the utilization efficiency of the available bandwidth: the normalized intermodulation output $\eta(k, x)$ is defined as the ratio of $I(a_k, k)$ to $\max_s \{I_o(k, s)\}$, and the normalized assigned bandwidth, x , is defined as the ratio of a_k to k . The normalized intermodulation level is then

$$\begin{aligned} \eta(k, x) &= \frac{I(a_k, k)}{I_o[k, s; s = k/2 + \{[1 - (-1)^k]/4\}]} \\ &= \frac{4}{(k-2)(3k-2) + \{[1 - (-1)^k]/2\}} \\ &\quad \cdot \left\{ (m-1)(k-1) + \frac{M(M+1)(2M-3m+1)}{3k} \right\} \end{aligned} \tag{14}$$

where
$$m \simeq \left(kx - \frac{1}{2}\right) - \sqrt{k^2(x^2 - 1) - k(x - 1) + \frac{1}{4}} \quad (15)$$

and M is the integer satisfying equation (9).

Figure 2 shows the relationship between normalized assigned bandwidth

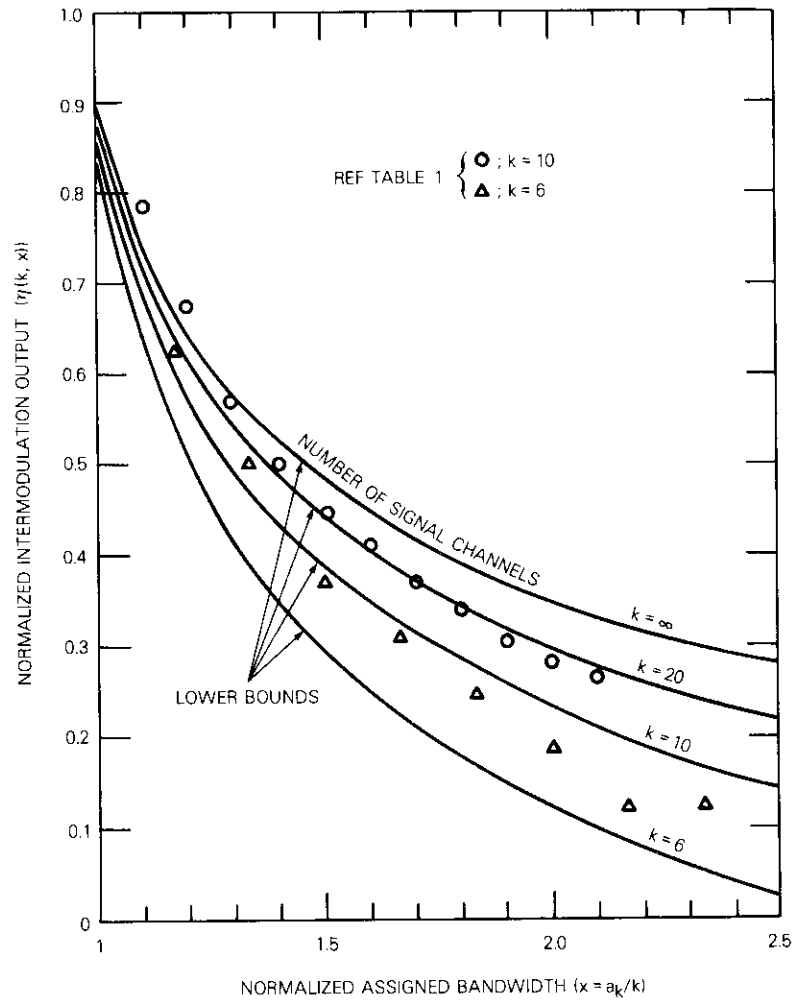


Figure 2. Normalized Intermodulation Products vs Assigned Frequency Bandwidth

and normalized intermodulation output with the number of signal channels as a parameter. Figure 3 indicates the relationship between the number of signal channels and the normalized required bandwidth with the normalized intermodulation output as a parameter. These figures demonstrate that the utilization efficiency of the assigned bandwidth decreases as the number of signal channels increases.

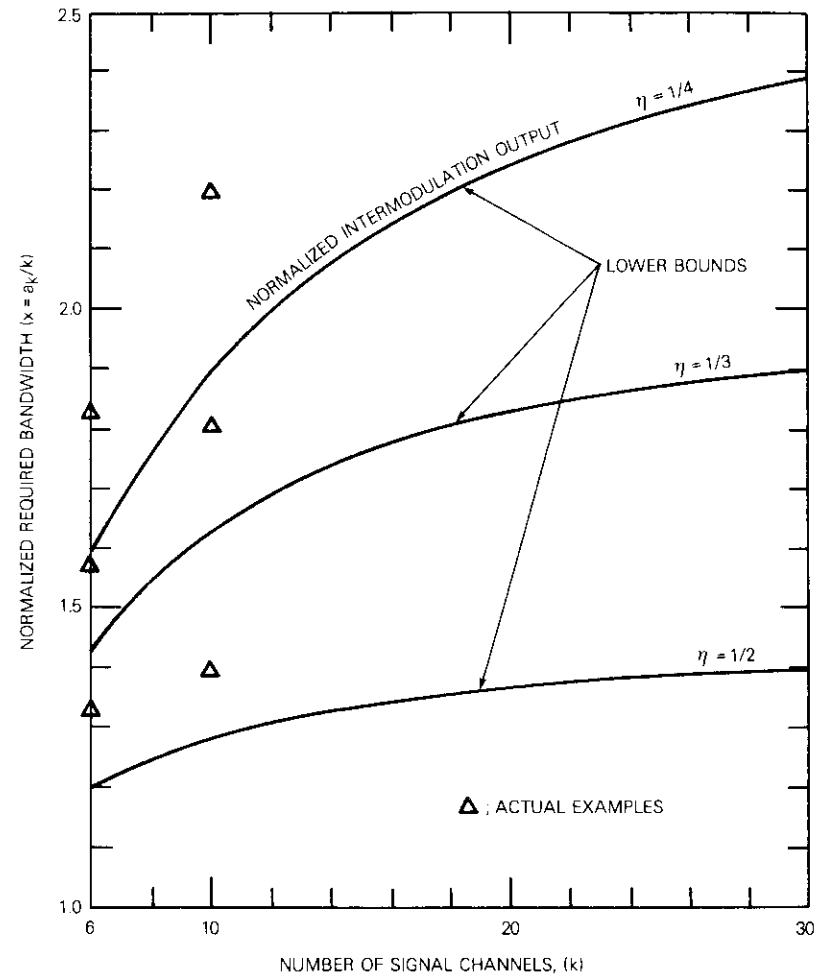


Figure 3. Required Frequency Bandwidth vs Number of Signal Channels

Optimum frequency assignment

For a small number of signal channels, the optimum solution of the intermodulation/minimum channel allocation can be obtained by computing all possible combinations, as shown in Table 1 and Figure 4 ($k = 6$ and 10). The results are also plotted in Figures 2 and 3. In Figure 2, the difference between the lower bound and the solution is about 14–23 percent except in the region of $k = 6$ and $x > 1.5$, where the difference increases because fewer intermodulation products fall into the signal channels. Therefore, the relationship between the intermodulation output and the assigned bandwidth can be estimated effectively by using the lower bound.

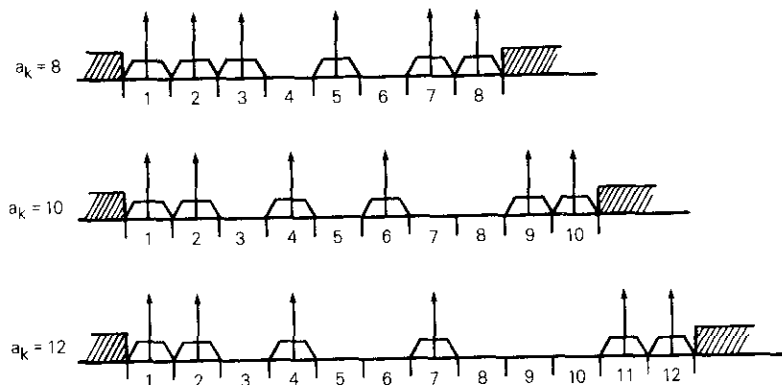


Figure 4. Examples of Optimum Frequency Assignment ($k = 6$)

Conclusions

A lower bound of the intermodulation products falling into the worst channel has been derived using the concept of the difference triangular set. The results show that the intermodulation products falling into the worst signal channel can be reduced by about one half compared to the case of equal-spacing allocation when the assigned frequency bandwidth has a 50-percent margin. Intermodulation/minimum frequency assignment sequences have been solved for practical application. Comparing such optimum solutions with the lower bound evidences that the lower bound derived herein is useful for evaluating the relationship between

TABLE 1. EXAMPLES OF OPTIMUM FREQUENCY ASSIGNMENT SEQUENCES

a. Number of Signal Channels, $k = 6$			
Top Channel, a_k	$x = a_k/k$	η	Channel Spacing
7	1.17	0.625	1 1 2 1 1
8*	1.33	0.500	1 1 2 2 1
9	1.50	0.375	1 1 3 2 1
10*	1.67	0.313	1 2 2 3 1
11	1.83	0.250	1 2 4 2 1
12*	2.00	0.188	1 2 3 4 1
13	2.17	0.125	1 2 4 4 1
14	2.33	0.125	1 1 4 4 3
15	2.50	0.125	1 2 5 4 2
16	2.67	0.125	1 5 2 3 4
17	2.83	0.125	1 2 6 5 2
18	3.00	0.0	1 3 6 5 2

*See Figure 4.

b. Number of Signal Channels, $k = 10$			
Top Channel, a_k	$x = a_k/k$	η	Channel Spacing
11	1.1	0.786	1 1 1 1 2 1 1 1 1
12	1.2	0.673	1 1 1 2 1 2 1 1 1
13	1.3	0.571	1 1 1 2 1 3 1 1 1
14	1.4	0.500	1 1 1 2 1 3 2 1 1
15	1.5	0.446	1 1 1 3 1 3 2 1 1
16	1.6	0.411	1 1 1 3 3 2 2 1 1
17	1.7	0.375	1 1 1 3 3 2 2 2 1
18	1.8	0.340	1 1 2 2 3 3 3 1 1
19	1.9	0.304	1 1 2 4 3 2 3 1 1
20	2.0	0.286	1 1 3 2 4 3 3 1 1
21	2.1	0.268	1 1 2 5 4 1 3 2 1

the utilization efficiency of the assigned bandwidth and the resultant intermodulation impairment level.

Acknowledgment

The author wishes to express his appreciation to Mr. J. C. Fuenzalida, COMSAT, for his kind suggestions. He also wishes to thank Mr. A. Ogawa

and Mr. Y. Yasuda of KDD Laboratories for their helpful advice and useful discussions. (This paper is based partly upon work performed in KDD Laboratories.)

References

- [1] W. C. Babcock, "Intermodulation Interference in Radio Systems Frequency of Occurrence and Control by Channel Selection," *Bell Systems Technical Journal*, Vol. 32, No. 1, 1953, p. 63.
- [2] R. J. F. Fang and W. A. Sandrin, "Carrier Frequency Assignment for Non-linear Repeaters," *COMSAT Technical Review*, Vol. 7, No. 1, Spring 1977, p. 227.
- [3] Y. Hirata and Y. Yasuda, "Intermodulation Free Channel Allocation," *Transactions of IECE*, Vol. 59-B, No. 12, 1976, p. 592.
- [4] R. J. Westcott, "Investigation of Multiple FM/FDM Carriers through a Satellite TWT," *Proc. IEEE*, Vol. 59, No. 2, February 1967.

Appendix A. Difference triangular set minimizing total intermodulation products

The realization of a channel allocation sequence whose difference triangular set exhibits the following characteristics would minimize the total intermodulation products falling into the signal channels:

- a. integers $a_k - l$, where $l = 1, 2, \dots, M$, appear l times,
- b. the other integers, $1, 2, \dots, a_k - M - 1$ (where m is the average number of appearances of integers $1, 2, 3, \dots, a_k - M - 1$, and M is an integer satisfying $m - 1 < M \leq m$) appear m times.

The total of the intermodulation products falling into signal channels, $T_i(a_k, k)$, is then

$$T_i(a_k, k) = 2\{A^2(a_k - 1) + A^2(a_k - 2) + \dots + A^2(2) + A^2(1)\} - k(k - 1) = 2\{1^2 + 2^2 + \dots + M^2 + \underbrace{m^2 + m^2 + \dots + m^2}_{c_k - M - 1}\}$$

$$= 2\{1^2 + 2^2 + \dots + M^2 + m^2(a_k - M - 1)\} - k(k - 1) \tag{A-1}$$

where $A(L)$ is the number of times integer L appears.

Another difference triangular set which contains the following elements is considered:

- a. integers from 1 to $a_k - M - 1$ except X_i and Y_j appear m times;
- b. integers X_i and Y_j appear $m - \Delta_i$ and $m + \Delta_j$ times, respectively, where $1 \leq X_i \leq a_k - M - 1$, $1 \leq Y_j \leq a_k - M - 1$, and $X_i \neq Y_j$;
- c. integers $a_k - l$ except $X_{i'}$ appear l times, where $l = 1, 2, 3, \dots, M$;
- d. integers $X_{i'}$ appear $a_k - X_{i'} - \Delta_{i'}$ times, where $a_k - M \leq X_{i'} < a_k - 1$.

Since the sum of the appearances of each integer is constant as shown in equation (6), the following relationships are obtained:

$$\sum_i \Delta_i + \sum_{i'} \Delta_{i'} = \sum_j \Delta_j \tag{A-2}$$

Then the total number of intermodulation products falling into signal channels, $T(a_k, k)$, is

$$T(a_k, k) = 2 \left\{ 1^2 + 2^2 + \dots + \sum_{i'} (a_k - X_{i'} - \Delta_{i'})^2 + \dots + M^2 \right\} + 2 \left\{ m^2 + m^2 + \dots + \sum_i (m - \Delta_i)^2 + \sum_j (m + \Delta_j)^2 + \dots + m^2 \right\} - k(k - 1) \tag{A-3}$$

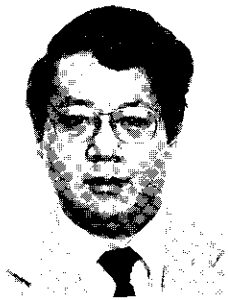
From equations (A-1) and (A-3),

$$T(a_k, k) - T_i(a_k, k) = 2 \left\{ \sum_{i'} \Delta_{i'}^2 - 2 \sum_{i'} (a_k - X_{i'}) \Delta_{i'} + \sum_i \Delta_i^2 - 2m \sum_i \Delta_i + \sum_j \Delta_j^2 + 2m \sum_j \Delta_j \right\} \tag{A-4}$$

Considering equation (A-2) and $a_k - X_{i'} \leq m$ yields

$$\begin{aligned} T(a_k, k) - T_l(a_k, k) &\geq 2 \left\{ \sum_{i'} \Delta_{i'}^2 + \sum_i \Delta_i^2 + \sum_j \Delta_j^2 \right\} \\ &\quad - 4m \left\{ \sum_{i'} \Delta_{i'} + \sum_i \Delta_i - \sum_j \Delta_j \right\} \\ &= 2 \left\{ \sum_{i'} \Delta_{i'}^2 + \sum_i \Delta_i^2 + \sum_j \Delta_j^2 \right\} > 0. \end{aligned} \quad (\text{A5})$$

Thus, $T_l(a_k, k)$ gives the lower bound of the total intermodulation products falling into signal channels.



Yasuo Hirata received B.S. and M.S. degrees in electrical engineering from Kyoto University in 1965 and 1967. Immediately thereafter, he joined KDD Laboratories, where he was engaged in research on digital satellite communications and maritime satellite communication systems. In 1977, he received a Ph.D. in electrical engineering from Kyoto University and joined the COMSAT Advanced System Division as an INTELSAT Nominee. Since that time, he has been engaged in the study of modulation/multiple access techniques

for the future INTELSAT System. He is a member of IECE of Japan and of IEEE.

Index: antenna depolarization, signal measurement, INTELSAT, earth terminals

Antenna depolarization measurements using satellite signals

D. F. DiFONZO AND W. S. TRACHTMAN

(Manuscript received November 3, 1977)

Abstract

Techniques using satellite signal sources for the polarization calibration of large earth station antennas have been developed and successfully utilized to measure the performance of several antennas in the INTELSAT system. If the satellite antennas have high polarization purity, simple relative power measurements determine an earth station antenna's cross-polarization performance. When the satellite antenna polarization is poor, a "reference antenna" technique is necessary for accurate measurements. Several simplified formulas and analysis techniques are described for the circular polarizations employed in the INTELSAT system.

Introduction

Frequency reuse by dual orthogonal polarizations has become an operational reality for several domestic communications satellite systems, such as COMSTAR and SATCOM, which utilize dual linear polarizations. The INTELSAT V satellite will reuse the 4- and 6-GHz satellite frequency bands by means of dual circularly polarized hemispheric and zone coverage antennas with at least 27-dB polarization isolation [1]. Stations being

built for this operation must have polarization isolations greater than 30 dB over their tracking beamwidths. Existing stations must be retrofitted with feed systems to satisfy isolations exceeding 27 dB. These requirements apply to both the down-link (3.7- to 4.2-GHz) and up-link (5.925- to 6.425-GHz) frequency bands.

Measurements of the polarization properties of large antennas require reliable and simple measurement techniques. Use of a satellite signal source to evaluate polarization performance is preferable to boresight and radio-star techniques. Most earth station sites do not have suitable far-field ranges which are free of multipath problems. The radio-star method requires a star source of random polarization and strong flux. On the other hand, a satellite signal source can be effectively stationary (unlike a star) in the antenna's far-field, virtually free of multipath, and accessible to a large number of users. In addition, the satellite source methods permit antennas to be evaluated close to their actual operating elevation angles.

This paper describes two basic methods which have been developed to calibrate the polarization performance of an earth station antenna by using satellite signals. With the reference antenna method, the performance of an earth station antenna is compared with that of a polarization-calibrated reference antenna.

The direct isolation method is applicable when a satellite is available with high-polarization-quality antennas onboard, such as the INTELSAT IV-A F2 and F3 satellites [2]. Since the present INTELSAT frequency reuse system utilizes left- and right-hand sense circular polarizations, several equation simplifications and analysis techniques which are applicable to circularly or nearly circularly polarized waves are presented.

The polarization performance of the Paumalu 1, Etam 2, Mill Village 1, Etam 1, Pleumeur-Bodou 4, and Pleumeur-Bodou 3 antennas has been measured. The results are summarized and used to illustrate various aspects of the testing procedures.

Polarization definitions

Key polarization relationships and several simplifications of polarization analysis for nearly circularly polarized waves will be discussed before describing specific polarization measurement methods. A fundamental relationship for depolarization measurements is the energy coupling (Γ) from a wave incident on an antenna to the output terminal of that antenna. This coupling is given by

$$\Gamma = \frac{(1 + r_w^2)(1 + r_A^2) \pm 4r_w r_A + (1 - r_w^2)(1 - r_A^2) \cos 2\delta}{2(1 + r_w^2)(1 + r_A^2)} \quad (1)$$

where r_w = voltage axial ratio of incident wave, $0 \leq |r_w| \leq 1$
 r_A = voltage axial ratio of antenna, $0 \leq |r_A| \leq 1$
 δ = angle between major axes of wave and antenna polarization ellipses, $\delta = |\tau_w - \tau_A|$.

Figure 1 illustrates the terminology employed to describe the polariza-

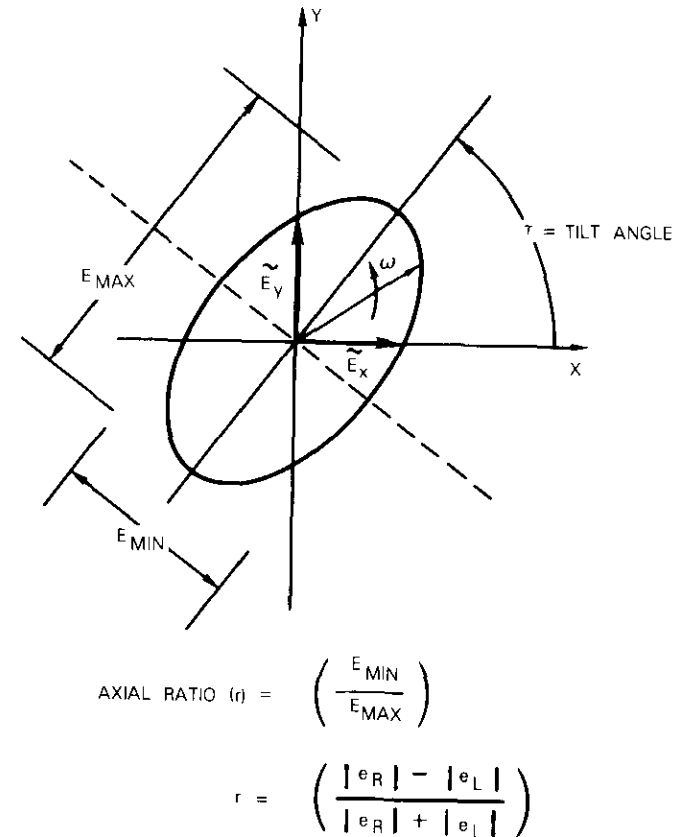


Figure 1. Definitions for Elliptically Polarized Wave

tion properties. The axial ratio, r , is the ratio of the minor axis amplitude of a wave to its major axis amplitude. For convenience, axial ratio is

often expressed in dB, as $R(\text{dB}) = 20 \log_{10} r$. The tilt angle, τ , is the angle of the major axis relative to a reference axis. An arbitrarily polarized wave is considered to be the sum of a right-hand (RH) circularly polarized (CP) wave ($r = 1$) component and a left-hand (LH) CP wave component. The rotation sense of an RH wave is clockwise as observed in a fixed plane with the wave receding from the observer. In equation (1) the plus sign is used when wave and antenna have the same sense of rotation, and the minus sign is used when the senses are opposite.

The polarization isolation, i , of an antenna is the ratio of the energy coupled between the antenna and an incident wave of a reference polarization state to the energy coupled between the antenna and a wave of the orthogonal state of polarization. The polarization state for which the antenna performance has been optimized is usually chosen to be the reference polarization state (co-polarization). The orthogonal polarization state becomes the cross-polarized state.

Sources of antenna depolarization

The basic configuration of a dual-polarized earth station antenna is shown in Figure 2. The antenna contains two transmit orthomode transducer (OMT) ports and two receive OMT ports, one for each sense of circular polarization. The block labeled "antenna system" contains the components that affect the antenna transmit and receive polarizations, including the polarizers, waveguide, tracking couplers, feed horn, subreflector and support spars, and the reflector. Some types of systems, such as beam waveguide, have additional reflectors and waveguides which form part of the feed system. Many arrangements of feed polarizers and duplexers are

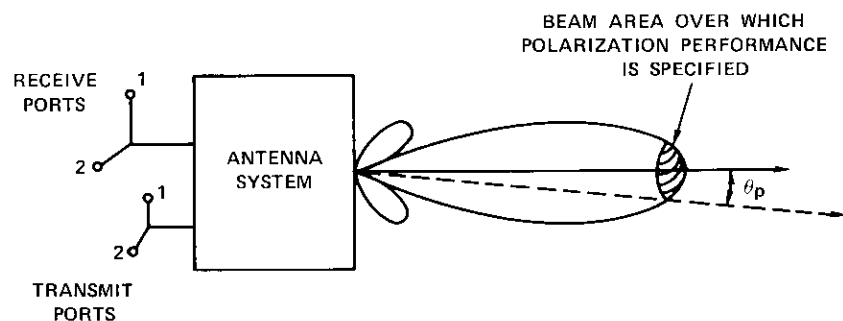


Figure 2. Basic Port Configuration of Dual-Polarized Earth Station Antenna

possible. Reference 3 provides an excellent summary of various types of frequency reuse feed systems.

Ideally, excitation of the RHCP transmit port would produce an RHCP beam with a 0-dB axial ratio, *i.e.*, a pure RHCP beam with no LHCP energy. This condition should apply over the antenna's tracking beamwidth. Various depolarization sources will cause cross-coupling of energy from one polarization sense to the other, resulting in a finite polarization isolation (non-zero axial ratio) in the antenna beam.

One source of depolarization in a CP system is the impedance mismatch at the antenna OMT ports. If the vertical transmit port of the antenna in Figure 2 is excited, transmission through the polarizer produces an RHCP signal incident at the interface between the polarizer and feed. Feed and subreflector mismatches cause some energy, converted to LHCP by the reversal of direction, to be reflected back through the polarizer. Hence, a signal will appear at the horizontal OMT port and if an additional mismatch exists at this port LHCP energy will also emerge from the antenna. The total cross polarization produced by these effects is the sum of the mismatch return losses of the feed/subreflector and the OMT. Typically, these return losses are each about -20 dB, which would result in an equivalent antenna axial ratio of 0.17 dB. Thus, the effects of VSWR place a minimum value on the antenna axial ratio even without other depolarizing effects. The effects of impedance matching in circularly polarized systems are extremely important and can, in some cases, become dominant in limiting the achievable performance.

Another significant depolarizing effect is due to the differential phase shift introduced by the polarizer. An ideal polarizer, producing perfect CP, would have a differential phase shift of exactly 90° . The axial ratio in dB produced by a polarizer with differential phase shift of 10° or less from 90° is almost a linear function of phase error and can be approximated by

$$R_p \approx 0.152 \theta \text{ dB} \quad (2)$$

where θ is the difference in degrees between the actual phase shift and 90° . A phase error less than 4° is sufficient to cause the axial ratio to exceed 0.5 dB.

Differential amplitude effects can also degrade the axial ratio by causing a difference in the transmission gain of otherwise equal amplitude wave components; however, in most systems this effect is small. The unequal E- and H-plane amplitude and phase patterns of the feed horn, which are a more common source of errors, affect off-axis performance. Other

sources of depolarization include differential phase shift in waveguides within the feed system, subreflector misalignment, reflector asymmetries, and dispersion in beam waveguides.

Limitations and source of error in depolarization measurements

The problems associated with antenna polarization measurements using satellite signal sources vary with the polarization quality of the satellite source. If the satellite signal is very nearly CP (less than 0.5-dB axial ratio) the actual satellite axial ratio is absorbed as a measurement uncertainty. For satellites with polarization that is not as pure, the axial ratio and tilt angle of the satellite polarization may be calibrated and the satellite contribution numerically removed from the measurement. For the latter case, the degree of accuracy of the satellite polarization calibration is usually the major error source.

For a pure CP wave ($r_w = 1$) incident on an antenna, tilt angle becomes irrelevant, and the antenna's isolation is related to the antenna's axial ratio by the expression

$$r_A = \frac{\sqrt{i} - 1}{\sqrt{i} + 1} \quad (3)$$

If the wave incident on the test antenna is not perfect CP, the isolation depends on both the axial ratios of the wave and the antenna and their respective tilt angles. Figure 3 shows the possible range of isolation for an incident wave with a 0.5-dB axial ratio. The two curves represent the extremes of coupling when the major axes of the wave and antenna ellipses are parallel ($\delta = 0^\circ$) and when they are perpendicular ($\delta = 90^\circ$).

A measured isolation value of 30 dB could have been obtained from antenna axial ratios between 0.05 and 1.05 dB. Unless the exact polarization state is known (axial ratio and tilt angle), the earth station antenna axial ratio can be determined only within these two extremes.

For the direct isolation measurement method using a satellite source such as INTELSAT IV-A F2 or F3, the satellite axial ratio imposes an uncertainty on the measured data, since only relative power is measured at co-polarized and cross-polarized antenna ports and no tilt angle information is obtained. The uncertainty has been minimized for these satellites by designing the satellite antennas to exhibit low axial ratio over the up-link and down-link frequency bands (axial ratio < 0.25 dB over channels 2 and 4 and < 0.5 dB worst case over the rest of the channels).

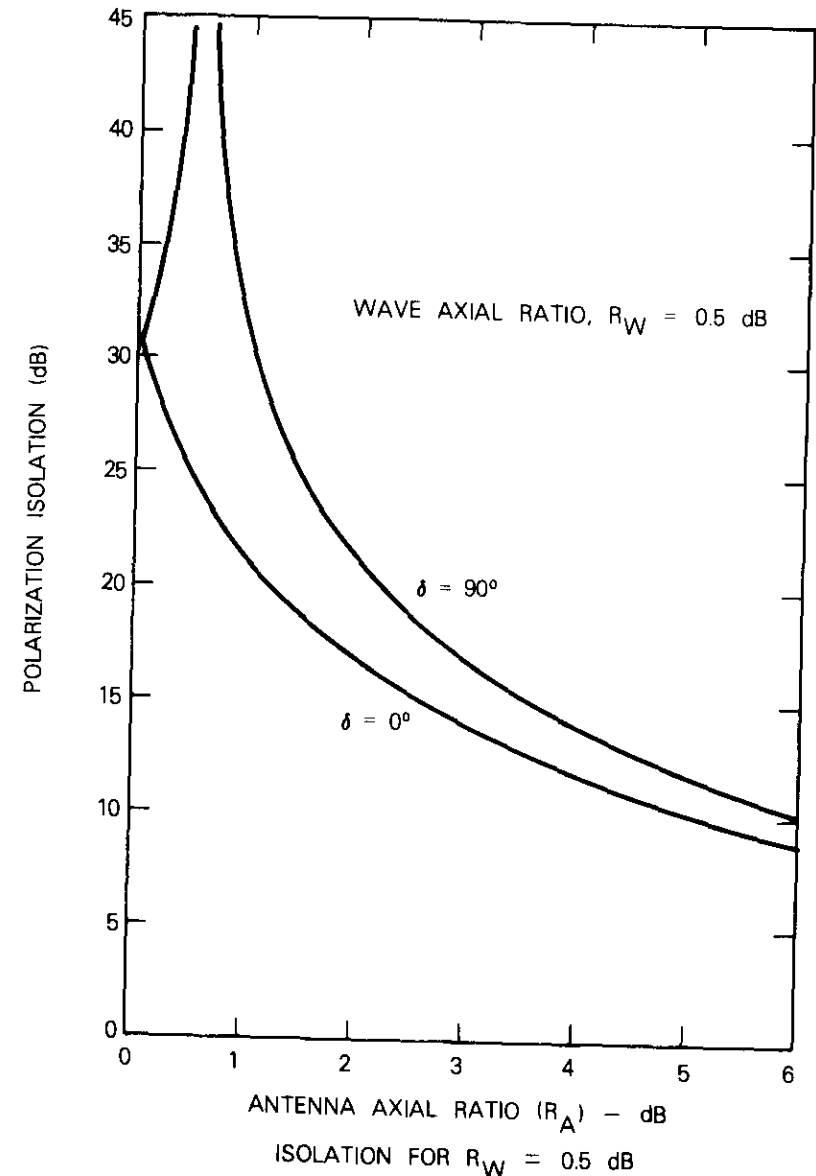


Figure 3. Polarization Isolation vs. Antenna Axial Ratio for a Wave with 0.5-dB Axial Ratio

Simplified formulas and polarization diagrams for CP isolation

Antenna isolation of 30 dB corresponds to a 0.55-dB axial ratio when the incident wave is perfect CP. The antenna axial ratios possible for a 30-dB measured antenna isolation and 0.5-dB axial ratio incident wave are the sum and difference in dB of the axial ratios of the wave and the corresponding antenna axial ratio assuming a CP source. While this relationship is not exact for all possible axial ratios, it is a remarkably good approximation for axial ratios near CP (less than about 3 dB). For such cases, a formula for isolation that is considerably simpler than equation (1) can be derived by using the first term of the Taylor series expansion for $\ln r$ (where \ln is the natural logarithm):

$$\ln r \approx 2 \left(\frac{r - 1}{r + 1} \right) \quad (4)$$

The axial ratio, R , in dB, can then be approximated as

$$R \text{ (dB)} \approx 17.37 \frac{r - 1}{r + 1} \quad (5)$$

If this approximation is used in equation (1) with the minus sign for opposite senses, when R is small (in the vicinity of circular polarization), the isolation can be expressed as:

$$\text{Isol (dB)} \approx 10 \log_{10} (R_{eq}^2) - 24.8 \quad (6)$$

where
$$R_{eq}^2 = R_w^2 + R_A^2 + 2R_w R_A \cos 2\delta \quad (7)$$

R_{eq} is an equivalent composite axial ratio in dB whose components, R_w and R_A , are the wave and antenna axial ratios in dB. The equivalent axial ratio, R_{eq} , is simply the sum of the two vectors R_w and R_A where the magnitudes are equal to the axial ratios in dB, and the angle between them is equal to twice the tilt angle. The error incurred is less than 0.35 dB for wave and antenna axial ratios less than 3 dB.

While the exact polarization formulas require ordered 4 x 4 matrices (see Appendix A), the simplified approximate formulas are linearized; therefore, the order in which depolarization effects occur is no longer

important. All depolarizing terms can be collected into a single R_{eq} for an antenna without evaluating the depolarization caused by each component.

Figure 4 illustrates the utility of this polarization mapping for antenna depolarization measurement. If both the incident wave, R_i , and the output wave from the antenna, R_o , have been calibrated in axial ratio magnitude and tilt angle, simple vector arithmetic will yield R_A , the antenna's equivalent axial ratio response. The linearized properties of this mapping allow

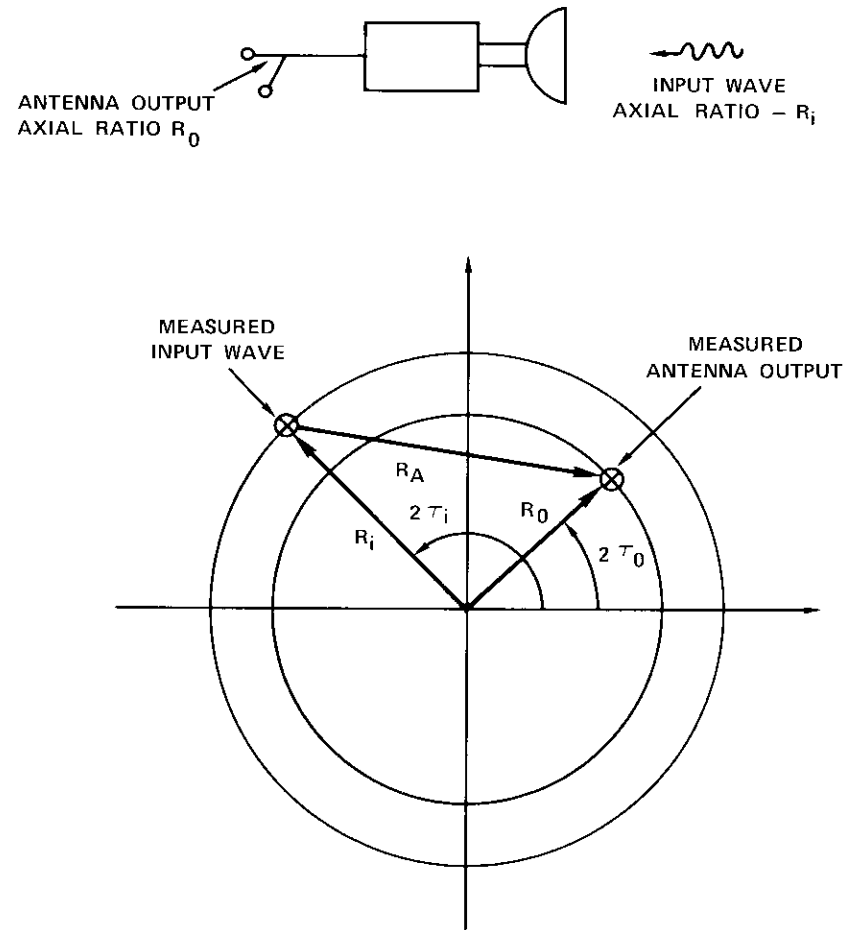


Figure 4. Antenna Depolarization Expressed as the Vector Difference of Input and Output Polarization States

R_A to be translated to the origin, implying that R_A would be the antenna's response to a pure CP input wave.

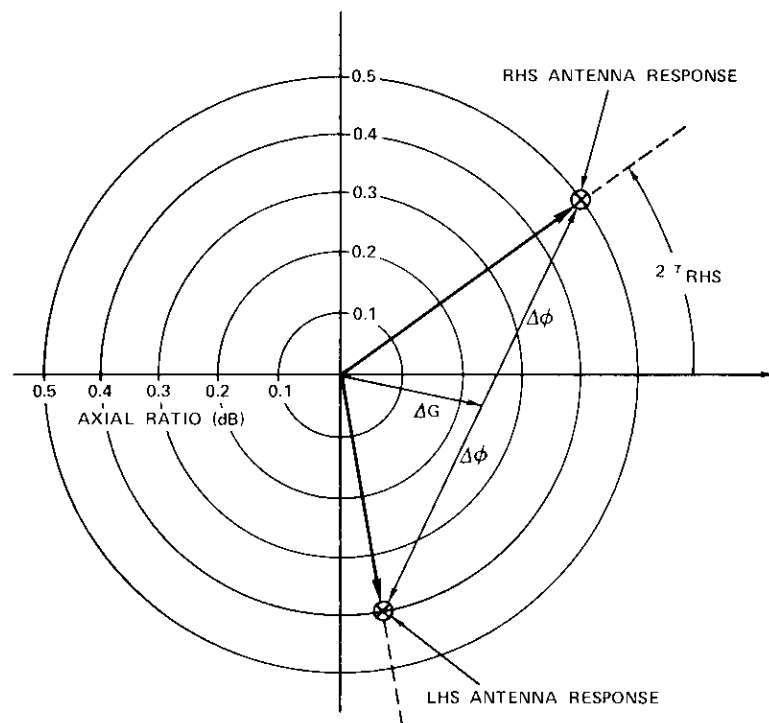
The results of this technique must be applied with caution. The process illustrated in Figure 3 is valid for a single sense of circular polarization. Because the equivalent R_A can consist of a series of independent polarization terms, some of these terms may be canceled for one polarization sense and added for the other polarization sense. In principle, the LHCP and RHCP polarization performance of an antenna may differ significantly. Thus, although an antenna may exhibit good polarization for a single sense of incident polarization, it will not necessarily have the same polarization for the opposite sense. Appendix A presents in more detail matrix relationships for determining antenna depolarization given input and output polarization states.

A measurement of the antenna system response for both polarization senses of incident waves (RHCP and LHCP) identifies both differential amplitude attenuation (ΔG) and differential phase delay ($\Delta\phi$) depolarization components within the antenna system (see Figure 5). The left- and right-hand sense antenna responses for a differential phase delay component are orthogonal ($|R_{LHS}| = |R_{RHS}|$; $2\Delta\tau = 180^\circ$), while the responses for a differential amplitude attenuation component are identical on the polarization ellipse diagram. The relationships of the polarization ellipse orientation angles to the spatial angles at which the differential phase delay or amplitude attenuation is introduced are given in Table 1.

TABLE 1. RELATIONSHIPS OF TILT ANGLE TO THE SPATIAL ANGLES OF INTRODUCTION OF DIFFERENTIAL PHASE DELAY OR ATTENUATION

Angle of Introduction of Differential Phase Delay, ϕ_{PD}	Angle of Introduction of Differential Amplitude Attenuation, ϕ_{AA}
$\tau (RHS) = \phi_{PD} + 45^\circ$	$\tau (RHS) = \phi_{AA} \pm 90^\circ$
$\tau (LHS) = \phi_{PD} - 45^\circ$	$\tau (LHS) = \phi_{AA} \pm 90^\circ$
$2\Delta\tau_{PD} = 180^\circ$	$2\Delta\tau_{AA} = 0^\circ$

Polarization diagrams demonstrate that proper sets of measurements allow error-contributing terms to be separated from the desired measurement data. The contribution of the polarizer used for the measurements can be separated from the contribution of the rest of the antenna feed and optics by two measurements if the axial ratio of the polarizer is known



$\Delta\phi$ = AXIAL RATIO COMPONENT DUE TO DIFFERENTIAL PHASE DELAY
 ΔG = AXIAL RATIO COMPONENT DUE TO DIFFERENTIAL AMPLITUDE ATTENUATION

Figure 5. Polarization Diagram for CP Antenna Analysis

through independent calibration. Figure 6 illustrates this approach. First, the antenna system response to one sense of polarization is measured with the polarizer in a given orientation. The measured isolation is shown as a circle whose radius is the equivalent axial ratio (R_1) in dB. The polarizer/OMT assembly is then physically rotated 90° in the antenna and isolation is measured again, yielding a circle of magnitude R_2 .

Since there is a 90° difference in the polarizer physical angle for the two measurements, the polarizer axial ratio contributions for each position are 180° out of phase. Hence, the two circles in Figure 4 will be spanned by a segment with a magnitude twice the axial ratio of the polarizer. The magnitude of the vector from the origin to the mid-point of this segment will equal the axial ratio in dB of the antenna system (R_A) minus

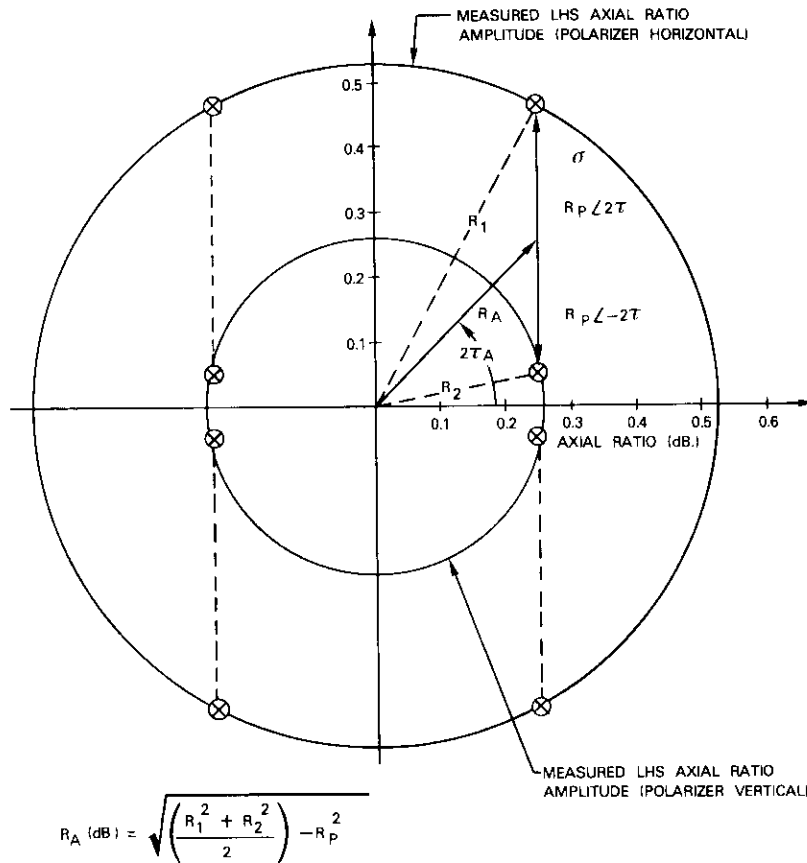


Figure 6. Polarization Diagram with Error Effects of Quarter-Wave Polarizer

the polarizer/OMT assembly (R_p). These quantities can be related by using simple vector arithmetic to yield

$$R_A (dB) = \sqrt{\left(\frac{R_1^2 + R_2^2}{2}\right) - R_p^2} \quad (8)$$

Figure 6 indicates that, in general, there are four locations where the segment of length $2R_p$ at a given orientation will exactly span the two circles. All the resulting antenna values (R_A) will have the same magnitude,

but the tilt angle will be ambiguous. Thus, even though two independent isolation measurements allow the polarizer contribution to be extracted from the antenna system contribution, there is insufficient information to determine the tilt angle of the antenna system depolarization [4].

Measurements using the direct isolation measurement method

The need for a high-quality satellite source to facilitate depolarization measurements contributed to the inclusion of the "Dual-Polarization Experiment" onboard the INTELSAT IV-A F2 and F3 satellites. These satellites have been fitted with up-link and down-link low-axial-ratio global beam antennas connected to the even-numbered transponders. For transponder channels 2 and 4, the global beam antennas are dual polarized using the redundant transponder elements.

Figure 7 is a simplified schematic of the INTELSAT IV-A F2 global transponders. The C-switches on receivers 5 and 6 can connect either receiver to either port of the dual-polarized up-link antenna. The channel 2 and 4 C-switches can route the down-link signal to transmit either sense of CP from the 4-GHz global horn. For channels 6, 8, 10, and 12, the down-link is constrained to be RHCP.

The dielectric-loaded satellite horn antennas, developed by Hughes Aircraft Company based on a design concept proposed by Satoh [5], have axial ratios less than 0.25 dB over the earth's field of view ($\pm 9^\circ$) in channels 2 and 4. Their performance in channel 12 is poorer, with a worst-case axial ratio of 0.5 dB. The actual axial ratio observed by an earth station antenna depends upon the position of the antenna in the satellite beam.

The actual depolarization measurements conducted by using the direct isolation method with INTELSAT IV-A F2 and F3 as a satellite source are straightforward. Figure 8 is a diagram of the test setup used by COMSAT Laboratories for such measurements. The receive system must be capable of narrow-bandwidth operation (< 1 -kHz noise bandwidth) to achieve a suitable dynamic range for the cross-polarized measurements. A single high-stability oscillator is used as the second local oscillator for the down-converter as well as the primary source for the up-converter. This allows the transmitted frequency to be changed by a single control while the received test carrier is maintained at a constant IF. The HP312B selective voltmeters are used as narrowband receivers (operating at ≈ 10 MHz), but any receivers with the appropriate effective bandwidth and dynamic range are suitable.

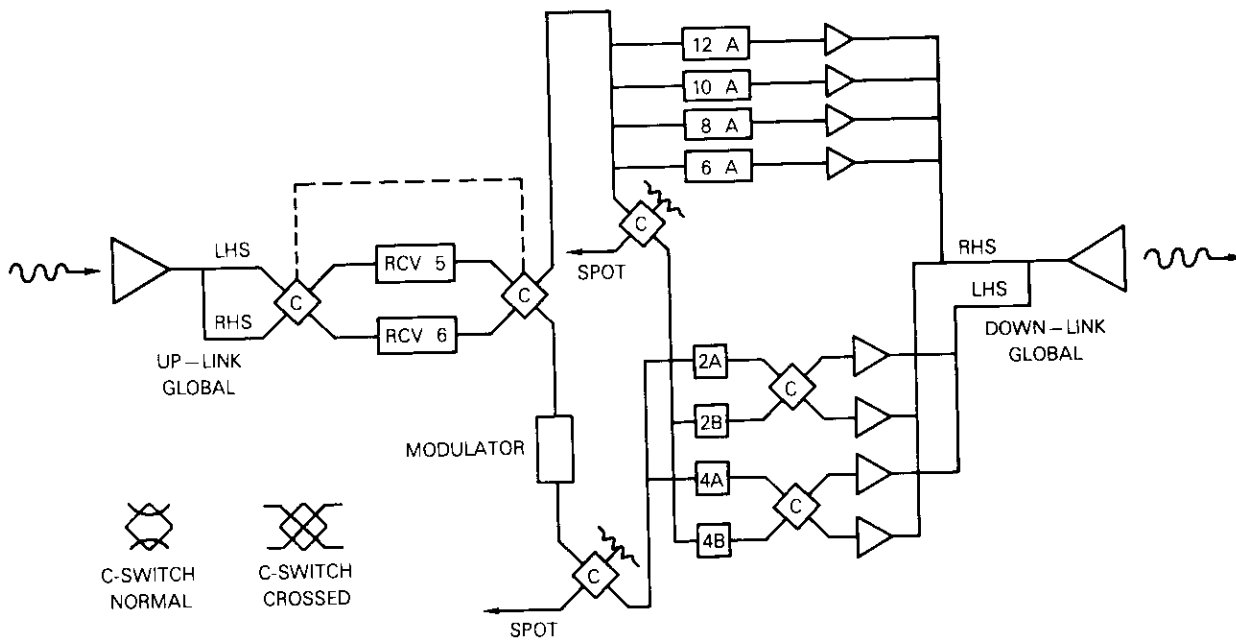


Figure 7. Simplified Block Diagram of INTELSAT IV-A F2 and F3 Dual Polarization Transponder

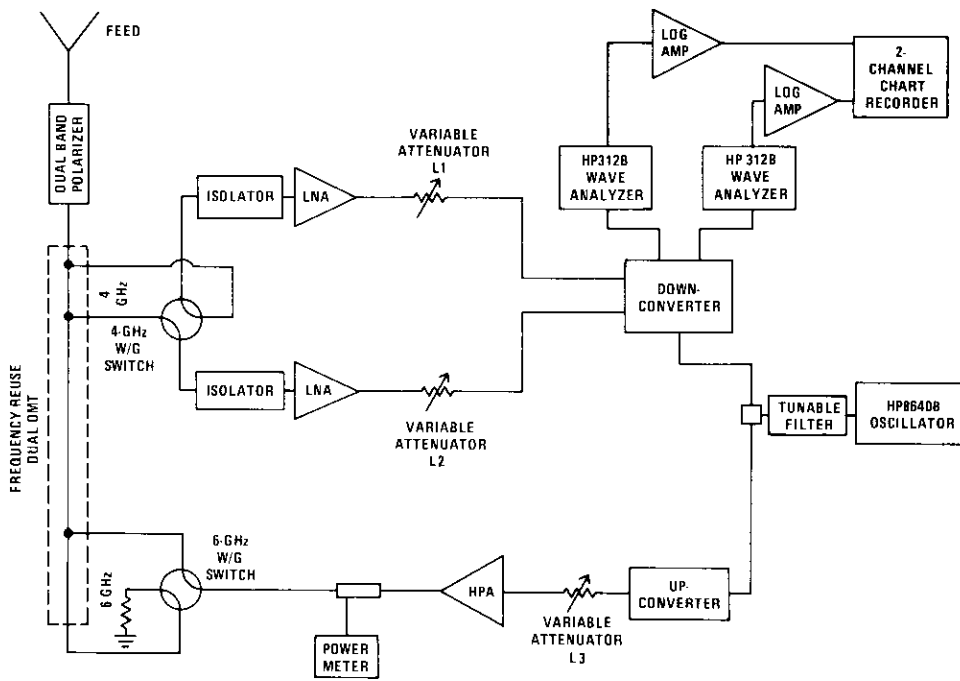


Figure 8. Test Setup for Direct Isolation Measurements

For the tests, the satellite is configured to operate with the same sense of polarization for which the antenna is being used, and a 6-GHz test carrier is transmitted to the satellite. The resulting 4-GHz down-link carrier power is measured on the receiver channel connected to the co-polarized antenna port. The 4-GHz waveguide switch at the OMT ports is then rotated and the cross-polarized level is measured with the same receiver channel. (This procedure eliminates any errors due to different receiver channel gains.)

The dB difference between the two power levels provides the down-link isolation. For channels 2 and 4, the down-link antenna isolation can be determined for both senses of polarization, since the satellite can operate in both polarizations over these channels.

The isolation measured by using this technique is not precisely the isolation of an antenna operating in a dual-polarized system. A strictly correct technique would require the power to be measured at the same antenna OMT port while the incident wave is changed from a co-polarized to a cross-polarized sense. This measurement, however, is difficult to implement because it requires a dual-polarized satellite and accurate knowledge of the incident wave power density for each sense of polarization.

The co-polarized responses for left- and right-hand sense polarizations are typically identical. Therefore, polarization isolation can be accurately measured by referring the cross-polarized energy in one port of the antenna's OMT to the co-polarized energy in the other OMT port, requiring only the comparison of two signals from a single incident wave.

Up-link measurement is equally straightforward. A single down-link receive chain is monitored, while a carrier is transmitted to the satellite through the co-polarized antenna OMT port and then transmitted with equal power through the cross-polarized antenna OMT port. The dB difference between the received down-link power levels for these two cases is the antenna up-link isolation. Satellite linearity must be maintained by proper choice of up-link power. If this is not practical, an alternate approach is to match the received down-link power levels for the two cases and to measure the dB difference in transmitted power when using the co-polarized and cross-polarized OMT transmit ports.

Down-link co-polarized and cross-polarized antenna patterns can be obtained simultaneously by equalizing the gains of the co-polarized and cross-polarized receive chains using variable attenuators. With a cooperating antenna providing an up-link carrier, the test antenna is slewed past the satellite while the received power in each OMT port of the test antenna is displayed on a 2-channel chart recorder. When the present equipment is

used, however, the up-link co-polarized and cross-polarized antenna patterns must be taken sequentially. The station under test transmits a co-polarized up-link carrier. The power received by and retransmitted from the satellite is recorded at a cooperating earth station while the transmit antenna is slewed. The antenna is returned to its original position, the transmit carrier is changed to cross-polarization, and the process is repeated. This test has some difficulties. The co-polarized and cross-polarized patterns must be aligned, since they are not recorded at the same time, and satellite linearity must be maintained. One way to allow simultaneous measurement of co-polarized and cross-polarized up-link antenna patterns would be to transmit two carriers (one LHCP and one RHCP) which are slightly offset in frequency.

Measurements using the reference antenna method

If the satellite source has a poor axial ratio, *e.g.*, 1-3 dB, as in the INTELSAT IV series, a different measurement method must be employed. This measurement technique relies on the calibration of the satellite polarization state and the removal of the satellite contribution from the measured antenna polarization response. If it is possible to determine both the axial ratio and tilt angle of a wave incident on a test antenna and those of that same wave as it appears at the output of the test antenna, the depolarization of the antenna can be mathematically extracted from these input and output polarizations [6].

The test setup used to perform this measurement, shown in Figure 9, requires an accurately calibrated reference antenna. For this purpose, a 4.57-m Cassegrain antenna system (see Figure 10) was used. This transportable antenna has a 2-section base assembly containing the azimuth and elevation drives. The main dish is composed of a central hub and six petal sections. This reference antenna has been calibrated at COMSAT Laboratories in both axial ratio magnitude and tilt angle so that the error of the reference antenna can be removed from the calibration of the satellite signal. The repeatability of this calibration is such that, after disassembly, shipping, and reassembly of the reference antenna, there is less than ± 0.2 dB of uncertainty in the calibration of the satellite signal polarization state.

The depolarization of the earth station antenna in the receive band (3.7 to 4.2 GHz) is measured by first sending a carrier from the test antenna and using the 4.57-m reference antenna located near the test antenna

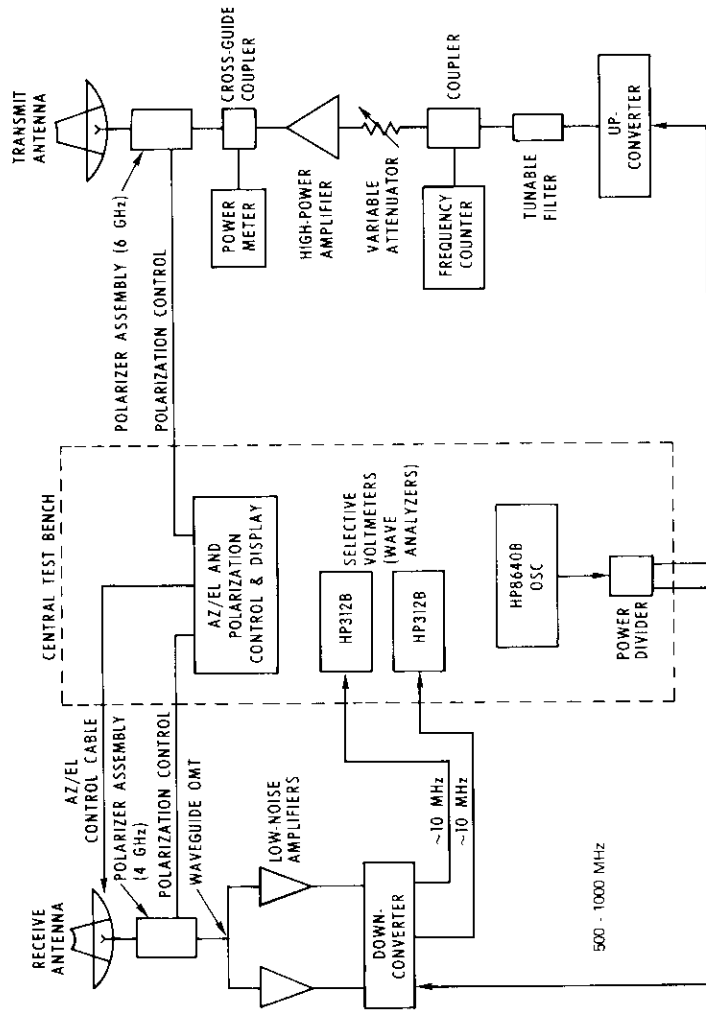


Figure 9. Test Setup for Reference Antenna Method

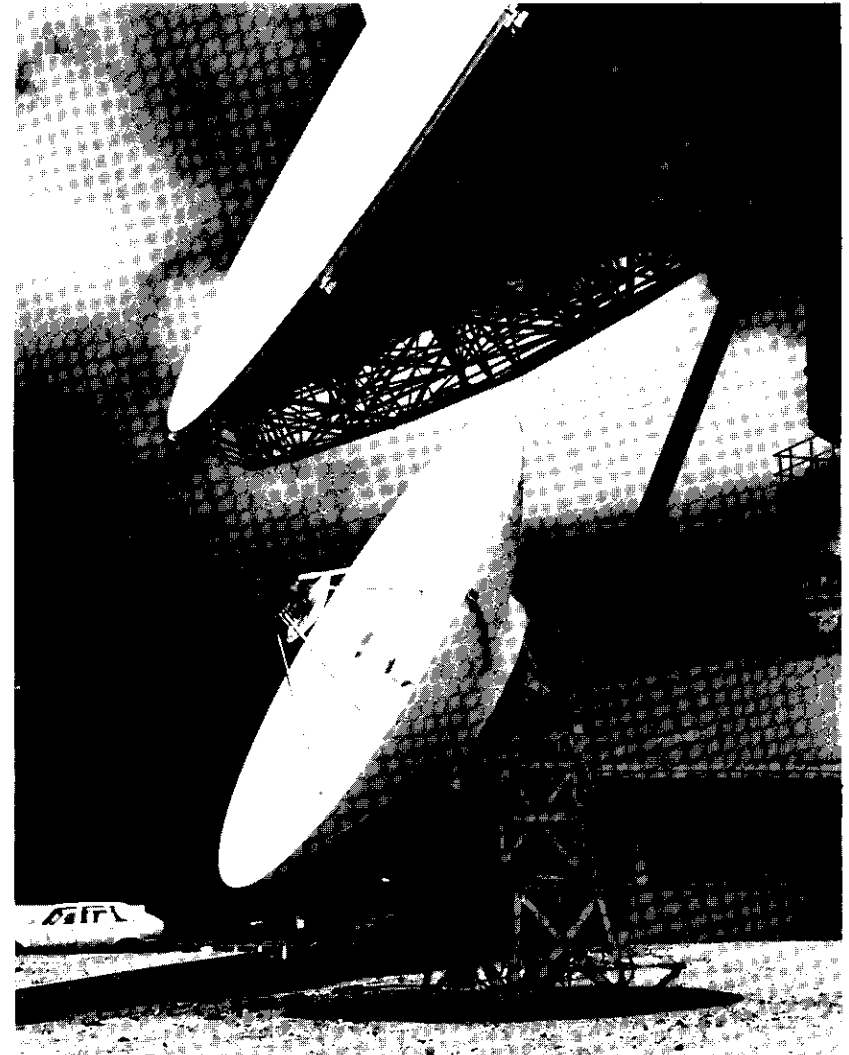


Figure 10. 4.57-meter Polarization Reference Antenna

to receive the signal from the satellite. The axial ratio and tilt angle of the wave incident at the site are measured by the reference antenna using the polarization matching feed network shown in Figure 11. This device consists of rotatable, cascaded, 90° ($\lambda/4$) and 180° ($\lambda/2$) polarizers which can

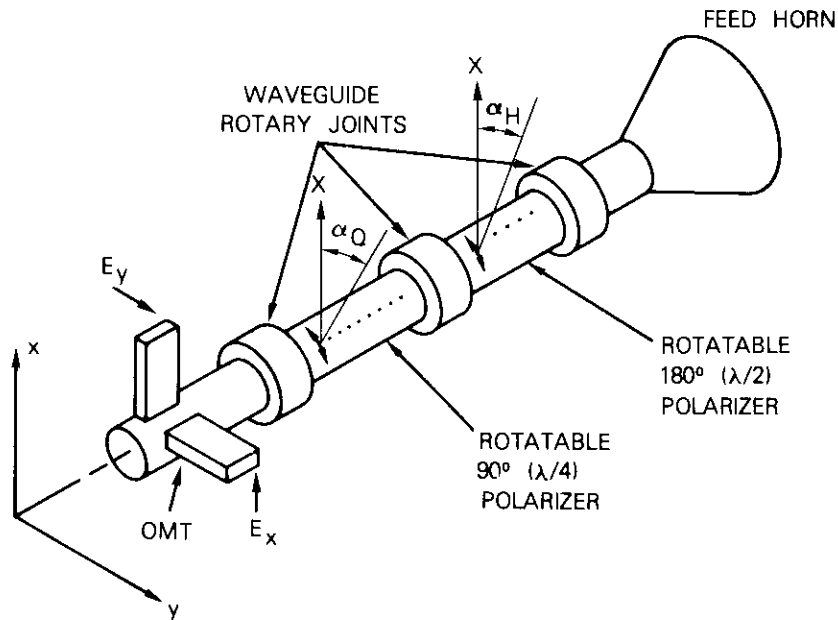


Figure 11. Circuit for Measuring Polarization State

produce any polarization state with respect to either OMT port. The angles of the two polarizers (α_Q and α_H) (*i.e.*, the angles of the phase delay planes) are adjusted to null a signal at one OMT port, thereby creating a polarization orthogonal to that of the incident wave at that port. The other port is "polarization matched," and the polarization state is uniquely related to the polarizer angles [7], [8] which are read out on a digital display. With perfect polarizers, the axial ratio, R , in dB and tilt angle, τ , are given by

$$R = 20 \log_{10} |\tan(\alpha_Q)| \quad (9)$$

and

$$\begin{aligned} \tau &= (2\alpha_H - \alpha_Q), & 0^\circ \leq \alpha_Q \leq 45^\circ \\ \tau &= (2\alpha_H - \alpha_Q) \pm 90^\circ, & 45^\circ < \alpha_Q \leq 90^\circ \end{aligned} \quad (10)$$

This procedure is used to calibrate the incident wave polarization state at each measurement frequency. The polarization matching network is

then connected to the test antenna, and the reference antenna is used to transmit to the satellite. A similar set of measurements, which provides new values of axial ratio and tilt angle, yields the combined values of satellite polarization state and the further depolarization due to the test antenna. The test antenna's polarization response can be calculated using the satellite polarization state calibrated by the reference antenna as an input polarization and the measured test antenna's output polarization. The approximate vector relationships described above permit the calculation of antenna depolarization as the vector difference between the input polarization state and the output polarization state (Figure 4).

This procedure can also determine the up-link (5.925- to 6.425-GHz) polarization response of the test antenna. For this case, a 6-GHz polarization matching network, similar to the one used at 4 GHz, is connected to the antenna under test. The reference antenna simply monitors the down-link power. Up-link polarization is adjusted until the down-link signal vanishes, indicating an up-link polarization state which is orthogonal to the combined satellite and test antenna polarization states.

After these data are obtained for all frequencies and off-axis angles of interest, the 6-GHz polarization matching network is installed in the reference antenna, and the axial ratio and tilt angle of the satellite polarization state are measured. The test antenna's up-link polarization response can then be extracted from those two sets of data.

Measurement results

From September 1975 through August 1977, the antenna polarization performance of the Etam 1 and Etam 2 antennas in West Virginia, the Mill Village 1 antenna in Nova Scotia, the Paumalu 1 antenna in Hawaii, and the Pleumeur-Bodou 3 and 4 antennas in France was measured by using these techniques. The following measurement results are presented to illustrate the use of the test techniques.

Figure 12 shows the on-axis up-link polarization isolation for the Paumalu 1 antenna, which is a 30-m Cassegrain antenna with its sub-reflector supported by a bipod structure. These measurements were performed using the direct isolation measurement method with the INTELSAT IV-A F2 satellite. Figure 12, which shows the isolation measured with the antenna polarizer in two positions 90° apart (parallel and perpendicular to the bipod), indicates the result of removing the polarizer's contribution to the depolarization. The polarizer contribution has been separated from

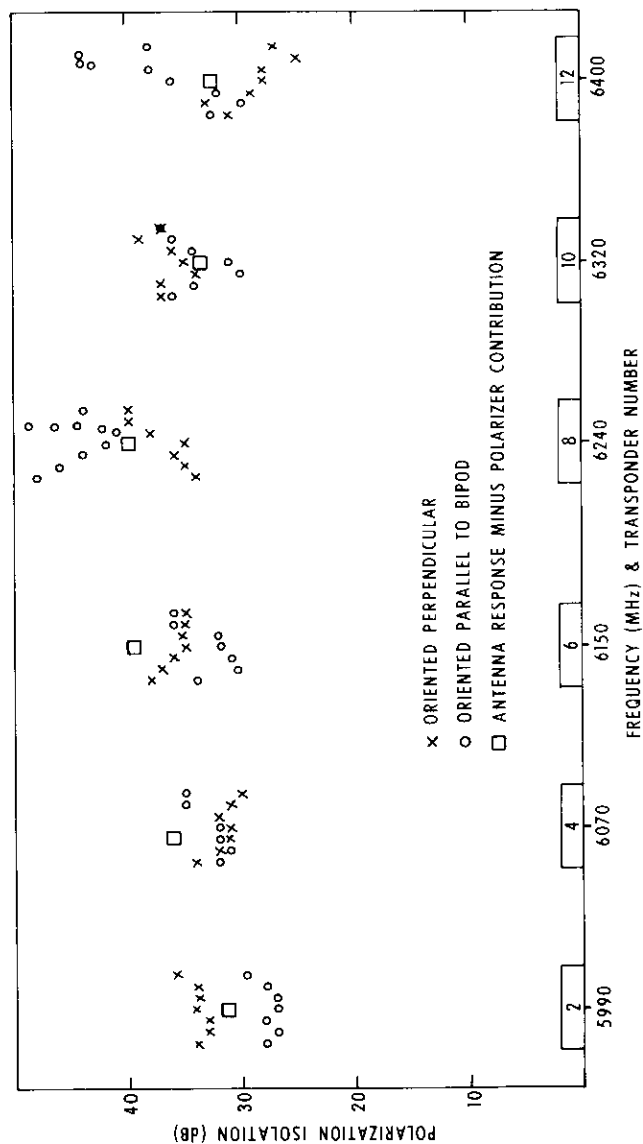


Figure 12. Paumalu 1 Antenna Up-Link Polarization Isolation, INTELSAT IV-A F2

the remainder of the antenna because the polarizer used for the tests is not the operational polarizer of the station.

Figure 13 presents the on-axis up-link axial ratios for the recently modified Etam 1 antenna. These measurements were conducted by using the direct isolation method with INTELSAT IV-A F2. The measurement results are given for both senses of CP in transponders 2 and 4 in which the satellite operates in both polarizations. The noticeable rise in axial ratio at the high end of the band is an error introduced by the satellite antenna axial ratio, which degrades at the upper frequencies. The station polarizer's contribution is included, since it is part of the operational station.

The direct isolation method is quite simple and very rapid; thus, it is practical to measure the antenna isolation off axis as well as directly on beam peak. Figure 14 shows isolation contours for the 26-m-diameter Mill Village 1 antenna over the angular extent of $\pm 0.12^\circ$ in azimuth and elevation around beam peak.

Figure 15 shows the down-link on-axis axial ratios for the Pleumeur-Bodou 4 beam waveguide antenna measured using the 4.57-m reference antenna method with the INTELSAT IV F3 satellite. Because this method does not rely on high polarization purity from the satellite, all available transponder frequencies may be used.

Conclusions

Procedures which facilitate the accurate measurement of large earth station antenna polarization characteristics using satellite signal sources have been developed and successfully utilized. When a satellite with high polarization quality is available, antenna polarization can be measured quickly and simply. If the source satellite has poor polarization quality, the reference antenna method, which is more involved, may be used to secure accurate results. Simplified analytical procedures for circularly polarized systems permit rapid analysis and contribute to a convenient geometric interpretation of depolarization effects.

Acknowledgments

The authors would like to acknowledge the significant contributions to the development of these test techniques by William J. English. The polarizers and OMTs used in the measurements were designed by Robert Gruner.

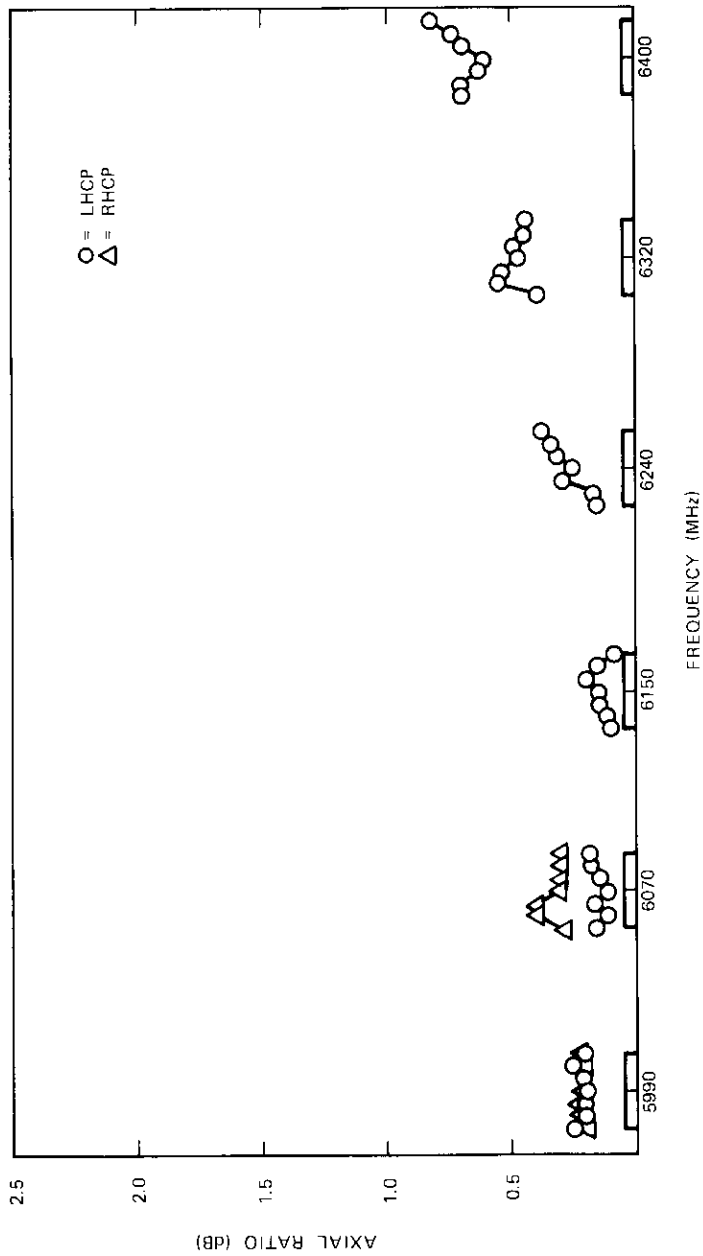


Figure 13. Etam 1 Antenna Up-Link Axial Ratio, INTELSAT IV-A F2

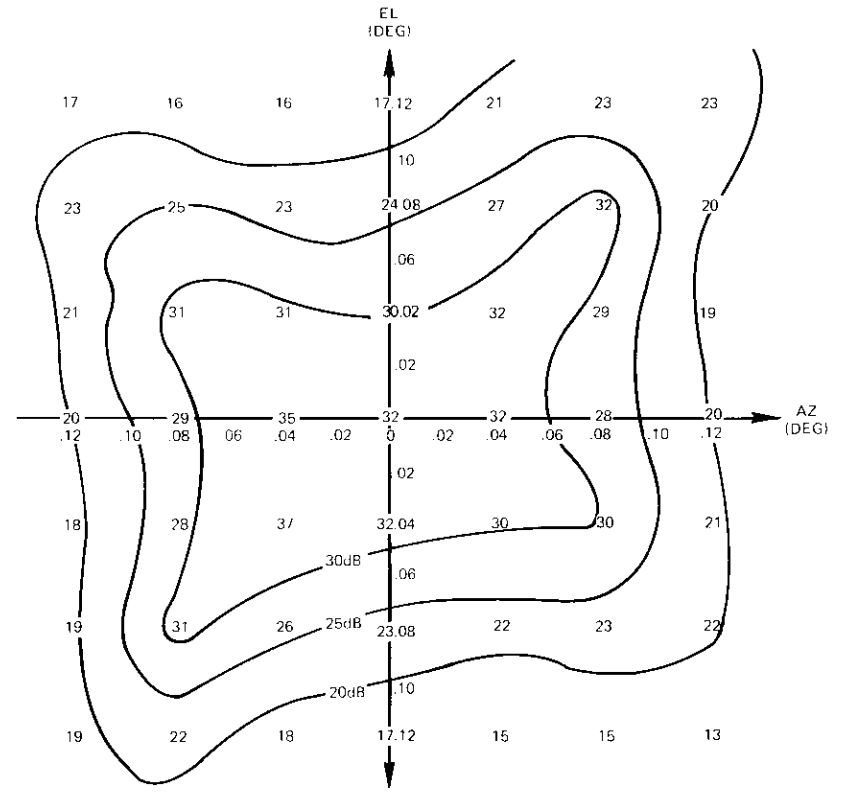


Figure 14. Mill Village Antenna Down-Link Isolation Contours, RHCP Source, $f = 3765$ MHz, INTELSAT IV-A F2

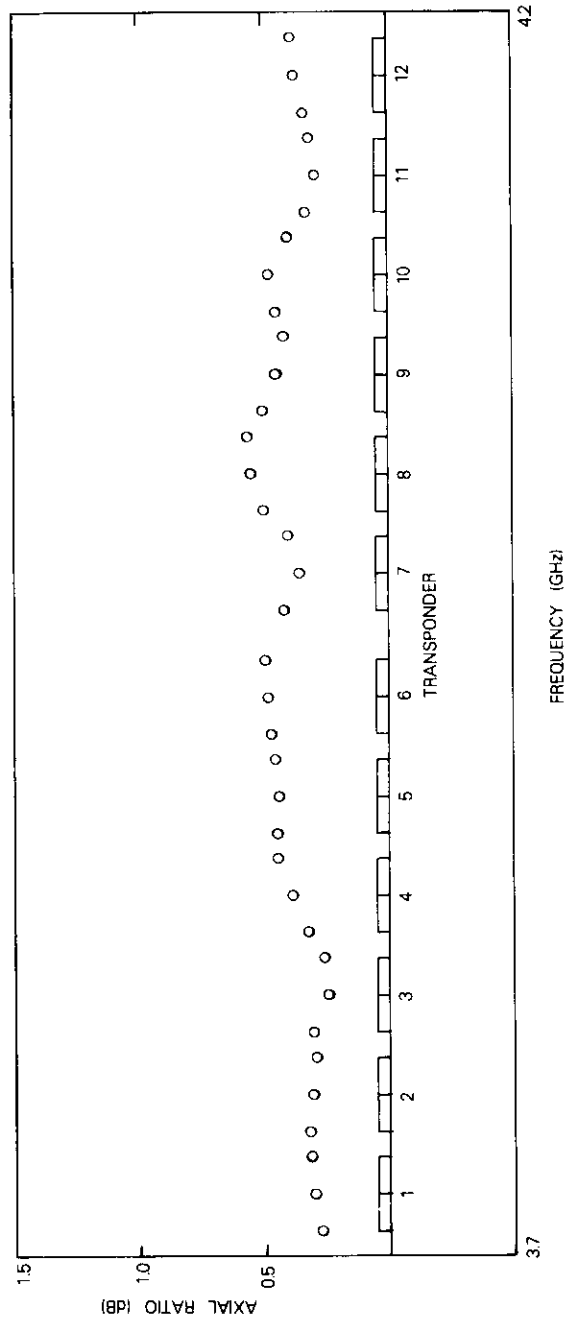


Figure 15. Pleumeur-Bodou 4 Antenna Down-Link On-Axis Axial Ratios, INTELSAT IV F3 Satellite Source
(reference antenna measurement, final reduced measurement result)

References

- [1] J. C. Fuenzalida, P. Rivalan, and H. J. Weiss, "Summary of the INTELSAT V Communications Performance Specifications," *COMSAT Technical Review*, Vol. 7, No. 1, Spring 1977, pp. 311-326.
- [2] J. Dicks and M. Brown, Jr., "INTELSAT IV-A Transmission System Design," *COMSAT Technical Review*, Vol. 5, No. 1, Spring 1975, pp. 73-104.
- [3] R. Gruner, "INTELSAT V Earth Station Antenna Technology," International Telecommunication Exposition, Atlanta, Georgia, October 1977, pp. 242-248.
- [4] W. J. English, Private Communication, May 24, 1976.
- [5] T. Satoh, "Dielectric Loaded Horn," *IEEE Transactions on Antennas and Propagation*, AP-20, No. 2, March 1972, pp. 199-201.
- [6] D. DiFonzo, Private Communication, June 9, 1975.
- [7] W. S. Trachtman, "Adaptive Orthogonalization of Polarized Signals with Applications to Satellite Communications," M.S. Thesis, M.I.T., June 1975.
- [8] D. DiFonzo, W. Trachtman, and A. Williams, "Adaptive Polarization Control for Satellite Frequency Reuse Systems," *COMSAT Technical Review*, Vol. 6, No. 2, Fall 1976, pp. 253-283.

Appendix A. Quantitative relationships for reference antenna method

Interaction between an incident wave and a receiving antenna can be considered to be a 4-port system. (The transmit case is analogous.) The incident wave can be represented by a vector $\vec{\epsilon}^i$, where

$$\vec{\epsilon}^i = \epsilon_1^i \hat{a}_1 + \epsilon_2^i \hat{a}_2 \quad (\text{A-1})$$

The vector representation is valid for arbitrary polarization components (e.g., linear, circular, or elliptical) if the unit vectors \hat{a}_1 and \hat{a}_2 are permitted to be complex. Let \hat{a}_1 and \hat{a}_2 represent two perpendicular linear components (\hat{x} and \hat{y}) with which the OMT ports of the antenna are aligned.

Two additional ports in space (ports 1 and 2 of Figure A-1) which are aligned with \hat{x} and \hat{y} can be postulated. The signals in these ports represent vector components of the incident wave which may be reradiated by the antenna if it is not perfectly matched to the incident wave.

If the input wave is the incident wave (ϵ_1^i and ϵ_2^i) plus any signals input to the OMT ports (ϵ_1^i and ϵ_2^i), the output waves at each of the ports are related to the inputs by the matrix relationship

$$\begin{bmatrix} \epsilon_1^0 \\ \epsilon_2^0 \\ \epsilon_3^0 \\ \epsilon_4^0 \end{bmatrix} = \begin{bmatrix} S_{11} & S_{12} & S_{13} & S_{14} \\ S_{21} & S_{22} & S_{23} & S_{24} \\ S_{31} & S_{32} & S_{33} & S_{34} \\ S_{41} & S_{42} & S_{43} & S_{44} \end{bmatrix} \begin{bmatrix} \epsilon_1^i \\ \epsilon_2^i \\ \epsilon_3^i \\ \epsilon_4^i \end{bmatrix} \quad (A-2)$$

where the superscript 0 stands for waves out of the ports.

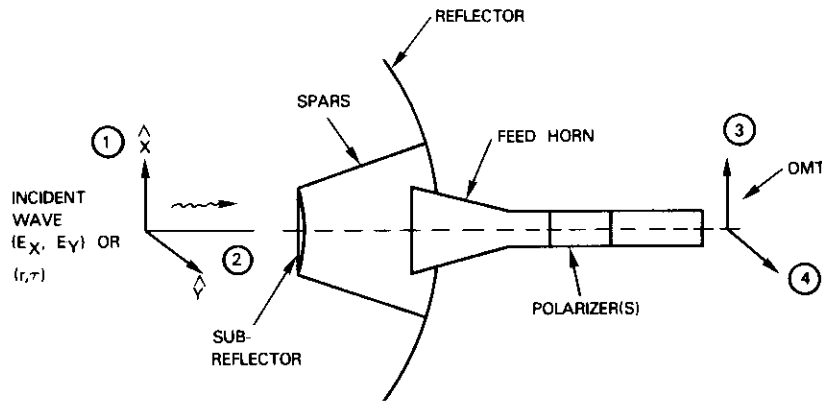


Figure A-1. Antenna Geometry and Depolarizing Mechanisms

For the idealized case in which all ports are matched and the only input energy is caused by the incident wave, ϵ_3^i and ϵ_4^i are both zero as are ϵ_1^0 and ϵ_2^0 . The results for the matched case can be extended to handle general but known mismatches. In the matched case, the matrix relationship becomes

$$\begin{bmatrix} 0 \\ 0 \\ \epsilon_3^0 \\ \epsilon_4^0 \end{bmatrix} = \begin{bmatrix} 0 & 0 & S_{13} & S_{14} \\ 0 & 0 & S_{23} & S_{24} \\ S_{13} & S_{23} & 0 & 0 \\ S_{14} & S_{24} & 0 & 0 \end{bmatrix} \begin{bmatrix} \epsilon_1^i \\ \epsilon_2^i \\ 0 \\ 0 \end{bmatrix} \quad (A-3)$$

This relationship assumes that the antenna matrix is reciprocal and that there is no coupling between ports 1 and 2 and between ports 3 and 4, since these

ports have been chosen to be orthogonal. Elements S_{13} and S_{24} represent the transmission between co-polarized ports, while S_{23} and S_{14} represent energy that is converted to cross-polarization. The system represented by equation (A-3) can be expressed as a simple 2 x 2 matrix

$$\begin{bmatrix} \epsilon_3^0 \\ \epsilon_4^0 \end{bmatrix} = \begin{bmatrix} S_{13} & S_{23} \\ S_{14} & S_{24} \end{bmatrix} \begin{bmatrix} \epsilon_1^i \\ \epsilon_2^i \end{bmatrix} \quad (A-4)$$

There are four matrix elements to be determined, but only two equations. If ports 1 and 2 can be excited independently and the output response determined separately for each input, all four matrix elements can be uniquely determined. However, this requires two orthogonal and independent incident waves, which may not always be available. With only a single available incident wave, it is not possible to solve exactly for the four matrix parameters.

One method of determining the matrix elements with only one incident wave is to assume that the antenna depolarization matrix of equation (A-4) is unitary. This implies that the antenna's depolarization can be modeled as a lossless process, e.g., an equivalent differential phase shift between the wave's vector components. Alternatively, a solution for the matrix parameters can be obtained if it is assumed that the depolarization is caused entirely by differential attenuation components. In fact, practical antennas exhibit both effects. Caution must be exercised when drawing conclusions about an antenna's response to both polarization senses based on information secured through testing with only a single polarization sense.

A wave incident on an antenna with a major axis amplitude of unity, voltage axial ratio, r , and tilt angle, τ , relative to the x axis will have rectangular components

$$E_x = \cos \tau - jr \sin \tau \quad (A-5)$$

$$E_y = \sin \tau + jr \cos \tau \quad (A-6)$$

The complex polarization ratio, p , of the wave is

$$p = \frac{E_y}{E_x} = \frac{\sin \tau + jr \cos \tau}{\cos \tau - jr \sin \tau} \quad (A-7)$$

If E_x and E_y are incident on a unitary depolarizing network, then the output wave (x and y outputs at ports 3 and 4, respectively) can be represented by E_3^0 and E_4^0 , with

$$E_z^o = S_{13}E_x + S_{23}E_y \tag{A-8}$$

$$E_y^o = S_{14}E_x + S_{24}E_y \tag{A-9}$$

These output voltages correspond to an output complex polarization ratio

$$p' = \frac{E_y^o}{E_x^o} = \frac{(S_{14}/S_{13}) + (S_{24}/S_{13})p}{1 + (S_{23}/S_{13})p} \tag{A-10}$$

at ports 3 and 4. The reciprocity and unitary conditions imply that

$$S_{14} = S_{23} \\ |S_{14}| = \sqrt{1 - |S_{13}|^2} \tag{A-11}$$

$$|S_{13}| = |S_{24}| \tag{A-12}$$

$$S_{24} = S_{13} e^{i\phi} \tag{A-13}$$

The expression $(S_{24}/S_{13}) = e^{i\phi}$ yields

$$p' = \frac{\beta + pe^{i\phi}}{1 + \beta p} \tag{A-14}$$

where $\beta = S_{14}/S_{13}$ is the normalized cross-polarization transfer function to be determined.

From equation (A-14), β is given by

$$\beta = \frac{pe^{i\phi} - p'}{pp' - 1} = \left(\frac{S_{14}}{S_{13}} \right) \tag{A-15}$$

The unitary conditions are also used to find ϕ , resulting in

$$e^{i\phi} = \frac{p^*(1 + |p'|^2) - p'(1 + |p|^2)}{p'^*(1 + |p|^2) - p(1 + |p'|^2)} \tag{A-16}$$

where the * denotes complex conjugation. Since p is known from measuring the axial ratio and tilt angle of the input wave and p' is known from similarly measuring the output wave at ports 3 and 4, ϕ and β are completely determined. The normalized antenna matrix equation

$$\begin{bmatrix} \epsilon_3^o \\ \epsilon_4^o \end{bmatrix} = S_{13} \begin{bmatrix} 1 & \beta \\ \beta & 1 \end{bmatrix} \begin{bmatrix} \epsilon_1^i \\ \epsilon_2^i \end{bmatrix}$$

can be solved for any postulated input incident wave to provide the antenna's predicted polarization response.

Daniel F. DiFonzo received a B.E.E. from Villanova University in 1962 and an M.S. from California State University in 1972. He is presently Manager of the Antenna Department of the Microwave Laboratory at COMSAT Laboratories. He is responsible for directing and carrying out research and development related to communications satellite and earth station antenna systems. He has performed extensive analytical and experimental studies of techniques for the control and measurement of microwave antenna polarization properties and the design of multiple-beam spacecraft antennas. He is a member of IEEE, APS and G-MTT.



Warren S. Trachtman received both a B.S.E.E. and an M.S.E.E. from M.I.T. in 1975. In July of 1975, he joined COMSAT Laboratories, where he is presently a member of the technical staff of the Antenna Department of the Microwave Laboratory. His major projects have involved adaptive interference reduction techniques, antenna cross-polarization measurements, and shaped-beam antenna coverage designs.

The COMSTAR Beacon Receiver

A. F. STANDING

(Manuscript received September 2, 1977)

Abstract

A receiver capable of collecting propagation data at 19 and 29 GHz and of performing the necessary in-orbit tests on the COMSTAR 19- and 29-GHz beacons is described. The receiver has two parts: an RF head mounted behind a 5-m antenna and the main receiver and control equipment located approximately 20 m away. A single frequency conversion with a 5-MHz-offset phase locked loop (PLL) locked to the 19-GHz vertical signal least affected by rain-induced signal attenuation (fading) is employed. An oscillator, controlled by an open loop servo to follow the predicted beacon frequency, is used to transfer lock when the fade depth exceeds the receiver dynamic range. This technique extends the range for amplitude data by 10 to 15 dB and ensures a rapid relock at the end of the fade; phase data are lost on transfer.

Measurement capability is provided for seven amplitude and four phase components. The amplitude components are 19-GHz vertical and cross polarization, 19-GHz horizontal and cross polarization, and 29-GHz carrier and sidebands. Phase components are 19-GHz vertical/horizontal polarization, 29-GHz carrier/sidebands, and 19/29-GHz carriers.

Introduction

The need for satellite-earth path propagation data initiated the installation of 19- and 29-GHz beacons [1]-[5] on the COMSTAR communications satellites. The 19-GHz beacon transmits a signal switched at a 1-kHz

rate (controlled by a crystal oscillator) coherently in phase between vertically and horizontally polarized antennas. The 29-GHz beacon transmits three signals, a carrier and two sidebands, all phase coherent with the 19-GHz carrier. The two sidebands are derived by phase modulating the 29-GHz carrier at 264 or 528 MHz, depending on whether the narrowband or wideband version of the beacon is used.

In addition to its primary function of propagation data collection, the beacon receiver was designed for in-orbit testing of the beacon. Carrier and sideband amplitudes and the beacon frequency are measured and compared with prelaunch data to determine the beacon status.

Receiver Concept

Seven amplitude and four phase measurements (Table 1) over a dynamic range of at least 30 dB below the clear sky levels are required to provide the desired propagation data. In addition, the in-orbit tests require the ability to measure, under clear sky conditions (Table 2), the various carrier and sideband amplitudes and the beacon frequency.

The large dynamic range requirement leads to narrowband (200-Hz) filters in the signal chains; at least 90 percent of the energy in the signal is specified to be within 100 Hz of the carrier. A translation PLL with an offset frequency of 5 MHz, derived from a high-stability crystal oscillator, meets the frequency stability requirements and allows the use of narrowband crystal filters in the IF chains. Of the three possible candidates for locking the loop (19 TVRV, 19 THRH, 29 C), the 19-GHz vertical carrier was chosen. This choice was based on the assumption, later substantiated in practice, that the 19-GHz vertical signal fades are less in magnitude than those of the 19-GHz horizontal carrier or the 29-GHz carrier.

The voltage controlled crystal oscillator (vxco) of the offset loop provides phase coherent local oscillator (LO) power for both the 19-GHz and 29-GHz carriers by means of two frequency multiplier chains. Two problems exist with this configuration: locking onto a sideband rather than the desired 19-GHz carrier, and relocking the loop to the carrier after a fade sufficiently deep to unlock the loop.

The method of square wave modulation used in the beacon, switching the carrier between vertically and horizontally polarized antenna feeds, ensures phase coherence between the vertical and horizontal channels. The addition of the vertical and horizontal signals, which are equal in amplitude and suitably phased, before the PLL considerably reduces the amplitudes of the sidebands so that the carrier is available for locking.

TABLE 1. REQUIRED MEASUREMENTS

Amplitude Signal Description	Designation
19-GHz Transmit Vertical/Receive Vertical	19 TVRV
19-GHz Transmit Horizontal/Receive Vertical	19 THRV
19-GHz Transmit Vertical/Receive Horizontal	19 TVRH
19-GHz Transmit Horizontal/Receive Horizontal	19 THRH
29-GHz Transmit Vertical/Receive Vertical	29 C
29-GHz Upper Sideband/Receive Vertical	29 USB
29-GHz Lower Sideband/Receive Vertical	29 LSB
Phase Signal Description	
19-GHz Vertical/Horizontal	19/19 phase
29-GHz Carrier/Upper Sideband	C/USB phase
29-GHz Carrier/Lower Sideband	C/LSB phase
19/29-GHz Carrier/Carrier	19/29 phase

TABLE 2. IN-ORBIT TEST MEASUREMENTS

Signal Description	Accuracy
19-GHz Transmit Vertical/Receive Vertical	± 0.5 dB
19-GHz Transmit Horizontal/Receive Horizontal	± 0.5 dB
29-GHz Transmit Vertical/Receive Vertical	± 0.5 dB
29-GHz Upper Sideband/Receive Vertical	± 0.5 dB
29-GHz Lower Sideband/Receive Vertical	± 0.5 dB
19-GHz Beacon Frequency	± 1 kHz

After it is locked, the loop is sufficiently narrow (approximately 70 Hz) to exclude the sidebands and can be returned to the vertical channel signal.

The dynamic range* is extended beyond that set by the PLL and the reacquisition of lock after a fade is facilitated by using a crystal oscillator to provide a frequency memory and automatically switching the receiver to the memory oscillator upon loss of lock. An open loop tracking system constrains the memory frequency to within ± 100 Hz (at 5 MHz) of the daily frequency variations of the beacon, hence maintaining the signal in the 200-Hz filter bandwidth, and allowing automatic reacquisition of the carrier after a fade. This technique provides amplitude data after the loss of lock until noise considerations (set by the 200-Hz crystal filters) predominate. Phase data, being dependent on the phase coherence of the

*Dynamic range is defined, for the 19-GHz vertical amplitude signal, as the range between clear sky and acquisition after a fade with a wet (290 K) sky, 70-Hz bandwidth.

signals, cannot be extended in this manner, and their dynamic range is that of the PLL.

The alternate horizontal and vertical polarization of the 19-GHz carrier is intended to provide the opportunity for cross-polarization measurements, which require time-synchronized switching of the signals into the appropriate polarization or cross-polarization channel. A pseudo-digital PLL locked to the 1-kHz modulation frequency provides the time synchronization. The dynamic range of the loop is greater (10 to 20 dB) than that of the translation loop to ensure time synchronization during a fade.

Mechanically the receiver consists of two sections: an RF head mounted behind the antenna containing the parametric amplifiers, mixers, signal amplifiers, and part of the LO multiplier chain; and the remaining signal processing and control equipment situated at a distance of approximately 20 m. Figures 1 and 2, which are basic block diagrams of the RF head,

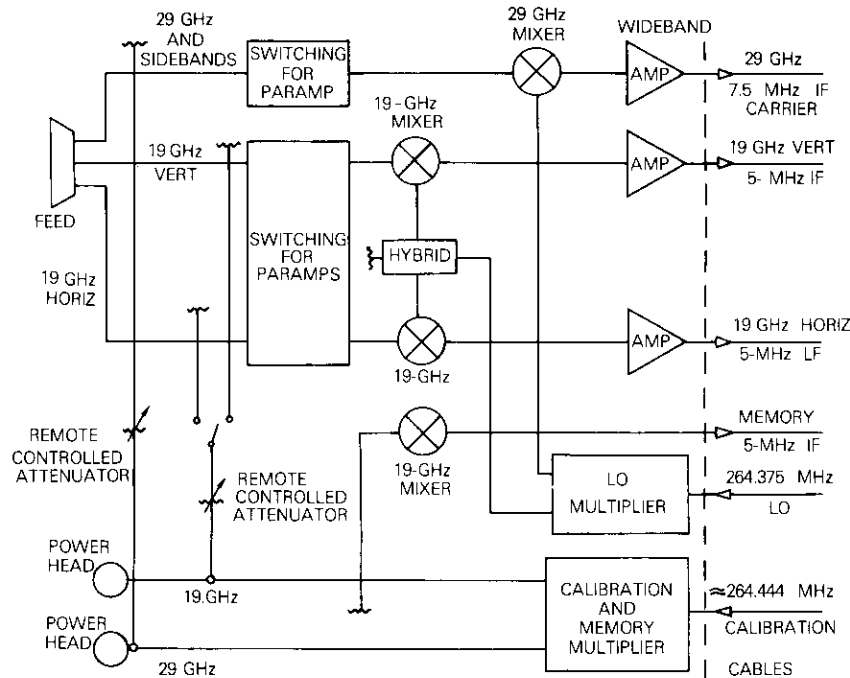


Figure 1. RF Head Block Diagram

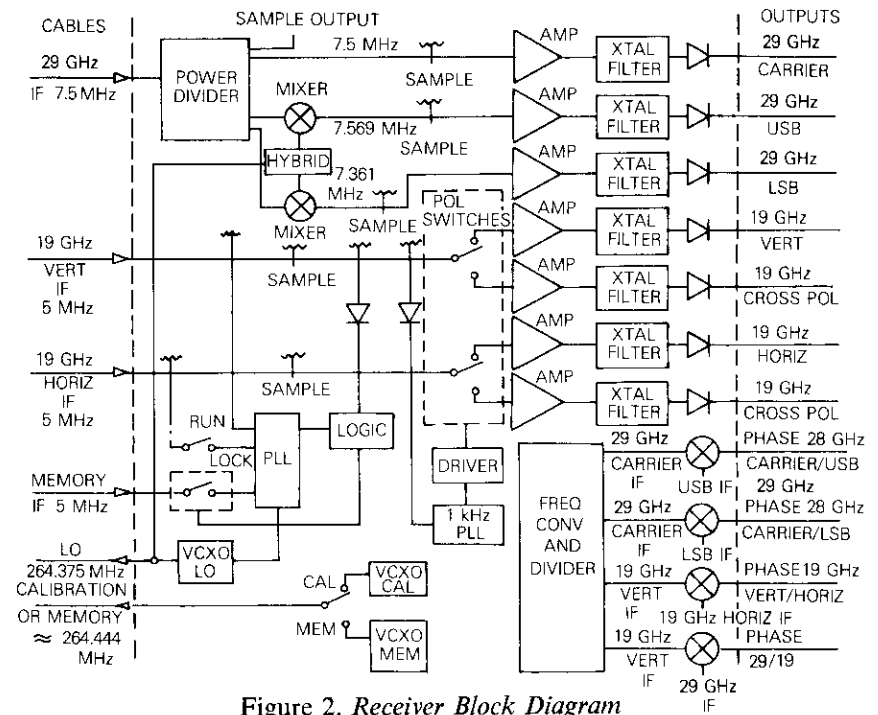


Figure 2. Receiver Block Diagram

the PLL, logic control, and signal outputs, show the interrelationship and position of the various system components.

Systems calculations

The receiver has been designed to achieve the desired dynamic range using mixer front-ends. Measured data on the system components, shown in Figure 3, allow the calculation of the 19-GHz system noise temperatures assuming a wet or noisy sky (see Table 3).

The clear-sky-carrier to wet-sky-noise ratio is then calculated as shown in Tables 4 and 5.

For a crystal filter noise bandwidth of 200 Hz (23 dB), the nominal carrier-to-noise ratio would amount to 42.5 dB, but, since a loss of 6 dB due to the 1-kHz modulation and incoherent detection is encountered, the actual value of the carrier-to-noise ratio is 36.5 dB. This is the carrier-to-noise ratio in an output channel (200-Hz crystal filter), rather than the dynamic range set by the PLL.

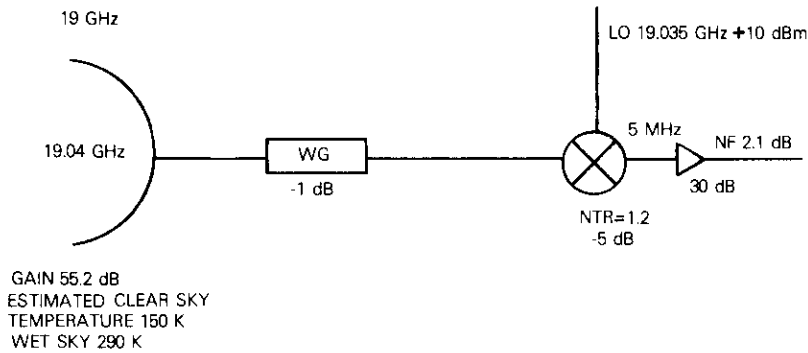


Figure 3. 19-GHz RF System

TABLE 3. 19-GHz SYSTEM NOISE TEMPERATURE

$T_e(\text{WG}) = (\alpha - 1) T_o$	75.4 K
$T_e(\text{IF}) = (F - 1) T_o$	180.4 K
$F(\text{mixer}) = 5 + 10 \log 1.2$	5.8 dB
$T_e(\text{mixer}) = 2.8 \times 290$	812 K
$T_e(\text{system})$	4,200.6 K

TABLE 4. 19-GHz RECEIVED SIGNAL

Satellite e.i.r.p.	+28 dBW
Path Loss*	-210 dB
Antenna Gain	55.2 dB
Received Signal	-126.8 dBW

*Atmospheric losses are neglected.

TABLE 5. 19-GHz CARRIER-TO-NOISE TEMPERATURE RATIO (C/KT)

Received Signal	-126.8 dBW
$T_e(4,200.6 \text{ K})$	-36.3 dB
K (Boltzmann's Constant)	228.6 dB
C/KT	65.5 dB/Hz

When switched into the RF input, the 19-GHz parametric amplifier (gain ≥ 15 dB, noise figure ≤ 4 dB) produces a system temperature of 1,944.7 K and changes the C/N in an output channel to

$$C/N = 39.9 \text{ dB}$$

Similarly, measured data on the system components (Figure 4) allow the calculation of the 29-GHz system noise temperature (see Table 6).

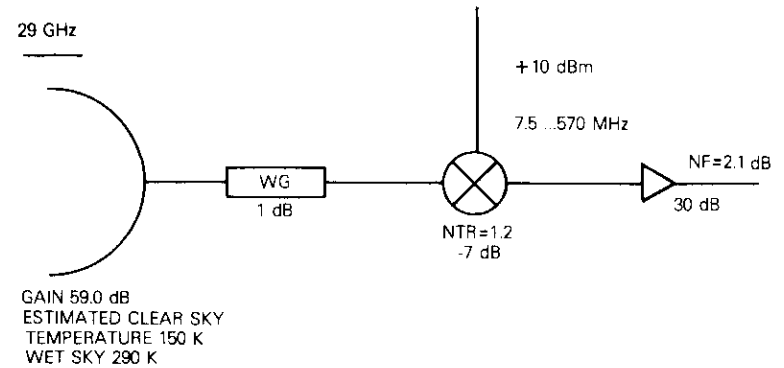


Figure 4. 29-GHz RF System

TABLE 6. 29-GHz SYSTEM NOISE TEMPERATURE

$T_e(\text{WG}) = (\alpha - 1) T_o$	75.4 K
$T_e(\text{IF}) = (F - 1) T_o$	180.4 K
$F(\text{mixer}) = 7 + 10 \log 1.2$	7.8 dB
$T_e(\text{mixer}) = 5.03 \times 290$	1,458.7 K
$T_e(\text{system})$	6,683.4 K

The clear sky carrier to wet sky noise ratio can now be calculated using Tables 7, 8, and 9.

TABLE 7. RECEIVED SIGNAL

Satellite e.i.r.p.	+28 dBW
Sideband	+22 dBW
Path Loss*	-213.5 dB
Antenna Gain	59 dB
Received Signal	-126.5 dBW
Received Signal Sidebands	-132.5 dBW

*Atmospheric losses are neglected.

TABLE 8. 29-GHZ CARRIER-TO-NOISE TEMPERATURE RATIO (C/KT)

	Carrier	Sidebands
Received Signal	-126.5 dBW	-132.5 dBW
$T_e(6,683.4\text{ K})$	-38.2 dB	-38.2 dB
K(Boltzmann's Constant)	228.6 dB	228.6 dB
C/KT, Received Signal	63.9 dB/Hz	57.9 dB/Hz

TABLE 9. 29-GHZ CARRIER-TO-NOISE RATIOS (C/N)

Filter Bandwidth	200 Hz (23 dB)
C/N carriers)	40.9 dB
C/N (sidebands)	34.9 dB

RF head design

The RF head consists of a heated, thermally insulated unit, mounted directly behind the feed of the 5-m antenna system. The necessary switching, the reference carrier injection couplers, and the remote monitoring power heads required for the in-orbit test functions of the receiver are contained in the four feed lines (19- and 29-GHz vertical and horizontal received signals) between the feed and the parametric amplifiers. The 19- and 29-GHz injected carriers are generated by two multiplier chains fed at approximately 2.4 GHz from a single chain, which is driven at approximately 264 MHz supplied from the main receiver section.

The parametric amplifiers feed low-loss mixers, one at 29 GHz and two at 19 GHz, followed by 500-MHz-bandwidth low-noise amplifiers. These amplifiers feed 30-dB-gain cable-driving amplifiers and a 500-MHz bandwidth filter for the 29-GHz signal, which transmit the IFS (5 MHz for the 19-GHz signals, and 7.5 MHz for the 29-GHz carriers) and the upper and lower sidebands to the receiver. At these IFS, phase effects due to temperature changes in the cables are small. The LO frequencies at 28.553 and 19.035 GHz are generated by common and split multiplier chains which are identical, except for minor tuning of the output stages, to the units used for the injected carriers.

Translation PLL

The translation PLL, shown in Figure 5, consists of a limiting amplifier feeding a 20-kHz-bandwidth filter which removes the harmonics from the amplifier output and guarantees that the phase detector threshold (-30

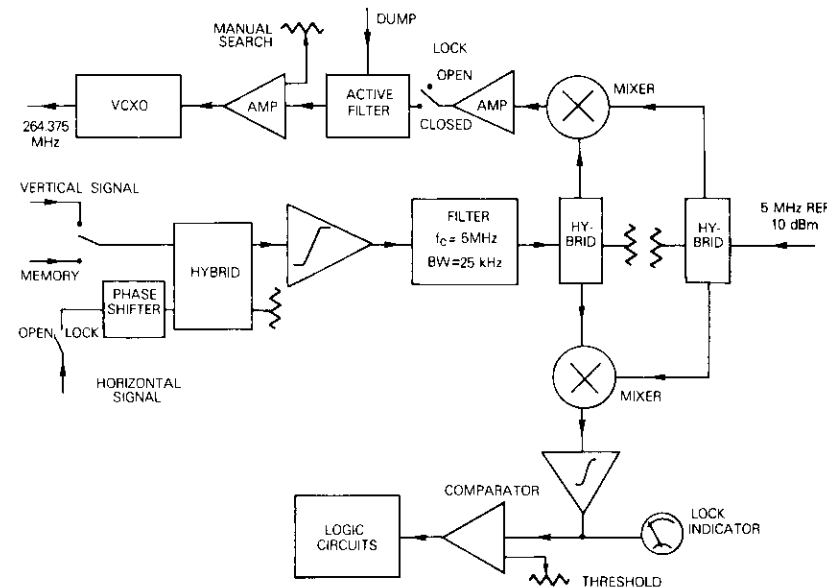


Figure 5. 5-MHz Offset PLL

dB below a nominal loop threshold of 0 dB) is well below the loop threshold. The vcxco controlled by the loop amplifier is identical to the beacon crystal oscillator, with the addition of a varactor across the crystal tuning capacitor and the appropriate frequency crystal. Large capacitors are eliminated by using an active filter in the loop to provide the bandwidth (Figure 6) required for the pull in frequency and tracking requirements (approximately 70 Hz).

The conventional lock indicator consists of a mixer, with its LO shifted 90° from the PLL LO, an integration amplifier for smoothing, and a meter. The output of the lock indicator also feeds a voltage comparator that switches the PLL input to the memory oscillator and disconnects the vertical signal input when the signal fades below a predetermined threshold. A second comparator on the 19-GHz vertical channel returns the loop from the memory to the signal when the vertical signal exceeds a preset level, usually 2 dB greater in S/N than the memory threshold level.

The dynamic range of the receiver applies only to the beacon locked mode. However, amplitude (but not phase) data are available in the memory mode until the S/N is too low for measurement (10 to 15 dB

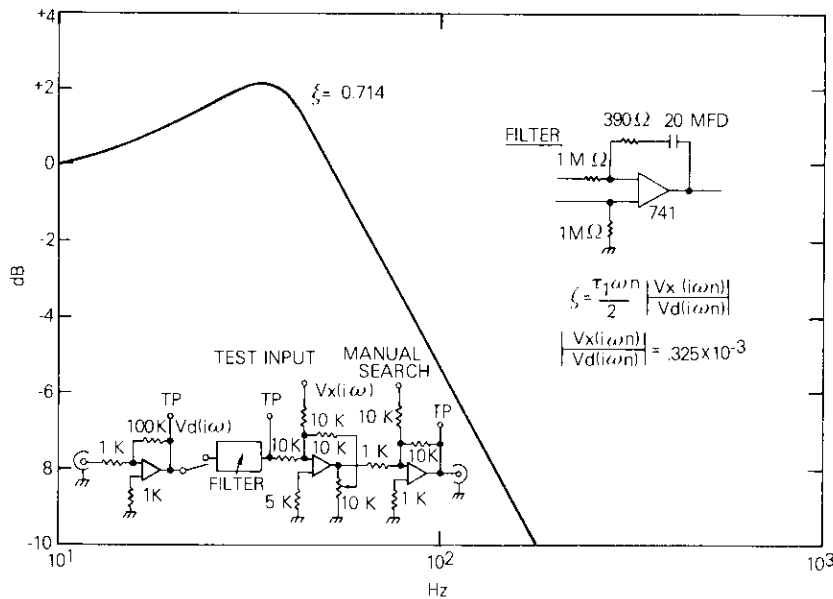


Figure 6. PLL Bandwidth

beyond the dynamic range), provided that the frequency difference between the memory and the beacon remains within the crystal filter bandwidth.

Frequency memory

The memory oscillator is a beacon design VCXO, modified by the addition of a varactor and enclosed in an oven for temperature stability. A curve-following servo provides a time variable voltage input to the memory oscillator varactor. Measurement of the beacon frequency, correcting for the 5-MHz loop offset and the multiplication factor, is simple and can be readily recorded over a 24-hour period. These data can be translated, by using the memory VCXO control characteristic, into a 24-hour graph on the servo card.

The automatic switching from the beacon to the memory and back does not remove the sidebands of the 19-GHz signal. To ensure that the receiver relocks to the carrier rather than to a sideband, the frequency of the memory must be within ±500 Hz of the carrier at the 5-MHz IF. While this ±500-Hz frequency difference ensures the locking of the receiver and

its recovery from a fade, a ±100-Hz difference must be maintained if the signal is to remain in the filter bandwidth. The PLL has a sufficiently low DC drift under all conditions to allow the loop to pull in from at least a ±500-Hz frequency offset.

1-kHz PLL

The 5-MHz square-wave-modulated signal from the 19-GHz vertical channel is fed via an automatic gain control (AGC) amplifier and 6-kHz bandwidth crystal filter into an amplitude detector to produce a square wave output. This output is fed via two cascaded operational amplifier limiters, which have a limiting range of 26 dB from clear sky values, into a 2-Hz bandwidth crystal filter; after passing through two phase shifters for time synchronization, the resulting sine wave feeds the 1-kHz loop, as shown in Figure 7. This combination removes the amplitude variations

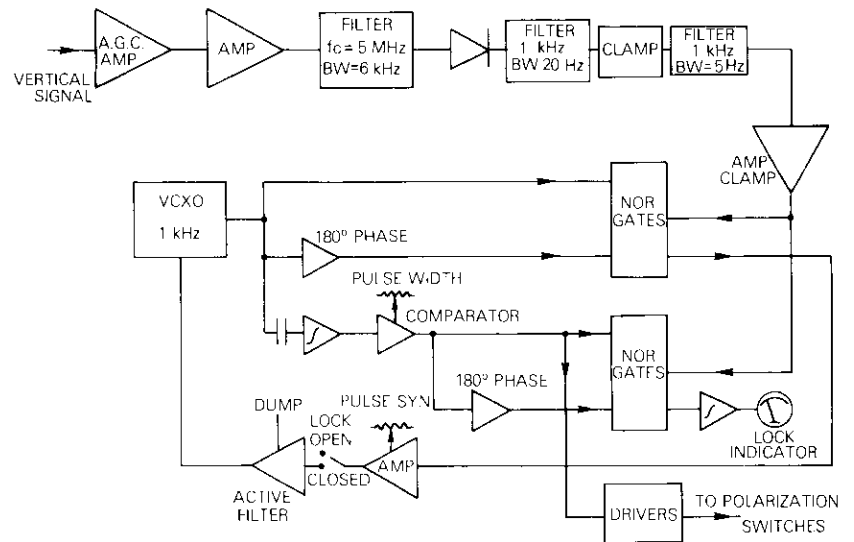


Figure 7. 1-kHz PLL

of the 1-kHz sine wave and sets the prephase detector bandwidth so that loop behavior depends on the loop bandwidth rather than on the phase detector threshold.

The phase detector lock indicator of the loop consists of four positive

logic NOR gates. The two inputs of the NOR gates are fed with positive-only square waves derived from the 1-kHz signal sine wave by processing in a limiting amplifier and from the square wave output of the 1-kHz VCXO. A phase detector of this type gives a triangular phase response when fed by square waves, and zero output when the inputs to the two gates are 180° out of phase. This is in contrast to the sine wave response of the conventional phase detector and a 90° phase shift. All the necessary pulse processing, *i.e.*, 180° and 90° phase shifting and time synchronization, is accomplished on the VCXO output, since it has low noise and constant waveform and amplitude.

The 90° phase shift necessary for the synchronization of the polarization switch drivers is achieved by removing the DC component at the square wave output of the VCXO and integrating to yield a triangular wave with zero crossings at the 90° points. When fed into a comparator this triangular waveform produces positive and negative pulses whose widths are controlled by the comparator threshold. These pulses are 90° out of phase from the original square wave. The polarization switch driver circuits are complementary emitter followers fed via series gating diodes that open circuit on input switching, transforming the emitter followers into the constant current sources required to drive the polarization switches. This configuration combines the high-speed switching capability of the emitter follower with the constant current drive required by the polarization switches.

Amplitude output channels

After time synchronization and amplification, the four 19-GHz signal outputs are passed through 200-Hz (noise bandwidth) crystal filters, which are centered at 5 MHz, to extract the carrier. These outputs are detected by a simple amplitude detector, passed through DC amplifiers, and presented as a 10-volt (clear sky) receiver output. For the main channels, *i.e.*, transmit vertical/receive vertical or transmit horizontal/receive horizontal, the crystal filter selects the carrier and rejects the sidebands. In the cross-polarization channel, two signals are present: the leakage due to the isolation (greater than 30 dB) of the polarization switches, and the cross-polarization component. During a fade, the cross-polarization signal increases as the main polarization decreases, thereby reducing the error resulting from the polarization switch isolation.

The 29-GHz carrier is similarly processed except that the 200-Hz-bandwidth crystal filter is centered at 7.5 MHz. Another frequency con-

version is required to obtain the 29-GHz upper and lower sidebands at an IF close to 7.5 MHz. The LO output at 264.375 MHz is mixed with the sidebands, producing outputs at approximately 7.569 and 7.431 MHz. If the wideband beacon is received, a times two multiplier is interposed between the LO and the mixer to yield slightly displaced sideband frequencies, *i.e.*, 7.639 MHz for the wideband beacon upper sideband frequencies and 7.361 MHz in the lower sideband case. Again, 200-Hz-bandwidth crystal filters feed the receive output via amplitude detectors and DC amplifiers.

The phase difference between the 19-GHz vertical and horizontal channels is derived from a directional coupler which samples the two outputs after the crystal filters, where only the 5-MHz IF exists. The outputs are then fed through AGC amplifiers into a phase detector and DC amplifiers. Further coherent frequency conversion of the sidebands before feeding the phase detector and DC amplifier is required to produce the phase difference between the carrier and the upper and lower sidebands at 29 GHz. The 7.5-MHz carrier is fed via an AGC amplifier and hybrid into the upper and lower sideband mixers as the LO input to achieve the coherent conversion, as shown in Figure 8. Samples of the two sidebands at approximately 7.5 MHz after the 200-Hz bandwidth crystal filters are amplified by AGC amplifiers and fed to the upper and lower sideband mixers. The mixer outputs at 69.4 kHz are then filtered by 50-Hz-bandwidth crystal filters and fed to two phase detectors.

The phase coherent LOS for these two phase detectors are derived by dividing the 5-MHz reference, to which the vertical signal is phase locked, by 72. The resultant DC voltages are amplified and become the appropriate receiver outputs. The phase difference between the 29-GHz and 19-GHz carriers is derived by mixing the constant amplitude 5-MHz reference with the 7.5-MHz IF from the 29-GHz carrier; the output is filtered, and the resultant 2.5 MHz is fed to a phase detector. The other phase detector input is obtained by dividing the 5-MHz reference by two in a regenerative ring modulator divider. The DC output of the mixer is then amplified as the required phase output.

An offset PLL has the property of locking with equal probability to both the 0 and 180° phase points of the offset frequency. On relocking the loop, the phase output can assume either of the two reference phases, shifting the phase detector zero by 180° between the two reference phases. As a result of the multiplication factor of 72, the two phase-stable reference points at 19 GHz represent 144 stable points separated by 2.5° at the LO frequency (264.375 MHz), yielding 144 equally probable zero phases for

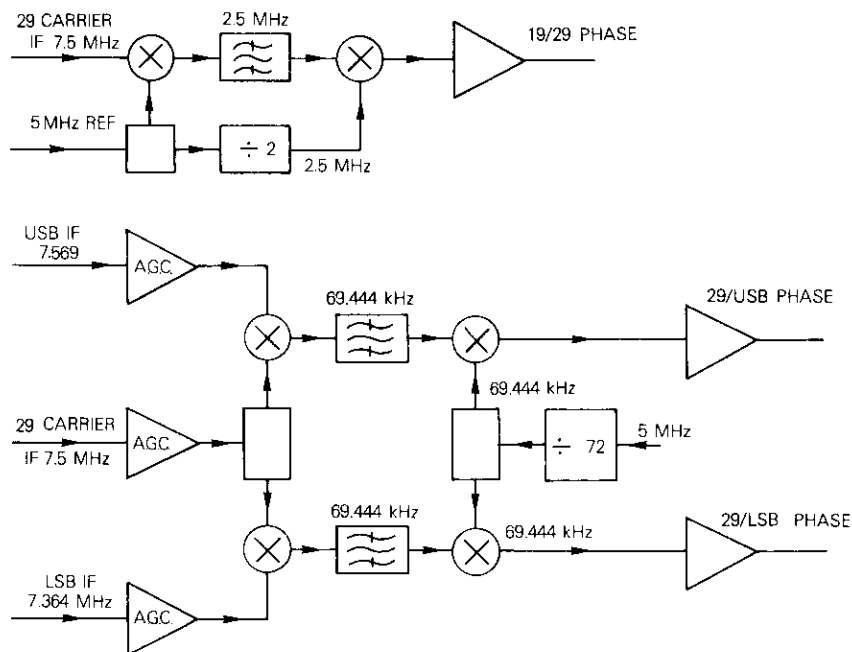


Figure 8. 19- and 29-GHz Phase Detectors

the phase detector. With a multiplication factor of 108, the stable points at 29 GHz are 270° apart, which from modulo-4 considerations gives 90° separation between the stable lock points. Since 2.5° bears an integer relationship to 90° , the stable points of the loop coincide with four of the VCXO's stable points. Consequently, the 29-GHz phase detectors can assume any one of 144 voltages because their phase zero depends on which of the 144 stable points locked the PLL. Adjustable phase shifters are provided in each phase channel for zero adjustment of the phase detectors. These require adjustment each time the receiver relocks to the beacon.

Receiver calibration and test

A calibration signal, which is required for in-orbit tests, is fed into the system before the receiver inputs. This permits receiver output calibration and provides a simple means of testing the 19-GHz and 29-GHz sections of the receiver. A calibration signal for the upper and lower sidebands is not provided at RF. However, a signal generator at the first IF (259 or

272 MHz) and previous calibration of the RF head can be used to calibrate these sidebands. In-orbit testing of the beacon with the absolute measurement of signal amplitudes necessitates a relationship between absolute power and the calibration remote control attenuator setting. This relationship is established by careful calibration of the waveguide runs and components before the calibration signal injection point, measurements of the calibration signal power, and use of the sample ports to view the resultant signals. Equating the CW calibration signal to the carrier of the square-wave-modulated 19-GHz beacon signal does not result in equal outputs after the polarization switches. The calibration signals, square wave modulated by the polarization switching, result in an output which is 6 dB lower than the clear sky signal.

Receiver performance

Measurements of the receiver give the following characteristics:

a. *Amplitude outputs.* The dynamic range (Figure 9) is 30 dB from clear-sky beacon (without parametric amplifiers) to PLL threshold. Amplitude measurements in the memory mode have a dynamic range 10 to 15 dB higher, depending on the post-detector bandwidth and the tracking accuracy of the memory oscillator.

b. *Phase outputs.* Without a parametric amplifier in the vertical chain, a 30-dB dynamic range is set by the PLL threshold.

c. *5-MHz PLL.* The bandwidth is 70 Hz, the dynamic range to threshold (without low-noise amplifiers) is 30 dB, and the maximum rate is 5.6 kHz/s.

d. *1-kHz PLL.* The bandwidth is 1.0 Hz, and the dynamic range to threshold (without parametric amplifiers) is greater than 35 dB.

Conclusion

This paper has described the design of a receiver which can be used for in-orbit testing of the COMSTAR centimeter wave beacons and the collection of propagation statistics. The receiver has been used for the initial in-orbit tests and periodic checks of the D1 and D2 beacons, and for the collection of data from D1 for about one year [6]. Propagation data are currently being collected from D2.

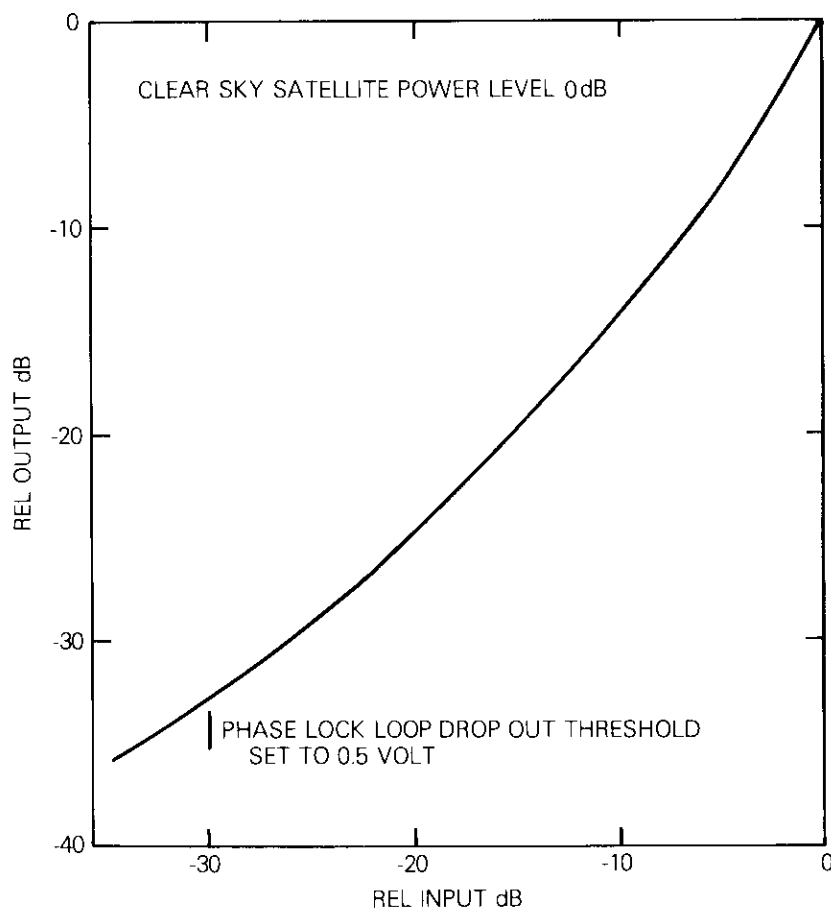


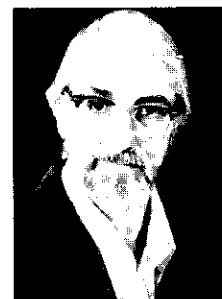
Figure 9. Receiver Dynamic Range

Acknowledgments

The author wishes to acknowledge the help and support of Dr. C. Mahle without which the receiver could not have been built, and that of K. Betaharon who was responsible for the in-orbit tests and the calibration section of the receiver.

References

- [1] L. Pollack, "Centimeter Wave Beacons for the COMSTAR Satellites," *COMSAT Technical Review*, Vol. 7, No. 1, Spring 1977, pp. 103-109.
- [2] W. J. Getsinger, "Centimeter Wave Beacon Transmitter Design," *COMSAT Technical Review*, Vol. 7, No. 1, Spring 1977, pp. 109-129.
- [3] M. J. Barrett, "19- and 28-GHz IMPATT Amplifiers," *COMSAT Technical Review*, Vol. 7, No. 1, Spring 1977, pp. 129-153.
- [4] R. E. Stegens, "Low-Jitter Local Oscillator Source for the COMSTAR Beacon," *COMSAT Technical Review*, Vol. 7, No. 1, Spring 1977, pp. 153-171.
- [5] N. L. Hyman et al., "Thermal and Structural Design Aspects of the Centimeter Wave Beacon," *COMSAT Technical Review*, Vol. 7, No. 2, Spring 1977, pp. 171-197.
- [6] J. Harris and G. Hyde, "Preliminary Measurements on the 19/29-GHz COMSTAR Beacons," *COMSAT Technical Review*, Vol. 7, No. 2, Fall 1977, pp. 599-625.



Arthur F. Standing received an M.S. in electrical engineering from Northeastern University in 1967, and the degree of engineer in Communications from George Washington University in 1976. Prior to joining COMSAT Laboratories in 1967, he worked on air-borne radar systems at the Telecommunications Radar Establishment in England, ground-based radar at Westinghouse, and interplanetary radar at Lincoln Lab. At COMSAT Laboratories, he has performed extensive studies of the communications characteristics of microwave tubes and associated mathematical modeling problems. He is presently a member of the Transponder Department of the Microwave Laboratory and is involved in satellite in-orbit performance monitoring and evaluation. He is a senior member of IEEE.

CTR Notes

QPSK bit-error rate performance as affected by cascaded linear and nonlinear elements

C. DEVIEUX, JR.

(Manuscript received June 20, 1977)

Introduction

The bit-error rate (BER) performance of QPSK (4-phase PSK) transmission over band-limited communications satellite channels with cascaded nonlinearities has been investigated by computer simulation. In particular, performance degradation caused by nonlinear gain and phase characteristics of amplifiers and by attenuation characteristics of filters has been examined.

A typical communications satellite transmission link is shown in Figure 1. A single carrier modulated by the input digital data stream, which consists of rectangular pulses, is assumed to access the appropriate satellite transponder. Modem transmit filter F_1 provides the desired waveform shaping before amplification by the earth station high-power amplifier (HPA). At the satellite, filter F_2 rejects adjacent channels. Amplification is provided by the satellite traveling wave tube amplifier (TWTA) and filter F_3 reduces the energy falling into the adjacent channels. Modem receive filter F_4 provides additional waveform shaping and reduces the noise at the input of the coherent PSK demodulator. The satellite channel

C. Devieux, Jr., is Assistant Manager of the Communications Systems Analysis Department of the Transmission Systems Laboratory at COMSAT Laboratories.

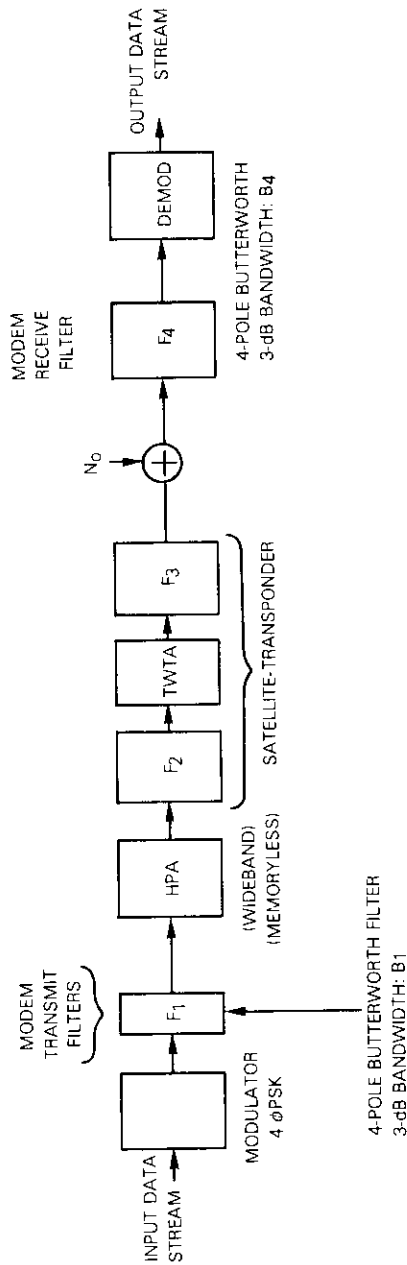


Figure 1. Block Diagram of Transmission Channel Used in Single-Channel Simulation

bandwidth-time product, BT , where B is the 3-dB bandpass bandwidth and T is the symbol duration (*i.e.*, twice the bit duration), is assumed to be moderately large (~ 2.5).

Thermal noise enters the satellite and earth station receivers. In the computer simulation the total noise contribution is represented as an equivalent additive white Gaussian noise source of density N_o (W/Hz) at the input to filter F_4 . The objective of the simulation is to obtain the BER of the output data stream as a function of required E_b/N_o , where

$$E_b = CT_b$$

and

C = unmodulated carrier power

T_b = bit duration

The input data stream is obtained from a pseudo-random sequence generator; an unmodulated preamble preceding the modulated carrier sequence provides the unmodulated carrier power level, C , at the input to filter F_4 . The average modulated power, P , at this point could be lower than C because of the filtering preceding filter F_1 . For P to be fully utilized at the demodulator, this filter must be matched to the received filtered pulses.

Figure 2 shows the attenuation characteristics of the filters and Figure 3 shows the assumed HPA and TWTA gain and phase characteristics.

System considerations

Since the available power, C , at the earth station receiver is related to the satellite e.i.r.p. (effective isotropic radiated power), *i.e.*, to the output power capability of the TWTA, a given power requirement affects the overall satellite weight, size, and prime power requirements.

In systems performance analyses for a given E_b/N_o , the system BER is obtained from the parametric performance curves generated either by measurements or by computer simulation. Parametric curves are usually given in the form of BER vs E_b/N_o for various values of HPA input backoff (B_{Hi}) and satellite TWTA input backoff (B_{Si}). Near-optimum satellite B_{Hi} and B_{Si} settings can thus be obtained to yield the minimum BER achievable.

Because of the moderately large available channel bandwidth, modem filters which attenuate gradually outside their passband can be used. Filters having such characteristics tend to produce moderate envelope variations of the modulated carrier, resulting in reduced overall impair-

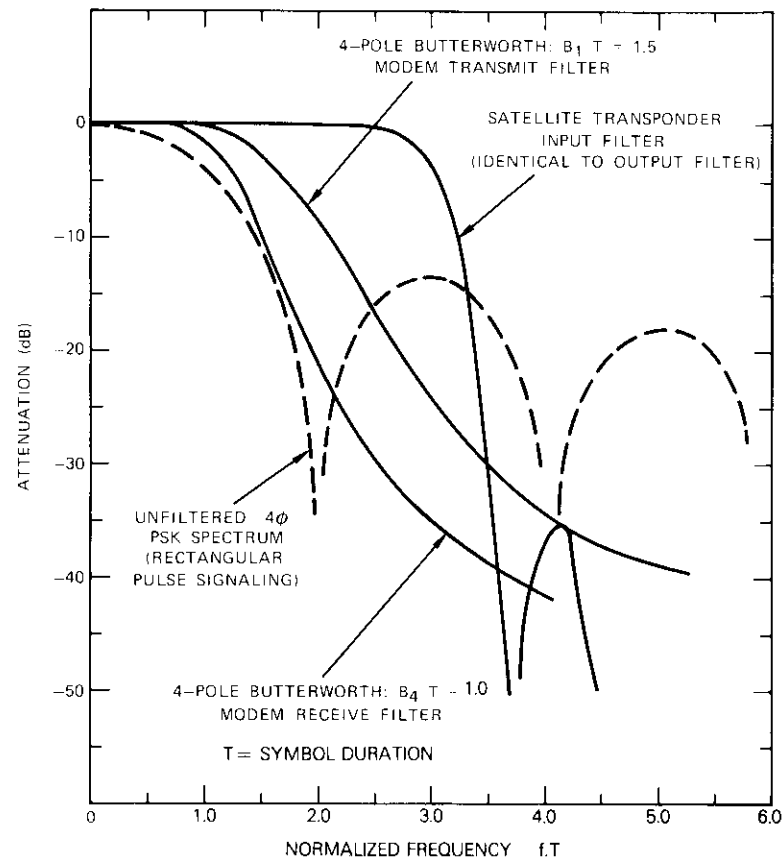


Figure 2. Amplitude Responses of Channel Filters

ments. For these filters, the sensitivity of transmission impairments to imperfect timing references is expected to be less pronounced than in the case of sharp cutoff filters. Four-pole Butterworth filters are used throughout this investigation.

In a wideband linear transmission channel with optimized modem transmit and receive filters, if coherent detection (ideal carrier and timing references at the demodulator) is assumed, the available power, C , is almost fully utilized and losses due to intersymbol interference caused by waveform distortion (overlapping pulses) are minimal. Then, for a given BER the required E_b/N_o approaches the minimum theoretical value. In

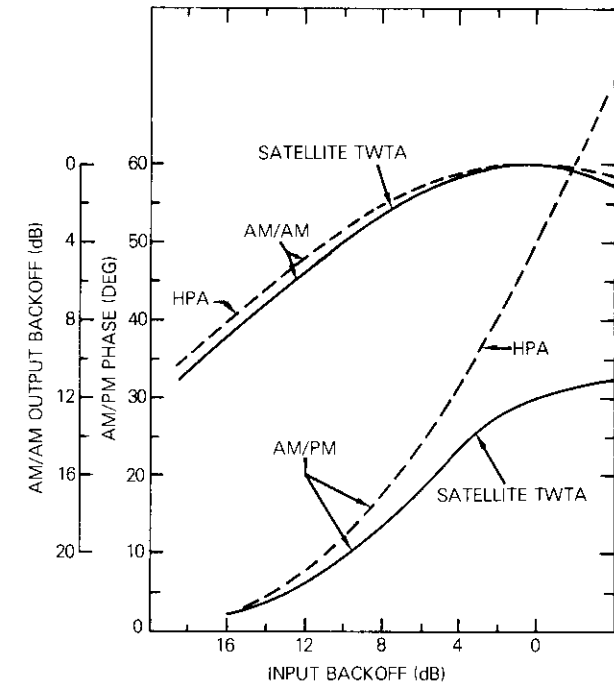


Figure 3. Assumed Earth Station HPA and Satellite TWTA Characteristics

practice, with non-optimized filters and nonlinear amplifiers, a larger value of E_b/N_o is needed to meet the desired BER objective. This increase is due partly to the reduction of received average power, P , at the input to filter F_4 and partly to receive filter mismatch losses and the random variations of the sampled signal levels at the input of the decision device of the demodulator (amplitude variations caused by intersymbol interference.)

Performance objective and method of investigation

A BER performance objective of 1×10^{-4} has been selected. Performance degradation, Δ (in dB), is defined as the difference between the E_b/N_o value required for a BER of 1×10^{-4} and that required under ideal wideband channel conditions. For differential encoding before modulation and differential decoding after demodulation, the ideal required E_b/N_o is 8.8 dB. The total degradation, Δ , is divided into two parts:

- a. a power loss component, R_p (dB), which is the ratio of the unmodulated carrier power, C , to the average modulated power, P ,

at the earth station receiver (input to filter F_4);

b. a waveform distortion loss component, WDL (dB), due to the combined effect of receive filter mismatch and intersymbol interference. Both Δ and R_p have been obtained by computer simulation; their difference yields the quantity WDL.

The impact of the BT product of the modem filters on the required E_b/N_o has been investigated for the satellite channel of Figure 1 with the input backoff levels of the earth station HPA and the satellite TWTA (B_{H_i} and B_{S_i} , respectively) set at 0 dB. (B_1T and B_4T are the BT products of the modem transmit and receive filters, respectively.)

The effects of HPA and TWTA backoff have been determined for two values of B_1T , 1.5 and 1.0. A more extensive investigation performed for the case of tight filtering emphasizes the effects of channel nonlinearities. The impact of the various components on the total degradation, Δ , and power loss, R_p , has been assessed by selectively idealizing certain characteristics (e.g., removing the satellite TWTA). For example, the performance obtained when the transmission chain is reduced to modem filters F_1 and F_4 and the earth station HPA has been compared with that achievable when the HPA is replaced by a hard limiter. Six cases have been considered:

- idealized HPA AM/PM characteristics (no HPA AM/PM conversion effects);
- idealized HPA and satellite TWTA AM/PM characteristics (no HPA AM/PM and no TWTA AM/PM);
- idealized HPA AM/PM characteristics and linear transponder (satellite TWTA removed);
- a transmission chain consisting of modem transmit filter F_1 , an HPA without AM/PM, and modem receive filter F_4 (transmission chain: F_1 -HPA- F_4);
- a transmission chain consisting of filter F_1 , a hard limiter, and filter F_4 ;
- a transmission chain consisting of modem filters F_1 and F_4 back-to-back.

IMPACT OF MODEM FILTER BT PRODUCT

Figure 4 shows the sensitivity of E_b/N_o to modem filter B_1T (transmit) and B_4T (receive) products. Both the HPA and satellite TWTA operate near saturation. A near-optimum modem receive filter B_4T product occurs at about 1.1; E_b/N_o is rather insensitive to B_1T over the range of 1.3 to 2.0. Transmission impairment losses tend to increase rapidly for B_1T values less than 1.3 because tight filtering increases the impairment caused by

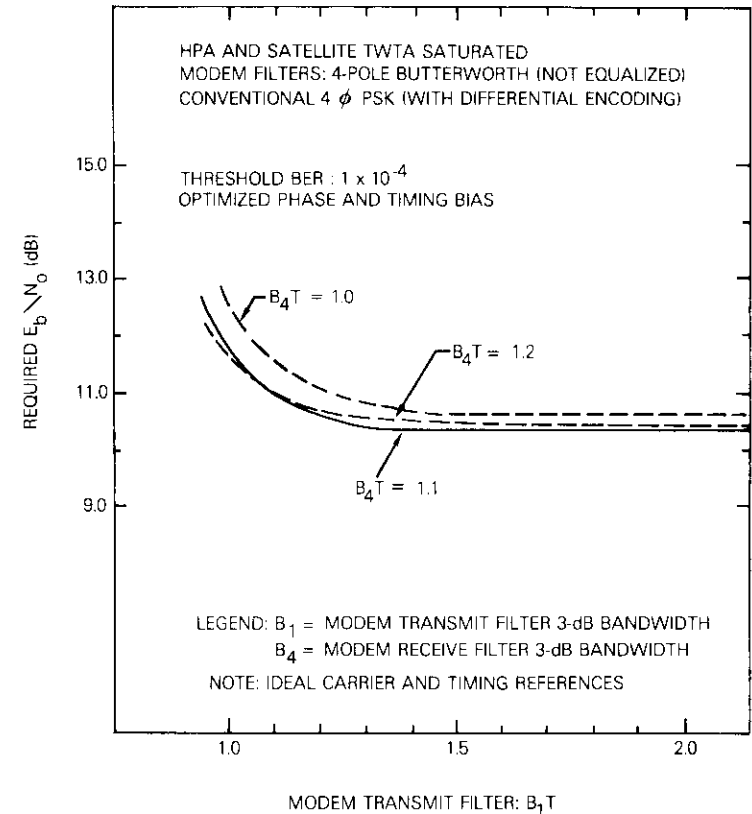


Figure 4. Required E_b/N_o vs Modem Filter BT Products

power loss and by spreading the filtered pulse waveform into the neighboring symbol intervals. Moreover, envelope fluctuations are accentuated by tight filtering in the modem transmit filter, resulting in additional impairment, primarily by the HPA nonlinearities. The modem receive filter contributes to the total degradation by producing additional waveform distortion. Although a wideband receive filter would minimize distortion, the total noise power reaching the coherent PSK demodulator would increase in proportion to bandwidth B_4 . Consequently, less latitude is available in the selection of B_4 than in the selection of B_1 . In the subsequent series of results, a B_4T of 1.0 has been selected.

IMPACT OF HPA AND TWTA OPERATING POINTS

Figure 5 shows the impact of B_{Hi} and B_{Si} for two values of transmit filter B_1T product, 1.5 and 1.0. The impact of the HPA and satellite TWTA nonlinearities is much less in the moderate filtering case than in the tight filtering case. With the satellite TWTA operating in the quasi-linear region ($B_{Si} = 14$ dB), a slightly lower E_b/N_o is required when B_{Hi} is set at 0 dB rather than at 14 dB.

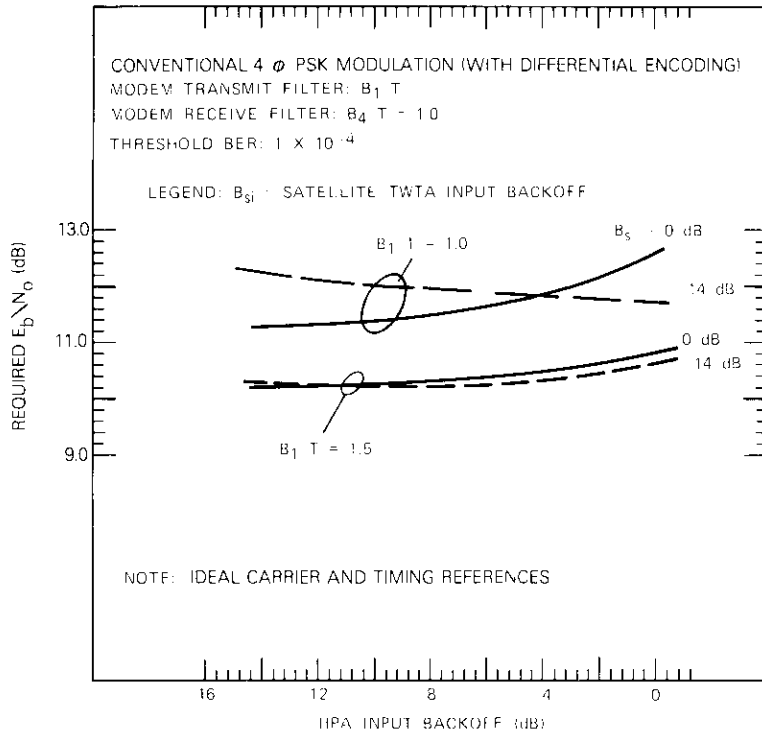


Figure 5. Effect of HPA and TWTA Backoff (modem transmit filter B_1T product, $B_4T = 1.0$)

BER PERFORMANCE FOR THE NARROWBAND CASE

BER performance with tight filtering ($B_1T = 1.0$) is summarized in Figures 6-8. Each curve shows the power loss ratio, R_p . Tables 1 to 3 give the required E_b/N_o for a BER of 1×10^{-4} . The total degradation, Δ , calculated with respect to the required E_b/N_o (8.8 dB) for ideal QPSK with

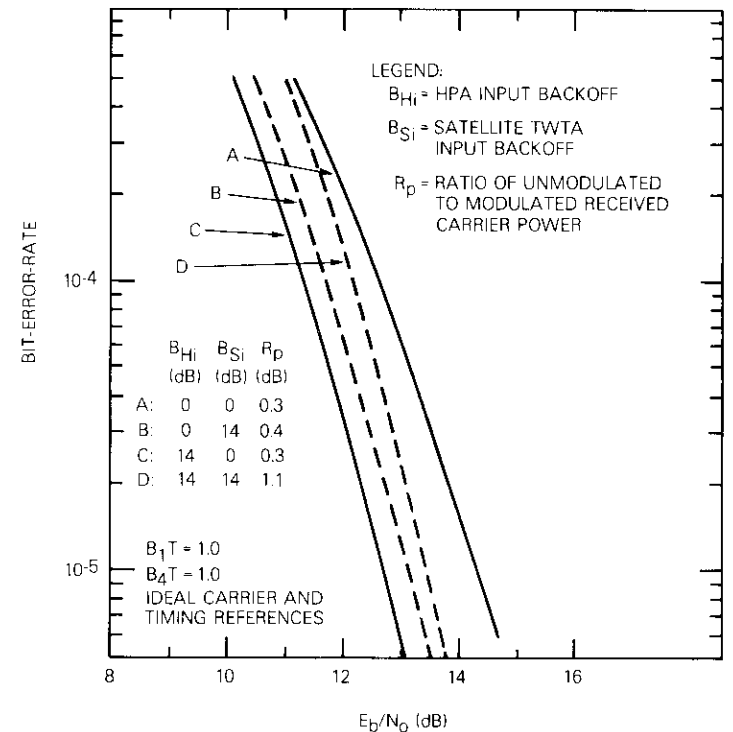


Figure 6. BER Performance for the Complete Transmission Link (all components included; $B_1T = 1.0$, $B_4T = 1.0$)

differential encoding, is broken down into power loss, R_p , and waveform distortion loss, WDL.

Table 1 shows the transmission impairments for various cases involving all the filters in the transmission link. Table 2 shows Δ , R_p , and WDL for the particular case of tight filtering with the satellite TWTA operating in a quasi-linear region. Table 3 summarizes the transmission impairments for the hypothetical cases in which the satellite transponder has been removed. Performance is given for modem back-to-back, for a hard limiter replacing the HPA, and for the HPA without AM/PM conversion.

NARROWBAND CASE WITH SATELLITE TWTA OPERATING IN A QUASI-LINEAR REGION

The impact of the earth station HPA on BER performance can be seen when the satellite TWTA is operating in a quasi-linear region ($B_{Si} = 14$ dB). Curves B and D in Figure 6 reveal that, at any given BER, the required

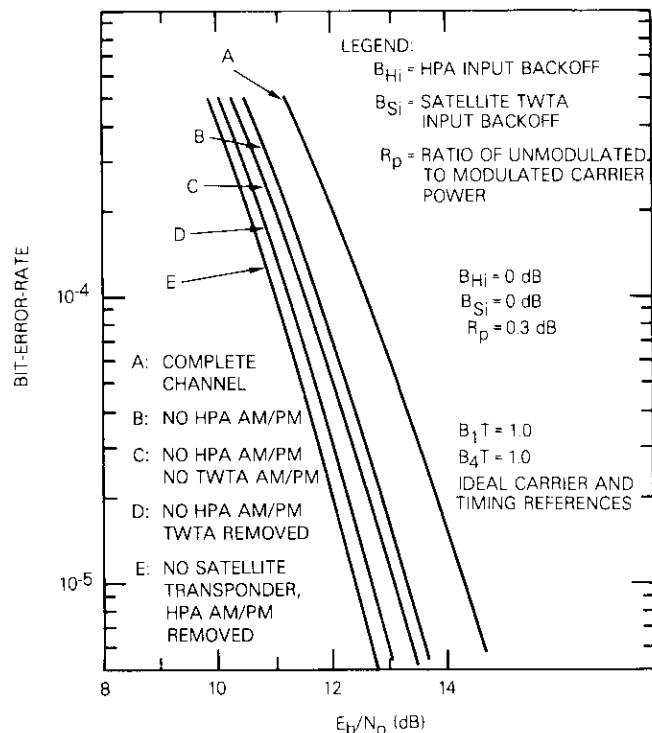


Figure 7. Effect of Component Characteristics on BER

E_b/N_0 is lower for an HPA input backoff of 0 dB than for a B_{Hi} of 14 dB. The respective values of Δ , R_p , and WDL are shown in Table 2 for these two cases. It can be seen that the WDL loss is actually higher by about 0.3 dB at a B_{Hi} of 0 dB than at a B_{Hi} of 14 dB. However, R_p is lower by about 0.7 dB when B_{Hi} is 0 dB. The net effect is that the total loss, Δ , is lower by about 0.4 dB near HPA saturation.

IMPACT OF HPA AND TWTA AM/PM CHARACTERISTICS ON NARROWBAND PERFORMANCE

The impact of the nonlinear AM/PM characteristics of the HPA and satellite TWTA is investigated for the case in which both devices operate near saturation. In Figure 7 curve A depicts the BER performance with HPA AM/PM conversion, and curve B shows the BER performance without AM/PM conversion at the HPA. Curve C shows the BER performance when

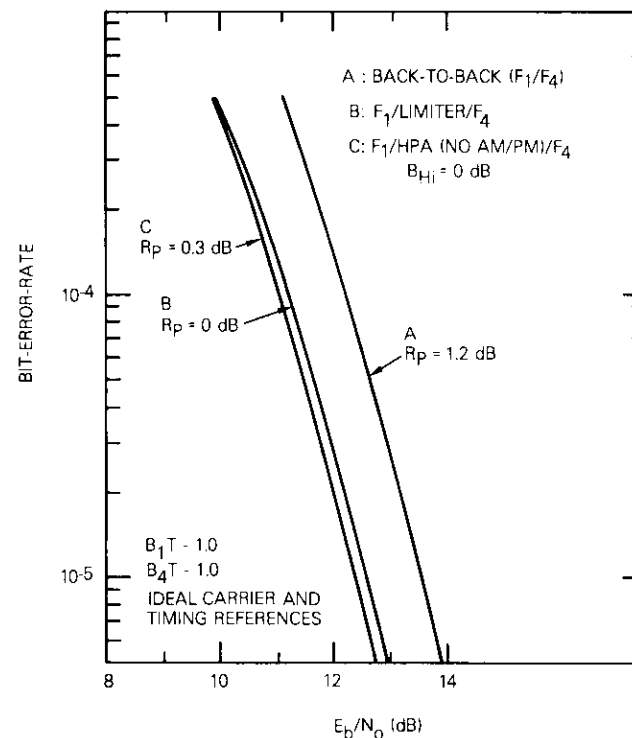


Figure 8. BER Performance with Modem Filters Only, with a Hard Limiter, or with an HPA without AM/PM

both the HPA and satellite TWTA have their AM/PM conversion characteristics removed. The various loss components are given in Table 1, which also includes the losses for various backoff combinations. The total loss caused by the HPA AM/PM conversion (about $5^\circ/\text{dB}$) at a BER of 1×10^{-4} is about 0.8 dB. The total loss caused by the satellite TWTA AM/PM characteristics (about $2^\circ/\text{dB}$) is about 0.2 dB. (The AM/PM characteristics of the HPA and TWTA appear to contribute losses of the order of 0.4 and 0.3 dB, respectively.)

EFFECT OF HARD LIMITER

In the case of tight filtering by the modem transmit filter, the nonlinear gain characteristics of the HPA improve the utilization of the available power while the nonlinear AM/PM characteristics cause a transmission

TABLE 1. SUMMARY OF QPSK TRANSMISSION IMPAIRMENTS^a FOR A BER OF 1×10^{-4}

Transmission Link Components	$B_{Hi} = 14 \text{ dB}$																
	$B_{Si} = 0 \text{ dB}^b$				$B_{Si} = 0 \text{ dB}^b$				$B_{Si} = 14 \text{ dB}^b$								
	E_b/N_o	Δ	R_p	WDL	E_b/N_o	Δ	R_p	WDL	E_b/N_o	Δ	R_p	WDL					
F_1 -HPA- F_2 - F_3 - F_4	11.5	2.7	0.3	2.4	11.7	2.9	0.5	2.4	11.3	2.5	0.3	2.2	12.1	3.3	1.2	2.1	No HPA AM/PM, TWTA removed.
F_1 -HPA- F_2 -TWTA- F_3 - F_4	11.8	3.0	0.3	2.7	11.4	2.6	0.4	2.2	11.2	2.4	0.3	2.1	12.1	3.3	1.1	2.2	No HPA AM/PM, TWTA AM/PM.
F_1 -HPA- F_2 -TWTA- F_3 - F_4	12.6	3.8	0.3	3.5	11.8	3.0	0.4	2.6	11.3	2.5	0.3	2.2	12.2	3.4	1.1	2.3	All characteristics included.

^a Δ (dB) is the loss with respect to theoretical performance ($E_b/N_o = 8.8 \text{ dB}$), R_p (dB) is the ratio of unmodulated carrier power to modulated carrier power, and [WDL (dB) = $\Delta - R_p$] is the waveform distortion loss.
^b Ideal carrier and timing references.
^c No TWTA.

TABLE 2. TOTAL DEGRADATION FOR A BER OF 1×10^{-4} IN THE TIGHT FILTERING CASE WITH THE SATELLITE TWTA OPERATING IN A QUASI-LINEAR REGION ($B_1T = 1.0$, $B_4T = 1.0$, $B_{Si} = 14 \text{ dB}$)

HPA Input Backoff, B_{Hi} (dB)	Total Degradation, Δ (dB)	Power Loss, R_p (dB)	Waveform Distortion Loss, WDL (dB)
0	3.0	0.4	2.6
14	3.4	1.1	2.3

TABLE 3. SUMMARY OF QPSK TRANSMISSION IMPAIRMENTS FOR A BER OF 1×10^{-4} (MODEM FILTERS $B_1T = 1.0$, $B_4T = 1.0$; NO SATELLITE TRANSPONDER)

Case	E_b/N_o (dB)	Total Degradation, Δ (dB)	Power Loss, R_p (dB)	Waveform Distortion Loss, WDL (dB)	Remarks
Ideal	8.8	—	—	—	Ideal carrier and timing references; QPSK with differential encoding (all cases).
Modem Back-to-Back	12.3	3.5	1.2	2.3	
F_1 -HPA- F_4	11.0	2.2	0.3	1.9	No AM/PM, $B_{Hi} = 0 \text{ dB}$.
F_1 -HDLM- F_4	11.2	2.4	0.0	2.4	

impairment of about 0.8 dB. This latter loss could be reduced if a modulated carrier with a nearly constant envelope were provided at the HPA input. A hard limiter with a low degree of AM/PM conversion after the modem transmit filter could contribute to this reduction.

The relative performance degradation caused by an ideal hard limiter with respect to that caused by the nonlinear gain of the HPA has been investigated for a channel consisting of filter F_1 ($B_1T = 1.0$), one nonlinear element (either an HPA without AM/PM conversion or an ideal hard limiter), and filter F_4 ($B_4T = 1.0$). Results are shown in Figure 8 and Table

3. It is observed that Δ is larger for the modem back-to-back case (non-linearity excluded) than for cases involving a nonlinearity (either a hard limiter or an HPA without AM/PM conversion). A substantial amount of this excess loss is due to the power loss caused by tight filtering. Table 3 shows that, for the case involving a hard limiter, Δ is 0.2 dB greater than for the case involving an HPA (without AM/PM). The hard limiter causes a WDL loss of about 2.4 dB, but produces no power loss. On the other hand, in the case involving the HPA, the WDL loss is about 1.9 dB, while the power loss is 0.3 dB. The net effect is that the hard limiter produces slightly worse performance than the HPA without AM/PM conversion. It is estimated that the tandem operation of a hard limiter preceding the HPA with nonlinear gain and phase characteristics would produce performance similar to that obtained herein for the hard limiter alone.

Conclusion

Computer simulation has been used to provide insight into the impairment mechanism of QPSK transmission caused by narrow modem filter bandwidth in the presence of cascaded nonlinear amplifiers. Good performance is obtained if the bandwidth of the modem transmit filter exceeds a certain minimum value, which corresponds to a BT product value of about 1.3. Narrowing the bandwidth increases the transmission impairments substantially; the AM/PM conversion characteristics of the HPA contribute appreciably to the impairment. The contribution of HPA nonlinear gain seems to have effects similar to those of the satellite TWTA nonlinearity. In certain cases with narrowband transmit modem filters the nonlinear gain of the HPA operating near saturation produces some performance improvement relative to the performance achievable in the quasi-linear region. This behavior can be attributed to an improved utilization of the satellite e.i.r.p.

Acknowledgment

The author wishes to acknowledge the helpful suggestions of Dr. R. Fang and the contributions of S. Lebowitz to the simulation effort.

Geosynchronous satellite log

W. L. MORGAN

(Manuscript received January 17, 1978)

This note updates a list of geosynchronous satellites published two years ago [1] to show their locations at year-end 1977. Table 1 incorporates the many satellites that have been successfully placed on-station and the newly announced programs as well as the satellites that have been moved to new orbital positions. In 1977, INTELSAT moved all of the INTELSAT I, II, and III (except INTELSAT III F3) out of the orbit by using the remaining fuel. Satellites previously listed which have completed their mission are not shown even if they are still drifting in the geosynchronous orbit.

The INTELSAT and DOD (USA) figures include new, spare, and replacement satellites currently on order. The figures for the USSR are for only initial quantities (except for the two replacements for Raduga-1 and Ekran) and thus may be understated or incomplete.

Growth is observable in several forms: continued deployment of replacement satellites for operational systems, new experimental satellites to test future systems (e.g., LES-8 and -9, SIRIO, and Kiku No. 2), plans for second generation satellites (Anik-B, and Advanced Westar), and the emergence of regional systems (as typified by the Andean, Arab, and Nordic nations). Figure 1 illustrates the overall growth and trends.

Table 2 provides a cross-referenced index. Table 3, which lists satellite locations by frequency bands, may be particularly useful in orbit-spectrum utilization and propagation studies.

Reference

- [1] W. L. Morgan, "Satellite Utilization of the Geostationary Orbit," *COMSAT Technical Review*, Vol. 6, No. 1, Spring 1976, pp. 195-205.

Walter L. Morgan is a Senior Staff Scientist on the Project Staff of the Assistant Director, Technical, at COMSAT Laboratories.

TABLE 1. GEOSYNCHRONOUS SATELLITE DATA

Longitude Dec 1977	Planned	Satellite Name	Sponsor	Launch Date	Communications Function	Up/Down-Bands (GHz)
0E		Meteosat	European Space Agency	1977	Meteorological	0.148, 0.402, 2.1/ 0.136, 0.468, 1.7
	0-35E	Geos	European Space Agency	1978	Experimental	0.149/0.137, 2.3
	0E	Nordsat	Nordic Nations ^a	1981	Domestic	14/12
	5-20E	Arabsats 1 and 2	Arab Satellite Comm Org	1981	Regional	6/2.5, 4
	^b	H-Sat, Phebus or LO-4	European Space Agency	^c	Experimental	14/11
	^b	EBS (Euro Broadcasting Sat)	Euro Broadcasting Union	1983	Direct TV	14/11
	10E	OTS (Orbital Test Sat)	European Space Agency	1978	Experimental	0.149, 14/0.138, 11
	10E	ECS (Euro Comm Sat) ^d	European Conf of Postal and Telecomm Admin (CEPT)	1983	Regional	14/11
	26E	Zohreh-2	Telecomm Co of Iran	1981	Domestic	14/11
	34E	Zohreh-1	Telecomm Co of Iran	1981	Domestic and Broadcasting	14/11, 12
35E		Raduga-3 (Stationsar-2A)	Min of Posts and Telecomm (USSR)	1977	Domestic	6/4
	40E	Marots-A ^{d,e} or Marecs	European Space Agency	^c	Maritime	1.6, 14/1.5, 11 1.6, 6/1.5,4
	45E	Loutch-P2	Min of Posts and Telecomm (USSR)	1981	Domestic	14/11
	45E	Stationsar-9	Min of Posts and Telecomm (USSR)	1980	Domestic	6/4
	45E	Gals-2	Min of Posts and Telecomm (USSR)	1979	Government Services	8/7
	45E	Volna-3 ^f	Min of Posts and Telecomm (USSR)	1980	Mobile	0.335-0.399, 1.6/ 0.240-0.328, 1.5
49E*	47E	Zohreh-3 Symphonie-1	Telecomm Co of Iran France and Fed Rep of Germany	^c 1974	Domestic Experimental	14/11 6/4
54E		DSCS-2 F4 (Defense Comm Sat Syst II)	DCA (USA)	1975	Military	7/8
	^b	DSCS-3 (Defense Comm Sat Syst III)	DCA (USA)	^c	Military	7, 30/8, 20
56.5E		INTELSAT III F3 ^d	INTELSAT	1969	International	6/4
	57.0E	INTELSAT (Indian Ocean)	INTELSAT	^c	International	6/4
	58E	Loutch-2	Min of Posts and Telecomm (USSR)	1981	Domestic	14/11
	58E	Stationsar-5	Min of Posts and Telecomm (USSR)	^c	Domestic	6/4
	58E	Volna-4 ^f	Min of Posts and Telecomm (USSR)	^c	Mobile	1.6/1.5
	60.0E	INTELSAT IV-A F6	INTELSAT	1978	International	6/4
	60.0E ⁱ	INTELSAT (Indian Ocean)	INTELSAT	^c	International	6, 14/4, 11
60.2E 62.9E		INTELSAT IV F5	INTELSAT	1972	International	6/4
		INTELSAT IV F1	INTELSAT	1975	International	6/4
	63.0E	INTELSAT IV-A F3	INTELSAT	1978	International	6/4
	63.0E ^j	INTELSAT (Indian Ocean)	INTELSAT	^c	International	6, 14/4, 11
	66.0E ⁱ	INTELSAT (Indian Ocean)	INTELSAT	^c	International	6, 14/4, 11
	70E	GOMS	USSR	1979	Meteorological	ⁱ
	70E ^k	GOES or SMS	NOAA or NASA (USA)	^c	Meteorological	0.402, 2/0.136, 0.137, 0.469, 1.7
	70E	STW-2 ^d	Radio Mgt Bureau (China, P.R.)	1979-80	Experimental	6/4
	71.0E	Insat ^l	ISRO (India)	1981	Experimental	6/2.5, 4

TABLE I. GEOSYNCHRONOUS SATELLITE DATA (continued)

Longitude Dec 1977	Planned	Satellite Name	Sponsor	Launch Date	Communications Function	Up/Down-Bands (GHz)
73E		Marisat Indian Ocean (102)	COMSAT General Corp ^m	1976	Maritime & Ship	0.3-0.312, 1.6, 6/0.248-0.26, 1.5, 4
	74E ^b	Insat ¹ Ariane Passenger Pay- load Experiment (APPLE) ¹	ISRO (India) ISRO (India)	1980 1980	Domestic Meteorology/ Hydrology	6/UHF, 2.5, 4 °
77E		Palapa-2	PERUMTEL (Indonesia)	1977	Domestic	Experimental 6/4
80E		Raduga-1B (Statsionar-1B)	Min of Posts and Telecomm (USSR)	1976 ⁿ	Domestic	6/4
83E		Palapa-1	PERUMTEL (Indonesia)	1976	Domestic	6/4
	85E	Gals-3	Min of Posts and Telecomm (USSR)	1979	Domestic	8/7
	85E	Loutch-P3	Min of Posts and Telecomm (USSR)	1978-81	Domestic	14/11
	85E	Statsionar-3	Min of Posts and Telecomm (USSR)	°	Domestic	6/4
	85E	Volna-5 ^f	Min of Posts and Telecomm (USSR)	1980	Mobile	0.335-0.399, 1.6/ 0.24-0.328, 1.5
	90E	Loutch-3	Min of Posts and Telecomm (USSR)	1981	Domestic	14/11
	90E	Statsionar-6	Min of Posts and Telecomm (USSR)	1979-80	Domestic	6/4
99E		Ekran-B (Statsionar-T)	Min of Posts and Telecomm (USSR)	1977 ⁿ	Direct TV Broadcast	6.2/0.714
	102E ^b	ISCOM ^o	ISRO (India) Australia	° °	Experimental Multipurpose	6/4 °
	110E	Broadcast Sat Exp (BS or BSE)	NASDA (Japan)	1978	Experimental Broadcast TV	14/12
	120-140E	Domestic Sat Comm Syst	NTT (Japan)	°	Domestic	6, 30/4, 20
	125E	STW-1 ^d	Radio Mgt Bureau (China, P.R.)	1979-80	Experimental	6/4
130E		Kiku No. 2 (ETS II)	NASDA (Japan)	1977	Experimental	0.148, 2.1/0.136, 1.7, 11.5, 34.5
135E		Sakura (Cherry Blossom, CS or CSE)	NASDA (Japan)	1977	Experimental	6, 30/4, 20
140E		Himiwari (Sunflower or GMS-1)	NASDA (Japan)	1977	Meteorological	0.149, 0.402, 2.0/ 0.137, 0.469, 1.7
	^b	GMS-2	NASDA (Japan)	1982	Meteorological	°
	140E	Loutch-4	Min of Posts and Telecomm (USSR)	1981	Government Services	14/11
	140E	Statsionar-7	Min of Posts and Telecomm (USSR)	1979-80	Domestic	6/4
	140E	Volna-6 ^f	Min of Posts and Telecomm (USSR)	1980	Mobile	1.6/1.5
	145E	Experimental Comm Sat (ECS)	NASDA (Japan)	1979	Experimental	6, 34.8/4, 31.7 °
174.0E		INTELSAT IV F8	INTELSAT	1974	International	6/4
	174.0E ⁱ	INTELSAT (Pacific) ¹	INTELSAT	°	International	6/4
175E		DSCS-2 F8 (Defense Comm Sat Syst II) W Pacific ^d	DCA (USA)	1977	Military	8/7
	^b	DSCS-3 (Defense Comm Sat Syst III) ^h	DCA (USA)	°	Military	8, 30/7, 20
176.5E		Marisat Pacific (103)	COMSAT General Corp ^m	1976	Maritime & Ship	0.3-0.312, 1.6, 6/ 0.248-0.26, 1.5, 4
179.0E		INTELSAT IV F4	INTELSAT	1972	International	6/4
	179.0E ⁱ	INTELSAT (Pacific)	INTELSAT	°	International	6/4

TABLE I. GEOSYNCHRONOUS SATELLITE DATA (continued)

Longitude Dec 1977	Planned	Satellite Name	Sponsor	Launch Date	Communications Function	Up/Down-Bands (GHz)
	189E (171W)	Tracking & Data Relay Sat (West) (TDRS) ^{d,e}	Western Union Space Comm Corp	1979	Leased Service to NASA (USA)	2.0, 15/2.2, 13
	190E (170W)	Gals-4	Min of Posts and Telecomm (USSR)	1979	Government Services	8/7
	190E (170W)	Loutch-P4	Min of Posts and Telecomm (USSR)	1978-81	Government Services	14/11
	190E (170W)	Stationsar-10	Min of Posts and Telecomm (USSR)	1980	Domestic	6/4
	190E (170W)	Volna-7 ^f	Min of Posts and Telecomm (USSR)	1980	Mobile	0.335-0.399, 1.6/ 0.24-0.328, 1.5
211E (149W)		ATS-1 ^d	NASA (USA)	1966	Experimental	0.149, 6/0.136, 0.137.4
220E (140W)		"	Canada	"	Broadcasting	14/12
220E (140W)		ATS-6	NASA (USA)	1974	Experimental	0.15, 1.6, 6, 13, 18/0.039-0.361, 0.86, 1.5, 2, 4, 20 30
220E (140W)		NATO-3B (F2) ^d East Pacific	NATO	1977	Military	1.8, 8/2.3, 7
	h	DSCS-3 (Defense Comm Sat Syst III)	DCA (USA)	"	Military	8, 30/7, 20
225E (135W)		SMS-2 (Sync Met Sat) West	NASA/NOAA (USA)	1975	Meteorological	0.402, 2/0.136, 0.468, 1.7
	225E (135W)	Geostationary Operational	NOAA (USA)	1978	Meteorological	0.402, 2/0.136, 0.468, 1.7
225E (135W)		Environ Sat (GOES) Satcom-1 (F-1)	RCA Americom	1975	Domestic	6/4

	227.2E (132.8W)	US Domestic ^p	"	"	Domestic	6/4
	231.8E (128.2W)	US Domestic ^p	"	"	Domestic	6/4
232E (128W)		Comstar 201 (D-1)	COMSAT General Corp. ^m	1976	Domestic (AT&T/GTE)	6/4, 18, 28
	236.4E (123.6W)	US Domestic ^p	"	"	Domestic	6/4
236.5E (123.5W)		Westar 2	Western Union Telegraph Co	1974	Domestic	6/4
	238.0E (122W)	US Domestic ^p	"	"	Domestic	14/12
	238E (122W)	SBS-A	Satellite Business Systems	1980	Domestic	14/12
	241E (119W)	US Domestic ^p	"	"	Domestic	6/4
241.0E (119W)		Satcom-2 (F-1)	RCA Americom	1976	Domestic	6/4
244E (116W)		Comm Tech Sat (CTS or Hermes)	NASA (USA) & Dept of Comm (Canada)	1976	Experimental	14/12
	244.0E (116W)	Anik-C2	Telesat Canada	1980	Domestic	14/12
246E (114W)		Anik-A3	Telesat Canada	1975	Domestic	6/4
	247.5E (112.5W)	Anik-C1	Telesat Canada	1980	Domestic	14/12
251E (109W)		Anik-A2	Telesat Canada	1973	Domestic	6/4
	251.0E (109W)	Anik-B1	Telesat Canada	1978	Domestic	6,14/4,12
	254.0E (106W)	US Domestic ^p	"	"	Domestic	14/12
	254E (106W)	SBS-B	Satellite Business Systems	1980	Domestic	14/12

TABLE I. GEOSYNCHRONOUS SATELLITE DATA (continued)

Dec 1977	Longitude Planned	Satellite Name	Sponsor	Launch Date	Communications Function	Up/Down-Bands (GHz)
	254.8E (105.2W)	ATS-3 ^d	NASA (USA)	1967	Experimental	0.149, 6/0.136, 0.137, 4
	255E (105W)	Sync Met Sat ^d (SMS-1)	NASA/NOAA (USA)	1974	Meteorological (Spare)	0.402, 2/0.136, 0.468, 1.7
	256E (104W)	Lincoln Exp Sat ^d (LES-8)	US Dept of Defense & MIT	1976	Experimental	UHF, 8, 36/UHF, 7, 32
	256E (104W)	Anik-A1	Telesat Canada	1972	Domestic	6/4
	257E (103W)	Advanced Westar ^e	Western Union Space Comm Corp	Early 80s	Domestic	2.0, 6, 14/2.2, 4, 12
	260E (100W)	FLTSATCOM (Fleet Sat Comm)	US Navy	1978	Military	0.29-0.32, 8/ 0.24-0.27, 7
	261.0E (99W)	US Domestic ^p	°	°	Domestic	6/4
	261E (99W)	Westar 1	Western Union Telegraph Co	1974	Domestic	6/4
	261E (99W)	Satcom-C	RCA Americom	°	Domestic	6/4
	261E (99W)	Tracking & Data Relay Relay Sat/Advanced Westar ^e	Western Union Space Comm Corp	1980	On-Orbit Spare for TDRS or Adv Westar Syst	2.0, 6, 14, 15/ 2.2, 4, 12, 13
	265.0E (95W)	US Domestic ^p	°	°	Domestic	6/4
	265E (95W)	Comstar 202 (D-2)	COMSAT General Corp.	1976	Domestic (AT&T/GTE)	6/4, 18, 28
	268E (92W)	°	Canada	°	Broadcasting	14/12
	269E (91W)	US Domestic ^p	°	°	Domestic	6/4

	270.3E (89.7W)	Comstar-C (D-3)	COMSAT General Corp	1978	Domestic (AT&T/GTE)	6/4, 20, 30
	274.3 (85.7W)	US Domestic ^p	°	°	Domestic	6/4
	275E (85W)	Geostationary Opera- tional Environ Sat (GOES-1)	NOAA (USA)	1975	Meteorological (Standby)	0.402, 2/0.136, 0.469, 1.7
	278.3E (81.7W)	US Domestic ^p	°	°	Domestic	6/4
	285E (75W)	Brasilsat	Brazil	°	Domestic	6/4
	285E (75W)	Geostationary Opera- tional Environ Sat (GOES-2)	NOAA (USA)	1977	Meteorological	0.402, 2/0.136, 0.469, 1.7
	285E (75W) b	Colombia	Colombia ^a	°	Domestic	6/4
	289E (71W)	International Ultra- violet Explorer (IUE) ^{d, r}	Andean Nations ^a NASA (USA)	1980s 1978	Regional Astronomy	6/4 0.149/0.137, 2.2
	290E (70W)	FLTSATCOM (Fleet Sat Comm)	US Navy	1978	Military	0.29-0.32, 8/ 0.24-0.27, 7
	290E (70W)	Brasilsat	Brazil	°	Domestic	6/4
	295E (65W)	Brasilsat	Brazil	°	Domestic	6/4
	300E (60W)	Brasilsat	Brazil	°	Domestic	6/4
	310E (50N)	NATO-3C	NATO	1979	Spare	1.8, 8/2.2, 7
	316E (44W)	Lincoln Exp Sat ^d (LES-9)	US Dept of Defense & MIT	1976	Experimental	UHF, 8, 36/UHF, 7, 32
	319E (41W)	Tracking & Data Relay Sat (TDRS) ^{e, d} (East)	Western Union Space Comm Corp	1979	Leased Services to NASA	2.0, 15/2.2, 13

TABLE 1. GEOSYNCHRONOUS SATELLITE DATA (continued)

Longitude Dec 1977	Planned	Satellite Name	Sponsor	Launch Date	Communications Function	Up/Down-Bands (GHz)
325.5E (34.5W)		INTELSAT IV-A F4	INTELSAT	1977	International	6/4
	325.5E ⁱ (34.5W)	INTELSAT (Atlantic)	INTELSAT	°	International	6, 14/4, 11
	329.0E ⁱ (31W)	INTELSAT (Atlantic)	INTELSAT	°	International	6, 14/4, 11
330.5E (29.5W)		INTELSAT IV-A F2	INTELSAT	1976 ^f	International	6/4
	330.0E ⁱ (27W)	INTELSAT (Atlantic)	INTELSAT		International	6, 14/4, 11
	335E (25W)	Gals-1	Min of Posts & Telecomm (USSR)	1979	Government	8/7
	335E (25W)	Loutch-P1	Min of Posts & Telecomm (USSR)	1979-81	Domestic	14/11
	335.0E (25W)	Stationsar-8	Min of Posts & Telecomm (USSR)	1980	Domestic	6/4
	335E (25W)	Volna-1 ^f	Min of Posts & Telecomm (USSR)	1980	Mobile	0.335-0.399, 1.6/0.24-0.328, 1.5
335.5E (24.5W)		INTELSAT IV-A F1	INTELSAT	1975	International	6/4
	336.0E ⁱ (24W)	INTELSAT (Atlantic)	INTELSAT	°	International	6, 14/4, 11
	337E (23W)	FLTSATCOM (Fleet Satellite Comm)	US Navy	1978	Military	0.29-0.32, 8/ 0.24-0.27, 7
	339E ⁱ (21W)	INTELSAT (Atlantic)	INTELSAT	°	International	6, 14/4, 11
340.5E (19.5W)		INTELSAT IV F3	INTELSAT	1971	International	6/4

	342.0E ⁱ (18W)	INTELSAT (Atlantic)	INTELSAT	°	International	6/14/4, 11
342E (18W)		NATO-3A (F-1)	NATO	1976	Military	1.8, 8/2.2, 7
	^b	NATO-4 SIRIO	NATO CNR (Italy)	°	Military Experimental	°
345E (15W)		Marisat Atlantic (101)	COMSAT General Corp	1976	Ship and Maritime	0.148, 17/0.136, 11
345E (15W)		Loutch-1	Min of Posts & Telecomm (USSR)	1976	Domestic	0.3-0.312, 1.6, 6/0.248-0.26, 1.5, 4
	346E (14W)	Volna-2 ^f	Min of Posts & Telecomm (USSR)	1981	Domestic	14/11
	346E (14W)	Volna-2 ^f	Min of Posts & Telecomm (USSR)	1980	Mobile	1.6/1.5
	346.5E (13.5W)	Stationsar-4	Min of Posts & Telecomm (USSR)	1978-79	Domestic	6/4
347E (13W)		DSCS-2 F7 (Defense Sat Comm Syst II) Atlantic	DCA (USA)	1977	Military	8/7
	^h	DSCS-3 (Defense Sat Comm Syst III)	DCA (USA)	°	Military	8, 30/7, 20
	347.5E (12.5W)	Marots-B ^e or Marecs	European Space Agency	°	Maritime	1.6, 14/1.5, 11 1.6, 6/1.5, 4
348.5E ^g (11.5W)		Symphonie-2	France & Fed Rep of Germany	1974	Experimental	6/4
	350E (10W)	°	Fed Rep of Germany	1985	Direct TV Broadcast	14/11
356.0E (4W)		INTELSAT IV F2	INTELSAT	1971	International	6/4
359.0E (1W)		INTELSAT IV F7	INTELSAT	1973	International	6/4
	359.0E ⁱ (1W)	INTELSAT	INTELSAT	°	Domestic Lease	6/4
	°	INTELSAT V	INTELSAT	1979 & later	International	6, 14/4, 11

TABLE 1. GEOSYNCHRONOUS SATELLITE DATA (continued)

Longitude Dec 1977	Planned	Satellite Name	Sponsor	Launch Date	Communications Function	Up/Down-Bands (GHz)
°		Syncom-4	° (USA)	°	Experimental	°
°		Stormsat	NASA (USA)	1985	Meteorological	°
°		Stationary Earth Obser- vation Sat (SEOS)	NASA (USA)	°	Earth Obser- vation	°
°		Disaster Warning	Dept of Commerce (USA)	°	Direct Broadcast	°
°		Public Service Satellite	NASA (USA)	°	Domestic	°
°		General Purpose Comm Sat Syst	DOD (USA)	°	Military	°
°		NATO-4	NATO	°	Military	°

^a The Nordic Nations consist of Denmark, Iceland, Finland, Norway and Sweden.

^b Estimated.

^c Undetermined.

^d These satellites have orbit inclinations of more than 2°: ECS (Europe), up to 3°; Marots, up to 3°; DSCS-IIIs and NATO IIIs, approximately 2°; INTELSAT III F-3, 5.17°; ATS-1, 8.4°; ATS-3, 6.9°; LES-8 and 9, 25.3°; SMS-1, 2.7°; TDRS at 189° and 319E, under 7°. The IFRB filings for STW-1 and 2 do not indicate the intended inclination control.

^e A decision between Marots and Marecs is in process and may involve the formation of a new consortium. The Marecs is a maritime mobile payload using the ECS (Europe) bus.

^f All Volna satellites have provision for the maritime mobile and aeronautical mobile satellite services. Some also include UHF equipment for land mobile communications.

^g 49E is being used by Symphonie-1 in support of an Indian test program. Eventually this satellite will return to 348.5E.

^h It is assumed that these locations will be used for DSCS-III.

ⁱ These locations may be used by the 6/4-GHz INTELSAT IV or

IV-A satellites or the INTELSAT Vs at 6,14/4,11 GHz.

^j Down-link and platform up-link frequencies may be similar to those of Meteosat (0E), Himiwari/GMS (140E), and GOES/SMS (70, 255 & 285E).

^k Potential interim location until GOMS can be established.

^l Apple and Insat are sometimes used interchangeably.

^m Leader of a consortium.

ⁿ Second launch of these satellites.

^o The Tracking and Data Relay Satellite System (TDRSS) is leased by NASA (US) from the Western Union Space Communications Corp. for 10 years. These satellites carry both TDRSS and Advanced Westar equipment. The spare at 262E is shared by both systems.

^p Future assignments by the Federal Communications Commission (USA).

^q The Andean Nations consist of Bolivia, Colombia, Ecuador, Peru, and Venezuela.

^r The International Ultraviolet Explorer is a satellite with a period of one sidereal day (~24 hours) in a very elliptical orbit inclined 28°. The IUE crosses the equatorial plane at 260E and 320E longitude.

Figure 1. Sources of Geosynchronous Satellites

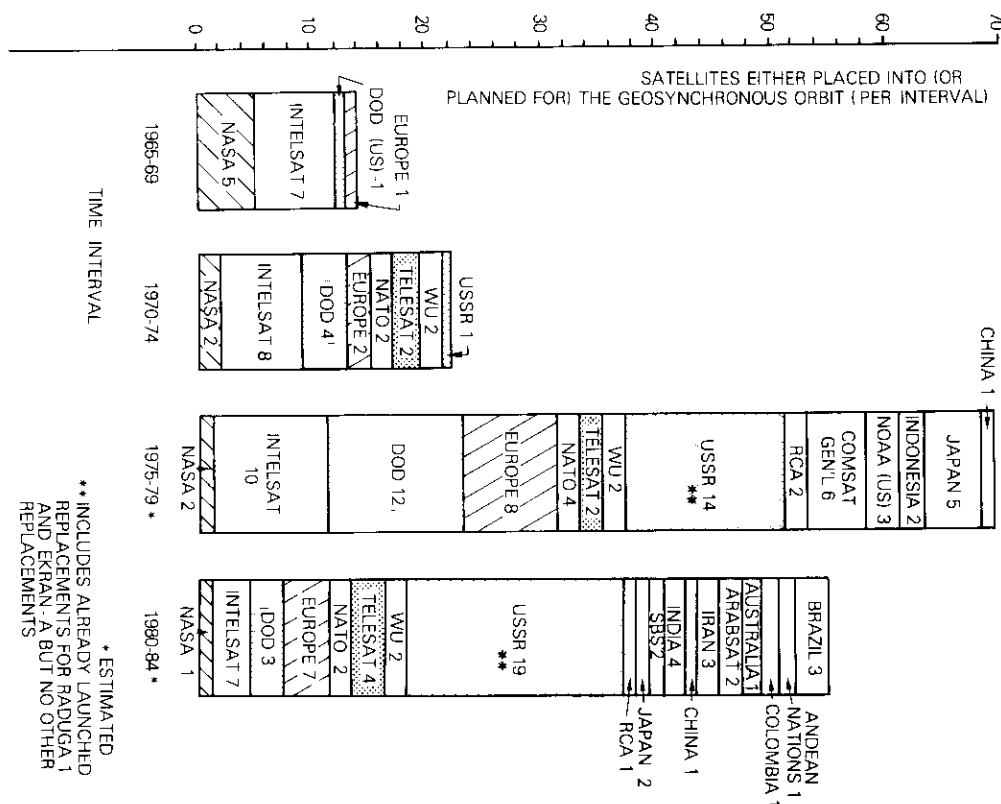


TABLE 2. ALPHABETICAL LISTING

Name	East Longitude
A Advanced Westar (see TDRS/AW)	257
AFSatCom (see FLTSAT)	
Andean Nations	285
Anik	244, 246, 247.5, 251, 256
APPLE	74
Applications Test Satellites (see ATS)	
Arab Satellite Communications Organization	
Arabsat (2)	5-20
Arcomsat (see Arabsat)	
Ariane Passenger Payload Experiment (see APPLE)	
ATS	211, 220, 254.8
AT&T (see COMSTAR)	
Australia	?
B Brasilsat	285, 290, 295, 300
Brazil	
Brasilsat	285, 290, 295, 300
Broadcast Satellite Experiment (see BSE)	
BS (see BSE)	
BSE	110
C Canada	220, 268
Dept of Communications	
Communications Research Center	
Hermes	244
Telesat Canada	
Anik	244, 246, 247.5, 251, 256
CEPT (see ECS-Europe)	10
Cherry Blossom (see Sakura)	135
China, Peoples Republic of	
Radio Management Bureau	
STW	70, 125
Chrysanthemum (see Kiku)	
Colombia (see also Andean Nations)	285
Communications Technology Satellite (see CTS or Hermes)	
COMSAT General Corp (see USA)	
Comstar	232, 265, 270.3
CS (see Sakura)	135
CSE (see Sakura)	135
CTS	244
D Defense Satellite Communications System (see DSCS-US)	
Disaster Warning	?
Domestic Satellite Communications System (Japan)	120-140
DSCS (Japan) (see Domestic Communications System)	
DSCS (US)	54, 175, 220, 347

E EBS	?
ECS (Europe)	10
ECS (Japan)	145
Ekran (or Ecran)	99
ESA (see European Space Agency)	
ETS-II (see Kiku No. 2)	
European Broadcasting Union (EBU) (see EBS)	
European Communications Satellite (see ECS-Europe)	
European Conference of Postal and Telecommunication Administration (CEPT, see ECS-Europe)	10
European Space Agency (ESA)	
ECS	10
GEOS	0-35
H-Sat	?
LO-4	?
Marots/Marecs	40, 347.5
Meteosat	0
OTS	10
Phebus	?
Eurosat (see H-Sat)	
Experimental Communications Satellite (see ECS-Japan)	
Experimental Test Satellite (see Kiku No. 2)	
F FLTSAT	290, 337
FLTSATCOM (see FLTSAT)	
Fleet Satellite Communications (see FLTSAT)	
France (with the Federal Republic of Germany)	
Symphonie	49, 348.5
G Gals	45, 85, 190, 335
General Purpose Communications Satellite System	?
GEOS (ESA)	0-35
Geostationary Earth Observation Satellite (see GEOS)	
Geostationary Meteorological Satellite (see GMS)	
Geostationary Operational Environmental Satellite (see GEOS)	
Germany, Federal Republic of	
Direct TV Broadcast Satellite	350
Symphonie (with France)	49, 348.5
GMS (Himiwari)	140
GEOS	70, 225, 275, 285
GOMS	70
H Heavy Broadcast Satellite (see H-Sat)	
Hermes	244
Himiwari	140
H-Sat	?

TABLE 2. ALPHABETICAL LISTING (continued)

	Name	East Longitude
I	India	
	Indian Space Research Organisation (ISRO)	
	APPLE	74
	INSAT	71, 74
	ISCOM	102
	Indian National Satellite (see INSAT)	
	INSAT	71, 74
	Indonesia	
	PERUMTEL	
	Palapa	77, 83
	International Telecommunications Satellite Organization	
	INTELSAT	56.5, 57, 60.0, 60.2, 62.9, 63.0, 66.0, 174.0, 179.0, 325.5 329.0, 330.5, 333.0, 335.5, 336.0, 339, 340.5, 342.0, 356.0, 359.0
	Iran	
	Telecommunications Company of Iran	
	Zohreh	26, 34, 47
	ISCOM	102
	Italy	
	Consiglio Nazionale della Ricerche (CNR)	
	SIRIO	345
J	Japan	
	National Space Development Agency (NASDA)	
	BS (or BSE)	110
	ECS	145
	Himiwari (Sunflower or GMS-1)	140
	Kiku No. 2 (ETS II or Chrysanthemum)	130
	Sakura (CS) (Cherry Blossom)	135
	Nippon Telephone and Telegraph (NTT)	
	Domestic Satellite Communications System	120-140
	JBS (see BSE)	
K	Kiku No. 2 (Chrysanthemum or ETS II)	130
L	Launch Opportunity 4 (see LO-4)	
	LES	256, 316
	Lincoln Experimental Satellite (see LES)	
	LO-4 (see H-Sat)	
	Loutch	58, 90, 140, 346
	Loutch P	45, 85, 190, 335
M	Marecs (see Marots/Marecs)	
	Marisat	73, 176.5, 345
	Marots/Marecs	40, 347.5
	Massachusetts Institute of Technology (MIT) (see LES)	
	Medium Scale Broadcasting Satellite for Experimental Purposes (see BSE)	
	Meteosat	0

N	NATO	220, 310, 342
	Nordic Nations	0
	Nordsat	0
	North Atlantic Treaty Organization (NATO)	
	NATO	220, 342
O	Orbital Test Satellite (see OTS)	
	OTS	10
P	Palapa	77, 83
	Phebus (see H-Sat)	
	Polyvalent Heavy Bus (see Phebus)	
	Public Service Satellite	?
R	Raduga (see Statsionar Numerical Series)	35, 80
	RCA (see Satcom) (see USA)	
S	Sakura	135
	Satcom (RCA)	225, 241, 261
	Satellite Business Systems (see USA)	
	SBS	238, 254
	SEOS (see Stationary Earth Observation Satellite)	
	SIRIO	345
	SMS	70, 225, 255
	Stationary Earth Observation Satellite (SEOS)	?
	Statsionar Numerical Series (aka Raduga after launch)	35, 45, 80, 85, 90, 140, 190, 335.0, 346.5
	Statsionar-T (see Ekran)	
	Stormsat	?
	STW	70, 125
	Sunflower (see Himiwari)	
	Symphonic	49, 348.5
	Synchronous Meteorological Satellite (see SMS)	
	Syncom-4	?
T	TDRS/AW	189, 257, 261, 319
	TDRSS (see TDRS/AW)	
	Tracking and Data Relay Satellite (see also TDRS/AW)	189, 261, 319
U	Union of Soviet Socialist Republics (USSR)	
	Ministry of Posts and Telecommunications	
	Ekran	99
	Gals	45, 85, 190, 335
	GOMS	70
	Loutch	58, 140, 335, 346
	Loutch P	45, 85, 90, 190
	Raduga	35, 80
	Statsionar	35, 45, 80, 85, 90, 99, 140, 190, 335.0, 346.5
	Volna	45, 58, 85, 140, 190, 335, 346
	United States of America (USA)	
	Department of Defense	
	Defense Communications Agency (DCA)	
	DSCS (US)	54, 175, 220, 347
	FLTSAT	290, 337

TABLE 2. ALPHABETICAL LISTING (continued)

Name	East Longitude
United States of America (USA) (continued)	
General Purpose Communications Satellite	?
LES	256, 316
Department of Commerce	
National Oceanic and Atmospheric Agency (NOAA)	
Disaster Warning	?
GOES	70, 225, 275, 285
SMS (with NASA)	70, 225, 255
National Aeronautics and Space Administration (NASA)	
ATS	211, 220, 254.8
CTS (with Canada)	244
Public Service Satellite	?
SEOS	?
SMS (with NOAA)	70, 225, 255
Stormsat	?
COMSAT General Corporation	
Comstar	232, 265, 270.3
Marisat	73, 176.5, 345
RCA American Communications, Inc. (RCA Americom)	
Satcom	225, 241, 261
Satellite Business Systems	
SBS	238, 254
Western Union Space Communications Corporation	
TDRS/AW	189, 257, 261, 319
Advanced Westar	257
Tracking and Data Relay Satellite	189, 261, 319
Western Union Telegraph Company	
Westar	236.5, 261
V Volna	45, 58, 85, 140, 190, 335, 346
W Westar	236.5, 261
Westar, Advanced	257
Western Union (see USA)	
Z Zohreh	26, 34, 47

TABLE 3. SATELLITE LOCATIONS BY FREQUENCY BAND

Frequency Band	East Longitude
136 to 750 MHz	0, 0-35, 10, 45, 70, 73, 85, 99, 130, 140, 176.5, 190, 211, 220, 225, 254.8, 255, 256, 260, 275, 285, 289, 290, 316, 335, 337, 345
1.5 to 3.0 GHz	0, 0-35, 5-20, 40, 45, 58, 70, 71, 73, 74, 85, 130, 140, 176.5, 189, 190, 220, 225, 255, 257, 261, 275, 285, 289, 319, 335, 342, 345, 346, 347.5
3.0 to 6.5 GHz	5-20, 35, 40, 45, 49, 56.5, 57, 58, 60, 60.2, 62.9, 63, 66, 70, 71, 73, 74, 77, 80, 83, 85, 90, 99, 102, 120-140, 125, 135, 140, 145, 174, 176.5, 179, 190, 211, 220, 225, 227.2, 231.8, 232, 236.4, 236.5, 241, 246, 251, 254.8, 256, 257, 261, 265, 269, 270.3, 274.3, 278.3, 285, 290, 295, 300, 325.5, 329, 330.5, 333, 335, 335.5, 336, 339, 340.5, 342, 345, 346.5, 347.5, 348.5, 356, 359
7 to 9 GHz	45, 54, 85, 175, 190, 220, 256, 260, 290, 316, 335, 337, 342, 347
14/11 GHz	10, 26, 34, 40, 45, 47, 58, 60, 63, 66, 85, 90, 130, 140, 190, 325.5, 329, 333, 335, 336, 339, 342, 345 ^a , 346, 347.5, 350
14/12 GHz	0, 34, 110, 189 ^b , 220, 238, 244, 247.5, 251, 254, 257, 261 ^b , 319 ^b
30/20 GHz	54, 120-140, 130 ^c , 135, 145 ^d , 175, 220, 232, 256 ^e , 265, 270.3, 316 ^e , 347

^a 11 and 17 GHz.

^b 13 and 15 GHz.

^c 34.5 GHz.

^d 31.7 and 34.8 GHz.

^e 32 and 36 GHz.

El receptor de baliza del COMSTAR

A. F. STANDING

Abstracto

Se describe un receptor capaz de recoger datos sobre propagación a 19 y 29 GHz y de realizar las necesarias pruebas en órbita con las radiobalizas del satélite COMSTAR, en las frecuencias de 19 y 24 GHz. El receptor consta de dos partes: una integrada por los componentes de radiofrecuencia que van montados detrás de una antena de 5 metros, y otra compuesta por el receptor principal y el equipo de control, situados a unos 20 metros de distancia. Se emplea un convertidor de una sola frecuencia con un circuito de fijación de fase desviada de 5 MHz, que está fijado a la señal vertical de 19 GHz menos afectada por la atenuación de la señal inducida por la lluvia (desvanecimiento). También se utiliza un oscilador —controlado por un servomecanismo de circuito abierto para seguir la frecuencia predicha de la baliza— para transferir la fijación de fase cuando la magnitud del desvanecimiento es mayor que la gama dinámica del receptor. Esta técnica prolonga de 10 a 15 dB la gama de los datos sobre amplitud y asegura que se pueda volver a fijar la fase con rapidez al final del desvanecimiento; los datos sobre la fase se pierden al efectuarse la transferencia.

Se incluye el equipo necesario para medir siete componentes de amplitud y cuatro de fase. Las de amplitud son: polarizaciones vertical y cruzada a 19 GHz, polarizaciones horizontal y cruzada a 19 GHz, y portadora y bandas laterales de 29 GHz. Las de fase son: polarizaciones vertical y horizontal a 19 GHz, portadora y bandas laterales de 29 GHz y portadoras de 19 y 29 GHz.

Author Index, CTR 1977

- ABUTALEB, B. E. A., Manning, K. F., Phiel, Jr., J. F. & Westerlund, L. H., "The COMSTAR Satellite System," Spring, pp. 35-83 [CTR77/116].
- ATOHOUN, I., See Dostis, I. [CTR77/123].
- BARRETT, M. J., "19- and 28-GHz IMPATT Amplifiers," Spring, pp. 129-152 [CTR77/120].
- BRISKMAN, R. D., "The COMSTAR Program," Spring, pp. 1-35 [CTR77/115].
- CALVIT, T. O., See Lipke, D. W. [CTR77/130].
- CHAKRABORTY, D., Sugiyama, M. † & Muratani, T., † "Field Tests of 120-Channel Hybrid Modems via Satellite," Spring, pp. 299-309 [CTR77/128].
- CHEN, M. H., "Singly Terminated Pseudo-Elliptic Function Filter," Fall, pp. 527-541 [CTR77/135].
- COOPERMAN, R. S., see Gribbin, W. J. [CTR77/117].
- DINSTEIN, I., "DPCM Prediction for NTSC Composite Signals," Fall, pp. 429-446 [CTR77/132].
- DODEL, H., see Lipke, D. W. [CTR77/130].
- DOSTIS, I., Mahle, C. E., Riginos, V. E. & Atohoun, I. G., "In-Orbit Testing of Communications Satellites," Spring, pp. 197-226 [CTR77/123].
- DUNLOP, J. D. & Stockel, J. F., "Orbital Performance of NTS-2 Nickel-Hydrogen Battery," Fall, pp. 639-647 [CTR77/141].
- FANG, R. J. & Sandrin, W. A., "Carrier Frequency Assignment for Nonlinear Repeaters," Spring, pp. 227-245 [CTR77/124].
- FLEMING, P. L., see Koskos, P. [CTR77/138].
- FLIEGER, H. W., see Hyman, N. L. [CTR77/122].
- FUENZALIDA, J. C., Rivalan, P. & Weiss, H. J., "Summary of the INTELSAT V Communications Performance Specifications," Spring, pp. 311-326 [CTR77/129].
- GATFIELD, A. G., "Characteristics of PCM Telephone Voice Channels," Fall, pp. 625-637 [CTR77/140].
- GETSINGER, W. J., "Centimeter Wave Beacon Transmitter Design," Spring, pp. 109-128 [CTR77/119].
- GETSINGER, W. J. & Hung, H. L., "Phase Correction of IMPATT Amplifiers," Fall, pp. 543-554 [CTR77/136].
- GRIBBIN, W. J. & Cooperman, R. S., "COMSAT General Satellite Technical Control Network," Spring, pp. 85-102 [CTR77/117].
- HARRIS, J. M. & Hyde, G., "Preliminary Results of COMSTAR 19/29-GHz Beacon Measurements at Clarksburg, Maryland," Fall, pp. 599-624 [CTR77/139].
- HORNA, O. A., "Echo Canceller with Adaptive Transversal Filter Utilizing Pseudo-Logarithmic Coding," Fall, pp. 393-428 [CTR77/131].

- HUNG, H. L., see Getsinger, W. J. [CTR77/136].
 HYDE, G., see Harris, J. M. [CTR77/139].
 HYMAN, N. L., Perlmutter, D., Flieger, H. W. & Schrantz, P. R., "Thermal and Structural Design Aspects of the Centimeter Wave Beacon," Spring, pp. 171-196 [CTR77/122].
 KAUL, A. K., "A Dynamic Model for Satellite Nonsynchronous ALOHA Systems," Spring, pp. 263-290 [CTR77/126].
 KOSKOS, P., Fleming, P. L. & Reynolds, J. H., "Reliable IMPATT Diodes for the COMSTAR Centimeter Wave Beacon," Fall, pp. 577-597 [CTR77/138].
 LEBOWITZ, S., see Palmer, L. C. [CTR77/134].
 LEE, Y. S., "Simulation Analysis for Differentially Coherent Quaternary PSK Regenerative Repeater," Fall, pp. 447-474 [CTR77/133].
 LIPKE, D. W., Swearingen, D. W., Parker, J. F., Steinbrecher, E. E., Calvit, T. O. & Dodel, H., "MARISAT—A Maritime Satellite Communications System," Fall, pp. 351-391 [CTR77/130].
 MAHLE, C. E., see Dostis, I. [CTR77/123].
 MOTT, R. C., "High-Performance Frequency Doublers for the COMSTAR Beacon," Fall, pp. 555-576 [CTR77/137].
 MURATANI, T., † see Chakraborty, D. [CTR77/128].
 PALMER, L. C. & Lebowitz, S., "Including Synchronization in Time Domain Simulations," Fall, pp. 475-526 [CTR77/134].
 PARKER, J. F., see Lipke, D. W. [CTR77/130].
 PERLMUTTER, D. see Hyman, N. L. [CTR77/122].
 PHIEL, J. F., see Abutaleb, B. E. A. [CTR77/116].
 POLLACK, L., "Centimeter Wave Beacons for the COMSTAR Satellites," Spring, pp. 103-108 [CTR77/118].
 REYNOLDS, J. H., see Koskos, P. [CTR77/138].
 RIGINOS, V. E., see Dostis, I. [CTR77/123].
 RIVALAN, P., see Fuenzalida, J. C. [CTR77/129].
 SANDRIN, W. A., see Fang, R. J. [CTR77/124].
 SCHRANTZ, P. R., see Hyman, N. L. [CTR77/122].
 STEGENS, R. E., "Low-Jitter Local Oscillator Source for the COMSTAR Beacon," Spring, pp. 153-169 [CTR77/121].
 STEINBRECHER, E. E., see Lipke, D. W. [CTR77/130].
 STOCKEL, J. F., see Dunlop, J. D. [CTR77/141].
 SUGIYAMA, M., † see Chakraborty, D. [CTR77/128].
 SWEARINGEN, D. W., see Lipke, D. W. [CTR77/130].
 WEISS, H. J., see Fuenzalida, J. C. [CTR77/129].
 WELTI, G. R., "SCPC Satellite Telephony with 4-Dimensionally-Coded Quadrature Amplitude Modulation," Spring, pp. 291-298 [CTR77/127].
 WESTERLUND, L. H., see Abutaleb, B. E. A. [CTR77/116].
 WILLIAMS, A. E., "A Dual-Polarized 4/6-GHz Adaptive Polarization Control Network," Spring, pp. 247-262 [CTR77/125].

INDEX OF PRESENTATIONS AND PUBLICATIONS BY COMSAT AUTHORS IN 1977

The following is a cross-referenced index of technical publications and presentations by COMSAT authors outside of *COMSAT Technical Review*. The code number at the end of an entry is the reprint code number by which copies may be ordered from Lab Records at COMSAT Laboratories, 22300 COMSAT Drive Clarksburg, MD. 20734.

- AGRAWAL, B. N. and Reiger, C., "Satellite Communications Technology," *JBIS*, Nov. 1977, pp. 433-440 [77CLR60].
 ASSAL, F. T., see Campanella, S. J. [77CLR17] & Chen, M. H. [77CLR24].
 ATIA, A. E., see Williams, A. E. [77CLR71].
 ATIA, A. E. & Williams, A. E., "Dual Mode Canonical Waveguide Filters," *IEEE MTT-S Int Microwave Symp June 76 DIGEST*, pp. 397-399 [77CLR28].
 BARGELLINI, P. L., see Edelson, B. I. [76CLR09].
 BARGELLINI, P. L., "Space and Communications," Int Meeting on Transportation and Communications, Genoa, Italy, *PROC*, Vol. 1, Oct. 77, pp. 5-20 [77CLR63].
 BARGELLINI, P. L., "Communications Satellites—The Second Decade and Beyond," *EUROCON 77, CONF PROC ON COMM*, pp. 2.6.2-601—2.6.2-607; revised version [UP052CL].
 BARGELLINI, P. L., "Invariants in the Teaching of Electrical Science," *IEEE E-21*, Feb. 78, pp. 22-25 [78 CLR01].
 BARGELLINI, P. L. & Golding, L. S.,* "Information Theory," *Electronics Designers' Handbook*, 2nd ed., ed. L. J. Giacoletto, N.Y.: McGraw-Hill, 1977, Sec. 27, pp. 27-1-27-28 [77CLR68].
 BERMAN, A. L., see Campanella, S. J. [77CLR17].
 BLEIWEISS, J. J. & Redman, P. C., "A Satellite Automatic Control System," Int Telemetering Conf, Oct. 77, *ITC/USA/77*, pp. 419-427 [77CLR51].
 BROWN, M. P., "INTELSAT V Standard "C" Earth Station Performance Objectives Applied to a Possible Eastern United States Location (14/11 GHz Frequency Band)," *IEEE EASCON 77 REC*, pp. 13-1A—A131I [77CLR38].
 CAMPANELLA, S. J., Assal, F. T. & Berman, A. L., "Onboard Regenerative Repeater," *IEEE ICC June 76 CONF REC*, pp. 6.2-121—6.2-125 [77CLR17].
 CAMPANELLA, S. J., Suyderhoud, H. G. & Wachs, M. R., "Frequency Modulation and Variable-Slope Delta Modulation in SCPC Satellite Transmission," *IEEE PROC*, Mar. 77, pp. 419-434 [77CLR08].
 CARLSON, H. E., see Fleming, P. L. [77CLR48].
 CARLTON, P. A., see Childs, W. H. [77CLR27].
 CHAKRABORTY, D., see Wolejsza, C. J. [77CLR20].